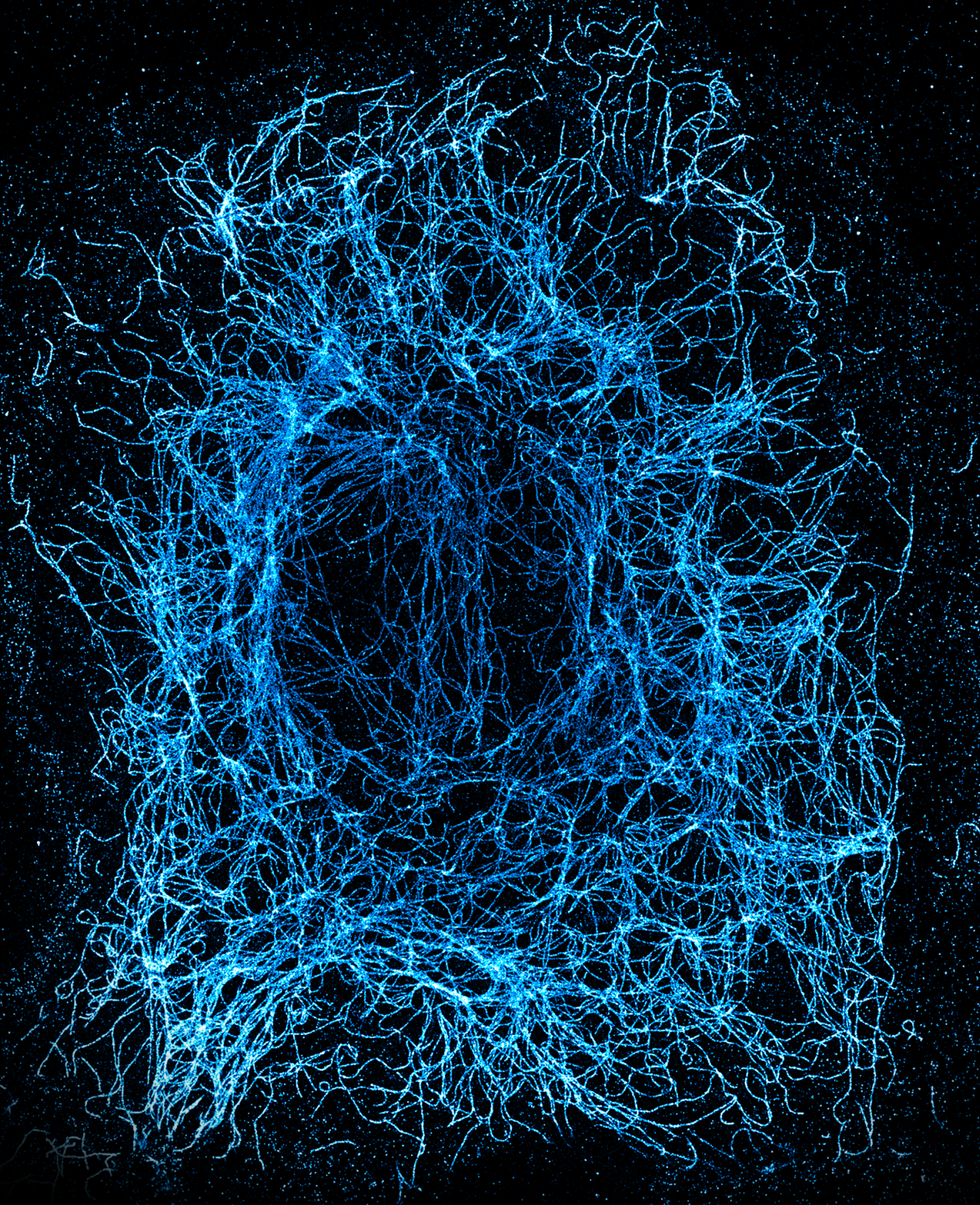


# Probes, Hardware and Software for Next-Generation Super-Resolution Microscopy

Alexander Auer





# Probes, Hardware and Software for Next-Generation Super-Resolution Microscopy

Alexander Auer

DISSERTATION  
durchgeführt an der Fakultät für Physik  
der Ludwig-Maximilians-Universität  
München, Deutschland

eingereicht am 16. März 2020  
von Alexander Vitus Auer  
geboren in Kitzbühel.

Datum der mündlichen Prüfung: 10. Juni 2020.

Erstgutachter: Prof. Dr. Ralf Jungmann  
Zweitgutachter: Prof. Dr. Joachim Rädler

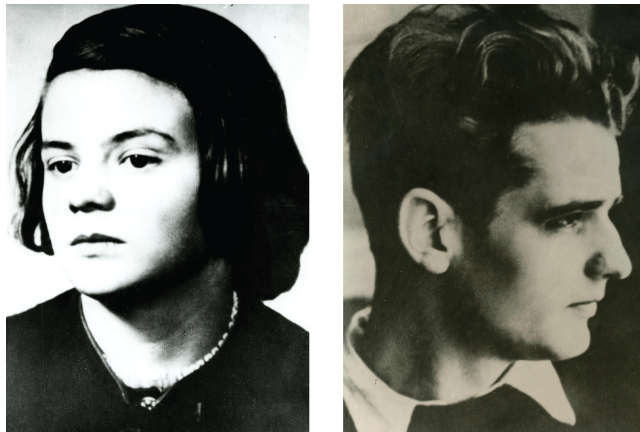


München, 2020



**2020**  
**75 Jahre Kriegsende**

*Es lebe die Freiheit.* - Hans Scholl



**Sophie und Hans Scholl** waren beide Studenten an der Ludwig-Maximilians-Universität München. Für ihre Glauben an die Freiheit haben sie sich mit ihrem Leben eingesetzt. Sie bildeten mit Alexander Schmorell, Christoph Probst, Willi Graf und Universitätsprofessor Kurt Huber den inneren Kreis der Widerstandsbewegung *Weißer Rose*. ©Deutsches Historisches Museum.



# Probes, Hardware and Software for Next-Generation Super-Resolution Microscopy

## ZUSAMMENFASSUNG

Die suprauflösende Mikroskopie ermöglicht die optische Abbildung mittels Fluoreszenzsonden unterhalb der Beugungsgrenze. In stochastischen Superauflösungsmikroskopie werden Moleküle zwischen dem nicht-fluoreszierenden Zustand (OFF-Zustand) und dem fluoreszierenden Zustand (ON-Zustand) "geschaltet", um ihre Position präziser als die Beugungsgrenze zu bestimmen. Die bekanntesten Mikroskopietechniken der lokalisationsbasierten Superauflösungsmikroskopie sind photo-activated localization microscopy (PALM) und stochastic optical reconstruction microscopy (STORM). Hier wird die Umschaltung zwischen Dunkel- und Hellzustand mithilfe photo-physikalischer oder photochemischer Prozesse durchgeführt. Eine kürzlich eingeführte Methode der Superauflösungsmikroskopie namens DNA-PAINT (deoxyribonucleic acid - point accumulation for imaging in nanoscale topography) basiert auf der DNA-DNA Wechselwirkung. Im Vergleich zu STORM oder PALM wechseln die Fluoreszenzmoleküle nicht zwischen dem dunklen und dem hellen Zustand. Das sogenannte "Blinken" in DNA-PAINT wird durch transiente Hybridisierung kurzer fluoreszierender DNA Stränge (Imager) an ihre Ziele erzeugt.

Die Arbeiten in dieser Dissertation konzentriert sich auf drei unterschiedliche Fortschritte im technologischen Aspekt der Superauflösungsmikroskopie.

### SONDEN

Im ersten Projekt dieser Arbeit zeige ich die Kombination von Einzelmolekül-Förster-Resonanzenergietransfer (englisch Förster resonance energy transfer (FRET)) mit DNA-PAINT Mikroskopie, um einige aktuelle Einschränkungen der DNA-basierten Superauflösungsmikroskopie zu überwinden. Ich evaluiere das neuartige Sondendesign mithilfe von *in vitro* Experimenten mit DNA nanostructure und zeige die Leistungsfähigkeit der FRET-basierten Sonden im zellulären Kontext.

### HARDWARE

Im zweiten Projekt beschreibe ich eine kosteneffiziente Mikroskop-Plattform für Einzelmolekülstudien, die um eine Größenordnung erschwinglicher ist und dennoch eine leistungsstarke Abbildungsfähigkeit bietet. Unter Verwendung von zweidimensionalen (2D) und dreidimensionalen (3D) *in vitro* Superauflösungsexperimenten von DNA Nanostrukturen bewerte ich die Leistung der Mikroskopie-Plattform. Schließlich zeige ich exemplarische Experimente für die zelluläre Bildgebung in mehreren Farben.

### SOFTWARE

Im letzten Projekt stelle ich ein Softwarepaket vor, das zur Unterstützung der Analyse von Daten in Superauflösungsmikroskopie entwickelt wurde. Es basiert auf dem Konzept des tiefen Lernens (englisch deep learning) mithilfe von künstlichen neuronalen Netzen und wurde entwickelt, um die Klassifikation von nanoskaligen Mustern zu automatisieren, die in supraaufgelösten Bildern zu finden sind. Ich evaluiere die Leistung des Softwarepakets anhand von *in vitro* Superauflösungsexperimenten von DNA Nanostrukturen sowie von in Zellproben.



# Probes, Hardware and Software for Next-Generation Super-Resolution Microscopy

## ABSTRACT

Super-resolution microscopy enables optical imaging using fluorescence probes below the diffraction limit. In stochastic super-resolution microscopy, molecules are „switched“ between non-fluorescent dark-state (OFF-state) and fluorescent bright-state (ON-state) in order to pinpoint their position with sub-diffraction precision. The most prominent techniques of localization-based super-resolution microscopy are photo-activated localization microscopy (PALM) and stochastic optical reconstruction microscopy (STORM). Here, the switching between dark- and bright-state is accomplished using photophysical or photochemical processes. A recently introduced super-resolution microscopy method called DNA-PAINT (deoxyribonucleic acid - point accumulation for imaging in nanoscale topography) is based on DNA-DNA interaction. In contrast to STORM or PALM, the fluorescence molecules do not switch between dark and bright states. The so-called „blinking“ in DNA-PAINT is created by transient hybridization of short fluorescent DNA strands (imagers) to their targets.

The work in this dissertation focuses on three different advancements in the technological aspect of super-resolution microscopy.

### PROBES

In the first project of this thesis, I demonstrate the combination of single-molecule Förster resonance energy transfer (FRET) with DNA-PAINT imaging to overcome some current limitations of the DNA-based super-resolution microscopy. I evaluate the novel probe design with *in vitro* experiments using DNA nanostructures and prove the performance of the FRET-based probes in a cellular context.

### HARDWARE

In the second project, I describe a cost-efficient single-molecule microscope platform, which is an order of magnitude more affordable, while still yielding high-performance imaging capacity. Using two-dimensional (2D) and three-dimensional (3D) super-resolution *in vitro* experiments using DNA nanostructures, I assess the performance of the microscopy platform. Finally, I present exemplary experiments for multiplexed cellular imaging.

### SOFTWARE

In the last project, I present a software package that is developed to assist during super-resolution data analysis. It is based on the deep learning concept of the artificial neural network (ANN) and designed to automate the classification of nano-scaled patterns found in super-resolution images. I evaluate the performance of the software package using super-resolution *in vitro* experiments of DNA nanostructures as well as targets in cellular samples.



# Acknowledgments

**MOM AND GRANDMOTHER**, thank you for the endless support and faith in me without any doubt.

**VITUS**, thank you so much for your never-ending support during all my 29 years. I am extremely thankful.

**RALF**, I am incredibly grateful for the support and the freedom and opportunity you have given me over the past years to pursue all my interests. Thank you for this great endeavor, not only in a scientific fashion but also the insights about oneself. I've learned a lot.

**JOACHIM**, thank you very much for introducing me to Ralf, ultimately making all this possible. Thank you also for evaluating my thesis.

**MAX, FLORIAN, THOMAS, AND PHILIPP**, thank you for the great atmosphere during the early days in the lab. Indeed a start-up spirit. I am very grateful for your help during all the years, I've learned a lot from you. I wish you guys all the best for the future.

**BIANCA**, thank you for your great support in every possible way.

**MAX, FLORIAN, EDUARD, SINAAN, MAX P., AND JONAS**, thank you guys for proof reading my thesis.

**SINAAN, HANNES, MAXI, MAX, CHRISTOPH, JONAS, AND CO.** Not only as flatmates but also as great friends I enjoyed every second of the time we spent together during the time of my Ph.D. Haters gonna hate, potatoes gonna potato!

**JULIA**, thank you for the wonderful time during the last years.

**MICHI**, thank you for being an awesome friend and for motivating me to exercise every week.

**ANDI, PAULI AND THE REST OF THE BAND**, thank you guys for the great time outside the lab and for the encouragement.

**AMELIE, SUSI, WOOLI, MAURICIO, AND FRIENDS AT THE LIEDL LAB**, thank you all for the wonderful collaborations and the fun parties.

**ENZO, JONATHAN, MARTIN AND FRIENDS AT THE SIMMEL LAB**, thank you for the fantastic cooperation and your help for the electrophoresis projects.

**BODO HECKER**, I would like to thank you very much for your countless help in electronics and technical questions, even years after our cooperation at the chair of Prof. Immanuel Bloch.

**MAX PLANCK MECHANICS SHOP, IMAGING FACILITY, AND ELECTRONICS SHOP**, thank you all for your support in technical issues.

**COLLABORATORS, CURRENT AND FORMER MEMBERS OF THE JUNGSMANN LAB**, thank you all for supporting me.

Thank you all!



# Publications

## PEER-REVIEWED PUBLICATIONS THAT ARE PART OF THIS CUMULATIVE THESIS

- P<sub>1</sub> **A. Auer**, M. T. Strauss, T. Schlichthaerle, and R. Jungmann. "Fast, Background-Free DNA-PAINT Imaging Using FRET-Based Probes". In **Nano Letters**, 17(10):6428–6434, Sep 2017b. ISSN 1530-6992. doi: 10.1021/acs.nanolett.7b03425
- P<sub>2</sub> **A. Auer**, T. Schlichthaerle, J. B. Woehrstein, F. Schueder, M. T. Strauss, H. Grabmayr, and R. Jungmann. "Nanometer-scale Multiplexed Super-Resolution Imaging with an Economic 3D-DNA-PAINT Microscope". In **ChemPhysChem**, 19(22):3024–3034, 2018. doi: 10.1002/cphc.201800630
- P<sub>3</sub> **A. Auer**, M. T. Strauss, S. Strauss, and R. Jungmann. "nanoTRON: a Picasso module for MLP-based classification of super-resolution data". In **Bioinformatics**, 2020. *in press*. doi: 10.1093/bioinformatics/btaa154

## OTHER PEER-REVIEWED PUBLICATIONS

1. N. S. Deußner-Helfmann, **A. Auer**, M. T. Strauss, S. Malkusch, M. S. Dietz, H.-D. Barth, R. Jungmann, and M. Heilemann. "Correlative Single-Molecule FRET and DNA-PAINT Imaging". In **Nano Letters**, 18(7):4626–4630, Jun 2018. ISSN 1530-6992. doi: 10.1021/acs.nanolett.8b0218
2. T. Schlichthaerle, M. Ganji, **A. Auer**, O. Kimbu Wade, and R. Jungmann. "Bacterially Derived Antibody Binders as Small Adapters for DNA-PAINT Microscopy". In **ChemBioChem**, 20(8):1032–1038, 2019a. doi: 10.1002/cbic.201800743
3. T. Schlichthaerle, M. T. Strauss, F. Schueder, **A. Auer**, B. Nijmeijer, M. Kueblbeck, V. Jimenez Sabinina, J. V. Thevathasan, J. Ries, J. Ellenberg, and R. Jungmann. "Direct Visualization of Single Nuclear Pore Complex Proteins Using Genetically-Encoded Probes for DNA-PAINT". In **Angewandte Chemie International Edition**, 58(37):13004–13008, 2019b. doi: 10.1002/anie.201905685
4. F. Schueder, J. Stein, F. Stehr, **A. Auer**, B. Sperl, M. T. Strauss, P. Schwille, and R. Jungmann. "An order of magnitude faster DNA-PAINT imaging by optimized sequence design and buffer conditions". In **Nature Methods**, 16(11):1101–1104, Oct 2019. ISSN 1548-7105. doi: 10.1038/s41592-019-0584-7



# Acronyms

<b>AFM</b>	atomic force microscopy
<b>AI</b>	artificial intelligence
<b>ANN</b>	artificial neural network
<b>bp</b>	base pair
<b>CAD</b>	computer-aided design
<b>CNN</b>	convolutional neural network
<b>CPU</b>	central processing unit
<b>DNA</b>	deoxyribonucleic acid
<b>Epi</b>	epifluorescence
<b>FC</b>	fully connected
<b>FRET</b>	Förster resonance energy transfer
<b>GPU</b>	graphical processing unit
<b>GUI</b>	graphical user interface
<b>HILO</b>	highly inclined and laminated optical sheet
<b>MINFLUX</b>	minimal photon fluxes
<b>MLP</b>	multilayer perceptron
<b>NA</b>	numerical aperture
<b>NGS</b>	next-generation sequencing
<b>PAINT</b>	point accumulation for imaging in nanoscale topography
<b>PALM</b>	photo-activated localization microscopy
<b>ReLU</b>	rectified linear unit
<b>RRO</b>	Rothemund rectangle origami
<b>PSF</b>	point spread function
<b>RESOLFT</b>	reversible saturable optical linear fluorescence transitions
<b>SGD</b>	stochastic gradient descent
<b>SMLM</b>	single-molecule localization microscopy
<b>STED</b>	stimulated emission depletion
<b>STORM</b>	stochastic optical reconstruction microscopy
<b>TIR</b>	total internal reflection
<b>TIRF</b>	total internal reflection fluorescence
<b>XOR</b>	exclusive OR
<b>2D</b>	two-dimensional
<b>3D</b>	three-dimensional



# Contents

1	Introduction	3
2	Theoretical Basis	9
2.1	Fluorescence	9
2.2	Total Internal Reflection Fluorescence	10
2.3	From the Diffraction Limit to Super-Resolution Microscopy	11
2.3.1	The Diffraction Limit	11
2.3.2	Single-Molecule Localization Microscopy	12
2.3.3	DNA-PAINT and Exchange-PAINT	14
2.3.4	Stimulated Emission Depletion Microscopy and MINFLUX Nanoscopy	16
2.4	Förster Resonance Energy Transfer	17
2.5	The DNA molecule	19
2.6	DNA origami as a Nanoscopic Pegboard	20
2.7	Deep Learning for Vision Systems	21
2.7.1	The Perceptron	22
2.7.2	A Multilayer Perceptron	25
2.7.3	Convolutional Neural Networks	27
3	Fast, Background-Free DNA-PAINT Imaging Using FRET-Based Probes	31
3.1	Naive speed acceleration for DNA-PAINT	31
3.2	FRET interaction for Background Reduction	31
3.3	Associated Publication P1	33
4	Nanometer-scale Multiplexed Super-Resolution Imaging with an Economic 3D-DNA-PAINT Microscope	43
4.1	Cost-efficient 3D Super-Resolution Microscopy	43
4.2	Associated Publication P2	45
5	nanoTRON: a Picasso module for MLP-based classification of super-resolution data	59
5.1	Super-Resolution Microscopy Processing of Nanopatterns using Picasso	59
5.2	Selection of Nanopatterns	60
5.3	Deep learning-assisted Classification	60
5.4	A MLP instead of a CNN Implementation	60
5.5	Associated Publication P3	63
6	Outlook	69
A	Appendix	71
A.1	Supporting Information for associated Publication P1	71
A.2	Supporting Information for associated Publication P2	93
A.3	Supporting Information for associated Publication P3	121
	References	161



# 1

## Introduction

This chapter introduces three prominent fields of current scientific research that are the subject of this thesis. The historical background is explained and a general picture of the respective research area is presented.

### SUPER-RESOLUTION MICROSCOPY

Light microscopy provides a powerful tool for scientists to study phenomena that are unobservable for the naked eye. Optical microscopy is particularly indispensable in biology and has become an integral part of life sciences. It is often the primary method of investigation for physical relationships. For several centuries, light microscopes were restricted in their imaging power. This limitation becomes particularly apparent when a light microscope is used to observe highly detailed features in the nanometer range. Typically, the captured images will appear fuzzy, and the structures in the nanometer range can no longer be identified due to this blurring. A fundamental physical phenomenon determines this limitation in the spatial resolution capability of the light microscope: Due to the wave nature of light, observations of details that were located closer than approximated half the wavelength of light were prohibited. The visible light ranges from 400 - 700 nm, which ultimately restricts the spatial resolution of conventional light microscopes to about 200 nm. If nano-scaled features are below this barrier, they are undetectable using a light microscope. This restriction in spatial resolution is the so-called *diffraction* or *Abbe limit* [8].

For a long time, researchers were forced to accept this limitation of conventional light microscopes. However, technological developments in recent decades presented approaches to overcome the diffraction limit [9, 10]. With these inventions, the research field of *super-resolution microscopy* or *nanoscopy* was formed, which marks a paradigm shift in light microscopy. For their ground-breaking innovations, the inventors of the super-resolution microscopy were honored with the Nobel Prize in Chemistry in 2014 [11]. **Figure 1.1** highlights the advancement in spatial resolution between diffraction-limited (**a**) and super-resolution microscopy (**b**).

The foundation for these technologies was the temporal separation of emission signals of individual molecules, often referred to as switching or blinking of fluorescence probes between bright and dark states. By sparsely or targeted activation of a small subset of fluorescence probes, the positions of the molecules can be localized with sub-diffraction-limited accuracy. This method allows researchers to investigate biological studies with nanometer-precise spatial resolution, which is crucial to study interplays between macromolecules in a cellular environment. The recently introduced super-resolution microscopy method called DNA-PAINT (deoxyribonucleic acid-point accumulation for imaging in nanoscale topography) accomplishes the switching of fluorescence by utilizing repetitive, transient interactions of short deoxyribonucleic acid (DNA) strands that are fluorescently labeled (termed imagers) with its complementary docking sites. These imagers dif-

fuse freely in solution and bind stochastically to the target site, which creates the single-molecule signals.

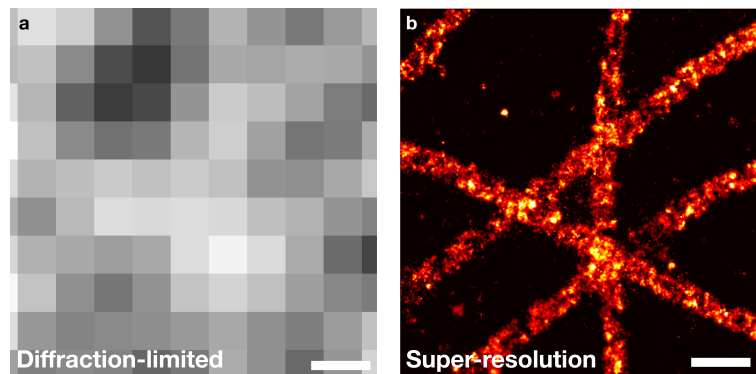


**Figure 1.1: Comparison, diffraction-limited versus super-resolution microscopy.** (a) Diffraction-limited image of alpha-tubulin filaments in a fixed cell. Bright areas indicate a higher density of fluorescently-labeled alpha-tubulin proteins. (b) Super-resolution microscopy rendering of the same area shown in (a) highlights the dramatically increased spatial resolution. This improvement enables the observation of the underlying tubulin network structure. Scale bars 200 nm. Adapted from [2]

## DNA AND DNA NANOTECHNOLOGY

The biomolecule deoxyribonucleic acid (DNA) is widely known as the carrier of genetic information in living organisms. Genetic instructions, the blueprint of cellular components like proteins, are encoded and stored in the sequence of genomic DNA.

In early research conducted by the Swiss doctor Friedrich Mischer, DNA was isolated from white blood cells for the first time in 1869 [12]. Half a century later, Phoebus Levene discovered the main components of DNA [13]. He observed that DNA is formed out of sugar deoxyribose, phosphate groups, and four nucleobases: adenine, thymine, guanine, and cytosine. While the compounds were identified, the molecular structure of DNA was still questioned until the year 1953. Based on an X-ray diffraction image of DNA recorded by Rosalind Franklin and Raymond Gosling in May 1952 [14], James Watson and Francis Crick published the first correct double-helix model of DNA a year later [15]. They unraveled that the DNA nucleobases interact in pairs. Adenine forms a bond with thymine and guanine pairs with cytosine [15]. This phenomenon is called the Watson-Crick base pairing.

In addition to its relevance for genetics in biological life, DNA has been used as a molecular building material. The interdisciplinary field of *DNA nanotechnology* was initiated in 1980s by Nadrian Seeman. He proposed to facilitate DNA and the Watson-Crick base pairing rule as a tool to engineer nanoscopic DNA complexes for structural protein analysis [16]. Seeman suggested to create nanoscaled cages out of short DNA strands to host proteins of interest. **Figure 1.2 a** illustrates macromolecules incorporated into a DNA cage and a sketch of the DNA stand arrangement for building a DNA lattice.

Another milestone for DNA nanotechnology was the invention of the so-called *DNA origami* by Paul Rothemund in 2006 [17]. He demonstrated that DNA nanostructures can be constructed using two types of DNA strands. A long single-stranded DNA molecule acts as a scaffold and gets folded into shape using short single-stranded DNA strands. Typically, the scaffold is derived from the genome of bacterial phages, while the short oligonucleotides, termed staples, are designed using computer software and then artificially synthesized. In his publication, Rothemund presented several two-dimensional (2D) DNA origami structures. A subset is shown in **Figure 1.2 b**. The initial 2D DNA origami design was later extended also into the third dimension, which led to the possibility of engineering almost arbitrary nanoscaled three-dimensional (3D) DNA complexes

[18, 19, 20].

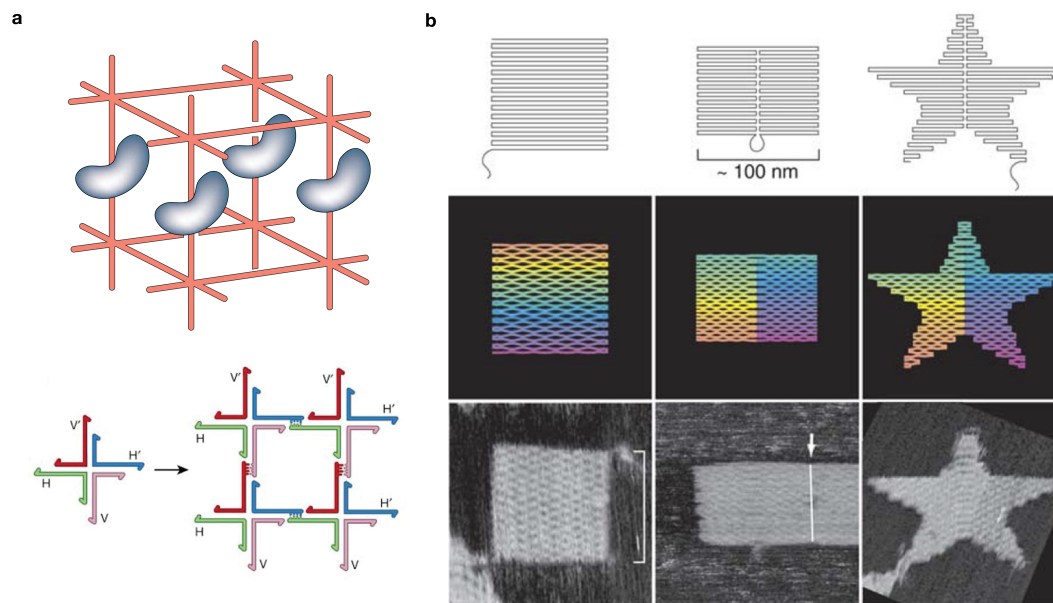


**Figure 1.2: DNA nanotechnology** (a) A sketch of a DNA lattice which represents nanoscaled cages to incorporate macromolecules of interests. Here, the macromolecules, for example proteins, are illustrated with gray objects. The lower sketch illustrates the DNA strand routing in a junction, the building block of a periodic DNA crystal. Reprinted by permission from Springer Nature [21], copyright (2003) (b) **DNA origami**, nanoscale objects formed out of DNA. A long DNA scaffold strand is folded into an artificial shape using smaller DNA strands, called staple strands. The first row illustrates the routing of the scaffold strand. In the second row, the scaffold is gradual colored according to the base pair (bp) index, starting with the first bp in red up to 7,000th bp in purple. The bottom row depicts atomic force microscopy (AFM) images of folded DNA origami. AFM images have a size of  $165 \times 165$  nm. Reprinted by permission from Springer Nature [17], copyright (2006).

## ARTIFICIAL INTELLIGENCE AND DEEP LEARNING

The computer science branch of *artificial intelligence (AI)* has gained tremendous attention in recent years. Because of its rapid progress in the last decade, applications of AI already dramatically interfere with our daily life, from the recommendation systems in video streaming platforms, online shops, or news feeds in social media to anomaly detection for fraud prevention with credit cards charges. Modern spam filters deploy artificial intelligence to detect unwanted scam or advertising emails. Online assistant systems on smartphones use AI-based speech recognition to interact with people in a human-like manner. Photos taken by smartphones are immediately put into face recognition algorithms to group the images according to the individuals on the picture. While research on AI has been carried out for almost a century, several essential accomplishments pushed AI into everyday technologies. First, the great available computation power allows the widespread adoption of AI, even on handheld devices like smartphones. Second, the enormous storage capability and universal accessibility of large amounts of data boost the performance of AI-assisted applications. And finally, the flourishing field of AI research, partly now also hosted at private companies, is propelling the progress at a fast pace with improved and more efficient algorithms.

Today, artificial intelligence (AI) describes the research on computational agents that act intelligently [22]. A computational agent is an abstract depiction of a device or software that performs actions whose behavior and actions can be attributed to intelligence. For example, a fitness tracker that records the exercise of a swimmer and automatically detects the turnaround at the poolside would represent a computational agent. It experiences the environment with the help of sensors and learns the swimming patterns from repeated training. All this with the overall aim of tracking the exercises in the best possible way.

In principle, hard-coded knowledge, a catalog of rules and information that allows a computer

agent to take action, is already a form of AI. This approach is known as *knowledge base* AI. It stores a large amount of information and facts and provides an intelligent interface engine that applies logical rules to derive new information. The well known IBM Watson is an example of a knowledge-based AI.

A more prominent area of AI research is the field of *machine learning*. In contrast to knowledge base AI, which is often human-annotated information, machine learning defines a set of methods that enable the computer agent to collect knowledge on his own. It learns from raw data, extracts patterns, and uses the discovered models to predict future data or to make decisions. Many calculation tasks in machine learning can be performed by providing the correct representation of the raw data. These representations are composed of so-called features. For example, to predict the future real estate market using machine learning, the raw data should include records about the past housing market with features like the number of rooms, the housing price, and the area of the real estate. However, correlations and features within the data are not always apparent to humans at first glance. Therefore, the computational agent can be formulated to not only extract patterns but also to discover the various features in the first place. The task of unraveling the features hidden in the raw data is referred to as *representational learning*. In the context of vision systems, representational learning is often falling short. Every pixel represents a feature, and it requires the computational agent to untangle the important from unimportant features, which can be very challenging. For example, the viewing angle in an image strongly influences the shape of objects like dogs. Two photos of the same "doggo" can result in different representations.

*This section is based on [23].*

In *deep learning* this limitation can be overcome with the introduction of simpler representations. The principle of deep learning is grounded in the hierarchical nature of the perceptual world. In other words, complex representations can be described with a composition of simpler representations. Objects are composed of motifs. Patterns likewise form motifs, and ultimately, patterns are constructed from simple shapes such as curves and lines. For example, a face can be represented with simpler shapes like circles for the eyes, lines for the eyebrows, and arcs for the lips. With artificial neural networks (ANNs), it is possible to create computational agents that can learn this hierarchical composition of motifs and patterns and store this gathered knowledge. The Venn diagram in **Figure 1.3** illustrates the relations between these areas in AI research.

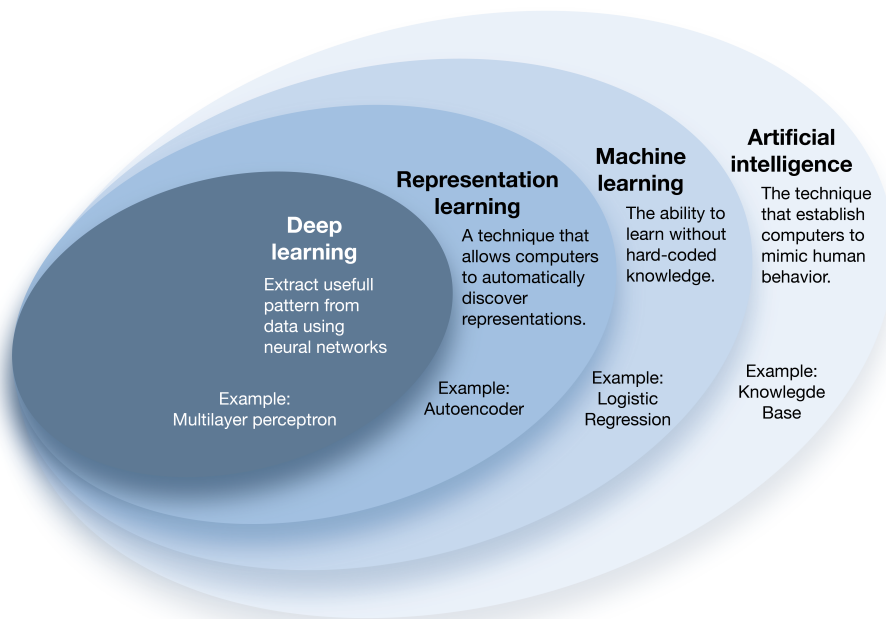
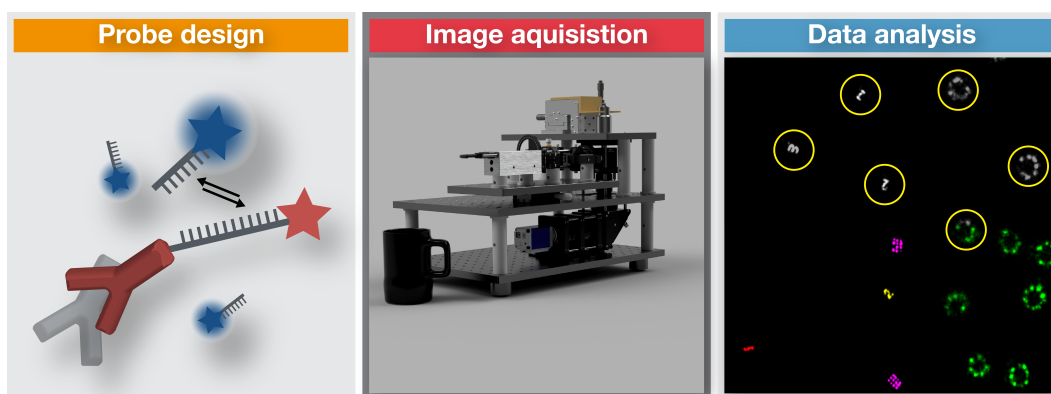


**Figure 1.3:** Venn diagram of areas in artificial intelligence. Adapted from [23].

## CONTENT OF THIS WORK

The structure of this work follows the sequence of a single-molecule experiment. It starts with a novel probe design for the super-resolution microscopy imaging, then focuses on the microscope hardware used to acquire the raw data and finally ends with the data analysis. Progress is presented at each step of the workflow.



In the following **chapter 2**, the theoretical framework relevant for this thesis will be presented. It introduces the physical background as well as technical concepts and methods related to DNA-based super-resolution microscopy and deep learning for image recognition. The content of this chapter is gathered from published research studies or specialist literature and is part of well-established knowledge. No novel scientific findings are described or claimed.

In **chapter 3**, a novel probe design for DNA-based super-resolution microscopy is described. Here, the imaging technology DNA-PAINT is extended with the molecular energy transfer FRET to overcome speed limitations in data acquisition.

The **chapter 4** presents a cost-efficient single-molecule fluorescence microscopy platform, termed LiteTIRF. This open-source setup requires only a tenth of the costs compared to a commercial system, while still offering high performance. The LiteTIRF system includes the possibility of operating in the so-called total internal reflection fluorescence (TIRF) mode, a sensitive imaging illumination, which improves the visualization of surface-bound fluorophores, essential for single-molecule studies.

The **chapter 5** focuses on the last step of a single-molecule experiment, the analysis of the gathered raw data. This part presents a software package named nanoTRON, which automates the classification of nanoscaled patterns observed in super-resolution images using deep learning.

The last part, **chapter 6**, gives an outlook to DNA-based super-resolution microscopy with an emphasis on biomedical applications.



# 2

## Theoretical Basis

### 2.1 FLUORESCENCE

Fluorescence describes the emission of photons by atoms or molecules, called fluorescent molecules or fluorophores, as a consequence of an energy release. This phenomenon belongs to the group of luminescence and can be explained as a multiple-step process and visualized with the so-called Jablonski diagram [24]. The Jablonski diagram illustrates the different electronic energy levels and their intra-molecular electronic energy transitions of atoms or molecules. Typically, radiative energy exchange processes like fluorescence emission or photon absorption are highlighted with straight arrows, while non-radiative energy changes are indicated with squiggly pointers. Every electronic energy state is again composed of multiple vibrational energy levels. **Figure 2.1 a** depicts the underlying mechanisms of fluorescence.

If a fluorescent molecule in the ground state  $S_0$  absorbs energy in the form of a photon, the molecule transitions into a higher energy electronic state  $S_1$ . Very rapidly, in the order of picoseconds, the molecule relaxes non-radiatively into the lowest excited state by dissipating energy into, for example, vibrations. After relaxation, the molecule can release the remaining excitation energy by the emission of a photon, switching it back into the energy-favorable ground state. The difference in absorption and fluorescent emission energy is called the Stokes-shift, first described by George Gabriel Stokes in the year 1852 [25]. This difference in energy results in different wavelengths, which can be exploited to separate the excitation and emission light using optical filters. Due to the multiple combinations between different vibrational energy levels and electronic energy states, transition energies are broadened from very narrow lines to expanded spectrum. This broadening is depicted in **Figure 2.1 b** with an exemplary fluorescence spectrum of an organic dye. A fluorescence molecule can undergo the cycle of energy absorption and dissipation up to a few thousand times, before they suffer structural changes, resulting in photobleaching; hence, the loss of fluorescence.

The adoption of the phenomenon of fluorescence for microscopy provides exquisite advantages over conventional transmission-based light microscopy. Among the most considerable benefits remains the excellent contrast. In combination with the ongoing emergence of highly sensitive cameras, fluorescence microscopy enables unique signal-to-noise imaging. Another remarkable feature of fluorescence microscopy is the precise labeling of the targets. Fluorescent probes can be delivered with high specificity using labeling agents like antibodies or even incorporated into the genome of the organism. Lastly, the use of different fluorescence probes in the same sample allows for multiplexed imaging. By choosing spectrally independent probes, it is possible to gather fluorescence images with commonly up to five colors. However, fluorescent molecules differ dramatically in performance [26], which often results in trade-offs between the multiplexing power and image quality.

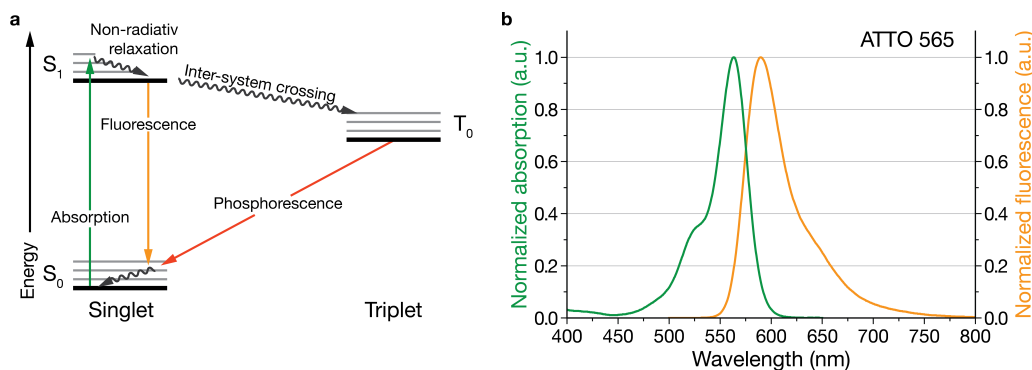


**Figure 2.1: Fluorescence.** (a) **Jablonski diagram** of a fluorescent molecule. Different energy levels with their vibrational sub-energy levels are horizontally grouped together. Straight arrows indicate radiative energy transitions. Here, absorption is marked in green and fluorescent highlighted in orange. Non-radiative transitions are plotted with squiggly pointers. Adapted from [27] (b) **Fluorescence spectrum** of the organic fluorophore ATTO 565 from ATTO-TEC GmbH. The excitation maximum is around 564 nm, the emission maximum at around 590 nm, resulting in a Stokes shift of approximately 26 nm. Spectrum data and permission for reuse from [28].

## 2.2 TOTAL INTERNAL REFLECTION FLUORESCENCE

Conventional wide-field microscopy or laser-scanning microscopy is often limited in contrast due to the large excitation volume, which results in the excitation of the vast majority of fluorescent molecules outside the field of depth. The out-of-focus signals increase the fluorescence background and reduce image contrast. Especially single-molecule studies require sensitive illumination to collect fluorescence emission with significant signal-to-noise ratios. The so-called total internal reflection fluorescence (TIRF) microscopy provides an attractive imaging modality for single-molecule studies [29, 30]. Fluorescence excitation is confined in a thin layer above the cover glass. This subtle excitation volume can be achieved with a coherent light source, e.g., a laser, that gets totally-reflected at the interface between glass and sample solution. Under these conditions, an evanescent field at the interface between the cover glass and sample is generated. The electric field of this standing wave can then excite fluorophores in the solution in a range of up to 200 nm.

TIRF setups commonly fall into different categories, which distinguish the configuration of how total internal reflection (TIR) is generated. In prism-based TIRF microscopes, traditionally, a prism made of quartz glass is placed onto the sample, and a coherent light source is coupled into the prism. The beam propagates through the quartz and the cover glass until it is reflected from the cover glass-water interface [30, 31]. Besides prism quartz, it was demonstrated that the cover glass itself could be coated with a thin layer of optical substrate to couple the light source into the sample and guide the beam for TIR. These TIRF microscopy setups are called waveguide-TIRF microscopes [32, 33].

One of the simple-to-implement solutions for TIRF is the so-called objective-based TIRF configuration [34], illustrated in **Figure 2.2 a**. Here, the objective, which collects the fluorescence emission, is also used to generate the evanescent wave. For this purpose, an objective with high numerical aperture (NA), the angular range of the objective, is available for collecting the light. Therefore, the coherent light source is coupled into the objective parallel to the optical axis of the objective. By displacing the beam to the periphery of the objective, while keeping the parallelism to optical axes of the objective, the angle between the beam and the normal to the interface glass-water gets increased. If the critical angle is reached, the beam will be totally-reflected, and the evanescent wave will protrude into the sample. A zoomed-in sketch of the optical path inside the objective is depicted in **Figure 2.2 b**.

Tokunaga et al. demonstrated that the objective-based TIRF setup can also be used to generate a laminar excitation sheet of light, which reaches deeper into to sample, while still illuminating

only a fraction of the entire specimen [35]. This mode of illumination is called highly inclined and laminated optical sheet (HILO) and is also shown in **Figure 2.2 b**.

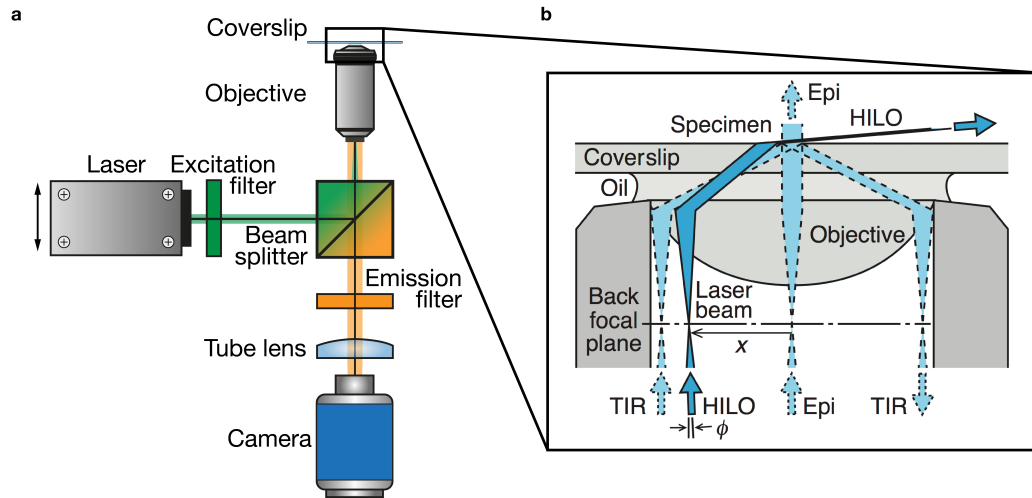


**Figure 2.2:** (a) **Objective-based TIRF setup.** The schematic drawing sketches a typical TIRF microscope setup. A laser serves as a coherent light source and a scientific camera as the detector. For objective-based TIRF, the laser beam is first spectrally cleaned-up using an excitation filter, then coupled through a beamsplitter into the high NA objective. By translating the laser beam parallel to the optical axes to the periphery of the objective lens, the laser beam can be controlled to get a totally-internal reflection. Fluorescent emission is guided and focuses on to the camera with a tube lens. Undesired laser light interferences in the emission are spectrally filtered using an emission filter. Adapted from [2]. (b) **Zoom-in cartoon of the objective** illustrates three different illumination modalities with an objective-based TIRF microscope. In epifluorescence (Epi), the laser beam co-aligns with the optical axes of the objective, which results in the excitation of the fluorescently labeled specimen above the field of view. By shifting the laser beam to the periphery of the objective lenses, the beam gets tilted. Before the angle of total-reflection is reached, a laminar sheet of excitation light (HILO) [35] can be used to excite volumes deeper in the sample. Upon the critical angle, the laser beam gets totally reflected, and an evanescent wave propagates into the specimen. The excitation volume in TIRF reaches up to 200 nm into the sample, yielding high contrast fluorescence images from targets near the coverslip. Figure part b is a reprint by permission from Springer Nature Methods [35], copyright (2008).

## 2.3 FROM THE DIFFRACTION LIMIT TO SUPER-RESOLUTION MICROSCOPY

### 2.3.1 THE DIFFRACTION LIMIT

Until the emergence of the first super-resolution techniques in the 21st century [9, 36, 37], optical microscopy was restricted by an alleged physical limitation. Ernst Abbe postulated 1873 that spatial resolution of optical microscopes is restrained by the physical nature of light, the diffraction of light [8]. He proposed in his work *“Beiträge zur Theorie des Mikroskops und der mikroskopischen Wahrnehmung”* that it is not possible to resolve two light points if they are placed closer together as half of the wavelength of emission [8]. Lord Rayleigh expressed the phenomenological observation of Abbe into mathematical equations [38]. Ultimately, the diffraction limit of a light microscope can be described with the wavelength  $\lambda$  and the distance  $d$  between the two light points [8]:

$$d = \frac{\lambda}{2 \cdot n \cdot \sin(\alpha)} = \frac{\lambda}{2 \cdot \text{NA}} \quad (2.1)$$

Rayleigh noted in his work that the formula originated from the Franco-Italian mathematician and astronomer Joseph-Louis Lagrange, who lived a century before Abbe [38]:

*...The application to the microscope was traced by means of a somewhat extended form of Lagrange’s general optical theorem,...*

Historically, Hermann von Helmholtz also published an article in the same year 1873 as Abbe and once again a year later the formalism of light microscopes [39, 40], where he characterized the performance of spatial resolution with the identical description as Rayleigh.

On a coarse-grained interpretation, the diffraction limit can be explained as the result of the incomplete transmission of information of optical components like the objective of the microscope.

*This section is based on [41] and [42].*

Intuitively, this can be compared to a radio transmitter that is not capable of reproducing the full spectrum of acoustic frequencies of a song. In the case of the microscope, the objective has a limited range of optical frequencies, which can be captured and transmitted through the tube lens onto the camera. The capability of transmission of optical frequencies is described as the optical (or modulation) transfer function  $OTF(\omega_x, \omega_y)$ , or transfer function. The imaging process of an arbitrary object  $A(x, y)$  described with the spatial coordinates  $x$  and  $y$  in the focal plane of an objective can be formulated mathematically as:

$$\mathcal{F}'[A(x, y)] = \mathcal{F}[A(x, y)] \cdot OTF(\omega_x, \omega_y) \quad (2.2)$$

$$|\omega| := \sqrt{\omega_x^2 + \omega_y^2} < \Omega \quad \text{with} \quad \Omega = 2\pi NA/\lambda \quad (2.3)$$

$\mathcal{F}'[A]$  is the resulting Fourier transformed image at the back focal plane. The complete transform of the object  $\mathcal{F}[A]$  is limited to the transmittable frequencies of the objective. It acts as a low-pass filter of optical frequencies of the object  $A(x, y)$ , meaning that the transfer function vanishes for all values of  $\omega$  obeying  $|\omega| \geq \Omega$ . For imaging a coherent light illumination the cutoff frequency  $\omega$  is given by  $\omega = 2\pi NA/\lambda$ . The tube lens operates as an inverse Fourier transformation of  $\mathcal{F}'[A]$  back into object space. The multiplication in Fourier space, corresponds to a convolution in object space. Hence, the whole image process can be formulated as:

$$A'(x, y) = A(x, y) \otimes PSF(x, y) \quad (2.4)$$

$PSF(x, y)$  is called the point spread function. As the name suggests, it is the mathematical description of the imaging process of a point light source. For a lens and a point light source at the optical axis of the lens, the  $PSF$  is given by the Airy function, illustrated in **Figure 2.3 a**. Since cameras can not detect the electric field, the image on the camera screen of the point emitter gets broadened with the intensity distribution  $I(r)$  shown in **Figure 2.3 b** with  $I(r) \propto [E(r)]^2$ .

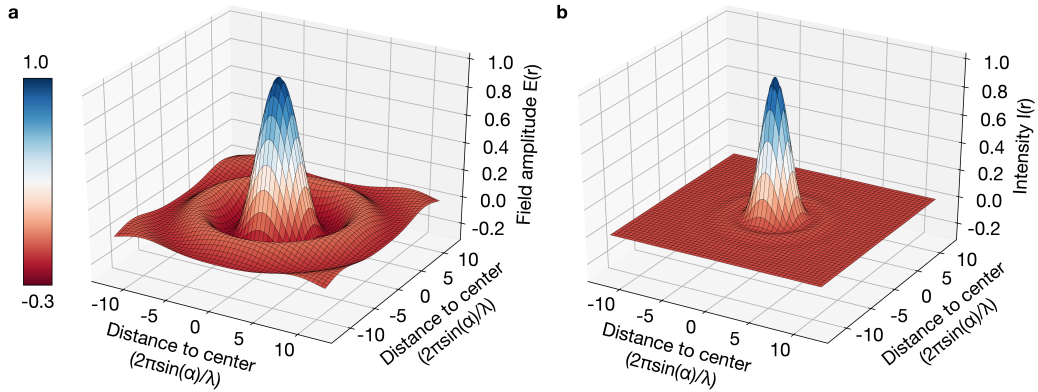


**Figure 2.3:** (a) 3D plot of 2D Airy function. Shown in the normalized electronic field distribution  $E(r)$  in the object plane of a point source as a function of the distance to the optical axis in optical units. (b) Intensity distribution  $I(r)$ , proportional to the square of the absolute values of the electronic field distribution  $E(r)$ . Adopted from [41].

### 2.3.2 SINGLE-MOLECULE LOCALIZATION MICROSCOPY

Since the invention of light microscopy, the limitation in spatial resolution due to diffraction was a fundamental barrier. Eric Betzig and Stefan Hell were honored with the Nobel Prize in Chem-

istry in the year 2014 for developing methods surpassing the diffraction limit [11]. Betzig and Hell published technologies for super-resolution microscopy to bypass the diffraction limit. Their approaches approximate the lost optical frequencies from the process of imaging or modify the operation of imaging itself [9, 10]. Revisiting the formula of the imaging process using an optical microscope in equation (2.4), we note that  $A'(x, y)$  describes the recorded image on the camera. The point-spread function  $PSF(x, y)$  for an objective is given by the intensity function (see **Figure 2.3 b**) with the assumption that the light source is a single point light source. The approximation is justified if individual fluorescent dyes or proteins with dimensions of single nanometers are recorded, which are small compared to the point spread function (PSF) with diameters in the several hundred-nanometer ranges. These circumstances enable the reconstruction (or approximation) of the distribution  $A(x, y)$ , hence the underlying sub-diffraction pattern.

In 2006, Betzig et al. published a technique for far-field fluorescence microscopy called photo-activated localization microscopy (PALM), where they exploit these circumstances [9]. The discovery of photoactivatable fluorescent proteins in 2002 from Lippincott-Schwartz et al. paved the way for Betzig's invention of the PALM super-resolution microscopy technology [43]. Fluorescent proteins were genetically attached to the target of interest. Through stochastic activation using weak laser pulses, a small subset of photoactivatable fluorescent proteins undergo a transition from the deactivate (dark) state into the activated (bright) state. Photons from the activated subset of fluorophores are collected until they photobleach and suffer the loss of fluorescence. PALM belongs to the group of single-molecule localization microscopy (SMLM) techniques.

In a SMLM experiment, a time series of images is recorded, where different subsets of distinct fluorophores are activated, as displayed in **Figure 2.4**. Reconstruction to a sub-diffraction, i.e., a super-resolved image, is typically performed with software algorithms. So far, a large variety of different frameworks were published [45, 46]. However, they usually operate along a basic workflow. First, single-molecule signals get identified in every frame. In the second step, the detected signals get localized by fitting a distribution function, for example, a 2D gaussian function. Here, the center of the fitted distribution function approximates the position of the fluorescent molecule with dedicated precision. It is worth to point out that in those steps, the data gets transformed from image data to a tabular list of localized molecules. This underlying method is illustrated in **Figure 2.5**. Super-resolved images are typically rendered from the localization table as 2D histograms. The precision of an individual localized single-molecule signal described by the standard deviation  $\sigma_{Loc}$  is proportional to the number of photons  $N$  and the standard deviation of the point spread function  $\sigma_{PSF}$  [47]:

$$\sigma_{Loc} \propto \frac{\sigma_{PSF}}{\sqrt{N}} \quad (2.5)$$

The achievable spatial resolution of diffraction-limited imaging from equation (2.1) is modified for super-resolution by a factor of  $1/\sqrt{N}$ , and neglecting higher order terms it results in [47]:

$$d \propto \frac{\lambda}{2 \cdot \sqrt{N} \cdot NA} \quad (2.6)$$

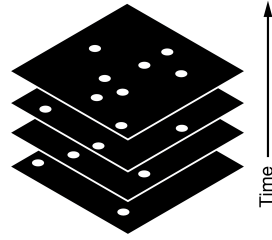


**Figure 2.4: SMLM movie sketch.** Every frame contains only a subset of fluorescent molecules that are activated and emit photons. The distance between the activated molecules is larger than the diffraction limit, which allows for sub-diffraction localization. Adapted from [44].

Zhuang et al. published a similar implementation in SMLM called stochastic optical reconstruction microscopy (STORM), where they utilize organic fluorescent dyes instead of genetically engineered fluorescent proteins [48]. While organic dyes offer higher photon emission and better photo-stability, these probes require labeling agents like antibodies or nanobodies to decorate the proteins of interest. Another notable difference of STORM is that the fluorescent molecules are switched between the deactivated and activated state until they are photo-bleached.

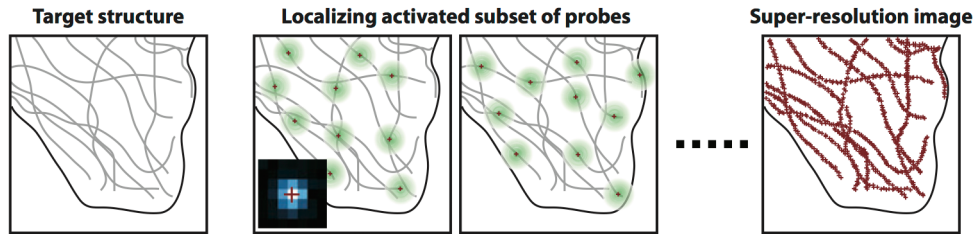


**Figure 2.5:** SMLM relies on the temporal separation of single-molecule signals. Therefore, the target structure in the examined sample is labeled with the fluorescence molecule. The fluorescence probes are switched between bright and dark states. The switching can be implemented with different approaches. After the movie is recorded, the single-molecule signals are localized in every frame. After reconstruction, a super-resolved image is created by plotting the localizations in a 2D histogram. Reprinted by permission from Annual Reviews, Inc. [49] copyright (2009).

### 2.3.3 DNA-PAINT AND EXCHANGE-PAINT

A more recent approach in localization microscopy-based super-resolution microscopy called DNA-PAINT was published by Jungmann et al. in 2010 [50]. The technique is based on the concept of point accumulation for imaging in nanoscale topography (PAINT), where in contrast to PALM or STORM, imaging is carried out using diffusing fluorescent molecules that interact transiently with the sample [51]. When the fluorescent molecule is bound to the sample, increased fluorescence from the binding site can be collected and subsequently localized with sub-diffraction resolution. However, a fundamental limitation of PAINT is achieving specificity in targeting the molecules or proteins of interest. The binding interaction relies on molecular processes like electrostatic coupling or hydrophobic interactions, which are challenging to control.

DNA-PAINT leverages the method of PAINT with the use of DNA hybridization reactions of short single-stranded DNA oligonucleotides, called imagers to their complementary single-stranded sequences. These complementary DNA strands, the so-called docking sites, are attached to the molecules of interest. Imagery are coupled with fluorescence dyes and diffuse freely in solution. Upon the binding to the docking site, amplified fluorescence due to the immobilization can be detected. This sequence-specific binding to the complementary target enables programmable interactions with high precision in targeting molecular components of interest. The so-called activated (bright) and deactivated (dark) states of the single-molecule signals are achieved by the repetitive, transient binding of imagers to the docking strand, see **Figure 2.6**. Unbound imagers in solution diffuse too fast for being localized during the camera exposure times, hence only increases the background fluorescence signal. In contrast to PALM or STORM, DNA-PAINT does not suffer from photobleaching as a reservoir of diffusing imagers can visit the docking site. Although this allows a virtually unlimited acquisition time, it also requires the application of imaging with small excitation volumes like TIRF or HILO due to the artificial background fluorescence.

Utilizing hybridization reactions of DNA strands to create the artificial blinking delivers a substantial advantage. By changing the DNA length and sequences, the kinetic parameters of the blinking reaction can be controlled and tailored to specific needs. The bright time  $\tau_{bright}$ , the period the imager is bound to the docking strand, is given by the length and the composition of the imager sequence, hence the number of complementary bases. The dissociation rate describes the stability of the duplex  $k_{off}$  and inverse proportional to  $\tau_{bright}$ :

$$\tau_{bright} = \frac{1}{k_{off}} \quad (2.7)$$

Whereas the dark time  $\tau_{dark}$ , the period between binding events, is controlled by the concentration of imagers  $c$  in solution.  $k_{on}$  is called the association rate and can be determined experimentally:

$$\tau_{dark} = \frac{1}{c \cdot k_{on}} \quad (2.8)$$

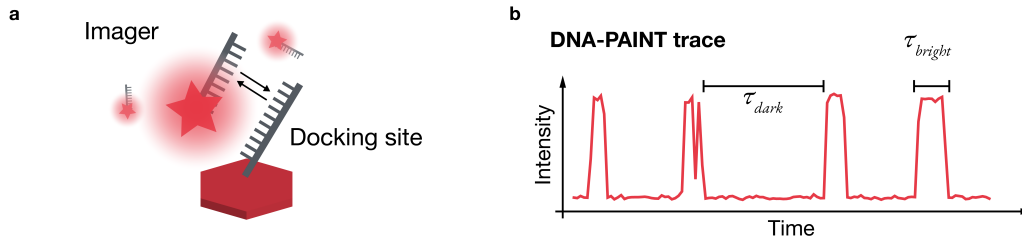


**Figure 2.6: DNA-PAINT super-resolution microscopy.** (a) Stochastic switching between fluorescence bright- and dark-states (blinking) is created using DNA fluorescent probes called imagers. The short single-stranded oligonucleotides labeled with fluorescent molecules interact transiently with single-stranded complementary DNA strands at the target, called docking strands. Adapted from [1]. (b) The time trace visualizes the fluorescent intensity captured from one docking site. The duration an imager is bound, the bright time  $\tau_{bright}$  for a given imaging buffer system at a specific temperature depends on the length of the formed duplex of the imager and docking strand. The phase between binding events, the dark time  $\tau_{dark}$  is given by the concentration of the imagers in solution. Adapted from [50].

In 2014, Jungmann et al. published an extension of DNA-PAINT called Exchange-PAINT, which enables comprehensive multiplexed imaging in a sequential fashion [52]. The concept of Exchange-PAINT is depicted in Figure 2.7. Initially, different targets are labeled with orthogonal docking strands. After labeling, single-molecule blinking data of the first target is acquired. As the imagers bind only transiently, the solution with the imagers can be removed by washing with an imager-free solution. After the sample is cleared, the next imager with a different sequence is introduced. Subsequent washing and imaging rounds are carried out until the data of all targets is acquired.

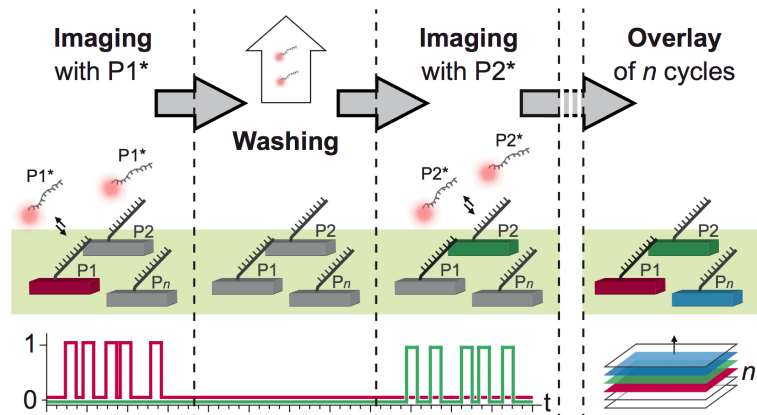


**Figure 2.7: Exchange-PAINT**, a multiplexing application using pseudo colors. The sample is labeled with single-stranded docking sites, where every target has a unique docking sequence. In sequential imaging rounds with imagers complementary to the docking sequences and subsequent washing rounds multiple targets can be imaged. Reprinted by permission from Springer Nature Methods [52], copyright (2014).

Exchange-PAINT does not rely on spectral multiplexing. The "pseudo" colors are encoded in the orthogonal nucleotide sequence of the imager strand. This sequential approach enables the usage of the same dye in every imaging round, preferably a fluorophore with the highest photostability and low unspecific interactions. Ultimately, Exchange-PAINT eliminates the compromise between emission wavelength and spatial resolution of conventional diffraction-limited or super-resolved spectral multiplexing.

#### 2.3.4 STIMULATED EMISSION DEPLETION MICROSCOPY AND MINFLUX NANOSCOPY

In the year 1994, Stefan Hell published the theory for a new scanning fluorescence microscope is called stimulated emission depletion (STED) microscope, which uses the principle of reversible saturable optical linear fluorescence transitions (RESOLFT) microscopy [10]. It is based on stimulated emission [53] using inhomogeneous illumination, which can switch fluorescence molecules into a fluorescence deactivated (dark) state. Spontaneous emission of photons, thus fluorescence, gets prevented by the STED laser as the excited fluorophore is forced to relax into the ground state via the radiation of a photon by stimulated emission. Photons from stimulated emission have a different wavelength than photons from fluorescence and can, therefore, be separated with optical filters. This process is illustrated with the Jablonski diagram in **Figure 2.8 a**. A typical STED microscope setup is depicted in figure **Figure 2.8 b** [49]. Besides the laser for fluorescence excitation, the microscope includes a STED laser. By excluding a small spot in the center of the STED laser, the effective area of fluorescence excitation gets shrunk, and the achievable resolution surpasses the diffraction limit. This is visualized in **Figure 2.8 c**. The "donut-shape" STED beam profile is usually generated via a phase mask in the STED path. During data acquisition, the sample is scanned point by point, and fluorescent signals are recorded with a photodetector instead of a camera. Half a decade after Hell proposed the STED microscope, the optical setup was manufactured, and Hell et al. published the first super-resolved microscopy images [36, 37].

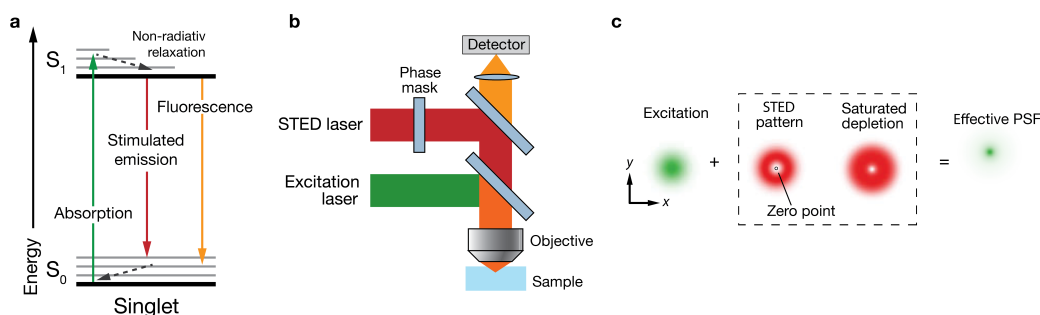


**Figure 2.8: STED microscopy** (a) Jablonski diagram visualizing the phenomenon of stimulated emission that is utilized in STED microscopy. It describes the process of a photon that interacts with an excited atom or molecule, causing it to release the excitation energy in the form of another photon. Importantly, the emitted photon shares identical physical properties like wavelength as the incoming photon. Adopted from [49]. (b) The basic schematic sketches a typical STED microscope used for super-resolution imaging. Besides the excitation laser, the STED laser with a phase mask is incorporated into the excitation path. The phase mask creates the "donut-shaped" STED beam profile. The objective focuses the excitation and STED beam onto the sample. The emission light is collected by the objective and recorded with a photon detector. Reprinted by permission from Annual Reviews, Inc. [49] copyright (2009). (c) By combining the "donut-shaped" STED pattern with the excitation beam, the effective PSF can be contracted below the diffraction limit. Fluorescent molecules in the high-intensity areas of the STED beam (saturated depletion area) are forced to undergo stimulated emission. Therefore, they do not release the excitation energy via fluorescence and can be excluded from the emission path using optical filters. In the center of the STED beam, the zero-point, fluorescence can occur and collected with a detector. Reprinted by permission from Annual Reviews, Inc. [49] copyright (2009).

In 2017, Balzarotti et al. demonstrated that the donut-shaped laser profile could also be utilized to "triangulate" fluorophores down to single-nanometer resolution [54, 55]. By probing the fluorescent emission of the molecule around the zero-point of the beam pattern, the localization of the fluorescent probe can be predicted. The technique is termed minimal photon fluxes (MINFLUX)

nanoscopy and promises versatile imaging modalities from nanometer super-resolution microscopy, nanometer-precise short-range tracking to micro-scale long-range tracking, although requiring very complex and sophisticated instrumentation.

## 2.4 FÖRSTER RESONANCE ENERGY TRANSFER

Various molecular processes can release the energy of an excited fluorophore. The non-radiative transfer of the energy from one fluorescent molecule to another at close proximity is called Förster resonance energy transfer (FRET) [56]. In this interaction, the molecule which releases the energy is called donor (D), whereas the energy receiving molecule is named acceptor (A). An excited donor can be approximated with a localized dipole, hence oscillating charges [57], and the surrounding area divided into different layers of interaction. **Figure 2.9 a** illustrates an excited fluorescence molecule and the nearby environment. If an acceptor molecule is right next to the excited donor with a distance smaller than  $\sim 1$  nm, in the range of the so-called contact zone, the energy can be transferred directly via the exchange of excited electrons. This process is called Dexter electron transfer and was theoretically proposed by D. L. Dexter in 1953 [58]. In the upper zone, the near-field zone, the excitation energy is predominantly transferred via dipole-dipole interactions, the traditional FRET. The oscillating donor charges create an electric field and can be described as a dipole, figuratively speaking, it acts as a nanoscopic antenna. The near-field zone extends typically up to  $\sim 10$  nm. If the distance between donor and acceptor is even greater, in the intermediate and radiation zone, the energy transfer can no longer be described with the FRET theory.

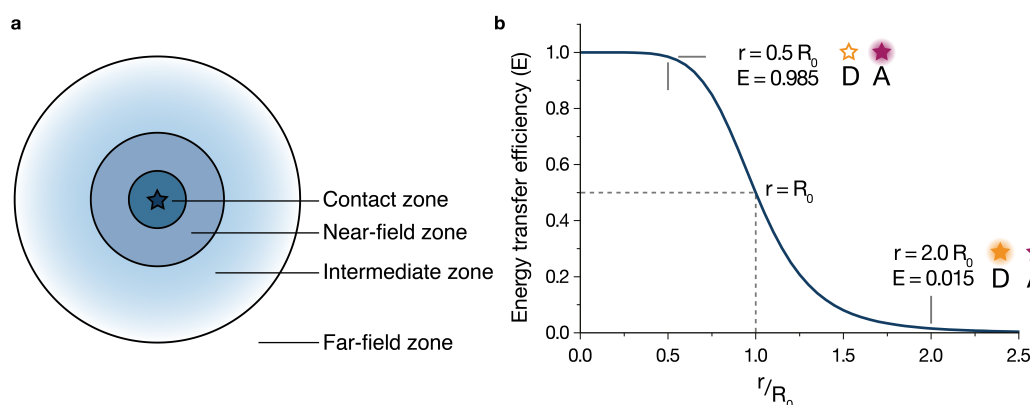


**Figure 2.9: FRET.** (a) The proximity area of an excited donor molecule can be divided into several zones of interaction for an acceptor molecule. The contact zone ( $< \sim 1$  nm) describes the area where excitation energy can be transferred via the direct exchange of electrons from the donor to the acceptor molecule. Here, FRET does not apply. In the higher zone, the near-field zone, FRET is the dominant process of energy transfer. The donor transmits the excitation energy via dipole-dipole interaction. In the intermediate and the far-field zone, radiative energy transfer can occur and FRET typically does not apply. Adapted from [57] (b) The energy transfer efficiency  $E(r)$  of FRET plotted against the separation distance  $r$  between donor and acceptor in units of the Förster radius  $R_0$ . At a distance of  $r = R_0$ , half of the excitation energy is transferred to the acceptor molecule. Adapted from [27]

In order for FRET to occur, several conditions must be met. First, the distance between donor and acceptor needs to be in the range of the near-field zone, in the order of nanometers. The energy transfer in FRET depends strongly on the distance  $r$  between donor and acceptor molecule. **Figure 2.9 b** plots the non-linear energy transfer efficiency function  $E(r)$  in terms of the so-called Förster-radius  $R_0$ , which denotes the radius  $r$ , where  $E(r)$  drops to 50%. Due to the dipole-dipole interactions, the energy transfer efficiency scales with the reciprocal 6th-power law:

$$E(r) = \frac{R_0^6}{R_0^6 + r^6} \quad (2.9)$$

The probability of the energy transfer from the donor to the acceptor per time can be described by the transfer rate  $k_T$ :

$$k_T = \frac{\Phi_D \kappa^2}{\tau_D r^6} \left( \frac{9000 \ln 10}{128 \pi N_A n^4} \right) \int_0^\infty F_D(\lambda) \varepsilon_A(\lambda) \lambda^4 d\lambda \quad (2.10)$$

where:  $r$  = distance between donor and acceptor  
 $\lambda$  = wavelength  
 $F_D(\lambda)$  = normalized fluorescence intensity of the donor  
 $\varepsilon_A(\lambda)$  = extinction coefficient of the acceptor  
 $\Phi_D$  = quantum yield of the donor  
 $\kappa$  = orientation factor  
 $\tau_D$  = lifetime of the donor in the absence of an acceptor  
 $N_A$  = Avogadro's number  
 $n$  = refractive index of the medium

A detailed derivation of the equation (2.10) can be found in [56, 57]. Besides the distance, also the fluorescence spectrum of both fluorescence molecules plays a crucial role. FRET can only occur if the emission spectrum of the donor molecule overlaps with the excitation (absorption) spectrum of the acceptor. **Figure 2.10 a** illustrates the spectra of a very common FRET dye pair: Cy3, as donor dye and Cy5 as acceptor dye. The integral in (2.10) can be derived by the so-called overlap integral  $J(\lambda)$ . The spectral overlap of the donor emission and the acceptor absorption curve is highlighted in **Figure 2.10 a**. Mathematically, it can be expressed with the integral:

$$J(\lambda) = \frac{\int_0^\infty F_D(\lambda) \varepsilon_A(\lambda) \lambda^4 d\lambda}{\int_0^\infty F_D(\lambda) d\lambda} \quad (2.11)$$

Using the overlap integral  $J(\lambda)$  the transfer rate equation (2.10) can be rewritten in a more compact form using the Förster radius  $R_0$ :

$$k_T = \frac{1}{\tau} \left( \frac{R_0}{r} \right)^6 \quad (2.12)$$

$$\text{where: } R_0 = 8.79 \times 10^3 [\Phi_D \kappa^2 n^{-4} J(\lambda)]^{1/6}$$

The last essential requirement for FRET is the orientation of the fluorescence molecules, which is described with orientation factor kappa-squared  $\kappa^2$  and included in the equations (2.10) and (2.12). For the calculation of kappa-squared, the fluorophores are described as point-dipoles with a transition dipole moment  $p = q\mu$ , where  $q = eD$  is the electron charge  $e$  multiplied with the amplitude of the dipole oscillations  $D$  and  $\mu$  is the unit vector of the direction of the dipole oscillations. **Figure 2.10 b** visualizes the geometric relation between the donor and acceptor dipole moments. Using the unit vectors of the dipole moments and the separation vector, kappa-squared is defined as:

$$\begin{aligned} \kappa &= \mu_D \cdot \mu_A - 3(\mu_D \cdot r_{DA}) \cdot (r_{DA} \cdot \mu_A) \\ &= \cos \Theta_T - 3 \cos \Theta_D \cdot \cos \Theta_A \end{aligned} \quad (2.13)$$

where:  $\mu_D$  = unit vector of the donor dipole direction  
 $\mu_A$  = unit vector of the acceptor dipole direction  
 $r_{DA}$  = unit vector of the separation direction between donor and acceptor  
 $\Theta_D$  = angle between the donor dipole and separation direction vector  
 $\Theta_A$  = angle between the acceptor dipole and separation direction vector  
 $\Theta_T$  = angle between donor and acceptor dipole direction

The orientation factor  $\kappa^2$  can range from 0 to 4, depending on the relative orientation of the transition dipole moments of the fluorescent molecules. For processes with isotropic and fast random dynamics of the dipole orientation, the average value  $\langle \kappa^2 \rangle = 2/3$  is commonly used [59].

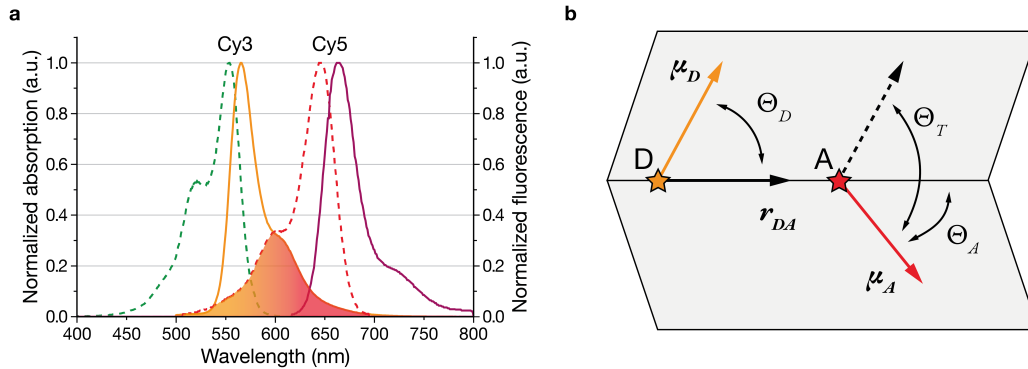


**Figure 2.10: Spectral overlap and dipole orientations.** (a) Normalized excitation and emission spectrum of the FRET dye pair Cy3 and Cy5, which is frequently used. The spectral overlap of the emission spectrum of the donor with the excitation spectrum is highlighted. Mathematically it is described as  $J(\lambda)$  in equation (2.11). Spectral data and permission for reprinting from [60]. (b) The orientation of the transition dipole moments represented by the unit vector of the donor  $\mu_D$  and the acceptor  $\mu_A$ . The direction of the distance between donor and acceptor is denoted with the unit vector  $r_{DA}$ .  $\Phi_D$  and  $\Phi_A$  mark the angle from the dipole moments of the donor (D) and acceptor (A) to the separation direction.  $\Phi_T$  is defined as the angle between donor dipole orientation and acceptor dipole orientation. Using geometric calculations kappa-squared  $\kappa^2$  can be derived, see (2.13). Adapted from [61].

The efficiency of the energy transfer  $E(r)$  plotted in **Figure 2.9 b** can be derived by the fraction of photons that are transferred to the acceptor divided by the total excitation energy released from the donor:

$$E = \frac{k_T}{k_T + \tau_D^{-1}} \quad (2.14)$$

Intuitively, the FRET process competes with all other possible processes of the energy release of the donor, which is described in the donor decay rate  $\tau_D^{-1}$ , the inverse of the donor lifetime. Efficient FRET means that the rate of transfer  $k_T$  is much faster than the decay rate  $\tau_D^{-1}$ . With the equation (2.12), the energy transfer efficiency can be rewritten into the equation from the beginning of this chapter:

$$E(r) = \frac{R_0^6}{R_0^6 + r^6} \quad (2.15)$$

This short-ranged interplay between fluorescent dyes presents a powerful imaging method for probing molecular processes with nanoscale-distance sensitivity.

## 2.5 THE DNA MOLECULE

Under biological conditions, the DNA molecule is typically observed as a complex of two single-stranded DNA polymers. Each polymer consists of repeating monomers called nucleotides. The nucleotide, in turn, consists of a backbone section and one of four nucleobases: adenine (A), thymine (T), guanine (G) or cytosine (C). In a single-stranded DNA polymer, nucleotide monomers are connected covalently by phosphodiester bonds, linking the 3'-hydroxyl (-OH) group of one backbone section and the 5'-hydroxyl group of the following backbone group. These connection positions providing the DNA strand with an intrinsic direction, described with the so-called 3' and 5' ends. **Figure 2.11 a** illustrates the chemical structure of the double-stranded complex. Two single-stranded DNA molecules join by the formation of hydrogen bonds between the nucleobases.

*This section is based on [62].*

Here, the hydrogen bonds are highlighted with dashed blue lines. With the so-called Watson-Brick base pairing, adenine pairs with thymine using two hydrogen bonds, and guanine with cytosine by three hydrogen bonds [15]. The antiparallel structure of the double-stranded DNA complex is highlighted with the complementary DNA directional ends at each duplex terminus.

**Figure 2.11 b** depicts a cartoon of the three-dimensional structure of a double-stranded DNA molecule in the so-called B-form. It describes a right-handed helix with a major and a minor groove and a diameter of 2 nm. Every 10.5 bps with a rise of 0.34 nm per bp, the DNA completes a full turn. In this configuration, the stability of the complex originates not only from the hydrogen bonds. The  $\pi$ -orbitals of the aromatic ring of one base with the  $\pi$ -orbital of the following base along a single-strand align to each and overlap. This effect is called  $\pi$ -stacking and greatly stabilizes the duplex.

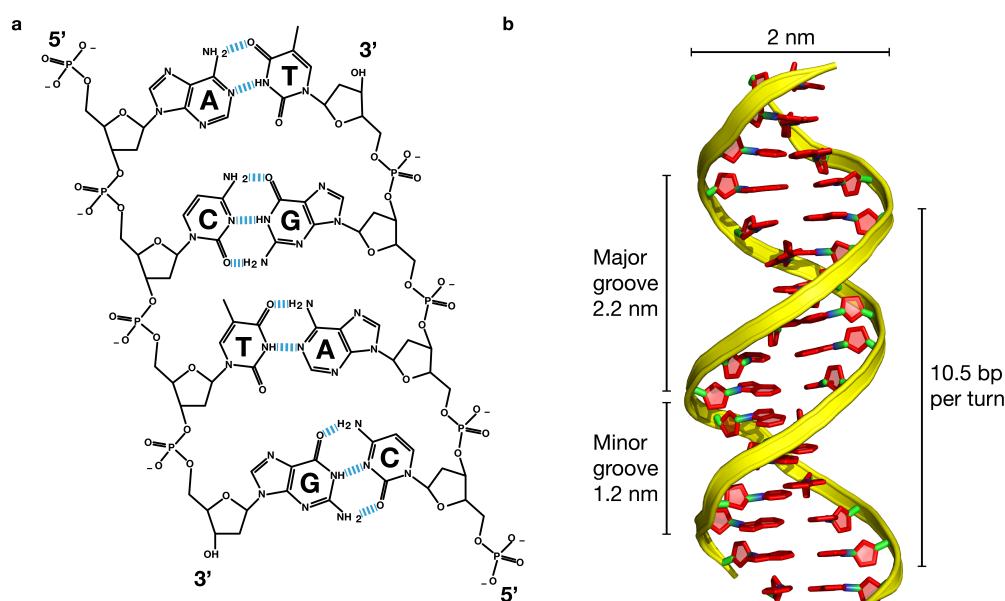


**Figure 2.11: DNA** (a) Chemical structure of a double-stranded DNA polymer. It forms out of two single-stranded DNA molecules that align antiparallel and form base pairs by hydrogen bonds, highlighted with dashed blue connection lines. (b) 3D cartoon of a 16-bp-long DNA helix in the B-form. The yellow represents the negatively charged backbone. Nucleobases are highlighted in red. The structure originates from the PDB model 3BSE and is plotted using the software package PyMOL [63, 64].

## 2.6 DNA ORIGAMI AS A NANOSCOPIC PEGBOARD

In 2006, Paul Rothemund presented the concept of DNA origami [17]. In contrast to Nadrian C. Seeman's strategy of engineering DNA crystals out of short DNA strands [16], a DNA origami is composed out of a long single-stranded DNA molecule, termed scaffold, and short oligonucleotides, called staples. The scaffold strand is typically derived from the 7249 bp long M13mp18 viral phage, while the staple strands can be synthesized artificially. The computer-designed staples bind to specific areas of the single-stranded scaffold and ultimately fold the scaffold molecule into a desired shape in the nanoscale. This assembly process is typically driven by thermal annealing, in a so-called folding ramp. **Figure 2.12 a** visualizes the folding process. Initially, scaffold and staple molecules are combined in a folding buffer. The solution is then heated up, typically cooled down in a controlled fashion. During this thermal ramp, the staples strands bind to the complementary DNA bases on the scaffold strand, highlighted here with colored scaffold sections. The synthesis of the DNA origami structures in solution is highly parallel and in a self-assembly fashion. **Figure 2.12 b** depicts the folded DNA origami, with the routed scaffold strand and the incorporated staple strands.

In the initial publication of Rothemund, he presented a single-layered DNA origami nanostructure with the dimensions  $100 \times 70$  nm, termed Rothemund rectangle origami (RRO) [17]. Jungmann et al. modified the design to correct internal twisting due to the underwinding of the DNA helices [65]. The resulting DNA origami nanostructure offers a highly symmetric and modular platform, which can be visualized in **Figure 2.12 c** as a grid of hexagons with 5 nm spacing [45]. Every hexagon represents a modification site. By extending specific staple strands (see **Figure 2.12 d**), the RRO can serve as a pegboard for the functionalization with DNA-conjugated molecules [66]. In the context of super-resolution microscopy, the rectangular DNA origami offers an exquisite platform for the evaluation of novel imaging techniques [67, 68, 69, 70, 71] as well as cutting edge microscopy setups [72, 73, 74, 33, 54, 75] using a nanoscopic ruler.

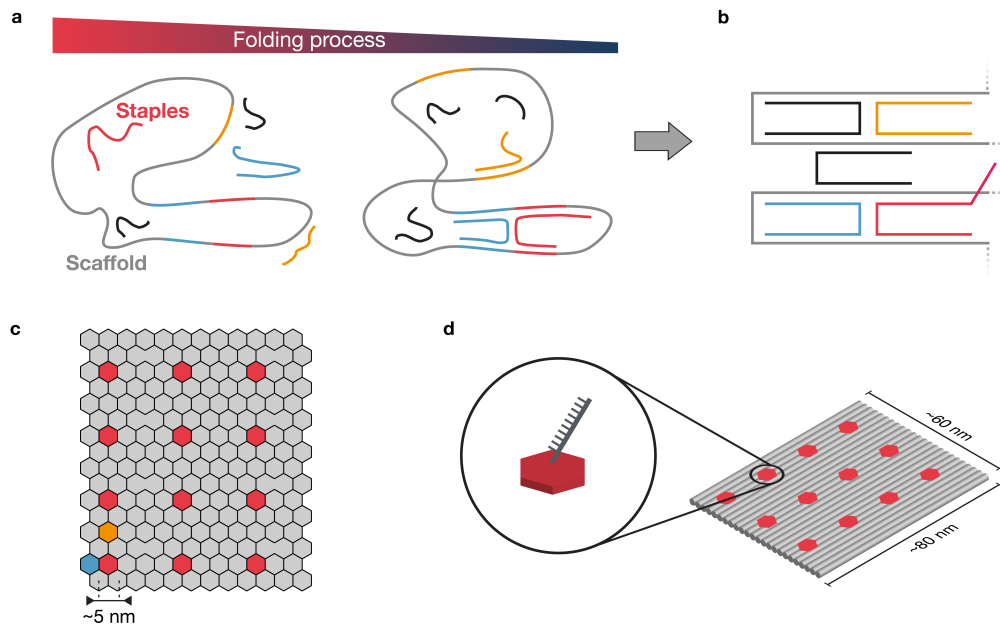


**Figure 2.12: RRO DNA origami.** The folding process to synthesize DNA origami nanostructures. The long scaffold strand (typically M13mp18 phage genome DNA) is combined with the short staple strands in a folding buffer. By thermal annealing, the staple strands bind to the corresponding region of the scaffold strand. Adapted from [17] (b) After the folding process is finished, the scaffold strands are routed in a controlled fashion using the complementary-binding staple strands. In the case of the RRO, the staple positions incorporate highly symmetric. Adapted from [45] (c) The symmetry leverages the RRO as an excellent molecular pegboard. Every staple strand can serve as a modification site, here illustrated as a grid of hexagons with a spacing of 5 nm. Adapted from [45] (d) By extending the staple strand, the modification sites get accessible for attachment of DNA-conjugated molecules or transient interaction, for example, DNA-PAINT imaging. Here the RRO is functionalized with the so-called 20-nm-grid DNA origami, with a  $3 \times 4$  grid of DNA-PAINT binding sites with a spacing of 20 nm. The red hexagons indicate the extended staple strands.

## 2.7 DEEP LEARNING FOR VISION SYSTEMS

One of the most popular areas for deep learning is the field of computer vision. Potential applications range from autonomous cars, designed to understand human automobile traffic [76] to camera-based surgery robots, which should minimize the invasiveness of operations [77]. These examples constitute only a minuscule fraction of the potential possibilities for deep learning-based vision systems. However, all those applications share the fundamental computational challenge of perceiving and recognizing images in an automated way. In the last three decades, artificial neural network (ANN) gained tremendous attention for solving these tasks of extracting the underlying patterns encoded in pictures, with as little human interaction involved as possible [78].

While there is a large variety of architectures of proposed artificial neural networks, the fundamental building block stays the same. From "shallow" neural networks with only a single layer

to profoundly deep neural networks with up to 250+ layers, all operate with the basic unit of the so-called perceptrons [79, 80].

### 2.7.1 THE PERCEPTRON

Similar to the DNA strands for DNA origami, so does the single-neuron perceptron reflect the fundamental element of an artificial neural network. Inspired by the work of McCulloch & Pitts [81] on a model of the neuron and Hebb's theory of biological learning [82], in 1958, Frank Rosenblatt presented the mathematical model of an artificial perceptron [83]. It consisted of a single neuron and featured synaptic weights and bias, and most importantly, a learning algorithm. Remarkably, although the learning algorithm has changed over the decades, this concept of an artificial neuron preserved and is still deployed in state-of-the-art ANNs.

*This section is based on [84] and [85].*

The perceptron model describes the central task of an artificial neuron. It operates as a single computational unit, which takes a set of inputs, for example, image pixel values, then performs calculations and outputs a response. In particular, the neuron receives inputs  $[x_0, \dots, x_n]$  and scales every input  $x_i$  with a weight factor  $w_i$ . All weighted inputs  $x_i \cdot w_i$  are summed up, and a bias  $b$  is added. Finally, the weighted sum  $\sum_i x_i w_i + b$  is passed through a so-called activation function to limit the output signal to a finite value. It squishes the output to a value between a given output range. Therefore it is sometimes also referred to as the squishification function. An analogy to the neurobiological action potential can motivate the application of activation function. Rosenberg proposed the binary threshold-based activation function for the perceptron, illustrated in **Figure 2.14 b**. Consequently, if the weighted sum exceeds a particular threshold value, the output  $y$  of the neuron jumps from 0 to 1. The neuron "fires". With the additional bias term  $b$ , the threshold value can be adjusted. **Figure 2.13** illustrates a single-neuron perceptron and the operations performed by the neuron. The calculation process of a perceptron is called the forward propagation and can be summarized in three essential steps:

1. **Weight:** All inputs  $x_i$  get multiplied by an input-specific weight factor  $w_i$ .
2. **Sum:** All weighted inputs are summed up, and a note-specific bias  $b$  is added.
3. **Activate:** The total sum is put into an activation function, which calculates the output  $y$ .

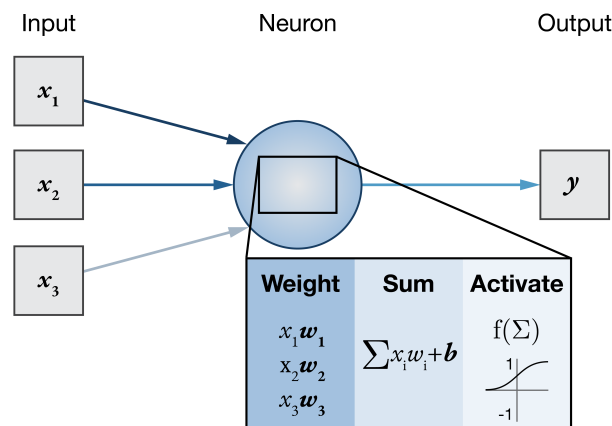


**Figure 2.13: Single-unit perceptron** is the elementary unit of an artificial neural network. It takes the inputs  $x_i$ , scales all inputs with the corresponding weight factor  $w_i$ , and adds the weighted inputs up to a total sum. Before the weighted sum is passed through an activation function, a bias  $b$  is added. The final output  $y$  is limited by the activation function to a finite value, here between  $[0, \dots, 1]$ . Modern ANN typically operate with non-linear activation function, as depicted with the sigmoid function. Adapted from [85].

The activation function plays a crucial role in the mapping of the input data to an output value. **Figure 2.14** displays different types of activation functions: linear, threshold-based, and modern non-linear activation functions. Threshold-based activation functions, like the step function shown in **Figure 2.14 b** were commonly used in the early neural network research [84]. Modern deep-learning developments [86, 80, 79, 87, 88, 89] are primarily achieved using non-linear activation functions, like the sigmoid (or logistic), hyperbolic tangent or most recent the rectified linear unit (ReLU) activation function, see **Figure 2.14 c-e** [90]. The non-linearity in the activation enables the complex mapping of non-linear inputs, which most real-world problems require [84].

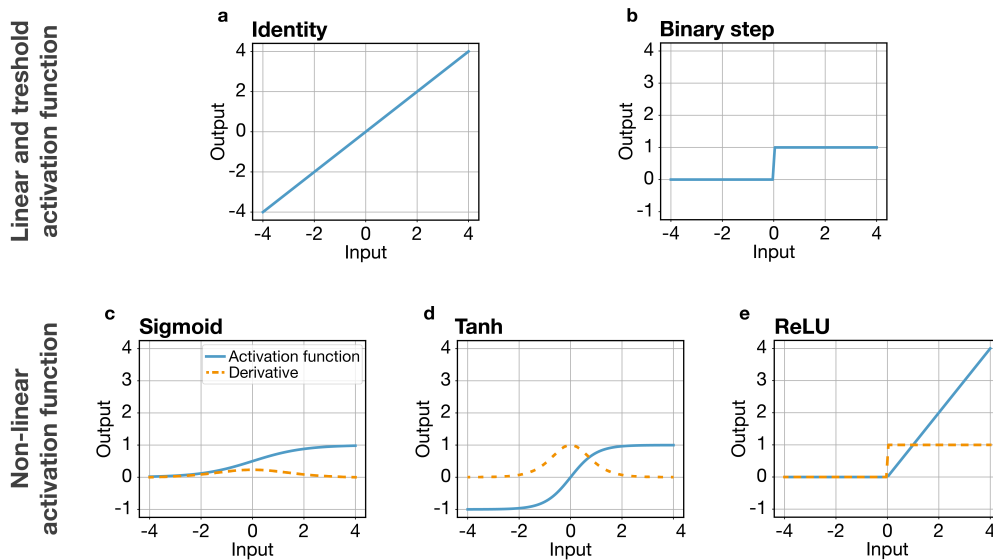


**Figure 2.14: Activation functions** (a) Identity, a linear activation function. (b) Binary step activation function. (c) Sigmoid or logistic activation function. (d) Hyperbolic tangent activation function. (e) ReLU activation function [90].

Importantly, a perceptron network (or just perceptron) is an artificial neural network with only a single layer of neurons, meaning that it can have multiple neurons in parallel, all having  $x_i$  as inputs and multiple outputs  $y_j$  with  $j$  corresponding to the number of neurons.

Following Rosenberg’s proposal of the perceptron, he engineered the ”Mark 1 perceptron” [91]. A hardware-based perceptron network, which captured a 400-pixel image and passed the pixel inputs via an array of 400 photocells into the artificial neurons. The weights of the neurons were controlled using potentiometers, adjustable resistors, driven by electric motors [84, 91]. **Figure 2.15** shows a photograph of the Mark 1 perceptron at the Cornell Aeronautical Laboratory. The early successes of Rosenblatt, Widrow & Hoff [92], and others, caused great excitement and anticipation in artificial neural networks and research about AI.

However, in the year 1969, the two mathematicians and cognitive scientists, Marvin Minsky and Seymour Papert, published a book with the unimposing title *Perceptrons: An Introduction to Computational Geometry*. Minsky and Papert demonstrated that Rosenblatt’s single-layer perceptron network with the threshold-based activation function is restricted to linearly-separable classification and, therefore, not capable of performing the exclusive OR (XOR) boolean operation. Ultimately, they proved that the single-layer perceptron with the threshold activation, which was used back then, is not a universal computing unit. The table Table 2.1 states the XOR logic. While pointing out this limitation, Minsky and Papert also presented a solution to overcome this issue. By expanding the artificial neural network from an individual single-layer perceptron to a stack of multiple consecutive single-layer perceptrons, it is possible to model every boolean operation. This concept of stacked perceptrons was initially also proposed by Rosenberg [94], and others [95]. At this point, however, an efficient learning algorithm was still missing. It is said that with their book, Minsky and Papert started a long regression around the field of AI, which is now often called the

*Minsky and Papert were not the first to point out the XOR problem. However, their book had the most significant impact in the research community.*

first winter of AI [96]. Funding was cut, pessimism increased, and the belief in the artificial intelligence gradually vanished. In the following decades, the field of AI research slowly recovered. During this period, essential concepts such as an efficient learning algorithm called back-propagation were introduced. In retrospect, AI research was a rollercoaster ride between success and setbacks [97].

Inputs		Output
$x_1$	$x_2$	$y$
True	True	False
True	False	True
False	True	True
False	False	False

**Table 2.1:** XOR boolean operation

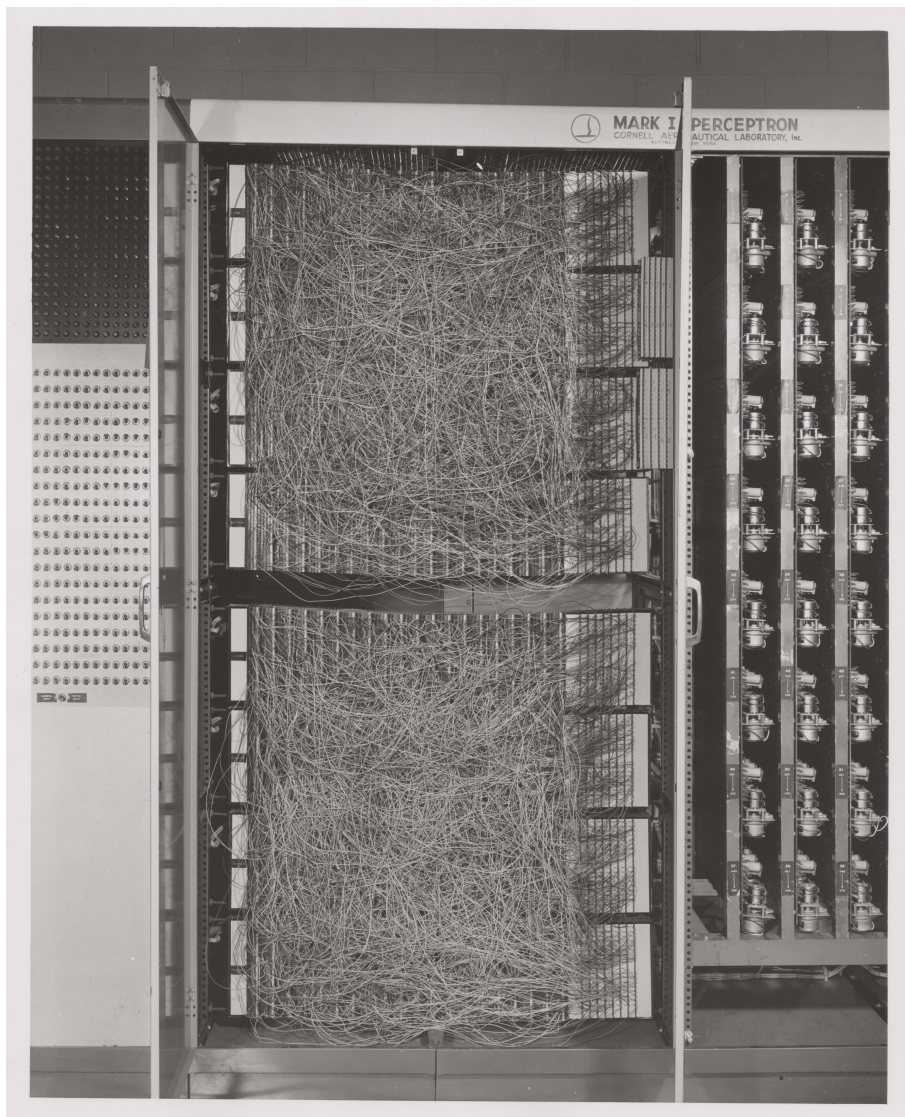


**Figure 2.15: Mark 1 perceptron.** Hardware-based implementation of Rosenberg’s perceptron algorithm processes a  $20 \times 20$  pixel image. Reprint with permission from ©Division of Rare and Manuscript Collections, Cornell University Library

### 2.7.2 A MULTILAYER PERCEPTRON

Minsky and Papert proposed that a multilayer perceptron (MLP), i.e., a ANN with multiple consecutive perceptrons, can overcome the limitations of Rosenblatt's perceptron. The XOR problem, for example, described in the previous chapter, can be solved by two layers of perceptrons. While the terminology refers to consecutive layers of single-layer perceptrons, in practice today, it is generally recognized as a single ANN with several layers of neurons, sometimes called nodes. The MLP consists of three different layer categories, the input layer, the hidden layers, and an output layer. The hidden and output layers are composed of artificial neurons with weighted inputs in contrast to the input layer, which can be seen as a transition layer. Here, inputs  $x_i$  are broadcasted into the MLP without processing. **Figure 2.16** sketches an exemplary MLP with two hidden layers and one output layer, i.e., three layers of neurons, ultimately a three-layer MLP.

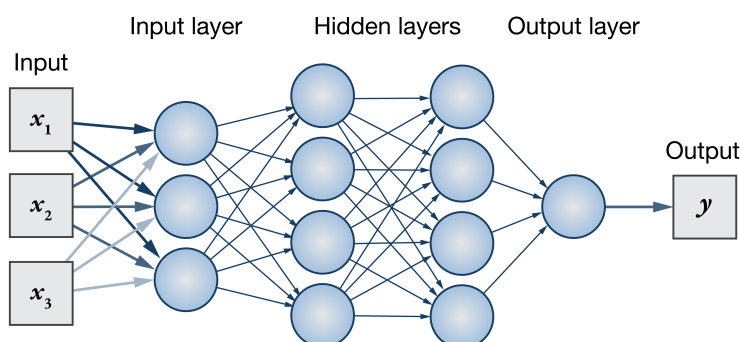


**Figure 2.16: Multilayer perceptrons** consist of consecutive layers of neurons. The input layer feeds the inputs  $x_i$  into the ANN by distributing every input to every neuron (node) in the first so-called hidden layer. Hidden layers are layers of nodes between the input layer and the final output layer. During the forward pass, every node performs the "Weight-Sum-Activate" calculation, described in **Figure 2.13**. After the data is passed through the first hidden layer, every calculated output is forwarded to every node in the second hidden layer for processing. Here, the outputs from the second layer are gathered in the final output layer, and a concluding value of  $y$  is determined. Adapted from [85].

During the forward propagation (or forward pass), the inputs  $x_i$  are transmitted from the input layer to the first hidden layer. Every input  $x_i$  is forwarded to every neuron of the first hidden layer. Same as for a perceptron, at the neuron, the inputs are weighted, summed up with a bias added, and finally passed through the activation function, which calculates the output  $y_j$ . This output, in turn, is broadcasted to every neuron in the second hidden layer. This "wiring" is called a fully connected (FC) network. After passing through every hidden layer, the output layer yields the final computed value of  $y$  for the given inputs  $x_i$ .

Without training of the MLP, the output  $y$  is nonsensical and has no meaningful value because the weights and biases are initialized with random numbers. By providing the network with labeled data and a learning algorithm, the weights and biases can be adjusted to bring the output  $y$  closer to the ground truth label. The learning enhances not only the efficiency on the labeled data, but it also increases the general "intelligence" of the ANN so that the performance is generalized beyond the training data.

During the learning algorithm, the labeled data is passed through the network. After the output  $y$  is determined, an error regarding the ground-truth value (target value) is calculated using a so-called loss (or cost) function. Importantly, the error is averaged over the whole training data. At the beginning of the learning, the loss usually starts at an arbitrary value, because the weights and biases are also initialized randomly. The loss gets decreased by correctly changing the weights and biases. This is typically achieved using an algorithm called back-propagation (back-prop), dis-

cussed already in the early AI years by various researchers [95], but usually referenced by a two-book overview published by the parallel distributed processing (PDP) research group [98, 99].

In the first step of the learning algorithm, the error is passed back into the network to determine gradients of the weights and biases and ultimately update the weights and biases of the ANN accordingly to reduce the error, thus decrease the loss. Therefore, the negative value of the computed gradients of weights and biases are multiplied with a so-called learning rate. The negative gradients determine the direction of the correction, and the learning rate controls the amount of change. The learning rate is typically in the range of  $10^{-5}$  to 5 and is manually set as a parameter. Since the error is calculated over the average of the training data, the performance of the ANN also increases for each data point. By repetitively performing the forward and back-propagation and subsequently modifying the weights and biases, the minimum of the loss function can be calculated. This process of repetitively changing the weights and biases is the so-called gradient descent. The underlying challenge is basically an optimization problem to find the minimum of the loss function, which results in the most suitable weights and biases to best approximate the target values. Common for classification tasks, the loss function is a cross-entropy loss [100]:

$$C = - \sum_i^N t_i \log(s_i) \quad (2.16)$$

$$\text{where: } t_i = \text{ground truth with } t_i = \begin{cases} 1 & \text{if correct} \\ 0 & \text{if false} \end{cases}$$

$$s_i = \text{prediction}$$

$$N = \text{classes}$$

*SGD is not limited to ANNs. It can be applied in many machine learning applications.*

In practice, these adjustments for optimizing the MLP are not performed using gradient descent, but instead with a method called stochastic gradient descent (SGD) [101, 102, 85]. Here only a random subset of the training data is selected to calculate the error, the gradients, and thus the changes for adjustment. By taking only subsets of the training data, the learning process is dramatically accelerated. **Figure 2.17 a** illustrates a simplified loss function with a single weight factor and the SGD approach to localize the minimum. After all subsets of the entire training data are used for the optimization, the first so-called epoch of learning is completed. Usually, the optimization continues in subsequent epochs with different and shuffled subsets until either a stop criterion or the maximum number of epochs is reached.

The learning process can be visualized with the help of a so-called learning curve by plotting the loss (cost) throughout the epochs. A schematic learning curve is depicted in **Figure 2.17 b**. To make the learning more robust, a common practice for deep learning is the train-validation split [85]. Here, a small fraction of the training data set is set aside. The reduced training set is used for learning, thus adjusting the weights and biases, while the validation set serves as an evaluation of the learning progress. By additionally observing the loss of the validation set, it is possible to identify potential learning artifacts, for example, overlearning. Overlearning (or overfitting) can happen when the loss of the training set decreases to zero, but the loss of the validation set starts to increase again. This deviation indicates that the ANN is beginning to learn specific features of the training data and will perform more inferior with unknown data. With the loss of the validation set, an early-stop criterion can be set to avoid the overfitting. Once the criterion is reached, the learning is terminated. Another approach to prevent potential overfitting is to reduce the complexity of the MLP by reducing the number of layers and nodes.

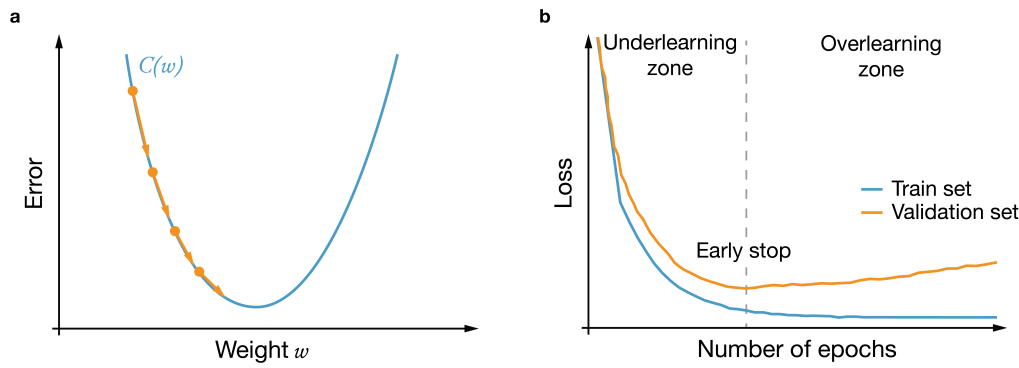


**Figure 2.17:** (a) Simplified loss function  $C(w)$  with one weight parameter  $w$  illustrates the SGD algorithm for finding the minimum of the loss function. By calculating the gradient of the weight using a subset of the training data, the adjustments to the weight factor  $w$  can be estimated. By repetitively performing the forward- and back-propagation, the value  $w$  approaches to the minimum of the loss function. Orange arrows indicate the single stochastic gradient descent steps, the product of the negative gradient and the learning rate. Every arrow is a single iteration of adjustment. The direction of change is determined by the negative value of the gradients. The scale of adjustment is set by the learning rate. Adapted from [84]. (b) Artificial learning curve visualizes the learning progress of the ANN. Typically, the total loss of training and validation set, which is calculated during forward-propagation in every epoch, is plotted throughout the training. In the early stage, the loss of both data sets declines rapidly. This period is the domain of underfitting, meaning that the ANN is still capable of increasing knowledge. While the training loss still decreases, after iterations of training, the validation loss starts to increase again. This divergence indicates that the ANN is beginning to learn specific features of the training set, and performs worst with new data. As a rule of thumb, the training should be stopped around the epoch, when the validation set to increase and the ANN starts to overlearn. Adapted from [85].

### 2.7.3 CONVOLUTIONAL NEURAL NETWORKS

In 1989, Lecun et al. published a specialized form of an ANN called the convolutional neural network (CNN) [103, 104, 95]. Over the last few decades, CNNs gained tremendous popularity in the processing of image data for object recognition [78]. Convolutional neural networks expand the concept of the MLP with new types of layers, the convolutional layers, and the pooling layers. By adding these layers, the strategy of the ANN was leveraged from operating on bare input values to more sophisticated processing of the data. In the MLP, described in the previous chapter, the input data is transformed into a one-dimensional vector, with the consequence that local image information from neighboring pixels is lost.

This limitation is overcome with CNN by the introduction of the convolutional and pooling layer, where neurons calculate their outputs using image filters, which capture local image patterns or features. These can be specific lines or curve segments, for example. Deeper layers combine the features to resemble larger patterns, spirals, or corners, for example. The last layers of the CNN are used for the identification and classification of the whole image using the more general elements composed out of the features. This higher level of perception is especially relevant for the classification of noisy real-world images with shadows and changing lighting, for example, cars and pedestrians for autonomous driving. However, this superior intelligence comes with the price of more extensive computation and is usually carried out using high-performance graphical processing units (GPUs) [105, 95].

**Figure 2.18** depicts a simple CNN with a single convolutional, pooling, and FC layer. The convolution layer can be described as the composition of three "sub-layers". First, the input image is convoluted with a convolution filter (or mask), a so-called kernel. Here, the  $3 \times 3$  kernel, composed of nine weights  $w_0 \dots w_8$ , is slid over the image, with specific step size, termed stride parameter. Contrary to MLP, a neuron in the folding layer works only in a limited space of the image, the so-called receptive field (area). Importantly, each neuron in the convolutional layer performs the processing of its responsible receptive field with the same weight matrix. The kernel is shared

between the neurons:

$$\begin{bmatrix} w_0 & w_1 & w_2 \\ w_3 & w_4 & w_5 \\ w_6 & w_7 & w_8 \end{bmatrix} \quad (2.17)$$

This convolution operation produces the second "sub-layer", the feature map, which is finally passed through a non-linear activation function "sub-layer". The sharing of the kernel allows the translation invariant feature detection, meaning that features can be detected in every area of the image. Every convolutional layer can apply multiple convolutional filters. Consequently, the output of the convolutional layer gets expanded to higher dimensions. The weights of the kernels are trained by the network, similar to the weights of the neurons in the FC layers.

It is common practice, after a convolutional layer, to down-sample the feature map using a pooling layer. Similar to the convolutional layer, a kernel is scanned over the feature map, which performs, for example, a max-pooling operation. In doing so, the maximum value of the receptive field of the pooling neuron is selected. Finally, these pooling layer outputs are broadcasted into a convolutional ANN layer with fully connected neurons. Each neuron of the FC layer receives all outputs of the pooling layer. The inputs get weighted, summed up, a bias is added, and passed through an activation function.

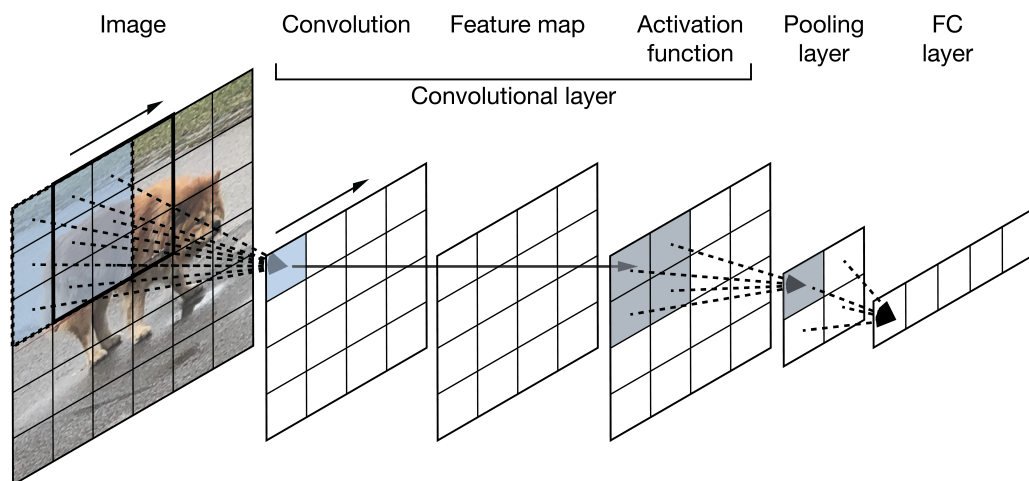


**Figure 2.18:** A simple CNN with a single convolutional layer, one pooling layer, and a single fully connected layer. The input image is a 2D grid of brightness values, showing "Fluff," a dog occasionally visiting the institute with its owner. For the processing in the first layer, the convolutional layer, a convolution mask (kernel), is passed over the image. Every neuron of the convolutional layer operates with a fraction of the input image, called the receptive field. Here, the image region highlighted with the blue square is the receptive field of the first neuron. The image area is convoluted with a  $3 \times 3$  kernel, and the output is passed through a non-linear activation function. Importantly, the weights of the kernel are shared between all neurons of the convolutional layer. The square with the black border in the image layer indicates the receptive area of the neuron next to the first neuron. In this configuration, the convolutional filter is shifted by one pixel, the so-called stride. The outputs of the convolution layer resemble the feature map. After the activation function is applied to the feature map, the output is down-sampled with a pooling layer. Same as for the convolutional layer, the neurons of the pooling layer operate on a local area of the feature map, indicated with the grey area. The outputs of the pooling layer are distributed to a fully connected layer. Adapted from [84]

In state-of-the-art CNNs like the AlexNet [87, 88], the block of the convolutional and pooling layer is typically repeated multiple times. Another very prominent 7-layer CNN architecture was published by LeCun et al. in 1998, the so-called LeNet-5 [86]. The design is illustrated in **Figure 2.19**. It is composed of three convolutional layers, two pooling layers, and three fully connected layers.

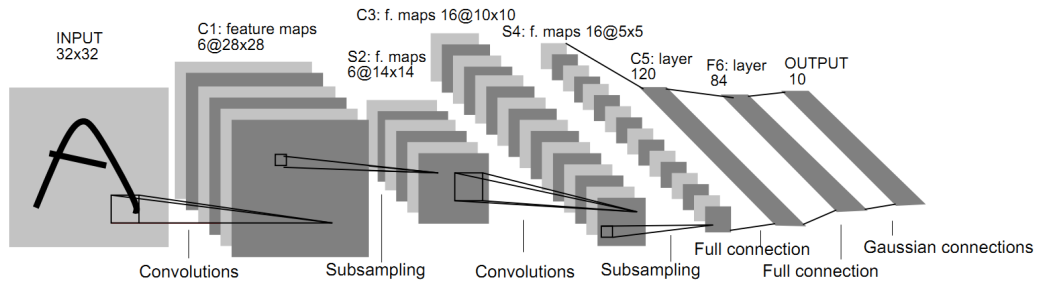


**Figure 2.19: LeNet-5** CNN architecture proposed by LeCun et al. in 1998. The 7-layer CNN features three convolutional layer (C1, C3, C5) with 6, 15 and 120 filters (feature maps). The first two convolutional layers are followed by a pooling layer (S2 and S4). F6 is a classical fully connected layer of 84 artificial neurons, followed by the output layer with ten nodes. Copyright ©1998 IEEE [86]



# 3

## Fast, Background-Free DNA-PAINT Imaging Using FRET-Based Probes

DNA-PAINT belongs to the group of single-molecule localization method in super-resolution microscopy [50]. Opposed to STORM [48] or PALM [9], the fluorescence molecules don't switch between dark and bright states. The necessary temporal single-molecule signal (blinking) is created by transient hybridization of short fluorescent DNA strands (imagers) to their targets, illustrated in **Figure 3.1 a**. In this implementation, DNA-PAINT suffers from the drawback of non-fluorogenic imaging probes. This means that the freely-diffusing imager strands contribute to the overall background fluorescence. This limitation, in turn, leads to the shortcoming that DNA-PAINT in its current implementation is rather slow compared to other SMLM methods [106]. Ultimately, DNA-PAINT is restricted to imaging of fixed samples or rather slow processes on the tens-of-minutes timescale.

### 3.1 NAIVE SPEED ACCELERATION FOR DNA-PAINT

A naive approach to speed-up DNA-PAINT can be directly derived from the central kinetic description of the dynamic behavior. The dark time  $\tau_{dark}$ , the time between the two consecutive binding events of an imager strand to the binding site is inverse proportional to the concentration of imager in solution, see equation 2.8. By increasing the imager concentration, the dark time will decrease, and the binding sites will be visited more frequently. Due to the non-fluorogenic, this will, however, lead to the scarification of imaging quality. The spatial resolution capability in SMLM methods is dependent on the signal-to-background ratio and therefore deteriorates with higher imager concentration.

### 3.2 FRET INTERACTION FOR BACKGROUND REDUCTION

With the introduction of FRET-based imaging probes, the limitation of non-fluorogenic probes in DNA-PAINT imaging was overcome. This is achieved by combining single-molecule FRET with DNA-PAINT. The novel approach is termed FRET-PAINT. It allows the decoupling of the concentration of imager probes from the fluorescence background. Two implementations of FRET-PAINT were presented. First, the so-called fixed FRET-PAINT., where the acceptor molecule is attached at the binding site, while the donor interacts transiently to the binding site. Upon hybridization of the donor and excitation using the donor excitation wavelength, the donor molecule transfers the excitation energy to the fixed acceptor via FRET. For downstream super-resolution reconstruction, the acceptor signal is recorded with a camera. The sketch **Figure 3.1 b** visualizes the probe design of fixed FRET-PAINT. With the introduction of the fixed acceptor to

the binding site, the photobleaching-resistant advantage of DNA-PAINT was sacrificed. Therefore, a second approach is presented, where both donor and acceptor interact transiently with the binding site. This method is termed dynamic FRET-PAINT and is illustrated in **Figure 3.1 c**. Since the acceptor is also stochastically exchanged here, the photobleaching-resistant imaging is restored.

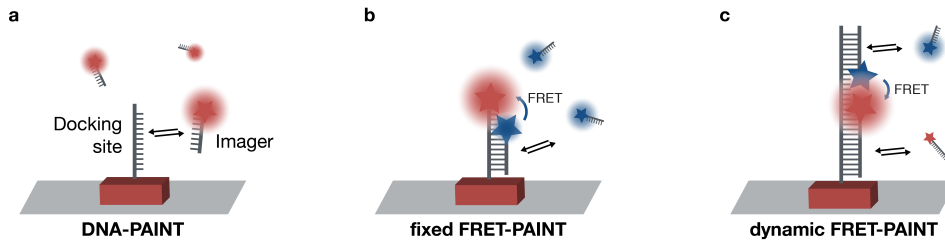


**Figure 3.1: Fluorescence.** (a) Conventional **DNA-PAINT**. The imager interacts transiently with the docking site, which is attached to the target (red box). The fluorescence molecules get excited using a coherent light source, and the fluorescence emission is collected. Since the freely diffusing imagers also emit fluorescence, the overall background in the acquired images is increased. (b) **Fixed FRET-PAINT**. Here the acceptor molecule is attached to the docking site. Donor molecules coupled to the imager transfer excitation energy to the acceptor molecule while binding to the target site. For super-resolution microscopy reconstruction, the acceptor emission is recorded. As there are acceptors at the target only activated by binding the donor, the image background is not artificially elevated. (c) **Dynamic FRET-PAINT** introduces the replenishment of the acceptor to overcome photobleaching of the fluorescence probes. The acceptor is attached to an orthogonal imager strand, which also binds transiently and repetitively to the extended docking site. Upon binding of both imager species, the excitation energy of the donor is transferred to the acceptor molecule, and the single-molecule signal can be acquired. Due to the short-range interaction of FRET and the orthogonal imager sequences, the collected signals originate only from the target sites.

The imaging performance of both FRET-PAINT variants were assayed in *in vitro* experiments using DNA origami structures. Therefore the speed-increase and spatial-resolution capability of FRET-PAINT was evaluated. Finally, to demonstrate the applicability in biological imaging, FRET-PAINT was used to perform *in situ* experiments in a cellular environment. Therefore, the microtubules were labeled with primary and secondary antibodies in fixed cells, with the secondary antibodies carrying the FRET-PAINT docking site.

**Fast, Background-Free DNA-PAINT Imaging Using FRET-Based Probes**

By

**Alexander Auer**, Maximilian T. Strauss, Thomas Schlichthärle, and Ralf Jungmann

PUBLISHED IN

*Nano Letters*, (2017), 17, 6428–6434

Reprinted with permission from [1].  
Copyright 2017, American Chemical Society.



# Fast, Background-Free DNA-PAINT Imaging Using FRET-Based Probes

Alexander Auer,<sup>†,‡</sup> Maximilian T. Strauss,<sup>†,‡</sup> Thomas Schlichthaerle,<sup>†,‡</sup> and Ralf Jungmann<sup>\*,†,‡,§</sup>

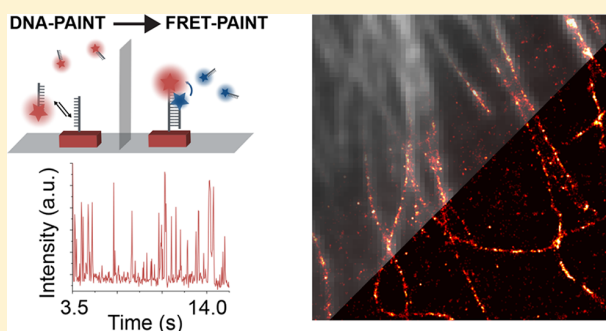
<sup>†</sup>Department of Physics and Center for Nanoscience, Ludwig Maximilian University, Munich, Germany

<sup>‡</sup>Max Planck Institute of Biochemistry, Martinsried, Germany

## Supporting Information

**ABSTRACT:** DNA point accumulation in nanoscale topography (DNA-PAINT) enables super-resolution microscopy by harnessing the predictable, transient hybridization between short dye-labeled “imager” and complementary target-bound “docking” strands. DNA-PAINT microscopy allows sub-5 nm spatial resolution, spectrally unlimited multiplexing, and quantitative image analysis. However, these abilities come at the cost of nonfluorogenic imager strands, also emitting fluorescence when not bound to their docking strands. This has thus far prevented rapid image acquisition with DNA-PAINT, as the blinking rate of probes is limited by an upper-bound of imager strand concentrations, which in turn is dictated by the necessity to facilitate the detection of single-molecule binding events over the background of unbound, freely diffusing probes. To overcome this limitation and enable fast, background-free DNA-PAINT microscopy, we here introduce FRET-based imaging probes, alleviating the concentration-limit of imager strands and speeding up image acquisition by several orders of magnitude. We assay two approaches for FRET-based DNA-PAINT (or FRET-PAINT) using either fixed or transient acceptor dyes in combination with transiently binding donor-labeled DNA strands and achieve high-quality super-resolution imaging on DNA origami structures in a few tens of seconds. Finally, we also demonstrate the applicability of FRET-PAINT in a cellular environment by performing super-resolution imaging of microtubules in under 30 s. FRET-PAINT combines the advantages of conventional DNA-PAINT with fast image acquisition times, facilitating the potential study of dynamic processes.

**KEYWORDS:** Super-resolution microscopy, DNA nanotechnology, DNA-PAINT, FRET, fluorogenic probes



Since their inception, super-resolution techniques have enabled researchers to perform optical microscopy below the classical diffraction limit of light with thus far unprecedented spatial resolution.<sup>1</sup> In most super-resolution implementations, molecules are “switched” between non-fluorescent dark- (or OFF-) and fluorescent bright-states (or ON-states) to pinpoint their position with subdiffraction precision. In the case where this switching happens in a targeted fashion, locations of fluorophores are “targeted” by a “focused” beam of light that actively defines local ON- and OFF-states. Methods based on this approach are generalized under the concept of reversible saturable/switchable optically linear fluorescence transition (RESOLFT),<sup>2</sup> a prominent example being stimulated emission depletion microscopy (STED).<sup>3</sup> In comparison, stochastic reconstruction methods such as photoactivated localization microscopy (PALM)<sup>4</sup> or (direct) stochastic optical reconstruction microscopy [(d)-STORM]<sup>5,6</sup> rely on stochastic switching of dye molecules between fluorescence ON- and OFF-states and subsequent single-molecule localization in a diffraction-limited area. A recently developed approach termed MINIFLUX<sup>7</sup> combines approaches from targeted and stochastic switching methods to

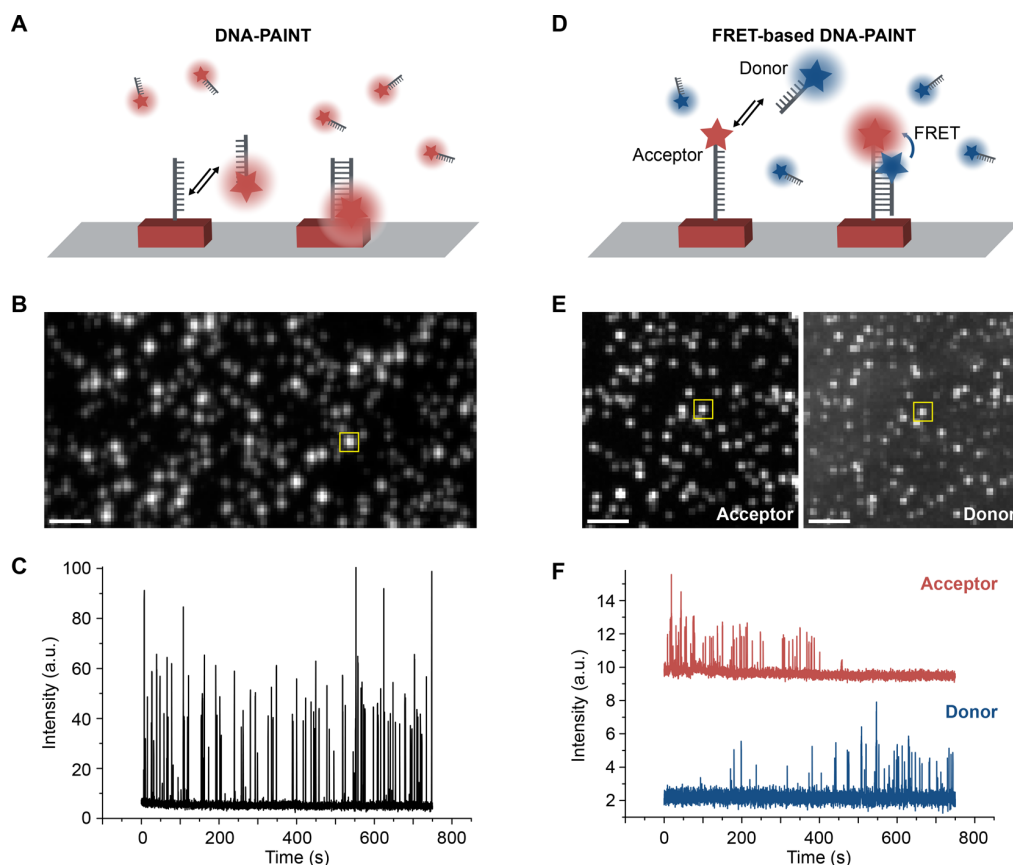
harness advantages of both implementations. In comparison, PAINT<sup>8</sup> and related techniques<sup>9,10</sup> achieve single-molecule switching and localization by using freely diffusing dye molecules that interact with targets either statically or transiently, thus creating the necessary “blinking” for stochastic super-resolution reconstruction. In DNA-PAINT,<sup>11–15</sup> a variation of the PAINT concept, dye-labeled imager strands transiently bind to their complementary (unlabeled) target-bound strands (Figure 1A).

Image acquisition in DNA-PAINT is usually performed using total internal reflection fluorescence (TIRF)<sup>16</sup> microscopy or highly inclined and laminated optical sheet (HILO)<sup>17</sup> illumination, only exciting imager strands close to the coverslip surface. While these imaging modalities reduce fluorescent background from unbound, freely diffusing imager strands in solution, the efficient detection of single fluorescent molecules in DNA-PAINT is furthermore facilitated by rather long camera integration times (up to hundreds of milliseconds),<sup>15</sup> roughly

**Received:** August 10, 2017

**Revised:** September 4, 2017

**Published:** September 5, 2017



**Figure 1.** FRET-based DNA-PAINT. (A) Original DNA-PAINT concept. Short, dye-labeled oligonucleotides transiently bind to complementary target strands, creating stochastic “blinking” that enables super-resolution imaging. (B) Typical diffraction-limited DNA-PAINT raw data obtained by calculating a standard deviation image of a 7500 frames long movie (integration time: 100 ms, imager concentration: 5 nM). (C) Intensity vs time trace of yellow highlighted region from panel B shows stochastic binding events observable as “spikes”. (D) FRET-PAINT concept. Docking strands are labeled with a fixed acceptor dye (e.g., Atto 647N), while transiently binding imager strands are labeled with a donor dye (e.g., Atto 488). Only donor dyes are excited, and upon binding to a docking strand, the energy from the excited donor is transferred to the acceptor, whose emission is then detected downstream. (E) Typical standard deviation image of the acceptor (left) and donor channel (right) of a 7500 frames movie. Note that the same spots are observed in the acceptor and donor channel. (F) Intensity vs time traces of the yellow highlighted areas in panel E for the acceptor (red) and donor channel (green). Note that almost all stochastic “blinking” events are observed in the acceptor channel only up to  $\sim 400$  s, at which point most likely all acceptor dye molecules in the area of interest are permanently photobleached. At the same time, stochastic blinking events become observable only in the donor channel from  $\sim 400$  s onward. This suggests that FRET with a high efficiency occurs between donor and acceptor dyes in FRET-PAINT. The integration time was 100 ms, and the donor strand concentration was 50 nM. Scale bars, 2  $\mu\text{m}$ .

matching the binding times of typical DNA-PAINT imager/docking pairs. The latter fact ensures a high signal-to-background ratio, as unbound imagers quickly diffuse through the “field of view”, thus contributing fewer photons per camera pixel than target-bound, immobilized imager strands. Typical diffraction-limited (i.e., not yet super-resolved) results of a DNA-PAINT image acquisition are obtained by calculating a standard deviation image from a movie acquisition<sup>11</sup> (Figure 1B). Intensity vs time traces of single spots show blinking due to transient binding of imagers to docking strands (Figure 1C). For typical imager concentrations of a few up to tens of nanomolar, high signal-to-background ratios in TIRF or HILO illumination can be obtained, resulting in high-quality super-resolution images.

However, the achievable temporal resolution in DNA-PAINT (for a moment not considering the binding duration of imager strands) is ultimately limited by the influx rate of imagers to docking strands, which in turn is determined by the association rate  $k_{\text{on}}$  of DNA hybridization reactions and the

concentration of imager strands. Association rates for DNA-PAINT are in the range of  $10^6$  ( $\text{M s}^{-1}$ ) under typical DNA-PAINT imaging conditions.<sup>11</sup> Assuming an imager concentration of, for example, 10 nM, this means that every docking strand is on average visited by an imager every 100 s, yielding a single-molecule blinking event used for downstream super-resolution reconstruction. As high-quality super-resolution images are usually reconstructed based on multiple binding (and thus blinking) events per docking site, image acquisition times in DNA-PAINT can quickly reach tens of minutes up to several hours depending on sample geometry, molecular density of docking sites, and desired spatial resolution. An easily accessible way to increase acquisition speeds would be to considerably raise the concentration of imager strands, and thus the influx rate of probes to target strands. While this seems straightforward to implement, one rapidly reaches an upper limit of the imager concentration due to the fact that probes are nonfluorogenic, meaning they get excited and emit fluorescence also if they are not bound to their respective target strands.

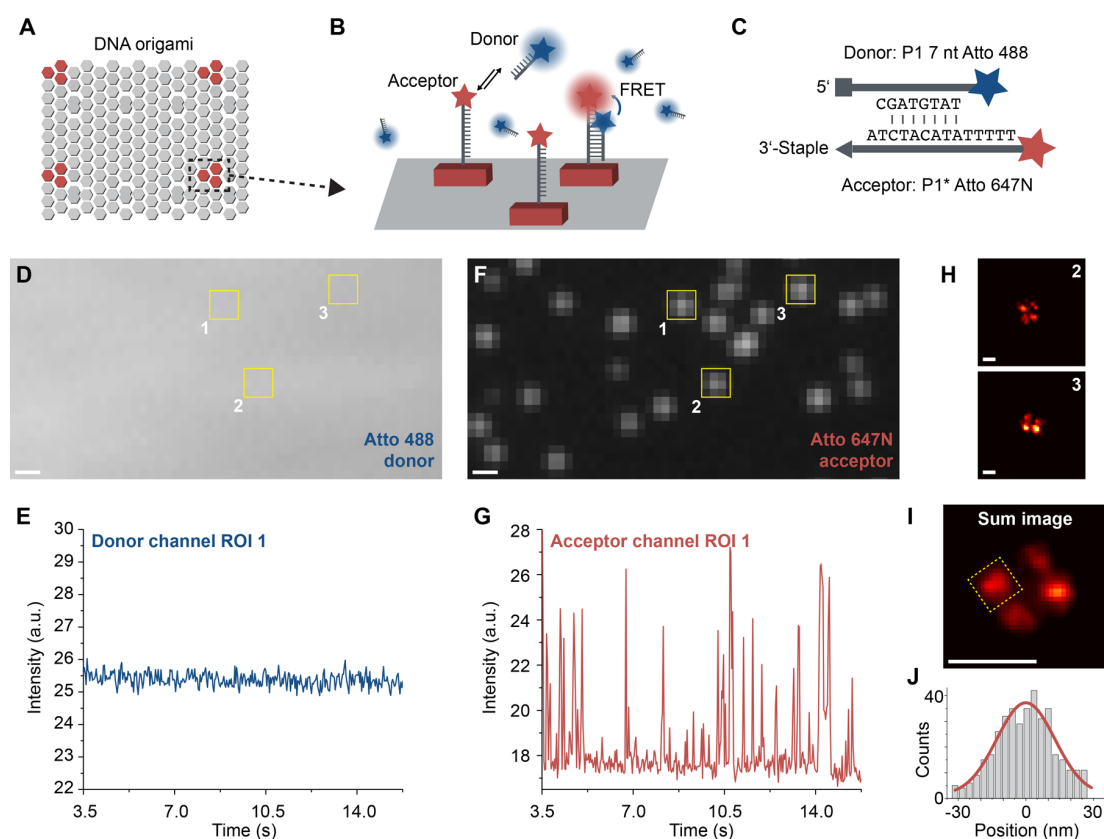


**Figure 2.** FRET-based probes enable fast DNA-PAINT imaging. (A) Schematic representation of a DNA origami with four spots containing Atto 647N-modified staple strands (three per spot, spaced 60 and 40 nm apart) for FRET-PAINT. (B) Imaging scheme showing Atto 488-labeled donor strands, which transiently bind to the fixed Atto 647N acceptor conjugated to a staple strand of the origami. (C) Design scheme detailing an Atto 488-labeled donor strand binding with 7 bp to the complementary part on the docking strand. Upon binding, the donor is spaced from the acceptor on the docking strand by a 5T spacer. The 7 bp binding region enables rapid dissociation of the donor strand (off-rate:  $k_{\text{off}} = 11.4 \text{ s}^{-1}$ ), while the 5T spacer between donor and acceptor allows for optimized FRET efficiencies. Both features enable fast FRET-PAINT imaging under appropriate imaging conditions such as high donor strand concentrations and fast camera integration times. (D) Standard deviation image of the donor channel obtained from 1000 frames acquired at a 35 ms integration time using a 1200 nM concentration of Atto 488-labeled donor strands. No single molecules are visible due to the overwhelming background of donor strand fluorescence. (E) Intensity vs time trace of the yellow highlighted region of interest (ROI) 1 from panel D shows no detectable single-molecule events, just “constant” fluorescence background due to the high concentration of donor strands (1200 nM). (F) The standard deviation image of the Atto 647N acceptor channel however shows identifiable diffraction-limited DNA-PAINT single-molecule events. (G) Intensity vs time trace of ROI 1 (same as in the donor channel) shows clear “spikes” upon binding of a donor strand and subsequent energy transfer to the acceptor. Note the fast blinking due to the high off-rate and concentration of donor strands. (H) Super-resolution reconstruction of the four-corner DNA origami structures from ROI 2 and 3 in panel F show clearly resolvable spots spaced 60 and 40 nm apart, respectively. (I) Sum image of 30 DNA origami structures underlines the achievable image resolution and quality obtained in 35 s acquisition time. (J) Fitting of the cross-sectional histogram of the localizations in the yellow highlighted area in panel I to a Gaussian yields a standard deviation of 12.9 nm, suggesting an achievable localization-precision-limited resolution of  $\sim 30$  nm under these conditions. Scale bars, 500 nm (D, F), 100 nm (H, I).

This very fact leads to the point, where single-molecule binding events become undetectable over the background of fluorescent, unbound imager strands, even in TIRF or HILO illumination. This is a well-accepted limitation of single-molecule experiments, where concentration of fluorescent analytes exceeds a few tens of nanomolars.<sup>18</sup>

To overcome this limitation and enable fast, background-free DNA-PAINT microscopy, we here introduce FRET-based imaging probes, inspired by experiments visualizing ligand–receptor interactions on cell membranes.<sup>19</sup> Using our FRET-based probes, we alleviate the concentration limit of imager strands and achieve an image acquisition speed-up by several orders of magnitude. We assay two approaches for FRET-PAINT based on fixed or transient acceptor dyes in combination with transiently binding donor-labeled DNA

strands and show high-resolution imaging on DNA origami structures in a few tens of seconds. We furthermore apply FRET-PAINT in a cellular environment and demonstrate efficient super-resolution imaging of microtubules in HeLa cells in under 30 s.

To reduce the fluorescent background created by unbound imager strands in solution and to speed up DNA-PAINT image acquisition, we first designed FRET-based imaging probes using a fixed acceptor dye (e.g., Atto 647N) conjugated to the docking strand combined with a donor dye (e.g., Atto 488) conjugated to the imager strand (Figure 1D). We chose Atto 488 and Atto 647N as FRET pair based on the large shift between the excitation wavelength of the donor and acceptor to minimize direct excitation of acceptor dye molecules upon 488 nm illumination of the donor (Figure S1). To assay the

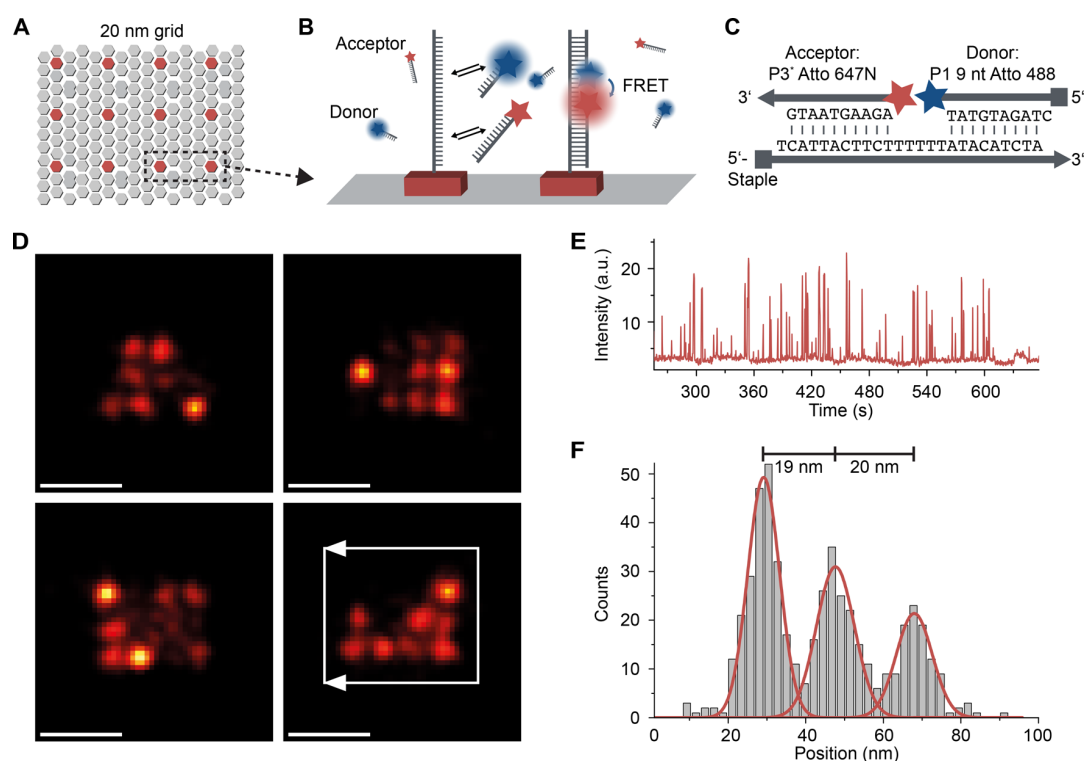


**Figure 3.** “Dynamic” FRET-based probes allow sub-20 nm-resolution imaging. (A) Schematic representation of a DNA origami with 12 positions containing docking strand extensions spaced 20 nm apart for dynamic FRET-PAINT. (B) Imaging scheme showing Atto 488-labeled imager strands, which transiently bind to the “dual” docking site, where also Atto 647N-labeled acceptor strands (with orthogonal sequence) can transiently (but independently) bind. (C) Design scheme detailing a 9 bp interaction region of the Atto 488-labeled donor strand and a 5T-spacer to the 10 bp interaction of the Atto647N acceptor strand with the docking sequence. In this scenario, docking strands are not labeled with a fixed acceptor dye. Again, only donor dyes are excited, and upon binding of a docking strand to a docking strand already (transiently) populated with an acceptor imager, energy from the excited donor is transferred to the acceptor, whose emission is downstream detected similarly to the fixed FRET case in Figure 2. Note that the interaction of the acceptor imager with the docking strand is designed to be more stable than the one of the docking site with the donor strand. This increases the overall probability of an acceptor strand being bound to the docking site upon donor imager binding. This facilitates efficient FRET-PAINT imaging, while simultaneously providing immunity to photobleaching due to replenishing of both donor and acceptor strands. (D) Representative super-resolution images of 20 nm grid structures highlighting the high-resolution capability of dynamic FRET-PAINT. (E) Intensity vs time trace of the acceptor channel shows transient FRET signals over an extended time frame due to replenishing of both donor and acceptor strands. (F) Cross-sectional histogram of the highlighted structure in panel D fitted to a three-component Gaussian clearly shows the resolved distance of 20 nm between docking strands. The average standard deviation of 4.5 nm of the Gaussian fits suggests an achievable localization-precision-limited resolution of  $\sim 11$  nm. Scale bars, 50 nm.

efficiency of our FRET-PAINT approach, we performed an initial proof-of-principle experiment using 50 nM concentration of donor strands and DNA origami-bound acceptor strands. We excite the donor strands using a 488 nm laser and simultaneously detect the donor and acceptor emission using a dual-EMCCD-camera system (see Supporting Information for details). A typical standard deviation image of the donor and acceptor channels is shown in Figure 1E, where the same single-molecule spots are visible in the donor and acceptor channel, respectively. This suggests specific binding of the donor strands to the acceptor-labeled docking strands and efficient FRET between them. To assay the resulting FRET process more quantitatively, we plotted intensity vs time traces for a single binding area (Figure 1F). There are two observations we want to highlight in the intensity vs time traces of the corresponding donor and acceptor channels: (1) Repetitive stochastic blinking events are observed in the acceptor channel up to  $\sim 400$  s, after which point blinking ceases, suggesting that acceptor dyes are permanently photobleached. (2) At the same time, stochastic blinking events become detectable in the donor intensity vs time trace after

$\sim 400$  s. These observations suggest that efficient FRET indeed occurs between the donor and the acceptor strand upon binding of the donor to the target in the first part of the image acquisition. In this case, the donor emission using our imaging system is not detectable anymore. Only after permanent photobleaching of the acceptor dye molecules on the target strands, transient binding of the donor strands is observed in the donor channel.

To assay the achievable speed-up in image acquisition with FRET-PAINT, we designed an in vitro experiment using 2D rectangular DNA origami structures<sup>20</sup> (Figure 2). In DNA origami, a long single-stranded molecule (called “scaffold”) is folded into a predesigned shape by  $\sim 200$  short DNA strands (called “staples”). Each staple has a unique sequence and specifically binds certain parts of the scaffold together. After completion of the self-assembly reaction, the scaffold is “folded” into the desired shape, and the staple strands are placed at prescribed positions in the final DNA origami structure. Here, we designed a DNA origami rectangle carrying 12 acceptor-labeled binding sites in four spots, spaced  $60 \text{ nm} \times 40 \text{ nm}$  apart and performed FRET-PAINT with Atto 488-labeled donor

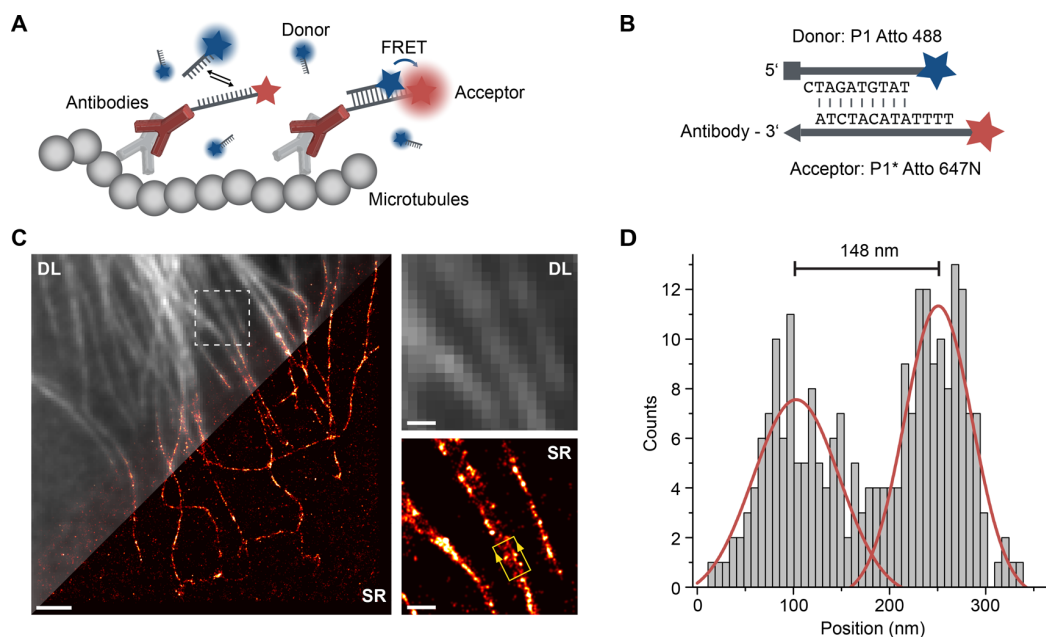


**Figure 4.** FRET-based probes allow high-speed DNA-PAINT imaging in cells. (A) Primary and secondary antibody labeling scheme. Primary antibodies target proteins of interest (e.g., tubulin). Secondary antibodies are conjugated to a docking strand carrying a fixed Atto 647N dye. Atto 488-labeled imager strands transiently bind to the docking strands. (B) Detailed imager and docking strand design. (C) Diffraction-limited (DL) alongside super-resolution (SR) of the microtubule network in a HeLa cell (left). Zoom-in diffraction-limited and super-resolved representations (right) of the highlighted area in the overview on the left demonstrate the increase in resolution. Imaging conditions are 500 nM donor imager, 14 ms integration time, and 2000 frames, resulting in a total imaging time of 28 s. (D) Cross-sectional histogram of the yellow highlighted region in the zoom-in super-resolution image in panel C fitted to a two-component Gaussian reveals two microtubules spaced 148 nm apart. Scale bars, 2  $\mu\text{m}$  (overview in C), 500 nm (zoom-in images in C).

strands (Figure 2A and B). To achieve optimal energy transfer between donor and acceptor, we used 5T bases as a spacer<sup>21</sup> to the donor on the acceptor strand (Figure 2C). We also designed a 7 bp interaction region between donor and acceptor strands, yielding a fast dissociation rate ( $k_{\text{off}} = 11.4 \text{ s}^{-1}$ , measured using Picasso<sup>15</sup>). We then performed FRET-PAINT using a 1200 nM concentration of Atto 488-labeled donor strands for 1000 frames using an integration time of 35 ms, resulting in a total image acquisition time of 35 s. While imaging was performed in TIRF, the high imager strand concentration prevented us—as expected—from detecting any single-molecule events in the donor channel (Figure 2D and E). However, analyzing the corresponding standard deviation image in the acceptor channel yields distinguishable single-molecule locations (Figure 2F), which is further supported by clearly detectable, rapid single-molecule blinking events in the corresponding intensity vs time trace of the acceptor channel (Figure 2G). Super-resolution reconstruction of the FRET-PAINT data set shows four detectable spots on the DNA origami structures, as designed (Figure 2H). To further assay our achievable localization-precision-limited resolution in an unbiased manner, we selected 30 origami structures and created a sum image by aligning them to their center of mass and subsequently used cross-correlation algorithms to overlay them on top of each other.<sup>15</sup> The respective cross-sectional histogram of one of the four spots on the origami yields a localization precision of 12.9 nm, translating to an achievable resolution of  $\sim 30$  nm using 1200 nM donor strands, a 35 ms integration time, and 1000 frames long acquisition.

Following these speed-optimized experiments, we next assayed our achievable spatial resolution with FRET-PAINT

(Figure 3). We designed so-called 20 nm grid DNA origami structures<sup>22</sup> containing 12 binding sites spaced 20 nm apart. (Figure 3A). When optimizing DNA-PAINT experiments for high resolution, it is crucial to extract the highest number of photons per single binding event to achieve optimal localization precision. One disadvantage of the “fixed” FRET-PAINT design introduced in Figures 1 and 2 is the nonreplenishable acceptor dye molecule. This necessitates budgeting of the available amount of emittable photons for several FRET events, eventually leading to permanent photobleaching of the acceptor dye. As one of the advantages of “standard” DNA-PAINT is its immunity to photobleaching (due to constant replenishment of imager strands), one would ideally like to port this ability to FRET-PAINT as well. To achieve this, we devised a modification to the acceptor strands (Figure 3B). Instead of a fixed acceptor dye modification of the docking strand, we now use transiently binding acceptor strands (in addition to the donor strands). The target docking strand consists of two binding sequences for acceptor and donor strands, spaced apart by a 5T-spacer (Figure 3C). The donor and acceptor strands exhibit a dissociation rate of  $k_{\text{off}} = 1 \text{ s}^{-1}$  and  $0.1 \text{ s}^{-1}$ , respectively. This helps to ensure that acceptor strands are bound for longer times than donor strands to the docking sites, which in turn leads to a higher probability of energy transfer to an already bound acceptor strand upon donor strand binding. Simultaneously, immunity to photobleaching due to replenishing of both donor and acceptor strands is maintained. The resulting super-resolution images of the DNA origami structures show clearly distinguishable grid points spaced 20 nm apart (Figure 3D), and long-lasting single-molecule blinking traces (Figure 3E). Cross-sectional histograms from one structure in Figure

3D fitted to a three-component Gaussian yield a standard deviation of 4.5 nm for single sites, suggesting an achievable localization-precision-limited resolution of  $\sim 11$  nm. While “dynamic” FRET-PAINT with transiently binding acceptor molecules is not prone to photobleaching of the acceptor, we want to note that this comes at the price of some reduction in the achievable imaging speed compared to the fixed FRET-PAINT approach due to a finite probability that a donor strand could bind to a docking site without an acceptor molecule being present. To assess this effect more quantitatively, we calculated the “effective” imager strand concentration in the case of “dynamic” FRET-PAINT from data shown in Figure 3. As the dark time  $\tau_d$  (or the time between binding events) in DNA-PAINT is directly linked to the influx rate of the probes ( $\xi = k_{\text{on}}c_i = \tau_d^{-1}$  with a concentration of imager strands  $c_i$  and the association rate  $k_{\text{on}}$ ), we can compute the apparent imager strand concentration for the dynamic FRET-PAINT case to  $\sim 72$  nM [assuming a typical association rate of  $10^6$  (M s) $^{-1}$ ], which would not yield high-quality standard DNA-PAINT data without the use of FRET-based probes. With FRET-based probes, it would thus still provide a speed-up compared to classical DNA-PAINT.

Finally, we designed FRET-PAINT probes for the rapid image acquisition of cellular structures (Figure 4). As an exemplary model target, we chose microtubules in HeLa cells. Immunostaining was performed using primary and DNA-conjugated (with fixed Atto 647N acceptor dye) secondary antibodies prepared as described before<sup>15,23</sup> (Figure 4A). As in the DNA origami case, Atto 488-labeled donor strands transiently bind to the acceptor-labeled docking strand (Figure 4B). The overview and zoom-in images in Figure 4C show the resulting diffraction-limited and super-resolution image of the microtubule network, clearly demonstrating an increased image resolution with FRET-PAINT using 500 nM donor strand concentration, 14 ms integration time, and 1000 frames acquisition, resulting in an image acquisition time of 28 s, thus far unprecedented with DNA-PAINT. The calculated localization precision from the tubulin super-resolution data yields 19.5 nm (Figure S4), translating to an achievable image resolution of  $\sim 46$  nm. Additionally, we performed line profile measurements of single microtubules (Figure S5) and measured diameters (fwhm) of  $\sim 62$  nm, which is in good agreement with earlier studies considering the combined size of primary and secondary antibodies used for labeling.<sup>24</sup>

In this study, we designed FRET-based imaging probes for DNA-PAINT and introduced FRET-PAINT, allowing us to speed up image acquisition times compared to conventional DNA-PAINT by several orders of magnitude thanks to the elimination of background fluorescence of freely diffusing imager strands. Both in vitro and in situ experiments yield high-quality super-resolution images in as low as 28 s with donor imager strand concentrations in the micromolar range. We assayed two different implementations of FRET-PAINT based on fixed or transiently binding acceptor strands in combination with transiently binding donor strands. The fixed acceptor version provides the fastest possible readout in FRET-PAINT due to the constant availability of an acceptor molecule for FRET upon binding of a donor strand. However, the fixed acceptor dye cannot be replenished, and thus this FRET-PAINT strategy is prone to photobleaching of the acceptor. To alleviate this limitation, we also introduced a “dynamic” FRET-PAINT implementation, where both donor and acceptor strands are transiently interacting with a complementary

target-bound docking site. While this implementation allows for high-resolution imaging with achievable localization precisions as good as 4.5 nm, it will most likely not provide the very fast acquisition times of a few tens of seconds due to the stochastic and independent nature of acceptor and donor target binding.

In conclusion, with acquisition times below 30 s, investigating dynamic processes and applications of FRET-PAINT on, for example, membrane-bound cell surface molecules in living cells are now within reach. In the future, complementary approaches to achieve single-molecule sensitivity under elevated analyte concentrations such as zero-mode waveguides (ZMWs)<sup>25</sup> or fluorescence field enhancement<sup>18</sup> could also be combined with DNA-PAINT to speed up image acquisition. While a combination of FRET-PAINT and, for example, ZMWs could be beneficial, it would also lead to more complex sample preparation for imaging.

## ■ ASSOCIATED CONTENT

### Supporting Information

The Supporting Information is available free of charge on the ACS Publications website at DOI: 10.1021/acs.nanolett.7b03425.

Materials and Methods alongside detailed information about the optical setups, DNA origami self-assembly, sample preparation and data processing; achievable localization precisions calculated based on the NeNA<sup>26</sup> metric in Figures S2–S4; details regarding image acquisition parameters for all data sets in this manuscript in Tables S1–S4; finally, sequences for DNA origami folding, DNA- and FRET-PAINT docking and imager sequences in Tables S5–S11 (PDF)

## ■ AUTHOR INFORMATION

### Corresponding Author

\*E-mail: jungmann@biochem.mpg.de. Phone: +49 89 8578 3410.

### ORCID

Ralf Jungmann: 0000-0003-4607-3312

### Author Contributions

A.A., M.T.S., and T.S. performed and analyzed experiments. R.J. designed and supervised the study. A.A. performed DNA origami experiments. A.A. and M.T.S. wrote software. A.A. and T.S. performed cell experiments.

### Funding

This work was supported by the German Research Foundation (DFG) through an Emmy Noether Fellowship (DFG JU 2957/1-1) and the SFB 1032 (Nanoagents for the spatiotemporal control of molecular and cellular reactions), the European Research Council (ERC) through an ERC Starting Grant (MolMap, grant agreement no. 680241), the Max Planck Society, the Max Planck Foundation, and the Center for Nanoscience (CeNS). A.A. acknowledges support from the DFG through the Graduate School of Quantitative Biosciences Munich (QBM). M.T.S. acknowledges support from the International Max Planck Research School for Molecular and Cellular Life Sciences (IMPRS-LS). T.S. acknowledges support from the DFG through the Graduate School of Quantitative Biosciences Munich (QBM).

## Notes

The authors declare the following competing financial interest(s): R.J. is a co-founder of Ultivue Inc., a US-based startup company with interest in the commercialization of DNA-PAINT technology.

## ACKNOWLEDGMENTS

We thank F. Schueder for fruitful discussions. We also thank M. Spitaler and the Imaging Facility of the Max Planck Institute of Biochemistry for imaging support.

## REFERENCES

- (1) Hell, S. W.; Sahl, S. J.; Bates, M.; Zhuang, X. W.; Heintzmann, R.; Booth, M. J.; Bewersdorf, J.; Shtengel, G.; Hess, H.; Tinnefeld, P.; Honigmann, A.; Jakobs, S.; Testa, I.; Cognet, L.; Lounis, B.; Ewers, H.; Davis, S. J.; Eggeling, C.; Klenerman, D.; Willig, K. I.; Vicidomini, G.; Castello, M.; Diaspro, A.; Cordes, T. *J. Phys. D: Appl. Phys.* **2015**, *48*, 48.
- (2) Schwentker, M. A.; Bock, H.; Hofmann, M.; Jakobs, S.; Bewersdorf, J.; Eggeling, C.; Hell, S. W. *Microsc. Res. Tech.* **2007**, *70*, 269–280.
- (3) Hell, S. W.; Wichmann, J. *Opt. Lett.* **1994**, *19*, 780–782.
- (4) Betzig, E.; Patterson, G. H.; Sougrat, R.; Lindwasser, O. W.; Olenych, S.; Bonifacino, J. S.; Davidson, M. W.; Lippincott-Schwartz, J.; Hess, H. F. *Science* **2006**, *313*, 1642–1645.
- (5) Rust, M. J.; Bates, M.; Zhuang, X. W. *Nat. Methods* **2006**, *3*, 793–795.
- (6) Heilemann, M.; van de Linde, S.; Schuttpelz, M.; Kasper, R.; Seefeldt, B.; Mukherjee, A.; Tinnefeld, P.; Sauer, M. *Angew. Chem., Int. Ed.* **2008**, *47*, 6172–6176.
- (7) Balzarotti, F.; Eilers, Y.; Gwosch, K. C.; Gynna, A. H.; Westphal, V.; Stefani, F. D.; Elf, J.; Hell, S. W. *Science* **2017**, *355*, 606–612.
- (8) Sharonov, A.; Hochstrasser, R. M. *Proc. Natl. Acad. Sci. U. S. A.* **2006**, *103*, 18911–18916.
- (9) Giannone, G.; Hossy, E.; Levet, F.; Constals, A.; Schulze, K.; Sobolevsky, A. L.; Rosconi, M. P.; Gouaux, E.; Tampe, R.; Choquet, D.; Cognet, L. *Biophys. J.* **2010**, *99*, 1303–10.
- (10) Schoen, I.; Ries, J.; Klotzsch, E.; Ewers, H.; Vogel, V. *Nano Lett.* **2011**, *11*, 4008–4011.
- (11) Jungmann, R.; Steinhauer, C.; Scheible, M.; Kuzyk, A.; Tinnefeld, P.; Simmel, F. C. *Nano Lett.* **2010**, *10*, 4756–4761.
- (12) Jungmann, R.; Avendano, M. S.; Woehrstein, J. B.; Dai, M. J.; Shih, W. M.; Yin, P. *Nat. Methods* **2014**, *11*, 313–U292.
- (13) Iinuma, R.; Ke, Y. G.; Jungmann, R.; Schlichthaerle, T.; Woehrstein, J. B.; Yin, P. *Science* **2014**, *344*, 65–69.
- (14) Dai, M. J.; Jungmann, R.; Yin, P. *Nat. Nanotechnol.* **2016**, *11*, 798–807.
- (15) Schnitzbauer, J.; Strauss, M. T.; Schlichthaerle, T.; Schueder, F.; Jungmann, R. *Nat. Protoc.* **2017**, *12*, 1198–1228.
- (16) Axelrod, D. *J. Cell Biol.* **1981**, *89*, 141–5.
- (17) Tokunaga, M.; Imamoto, N.; Sakata-Sogawa, K. *Nat. Methods* **2008**, *5*, 159–161.
- (18) Acuna, G. P.; Moller, F. M.; Holzmeister, P.; Beater, S.; Lalkens, B.; Tinnefeld, P. *Science* **2012**, *338*, 506–510.
- (19) Winckler, P.; Lartigue, L.; Giannone, G.; De Giorgi, F.; Ichas, F.; Sibarita, J. B.; Lounis, B.; Cognet, L. *Sci. Rep.* **2013**, *3*, 2387.
- (20) Rothemund, P. W. K. *Nature* **2006**, *440*, 297–302.
- (21) Funke, J. J.; Dietz, H. *Nat. Nanotechnol.* **2015**, *11*, 47–52.
- (22) Jungmann, R.; Avendano, M. S.; Dai, M.; Woehrstein, J. B.; Agasti, S. S.; Feiger, Z.; Rodal, A.; Yin, P. *Nat. Methods* **2016**, *13*, 439–42.
- (23) Agasti, S. S.; Wang, Y.; Schueder, F.; Sukumar, A.; Jungmann, R.; Yin, P. *Chem. Sci.* **2017**, *8*, 3080–3091.
- (24) Bates, M.; Huang, B.; Dempsey, G. T.; Zhuang, X. *Science* **2007**, *317*, 1749–53.
- (25) Zhu, P.; Craighead, H. G. *Annu. Rev. Biophys.* **2012**, *41*, 269–93.
- (26) Endesfelder, U.; Malkusch, S.; Fricke, F.; Heilemann, M. *Histochem. Cell Biol.* **2014**, *141*, 629–638.



# 4

## Nanometer-scale Multiplexed Super-Resolution Imaging with an Economic 3D-DNA-PAINT Microscope

In the previous chapter 3, the DNA-PAINT imaging was accelerated using FRET-based probes. With this approach, an essential limitation regarding the imaging speed was eliminated, and ultimately a potential solution against a major criticism of DNA-PAINT was demonstrated.

This chapter focuses on a more general problem in terms of super-resolution microscopy. In particular, there is still no widespread acceptance of super-resolution microscopy as a standard characterization technique in biological laboratories. This fact can be attributed to two points: (1) cumbersome sample preparation, especially in multiplex imaging, and (2) costly and complicated instrumentation, which requires mainly experts in super-resolution microscopy for operation.

### 4.1 COST-EFFICIENT 3D SUPER-RESOLUTION MICROSCOPY

Recent discoveries in biological research were often achieved using sophisticated microscopy instrumentation [55, 107]. Unfortunately, the commercial adaption of these advanced instrumentation outpaces the community's needs, restricting the application of modern super-resolution techniques to expert labs [108]. To overcome this obstacle, we here introduce a combination of the easy-to-perform super-resolution technique DNA-PAINT with an easy-to-replicate, custom-built 3D single-molecule microscope termed LiteTIRF. The fully-assembled platform is depicted in **Figure 4.1 a** with a coffee mug as a scale.

The setup is an order of magnitude more economical in terms of component cost while simultaneously outperforming commercial systems in spatial resolution and multiplexing capability. The mechanical scaffold, for the most part, is based on off-the-shelf optical components, which can be ordered straightforwardly. Critical elements like camera and objective were selected to maximize performance, while still balancing the overall budget. During the design process, special attention was spent on the sample stage (see **Figure 4.1 b**) in combination with the objective mount to minimize sample drift. The performance of the optical setup is evaluated with *in vitro* experiments using DNA origami. The compact design results in high mechanical stability, which reduces the need for active mechanical drift correction.

Additionally, the multiplexing capability using Exchange-PAINT with *in situ* experiments in the context of the cellular environment is demonstrated. Finally, a 3D super-resolution imaging modality is presented, which does not require expensive piezo stages for calibration. The approach is based on 3D super-resolution imaging via optical astigmatism [109] and the adoption of piezo-free calibration with latex microspheres [110]. To accelerate the adoption of the LiteTIRF plat-

form, digital computer-aided design (CAD) schematics and a ready-to-order component list are provided online.

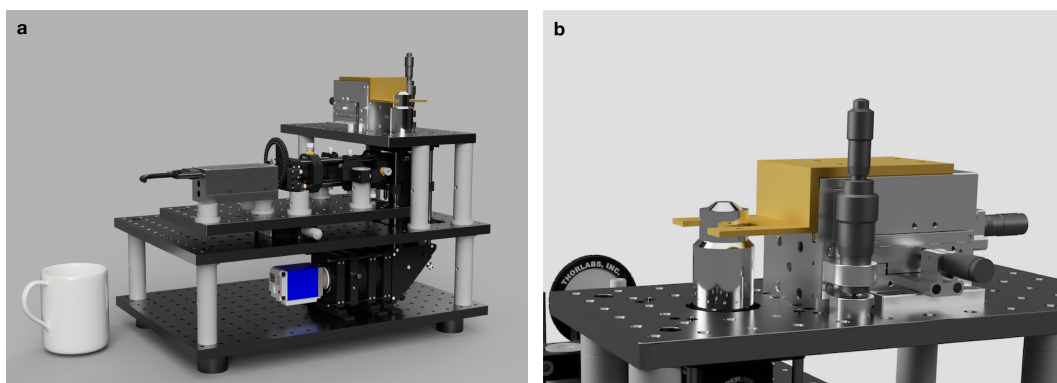


**Figure 4.1: Fluorescence.** (a) LiteTIRF visualized as CAD rendering. (b) The **Sample stage** hold the only custom part, the sample holder. The objective is firmly mounted to the breadboard, which reduces sample drift.

## **Nanometer-scale Multiplexed Super-Resolution Imaging with an Economic 3D-DNA-PAINT Microscope**

By

**Alexander Auer**, Thomas Schlichthärle, Johannes B. Wöhrstein, Florian Schüder, Maximilian T. Strauss, Heinrich Grabmayr, and Ralf Jungmann

PUBLISHED IN

*ChemPhysChem*, (2018), 19, 3024–3034

Reprint with permission from ref. [2].  
Copyright 2018, WILEY-VCH.



VIP Very Important Paper

# Nanometer-scale Multiplexed Super-Resolution Imaging with an Economic 3D-DNA-PAINT Microscope\*\*

Alexander Auer,<sup>[a]</sup> Thomas Schlichthaerle,<sup>[a]</sup> Johannes B. Woehrstein,<sup>[a]</sup> Florian Schueder,<sup>[a]</sup> Maximilian T. Strauss,<sup>[a]</sup> Heinrich Grabmayr,<sup>[a]</sup> and Ralf Jungmann\*<sup>[a]</sup>

Optical super-resolution microscopy is rapidly changing the way imaging studies in the biological and biomedical sciences are conducted. Due to the unique capability of achieving molecular contrast using fluorescent labels and sub-diffraction resolution down to a few tens of nanometers, super-resolution is developing as an attractive imaging modality. While the increased spatial resolution has already enabled structural studies at unprecedented molecular detail, the wide-spread use of super-resolution approaches as a standard characterization technique in biological laboratories has thus far been prevented by mainly two issues: (1) Intricate sample preparation and

image acquisition and (2) costly and complex instrumentation. We here introduce a combination of the recently developed super-resolution technique DNA-PAINT (DNA points accumulation for imaging in nanoscale topography) with an easy-to-replicate, custom-built 3D single-molecule microscope (termed liteTIRF) that is an order of magnitude more economic in cost compared to most commercial systems. We assay the performance of our system using synthetic two- and three-dimensional DNA origami structures and show the applicability to single- and multiplexed cellular imaging.

## 1. Introduction

Recently developed super-resolution methods<sup>[1]</sup> are paving the way for new discoveries in the life sciences. They enable researchers to perform optical microscopy below the diffraction limit of light with unprecedented spatial resolution, while maintaining the key benefits of fluorescence detection: operation under physiological conditions, molecule-specific contrast using affinity reagents (e.g. antibodies), and readily achievable multitarget detection (e.g. through spectral multiplexing). Popular super-resolution implementations include stochastic switching and readout methods such as photoactivated localization microscopy<sup>[2]</sup> (PALM) or stochastic optical reconstruction microscopy<sup>[3]</sup> (STORM) as well as targeted switching and readout approaches such as stimulated emission depletion (STED) microscopy.<sup>[4]</sup> In stochastic (e.g. STORM or PALM) super-resolution implementations, dye molecules (attached to a target of interest) are 'switched' between non-fluorescent dark- (or OFF-) and fluorescent bright-states (or ON-states) in order to sequentially pinpoint their position with sub-diffraction precision using single-molecule localization. By recording multiple

(usually ten to hundreds of thousand) images, each containing a stochastic subset of single-molecule signals, super-resolution images can be reconstructed.

While super-resolution techniques<sup>[1]</sup> are already starting to resolve structures thus far elusive to light microscopy,<sup>[5]</sup> they have still not made their way into many biological labs as standard characterization tools. This could be based on several factors: First, recent technological advancements require rather complex microscopy setups, which in turn rely on specially trained personnel for operation, prohibiting novice users to use super-resolution as a standard research tool. Second, costly commercial super-resolution platforms (usually hundreds of thousands of Euros) can mostly only be purchased in the context of larger, specific research or instrumentation grants. Without concrete single-molecule expertise or preliminary data obtained through collaborations it is unlikely that novice, single research groups are willing to spend this large amount of money or, as a matter of fact, apply for such instruments. Lastly, the complex sample preparation, especially for multi-target detection and cumbersome labeling strategies may hinder novice researchers from choosing super-resolution as an attractive characterization approach.

Most single-molecule localization microscopy (SMLM) approaches are relying on specific photophysical properties of target-bound fluorophores to achieve switching between OFF- and ON-states. However, this switching is hard to control for many distinct dye molecules, which makes multiplexed detection especially hard to implement. DNA-PAINT<sup>[6]</sup> is an SMLM-based approach that uses transient binding of dye-labeled oligonucleotides (called imager strands) to their target-bound complements (called docking strands) to create an apparent "blinking" of the target. This blinking can then be used for downstream super-resolution reconstruction. Spectrally-unlim-

[a] A. Auer, T. Schlichthaerle, Dr. J. B. Woehrstein, F. Schueder, M. T. Strauss, Dr. H. Grabmayr, Prof. R. Jungmann  
Faculty of Physics and Center for Nanoscience  
LMU Munich  
Geschwister-Scholl-Platz 1, 80539 Munich  
and  
Max Planck Institute of Biochemistry  
Am Klopferspitze 18, 82152 Martinsried  
E-mail: jungmann@biochem.mpg.de

[\*\*] DNA-PAINT: DNA Points Accumulation for Imaging in Nanoscale Topography

Supporting information for this article is available on the WWW under <https://doi.org/10.1002/cphc.201800630>

ited detection is relatively straightforward to implement using a technical variation called Exchange-PAINT.<sup>[7]</sup> Here, targets are simultaneously labeled using orthogonal docking strands followed by sequential, sequence-specific imaging using the corresponding imager strands. Furthermore, the predictable hybridization kinetics of imager to docking strands can be used for precise and accurate target quantification.<sup>[8]</sup>

While DNA-PAINT alleviates some of the limitations discussed above, an easy-to-operate, yet economic 3D single-molecule microscope that outperforms current commercial systems – while at the same time being affordable for a large number of biological laboratories – is still elusive. Recent efforts towards the realization of this goal were made by describing cost-efficient (<20,000 Euro) 2D super-resolution instrumentation for STORM and PALM imaging.<sup>[9]</sup> However, these approaches lack the possibility to perform 3D super-resolution and the switching between different illumination modes (e.g. such as TIRF,<sup>[10]</sup> HILO<sup>[11]</sup> or epifluorescence) as well as compromise spatial resolution performance compared to commercially available instruments.

Here, we introduce liteTIRF, a cost-efficient platform for DNA-PAINT microscopy, which is easy to replicate while at the same time delivers high performance, enabling researchers – for the first time – to achieve sub-10-nm spatial resolution, spectrally unlimited multiplexing, and 3D super-resolution using biological samples with hardware costs below 25,000 Euros.

## 2. Results and Discussion

### 2.1. liteTIRF Implementation

To realize a microscope system that on one hand achieves high performance, but on the other hand lowers the entry barrier (both from a cost as well as an ease-of-use perspective) for non-experts, we expanded on previous cost-efficient microscope developments.<sup>[9a]</sup> These systems were mainly built from off-the-shelf components with a specific focus on reducing

overall cost and complexity. We designed our setup (Figure 1, Supplementary Table 1) to be as compact as possible while still allowing for downstream custom modifications. We almost exclusively rely on standard off-the-shelf components (Figure 1a) and specifically focus on a compact and robust design of the platform, which minimizes mechanical and thermal drift (Supplementary Figure 1). This very fact allows the operation of the microscope without active drift correction (e.g. without a z-autofocusing system). Additionally, equilibration time of the sample on the stage further improved the stability. Compared to previous cost-effective setups,<sup>[9a]</sup> we furthermore include the possibility to operate the microscope in Total Internal Reflection Fluorescence<sup>[10]</sup> (TIRF) mode, with easily adjusted TIRF angles and thus sample penetration depths. For ease-of-implementation and operation, we opted for an objective-type TIRF implementation, where the beam of a coherent light source (e.g. a laser) is shifted towards the edge of the objective lens parallel to its optical axis in order to achieve total internal reflection. The evanescent field used to excite fluorescent molecules close to the surface of the glass slide helps to increase signal-to-noise in DNA-PAINT experiments, which is limited in epifluorescence illumination due to the non-fluorogenic nature of the imager strands. While it is vital for PAINT-type experiments, TIRF or oblique illumination is also advantageous for other implementations of SMLM-based super-resolution microscopy approaches, as it generally increases signal-to-noise performance for detecting single molecules<sup>[10]</sup> and thus resolution. The easy adjustment of the TIR penetration depth is equally essential for the quality and performance of single-molecule localization experiments. To enable this, we equipped the liteTIRF platform with a breadboard mounted on a translation stage (Figure 1), which allows the user to easily switch between different modes of illumination by simply displacing the excitation laser and telescope relative to the beam splitter. Finally, previous implementations of cost-efficient single-molecule platforms were restricted to two-dimensional imaging, limiting their applicability in many cell biology applications. There are a few relatively straightforward, yet powerful methods to achieve 3D super-resolution in SMLM.

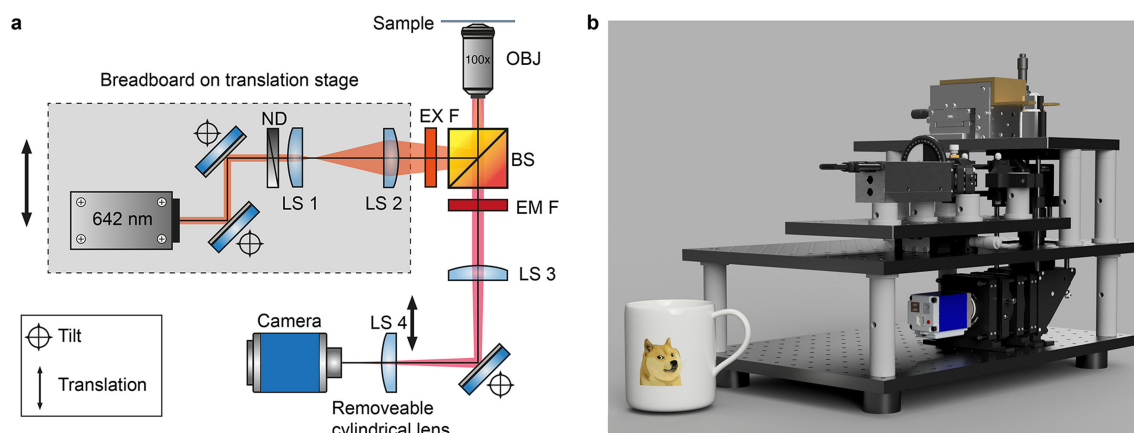


**Figure 1.** liteTIRF microscope platform. (a) Schematic drawing of the cost-effective 3D single-molecule setup for DNA-PAINT highlighting all major optical components of the system (Drawing is not to scale). (b) Corresponding CAD rendering of the microscope and components. Mug height as scale: 10 cm.

One of the most prevalent techniques uses depth-dependent point-spread-function engineering by employing an optical astigmatism with a cylindrical lens in the detection path.<sup>[12]</sup> While straightforward and relatively inexpensive to implement, the Achilles Heel of this approach is usually the need for quite costly piezo stage hardware for initial calibration of the depth-dependent astigmatism to real-world  $z$  values. Not only is this calibration procedure necessary once, but usually needs to be repeated for any ever so slightly change to the optical path of the microscope (e.g. change of objective, excitation wavelength, etc.). To overcome this rather costly limitation, we here apply a recently developed aberration-free calibration approach, which uses micrometer-sized spheres for calibration,<sup>[13]</sup> and extend it to DNA-PAINT imaging. This allows us to keep the microscope cost low and furthermore overcome some of the drawbacks of piezo-stage-based calibration methods, which we will discuss in greater detail later in the manuscript. Figure 1b illustrates the liteTIRF platform as CAD model, which is accessible as an interactive version at [www.jungmannlab.org](http://www.jungmannlab.org), making it easy to visualize all components and to assemble the system for users. Furthermore, we plan to provide an online forum, where novice users can exchange knowledge and share their modifications.

## 2.2. Performance Evaluation of liteTIRF Using DNA Origami

To assay the achievable optical resolution of the liteTIRF with DNA-PAINT, we designed an *in vitro* experiment using 2D rectangular DNA origami structures (Figure 2). DNA origami<sup>[14]</sup> are self-assembled nanostructures, which consist of a long single-stranded DNA molecule (called “scaffold”, usually derived from a phage plasmid), which is folded into a predefined shape using hundreds of short synthetic DNA oligonucleotides (called “staples”). Here, we designed a flat DNA origami rectangle functionalized with 20 single-stranded docking sites for DNA-PAINT imaging (Figure 2b, inset). 16 out of these 20 docking sites form a 10-nm-grid-pattern, while the remaining 4 docking sites facilitate alignment for further downstream analysis. Using these DNA origami immobilized onto a coverslip surface,<sup>[6b]</sup> we performed DNA-PAINT with ATTO 647N-labeled imager strands and an un-cooled and cost-efficient scientific (s) CMOS camera (for experimental conditions see Supplementary Table 2). To furthermore demonstrate liteTIRF’s mechanical stability due to its compact design, we performed the experiment on an office desk, without the use of passive or active vibration isolation (e.g. without optical table or piezo-controlled isolation). The super-resolution reconstruction and

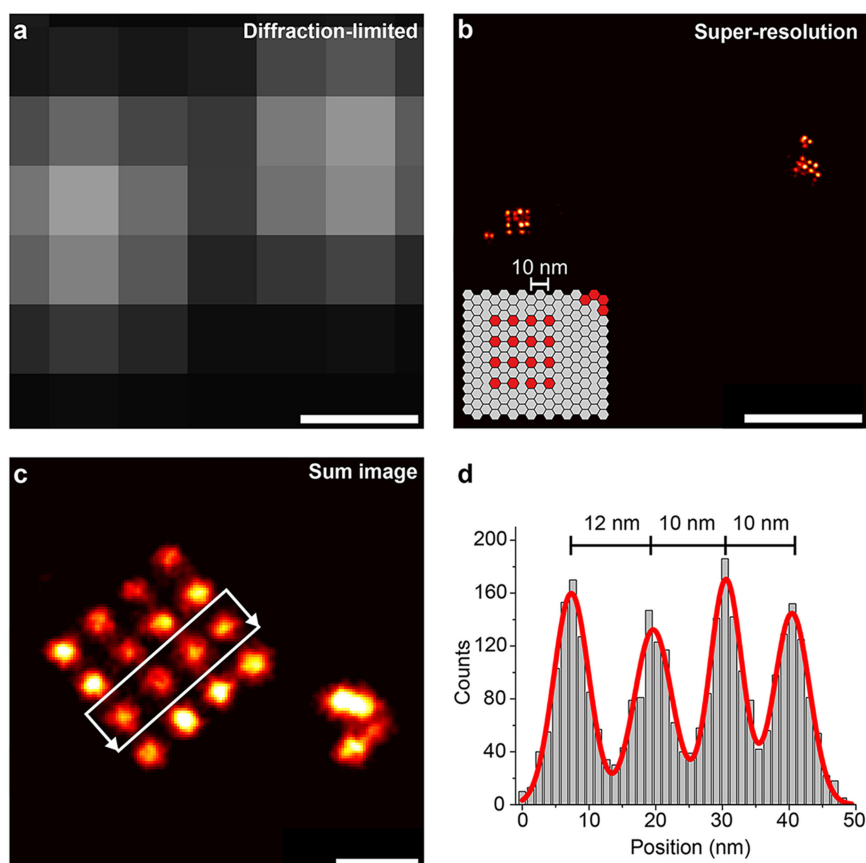


**Figure 2.** 2D resolution capabilities of liteTIRF. (a) Diffraction-limited image of 10-nm-grid DNA origami structures. (b) 10-nm-grid structures imaged with the liteTIRF microscope using DNA-PAINT employing a sCMOS camera and ATTO 647N-labeled imager strands. Inset: DNA origami design, red strand positions are extended for DNA-PAINT. (c) Sum image of  $n = 16$  structures reveals the clearly resolved 10-nm-grid-pattern. (d) Cross-sectional histogram analysis of the highlighted area in (c) shows the sub-10-nm resolution capability of the liteTIRF platform in combination with DNA-PAINT. Single sites are localized with 2.5 nm precision. Scale bars: 200 nm (a, b), 20 nm (c).

subsequent drift correction (described in the methods part) of the DNA-PAINT data set shows the clearly resolved 10-nm-grid-pattern on individual DNA origami (Figure 2b). To quantify the achievable localization-precision-limited resolution in an unbiased manner, we then selected 16 origami structures and created a sum image (similar to an EM class average) by 2D cross-correlation following center-of-mass alignment in order to overlay the structures on top of each other<sup>[6b,15]</sup> (Figure 2c). The respective cross-sectional histogram of four of the 16 spots yields a spacing of  $\sim 10$  nm with a localization precision of 2.5 nm (in good agreement with the calculated NeNA<sup>[16]</sup> value of 2.5 nm), translating to an achievable FWHM-resolution of  $\sim 6$  nm (Figure 2d). Localization precision analysis of a single particle yields a FWHM-limited resolution of 4.3 nm (Supplementary Figure 2). This supports the fact, that the sum image from multiple structures does not necessarily yield a higher spatial resolution. However, the sum over multiple structures increases the sampling of all binding sites. We further characterized the imaging performance of the liteTIRF platform using an economic scientific interline-transfer CCD camera and DNA origami structures (Supplementary Figure 3). Similar histogram analysis as before yields an average localization precision of 3.6 nm (Supplementary Figure 3). To further assay the capabilities of liteTIRF using even more economic components, we performed another experiment with a non-scientific CMOS camera prized at  $\sim 340$  Euro, imaging DNA origami structures carrying docking sites for DNA-PAINT in a  $3 \times 4$  grid with a spacing of 20 nm (Supplementary Figure 4). Super-resolution reconstruction of the DNA-PAINT data with subsequent overlay of individual DNA origami using cross-correlation as described above clearly reveals the individual spots of the designed

pattern (Supplementary Figure 4). To show that liteTIRF is not necessarily limited to DNA-PAINT super-resolution microscopy, we also performed a dSTORM experiment (Supplementary Figure 5) using a DNA origami which carries a total of 12 Alexa 647-labeled DNA strands (three stably bound in every corner, Supplementary Figure 5). We were able to visualize the resulting  $50 \times 70$  nm rectangle as designed. Sum image analysis of 13 DNA origami structures (similar as described above) yields a localization precision of 4.1 nm (Supplementary Figure 5), translating to a FWHM-limited resolution of  $\sim 9.6$  nm.

### 2.3. Cellular Imaging with liteTIRF

Next, we investigated the feasibility of imaging cellular targets using the liteTIRF platform in fixed cells. As exemplary target structure, we chose microtubules, which are one of the most widely used model systems for super-resolution microscopy.<sup>[12b,17]</sup> First, we coupled short oligonucleotides covalently to a secondary antibody<sup>[6b,18]</sup> (Figure 3a, inset). After immunostaining using primary antibodies against alpha-tubulin followed by subsequent incubation with the DNA-conjugated secondary antibodies, we performed a DNA-PAINT experiment using ATTO 647N-labeled imager strands (Figure 3a and Supplementary Figures 6 and 7, for experimental conditions see Supplementary Table 3). The zoom-in images in Figure 3b and c show the resulting diffraction-limited and super-resolution image of the microtubule network. Based on the nearest neighbor analysis<sup>[16]</sup> (NeNA) metric, we localize single molecules with a precision of  $\sim 9$  nm, resulting in a FWHM-resolution of  $\sim 21$  nm in cells. This resolution, in combination with a sufficiently high labeling

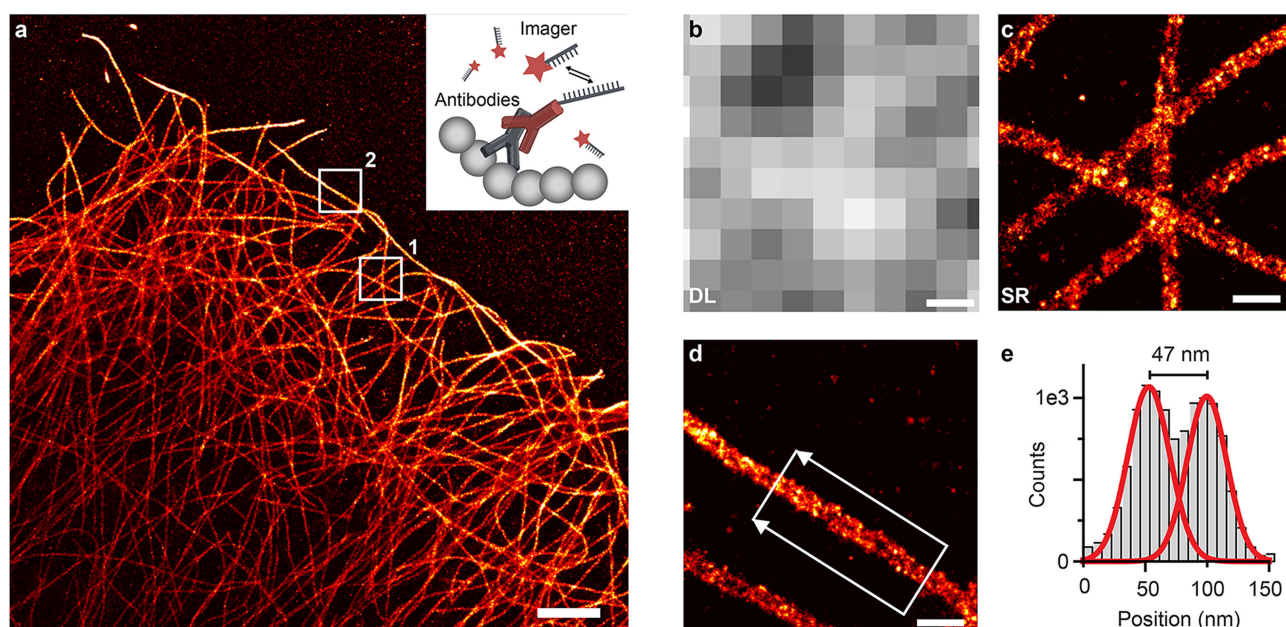


**Figure 3.** Cellular DNA-PAINT imaging using liteTIRF. (a) Microtubules are labeled with primary and DNA-conjugated secondary antibodies and imaged using ATTO 647N-labeled imager strands and an interline-transfer CCD camera. (b) Diffraction-limited (DL) and (c) super-resolution (SR) zoom-in of the highlighted area 1 in (a) shows the increased spatial resolution. (d) Zoom-in of the highlighted area 2 in (a) shows a single microtubule. (e) Cross-sectional histogram of the area marked in (d) demonstrates the ability of liteTIRF to resolve the hollowness of microtubules with an apparent diameter of  $\sim 47$  nm (broadened due to the use of primary and secondary antibodies for labeling). Scale bars: 2  $\mu$ m (a), 200 nm (b, c, d).

density, allowed us to visualize the “hollowness” of microtubules using liteTIRF as seen in 2D projections in earlier works<sup>[6b,17a]</sup> (Figure 3d). Using line profile measurements (Figure 3e) along single microtubules, we measured a peak-to-peak distance (microtubule width) of  $\sim 47$  nm, which is in good agreement with earlier studies considering the offset from target and DNA-PAINT docking site due to the size of primary and DNA-conjugated secondary antibody label.

## 2.4. Multicolor Imaging Using Exchange-PAINT and liteTIRF

Next, we turned our attention to implementing Exchange-PAINT multiplexing<sup>[7]</sup> with liteTIRF. Exchange-PAINT allows researchers to perform spectrally-unlimited multiplexing using a single excitation laser line and spectral dye. Instead of imaging multiple targets simultaneously with spectrally distinct dyes, Exchange-PAINT uses orthogonal docking sequences linked to target species of interest. Imaging is then performed sequentially using one complementary imager strand at a time, always labeled with the same spectral dye. As a proof-of-concept implementation of Exchange-PAINT with liteTIRF, we performed a two-target experiment (Figure 4 and Supplementary Figure 8). Here, we chose alpha tubulin (akin to the singleplex case) and TOM20 (a mitochondrial outer membrane marker) as cellular targets (see Supplementary Tables 4 and 5 for experimental details). After super-resolution reconstruction of both data sets, the two colors were aligned using image cross-correlation and fiducial markers (i.e. gold particles attached to the surface) present in both imaging rounds (Figure 4b). To illustrate the achievable alignment accuracy, white arrows pointing at multiple side walls of microtubule filaments are marked (Figure 4c) at the zoom-in from Figure 4b. The same position is highlighted in Figure 4d, showing that the

border of the TOM20 labeled mitochondria is associated to the microtubule network.<sup>[19]</sup>

## 2.5. Calibration Using Microspheres for 3D Super-Resolution Imaging with liteTIRF

Next, we extended the liteTIRF platform to three-dimensional super-resolution imaging by placing a removable cylindrical lens into the emission path (LS 4 in Figure 1a and Supplementary Figure 9). This lens introduces a depth-dependent PSF by creating two slightly offset focal planes for the x- and y-dimension. This results in different degrees of ellipticity and orientation of the PSF depending on the z-position of the fluorescence emitter with respect to the focal plane of the objective lens.<sup>[12a,20]</sup> Ellipticity (i.e. the width of every Gaussian fit in x- and y-direction) is used to determine the z-positions with the use of a calibration curve (basically a look-up table). These calibration curves are usually acquired using fluorescent beads immobilized on the coverslip and a z-piezo stage to perform z-stacks. Due to the nanometer-precise positioning of the sample relative to the objective by the piezo stage, the ellipticity and orientation of the PSF can be linked to unambiguous z-positions with sub-diffraction precision.<sup>[20]</sup>

Here, we present an approach combining PSF-shaping based on astigmatism with a recently developed method to perform 3D calibration<sup>[13]</sup> without relying on expensive piezoelectric stages (Figure 5). This allows three-dimensional super-resolution imaging with an axial thickness between 0.6–1.5  $\mu\text{m}$ , depending on the position of the cylindrical lens relative to the camera. For calibration, avidin-coated latex microspheres (16  $\mu\text{m}$  diameter) were immobilized on a biotinylated-PEG surface. Short oligonucleotides (10 nt) functionalized with biotin (serving as DNA-PAINT docking sites) were subsequently

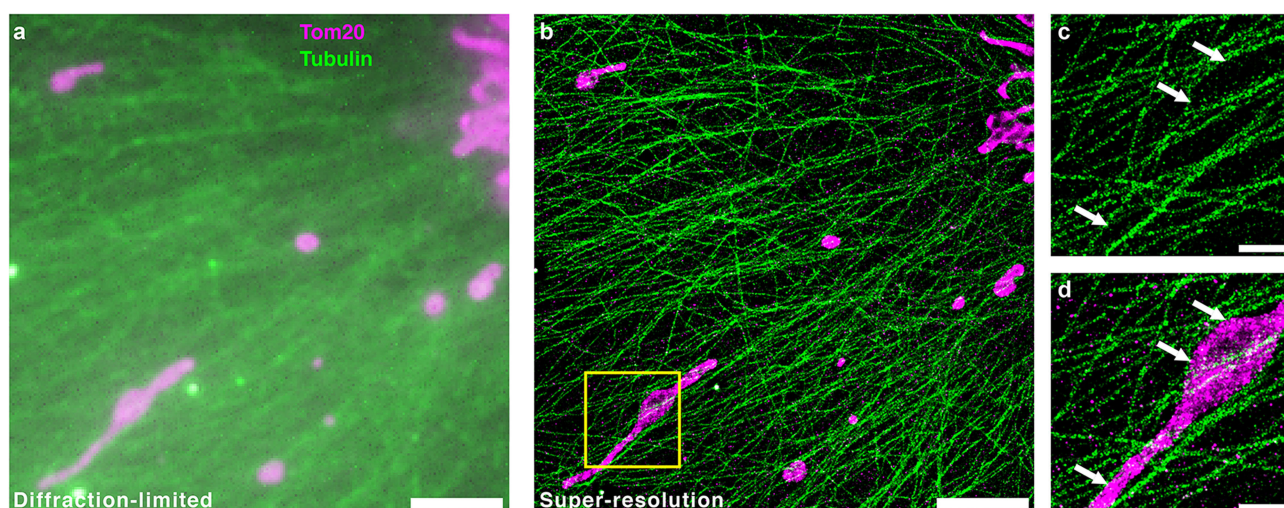


**Figure 4.** Two-target Exchange-PAINT using liteTIRF. (a) Diffraction-limited representation of the mitochondrial (TOM20 labeled using primary and secondary antibodies) and microtubule (Tubulin labeled using primary and secondary antibodies) network inside fixed COS7 cells. (b) Super-resolved Exchange-PAINT image of the same sample. (c) Zoom-in of highlighted area in (b) showing microtubules. White arrows mark the side walls of individual microtubules. (d) Zoom-in of the same area showing microtubules and mitochondria. White arrows indicate that the mitochondrial membrane is located in close proximity to the individual microtubule filaments. Scale bars: 5  $\mu\text{m}$  (a, b), 1  $\mu\text{m}$  (c, d).

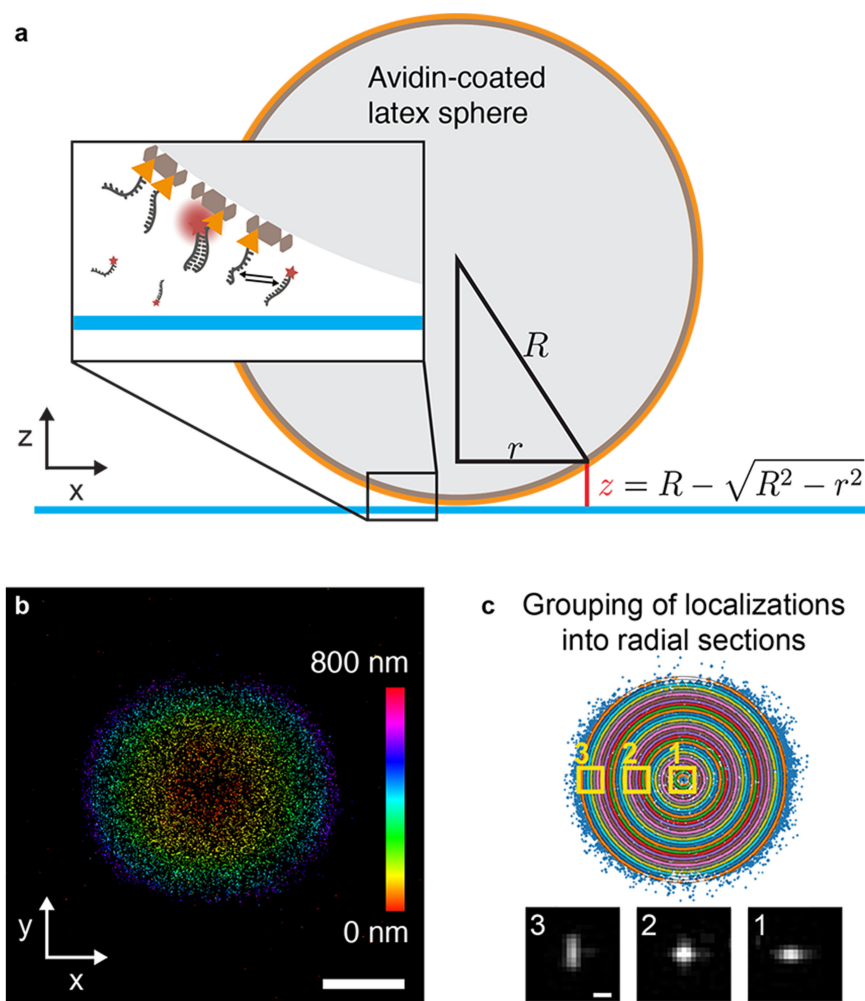


**Figure 5.** Z-piezo-free three-dimensional calibration using latex microspheres. (a) Schematic representation of the calibration sample with avidin-coated microspheres immobilized on the coverslip surface. Zoomed-in area shows biotinylated oligonucleotides attached to the microsphere providing docking sites for DNA-PAINT imaging. (b) x-y projection of the 3D super-resolution reconstruction with a total of 70946 single-molecule localization events. Color gradient displays the z position. (c) Grouping of localizations into radial sections of identical thickness for the determination of the PSF width in x and y direction per section. (1) Ellipticity of an exemplary PSF from the center of the x-y projection shows elongation in x direction. (2) Exemplary PSF with similar width in x and y direction. (3) Exemplary PSF taken from the outer section shows elongation in y direction. Using the radius information  $R$  of the microsphere and the radius  $r$  measured from x-y projection and the extracted width of the PSFs the z position of every localization event can be calculated using the formula shown in (a) to generate a calibration curve (Supplementary Information Figure 9. Scale bars: 5  $\mu\text{m}$  (b), 500 nm (c).

incubated and thus attached to the microsphere surface (Figure 5a). Next, we performed DNA-PAINT with ATTO 647 N-labeled imager strands of the lower part ( $\sim 800$  nm) of the latex microsphere (for experimental parameters see Supplementary Table 6). Super-resolution reconstruction reveals the 2D projection of the lower curvature of the microsphere, which was sampled with  $\sim 71,000$  single-molecule localization events (Figure 5b). After the center-of-mass of the sphere was calculated from the 2D projection, localizations were grouped in radial sections to determine the mean ellipticity within every section (Figure 5c).

Using the 2D radius information  $r$  in the xy-projection and the total radius  $R$  the z position of every section was calculated, and a calibration curve was generated (Supplementary Figure 10). In addition to saving on component cost for the piezo stage, another key advantage compared to more classical methods used to generate calibration curves is that no

magnification factor due to refractive index mismatch<sup>[20]</sup> needs to be taken into account. This is based on the fact that the “calibration signal” is emitted from within the sample chamber and not immediately above the interface between coverslip glass and imaging media interface. Recent studies reckon that this index mismatch results in an axial localization bias of up to 200 nm due to spherical aberrations.<sup>[13]</sup>

## 2.6. Three-dimensional Super-Resolution Imaging of 3D DNA Origami

To evaluate the 3D performance of the liteTIRF platform, we designed an *in vitro* experiment with 3D DNA origami structures (Figure 6). First, we immobilized 3D DNA origami tetrahedrons, which carry multiple DNA-PAINT docking sites at each vertex,<sup>[21]</sup> on the coverslip surface (Figure 6b). Next, we

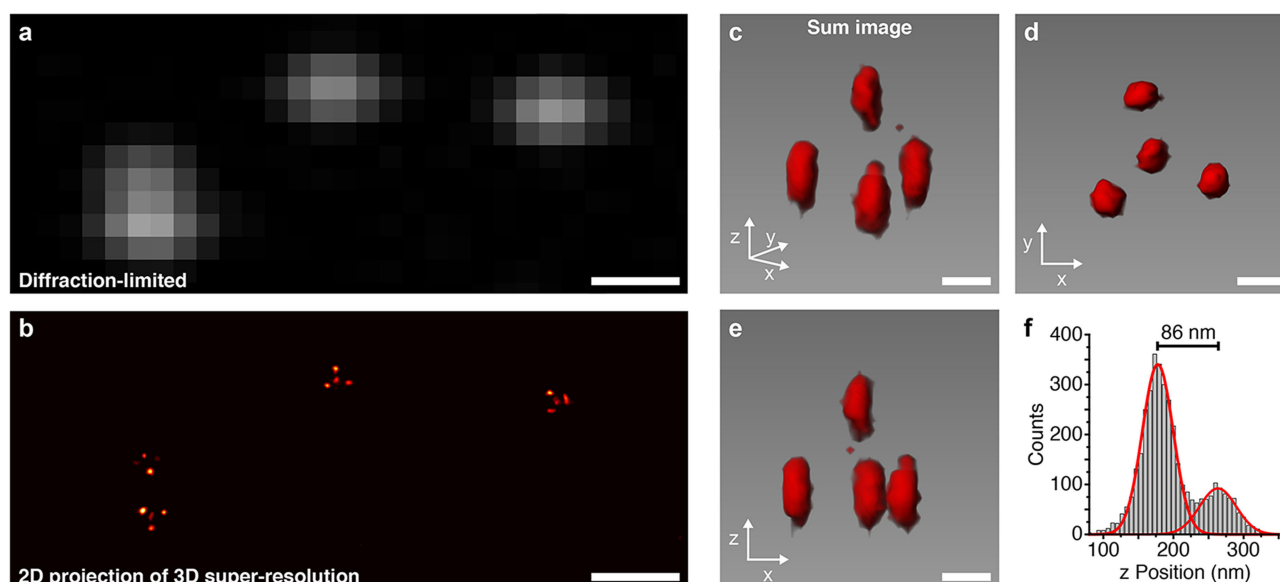


**Figure 6.** 3D DNA-PAINT super-resolution imaging with liteTIRF of polyhedra DNA origami structures. (a) Diffraction-limited representation of an area showing multiple DNA origami tetrahedrons. (b) 2D projection of the 3D super-resolved image with DNA-PAINT and liteTIRF of the area shown in (a). Super-resolution reconstruction clearly shows the three spots located at the base (designed spacing of  $\sim 100$  nm between each corner) and one spot from the tetrahedron top (center spot). (c) Isometric view of the sum image of  $n = 12$  DNA origami structures underlines the achievable imaging resolution in three-dimensions. (d) x-y projection of the summed image shown in (c). (e) x-z projection of the sum image. (f) Height measurement of the tetrahedron obtained from the cross-sectional histogram in the x-z projections yields  $\sim 86$  nm. Scale bars, 500 nm (a, b), 50 nm (c, d, e).

performed 3D DNA-PAINT using ATTO 647 N-labeled imager strands (for experimental parameters see Supplementary Table 7). After 3D super-resolution reconstruction, four spots from individual DNA origami were clearly resolvable in the 2D projection, three spots from the base vertex and one spot originating from the top vertex (Figure 6b). Using the calibration curve obtained from Figure 5, we are now able to resolve the tetrahedron as full 3D structure (Figure 6c). To quantify the achievable localization-precision-limited resolution in an unbiased manner, we then selected 12 origami structures and created a sum image by center-of-mass alignment and 2D cross-correlation in x-y direction and subsequent 2D cross-correlation in y-z direction to overlay the structures on top of each other (Figures 6c, d and e). Finally, we measured the height-profile in the x-z projection (Figure 6e). A cross-sectional histogram analysis (Figure 6f) yields an average localization precision of  $\sim 24$  nm in z direction and a distance of 86 nm between base vertices and top vertex. This result is in good agreement with the designed height of 82 nm.

### 3. Conclusions

In summary, we have demonstrated that sub-10-nm lateral resolution using DNA-PAINT in combination with the liteTIRF platform can be achieved. By performing one- and two-color DNA-PAINT imaging in cells, we showed that liteTIRF also enables multiplexed cellular super-resolution imaging. Most importantly, using a DNA-PAINT adoption of a recently demonstrated aberration-free calibration method for 3D calibration, we showed that liteTIRF can be extended to three-dimensional

imaging without the use of piezoelectric-controlled sample stages. Due to the rigid instrument design the liteTIRF platform could eventually allow “point-of-care” operation in field studies, as we show that the usage without optical table isolation is feasible. Further improvements for stability could be made by replacing the manual z-direction actuator with a piezo actuator, which is controlled using image-based drift feedback. With the modular design the liteTIRF platform could also be extended with an IR-based total internal reflection focus stabilization and an active objective-piezo. However, this would increase cost up to 35,000 Euro. Besides pure super-resolution studies we expect that liteTIRF could also serve as a basis for correlative methods, e.g. combining super-resolution with complementary modalities such as optical<sup>[22]</sup> or magnetic tweezers<sup>[23]</sup> or atomic force microscopy.<sup>[24]</sup> We expect that the liteTIRF platform provides an attractive opportunity for researchers new to the single-molecule field to adopt super-resolution microscopy as a standard characterization tool. We believe that due to the economic design and high performance, it will be possible to increase the adoption rate of super-resolution. As super-resolution microscopy is slowly reaching university teaching and practical courses, we expect that the liteTIRF platform will also fulfill educational and outreach purposes by providing a cost-efficient opportunity to teach and demonstrate the potential of super-resolution microscopy for biological studies to new generations of young researchers.

## Experimental Section

### Materials

Unmodified DNA oligonucleotides, fluorescently modified DNA oligonucleotides and biotinylated DNA oligonucleotides were purchased from MWG Eurofins. M13mp18 scaffold was obtained from New England BioLabs (cat: N4040S). p8064 scaffold for the tetrahedron DNA origami structure was prepared by replacement of the BamHI-XbaI segment of M13mp18 by a PCR-amplified fragment of bacteriophage  $\lambda$  DNA, flanked by positions -25 to +25 of the middle of the XbaI cut site (TCTAGA or base 6258). Agarose (cat: 01280.100) was purchased from biomol. SYBR safe (cat: SS33102) was ordered from Invitrogen. DNA gel loading dye (cat: R0611) was purchased from ThermoFisher. Freeze 'N Squeeze columns (cat: 732-6165) were ordered from Bio-Rad. BSA-Biotin was obtained from Sigma-Aldrich (cat: A8549). Streptavidin was ordered from Invitrogen (cat: S-888). Avidin coated silicon beads (cat: PC-A-16) were ordered from Kisker Biotech. Tris 1 M pH 8.0 (cat: AM9856), EDTA 0.5 M pH 8.0 (cat: AM9261), Magnesium 1 M (cat: AM9530G) and Sodium Chloride 5 M (cat: AM9759) were ordered from Ambion. Ultrapure water (cat: 10977-035) was purchased from Gibco. Glass slides (cat: 48811-703) were obtained from VWR. Coverslips were purchased from Marienfeld (cat: 0107032). Silicon (cat: 1300 1000) was ordered from picodent. Double sided tape (cat: 665D) was ordered from Scotch. COS7 cells (cat: CRL-1651) were purchased from ATCC. Secondary antibodies Anti-Rat IgG (cat: 712-005-150) and Anti-Rabbit (cat: 711-005-152) were purchased from Jackson ImmunoResearch. 16% Paraformaldehyde (cat: 15710) was obtained from Electron Microscopy Sciences. 25% Glutaraldehyde (cat: 23115.01) was ordered from SERVA. Sodium borohydride (cat: 4051.1) and Triton X-100 (cat: 6683.1) were purchased from Carl Roth. BSA (cat: A4503-10g) was obtained from Sigma-Aldrich. 1  $\times$  PBS (cat: 20012-019) was purchased from Thermo Fisher Scientific. DMEM (cat: 10566-016), fetal bovine serum (cat: 10500-064), Penicillin-Streptomycin (cat: 15140-122) and Trypsin-EDTA (cat: 25300-054) were obtained from Thermo Fisher Scientific. Primary monoclonal rat  $\alpha$ -Tubulin (Y/L) antibody (cat: MA1-80017) was ordered from Thermo Fishes Scientific. Tom20 primary rabbit polyclonal antibody (cat: sc-11415) was purchased from Santa Cruz. Maleimide-PEG2-succinimidyl ester (cat: 746223) was purchased from Sigma-Aldrich. 90 nm gold nanoparticles were purchased from Cytodiagnosics, (cat: G-90-100). No-Weigh Format DTT (cat: 20291) was purchased from Thermo Fisher Scientific. Micro BCA Protein Assay Kit was obtained from Thermo Fisher Scientific (cat: 23235). Amicon spin filters, 100 kDa and 3 kDa cat: UFC510096 and UFC500396) and 0.22  $\mu$ m sterile filters (cat: SLG50335S) were purchased from Merck/EMD Millipore. Nap5 columns (cat: 17-0853-02) were ordered from GE Healthcare. Zeba desalting spin columns (cat: 89882) were obtained from Thermo Fisher Scientific. Silicon tubing, inner diameter = 0.5 mm, outer diameter = 1 mm (GM GmbH, cat: 35605). FINE-JECT Needle, 1.1  $\times$  40 mm (Henke Sass Wolf, cat: 4710011040). NORM-JECT 10-ml syringe (Henke Sass Wolf, cat: 4100-000 V0). PEG5k-NHS (cat: 12500-35) and Biotin-PEG5k-NHS (cat: 135000-25-35) were ordered from Rapp Polymere. Amino-silane (cat: 104884-100 ML) and Sodium Bicarbonate (cat: S5761-1kg) were ordered from Sigma.

Three buffers were used for sample preparation and imaging: Buffer A: 10 mM Tris-HCl pH 7.5, 100 mM NaCl, 0.05% Tween 20, pH 7.5); Buffer B: 5 mM Tris-HCl pH 8, 10 mM MgCl<sub>2</sub>, 1 mM EDTA, 0.05% Tween 20, pH 8); Buffer C: 1  $\times$  PBS pH 7.2, 500 mM NaCl). 100  $\times$  Trolox: 100 mg Trolox, 430  $\mu$ l 100% Methanol, 345  $\mu$ l 1 M NaOH in 3.2 ml H<sub>2</sub>O. 40  $\times$  PCA: 154 mg PCA, 10 ml water and NaOH were mixed and adjusted to pH 9.0. 100  $\times$  PCD: 9.3 mg PCD, 13.3 ml of buffer (100 mM Tris-HCl pH 8, 50 mM KCl, 1 mM EDTA, 50% glycerol). 1.2  $\times$  BME: Tris pH 8.0 50 mM, beta Mercaptoethanol

179 mM, MgCl 50 mM, Glucose 12.5 mM in H<sub>2</sub>O. 6  $\times$  GLOX: Glucose Oxidase 2.5 mg, Tris 50 mM, Glycerol 10 mM, Catalase 200 mg/ml in H<sub>2</sub>O.

### DNA Origami Self-assembly

The Rothmund rectangular origami (RRO) from Figure 2, Supplementary Figures 3, 4 and 5 were synthesized in one-pot reactions with 50  $\mu$ l total volume containing 10 nM scaffold strand (M13mp18), 100 nM core staples, 1  $\mu$ M biotinylated staples and 1  $\mu$ M DNA-PAINT handles. The folding buffer was 1  $\times$  TE buffer with 12.5 mM MgCl<sub>2</sub>. Structures were annealed using a thermal ramp. First, incubating for 5 min at 80  $^{\circ}$ C, then going from 65  $^{\circ}$ C to 4  $^{\circ}$ C over the course of 3 hours. After self-assembly, the structures were mixed with 1  $\times$  loading dye and then purified by agarose gel electrophoresis (1.5% agarose, 0.5  $\times$  TAE, 10 mM MgCl<sub>2</sub>, 1  $\times$  SYBR Safe) at 3 V/cm for 2 hours. Gel bands were cut, crushed and filled into a Freeze 'N Squeeze column and spun for 5 min at 1,000  $\times$  g at 4  $^{\circ}$ C. The tetrahedron DNA origami structures used in Figure 6 were formed in a one-pot reaction with a 50  $\mu$ l total volume containing 10 nM scaffold strand (p8064), 100 nM core staples, 100 nM connector staples, 100 nM vertex staples, 100 nM biotin handles, 100 nM DNA-PAINT handles, and 1400 nM biotin anti-handles in folding buffer (1  $\times$  TE (5 mM Tris, 1 mM EDTA) buffer with 10 mM MgCl<sub>2</sub>). The solution was annealed using a thermal ramp cooling from 80 to 4  $^{\circ}$ C over the course of 15 h. After self-assembly, the structures were mixed with 1  $\times$  loading dye and then purified by agarose gel electrophoresis (1.5% agarose, 0.5  $\times$  TAE, 10 mM MgCl<sub>2</sub>, 1  $\times$  SYBR Safe) at 3 V/cm for 3 h. Gel bands were cut, crushed and filled into a Freeze 'N Squeeze column and spun for 5 min at 1000  $\times$  g at 4  $^{\circ}$ C.

### Super-resolution DNA-PAINT Imaging with DNA Origami

First, 20  $\mu$ l of biotin-labeled bovine albumin (1 mg/ml, dissolved in buffer A) was flown into the chamber and incubated for 2 min. Then the chamber was washed using 40  $\mu$ l of buffer A. Second, 20  $\mu$ l of streptavidin (0.5 mg/ml, dissolved in buffer A) was then flown through the chamber and incubated for 2 min. Next, the chamber was washed with 20  $\mu$ l of buffer A and subsequently with 20  $\mu$ l of buffer B. Then  $\sim$ 500 pM of the DNA origami structures were flown into the chamber and allowed to attach to the surface for 2 min. Finally, the imaging buffer with buffer B with dye-labeled imager strands was flown into the chamber. The microscopy chamber was placed at the microscope and using low laser power the focal plane was adjusted. After equilibrating for 30 min without laser illumination, the focal plane was checked and if necessary re-adjusted before starting the acquisition. For Figure 2 3 nM ATTO 647N labeled imager with sequence P1 and 1  $\times$  PCA, 1  $\times$  PCD, 1  $\times$  Trolox in buffer B was used. In Figure 6 500 pM ATTO 647N labeled imager strands P1 and 1  $\times$  PCA, 1  $\times$  PCD, 1  $\times$  Trolox in buffer B was used. The experiment in Supplementary Figure 3 was carried out using 4 nM ATTO 647 N with sequence X61 and 1  $\times$  PCA, 1  $\times$  PCD, 1  $\times$  Trolox in buffer B. For Supplementary Figure 4 7 nM ATTO 647N labeled imager strands P1 and 1  $\times$  PCA, 1  $\times$  PCD, 1  $\times$  Trolox in buffer B was used.

### Super-Resolution dSTORM Imaging with DNA Origami

For sample preparation of Supplementary Figure 5, a piece of coverslip (no. 1.5, 18  $\times$  18 mm<sup>2</sup>,  $\sim$ 0.17 mm thick) and a glass slide (75  $\times$  25 mm<sup>2</sup>, 1 mm thick) were sandwiched together by two strips of double-sided tape to form a flow chamber with inner volume of  $\sim$ 20  $\mu$ l. First, 20  $\mu$ l of biotin-labeled bovine albumin (1 mg/ml, dissolved in buffer A) was flown into the chamber and incubated

for 2 min. Then the chamber was washed using 40  $\mu$ l of buffer A. Second, 20  $\mu$ l of streptavidin (0.5 mg/ml, dissolved in buffer A) was then flown through the chamber and incubated for 2 min. Next, the chamber was washed with 20  $\mu$ l of buffer A and subsequently with 20  $\mu$ l of buffer B. Then  $\sim$ 500 pM of the DNA origami structures were flown into the chamber and allowed to attach to the surface for 2 min. Finally, the imaging buffer containing 1 $\times$ BME and 1 $\times$ GLOX was flown into the chamber. The microscopy chamber was placed at the microscope and using low laser power the focal plane was adjusted. After equilibrating for 30 min without laser illumination, the focal plane was checked and if necessary re-adjusted before starting the acquisition.

### Super-Resolution DNA-PAINT Imaging with Latex Microspheres

For chamber preparation, a piece of pegylated coverslip (as described below) and a glass slide (75 $\times$ 25 mm<sup>2</sup> 1 mm thick) were sandwiched together by two strips of double-sided tape to form a flow chamber with inner volume of  $\sim$ 20  $\mu$ l. First, 20  $\mu$ l of 1:20 avidin coated microspheres diluted in 1 $\times$ PBS was flown into the chamber and incubated for 10 min. Then the chamber was washed using 40  $\mu$ l of 1 $\times$ PBS. Second, 500 nM biotinylated oligonucleotides (10nt, P1 docking site sequence) was then flown into the chamber and incubated for 10 min. Next, the chamber was washed with 100  $\mu$ l of 1 $\times$ PBS. Next, the chamber was incubated with 1:10 dilution of 90 nm gold particles in 1 $\times$  PBS as drift markers for 5 min and subsequently washed with 40  $\mu$ l 1 $\times$ PBS. Finally, the imaging buffer with buffer B with dye-labeled imager strands was flown into the chamber. For Figure 5 150 pM ATTO 647N labeled imager with sequence P1 and 1 $\times$ PCA, 1 $\times$ PCD, 1 $\times$ Trolox in buffer B were used. The microscopy chamber was placed at the microscope and using low laser power the focal plane was adjusted. After equilibrating for 30 min without laser illumination, the focal plane was checked and if necessary re-adjusted before starting the acquisition.

### PEG Surface Preparation

PEG surfaces were created as previously reported.<sup>[25]</sup> In short, the microscopy coverslips (no. 1.5 high precision, 18 $\times$ 18 mm<sup>2</sup>) were put into a Teflon-based custom-made slide holder, rinsed twice and bath-sonicated in Milli-Q water for 10 min. The rinsing and washing process was repeated with methanol and acetone. For surface activation, the coverslips were bath-sonicated in 1 M KOH for 20 min and rinsed with Milli-Q water afterwards. The slides were then blow dried with nitrogen and 95 ml of methanol was mixed with 5 ml acetic acid as well as 1 ml aminosilane and was immediately poured over the slide holder. The reaction was incubated for 10 min in the dark, briefly sonicated for 1 min and incubated for another 10 min in the dark. The coverslips were then washed two times with methanol and water for 1–2 min per wash. After blow drying with nitrogen, the aminosilane coverslips were stored under Argon atmosphere for <2 weeks until further use. One day before use, the chambers were assembled with the aminosilane coverslips with double sided sticky tape. 16 mg of mPEG was dissolved in 70  $\mu$ l of freshly prepared sodium bicarbonate buffer (10 mM sodium bicarbonate, pH 8.5) and mixed 20:1 with biotin-PEG. To remove bubbles, the mix was briefly spun down for 30 s and added to the assembled chamber. The chamber was sealed with silicon (picodent) and stored at room temperature overnight in the dark. Before use, the silicon was removed and the chamber was washed with 1 ml Milli-Q water.

### Antibody Conjugation

Antibodies were labeled with DNA strands as previously described.<sup>[26]</sup> In short, secondary antibodies were concentrated via amicon 100 kDa spin filters to 1–3 mg/ml. 100  $\mu$ l of antibody was labeled using a Maleimide-Peg2-succinimidyl ester for 90 min at 10 $\times$ molar excess at 4  $^{\circ}$ C on a shaker. Crosslinker stocks of 10 mg/ml in DMF were diluted in 1 $\times$ PBS to reach 10 $\times$  molar excess in 5  $\mu$ l, which were subsequently added to the antibody. After the reaction had been done, unreacted crosslinker was removed via a zeba spin column. Thiolated DNA was reduced using DTT for 2 h at room temperature. DTT was purified from the reduced DNA via a Nap5 column and fractions containing DNA were concentrated via 3 kDa amicon spin filters. The reduced DNA was then added to the antibody bearing a functional maleimide group in 10 $\times$  molar excess and incubated over night at 4  $^{\circ}$ C on a shaker in the dark. Antibody-DNA constructs were finally purified via 100 kDa amicon spin filters.

### Cell Culture

Cells were cultured in Dulbecco's Modified Eagle Medium (DMEM) supplemented with 10% FBS and 1% Penicillin and Streptomycin, they were passaged every other day until 90% confluency was reached using standard cell culture methods. HeLa cells for imaging were used between passage number 6 and 20.

### Immunofixation

24 h before fixation, COS7 cells were seeded to 70% confluency. For microtubule imaging cells were prefixed with prewarmed 0.4% Glutaraldehyde and 0.25% Triton X-100 in 1 $\times$ PBS for 90 s and fixed with 3% Glutaraldehyde in 1 $\times$ PBS for 15 min. For dualcolor imaging, the cells were fixed with prewarmed 3% Paraformaldehyde and 0.1% Glutaraldehyde in 1 $\times$ PBS for 15 min. Quenching was performed via freshly prepared 1 mg/ml Sodium Borohydride in 1 $\times$  PBS for 7 min. Cells were washed 1 $\times$  for 1 min and 3 $\times$  for 5 min in 1 $\times$ PBS. Blocking and permeabilization were performed using 3% BSA and 0.25% Triton X-100 in 1 $\times$ PBS for 90 min. Microtubule and TOM20 primary antibodies were incubated overnight at 4  $^{\circ}$ C. with gentle shaking in 5% BSA in 1 $\times$ PBS in the dark. Cells were washed 3 $\times$  in 1 $\times$ PBS for 5 min. Conjugated secondary antibodies were incubated for 1 h at RT in the dark in 5% BSA in 1 $\times$ PBS. The cells were finally washed 3 $\times$  in 1 $\times$  PBS for 5 min and incubated with 90 nm gold nanoparticles 1:10 diluted in 1 $\times$ PBS for 10 min and washed again 1 $\times$  in 1 $\times$  PBS for 2 min.

### Super-Resolution DNA-PAINT Imaging with Cells

The experiment in Figure 3 was performed using 3 nM ATTO 647N labelled imager strands with sequence X61 and 1 $\times$ PCA, 1 $\times$ PCD, 1 $\times$ Trolox in buffer C. In Supplementary Figures 6, 7 1 nM ATTO 647N labelled imager strands with sequence P1 and 1 $\times$ PCA, 1 $\times$ PCD, 1 $\times$ Trolox in buffer C was used. The microscopy chamber in both cases was placed at the microscope and using low laser power the focal plane was adjusted. After equilibrating for 30 min without laser illumination, the focal plane was checked and if necessary readjusted before starting the acquisition. Multicolour cell imaging of alpha tubulin in Figure 4 was performed with 500 pM ATTO 647N labelled imager strands with sequence P1 and 1 $\times$ PCA, 1 $\times$ PCD, 1 $\times$ Trolox in buffer C. TOM20 imaging in Figure 4 was performed using 1 nM ATTO 647 N labelled imager strands with sequence P3 and 1 $\times$ PCA, 1 $\times$ PCD, 1 $\times$ Trolox in buffer C. Multicolour cell imaging of alpha tubulin in Supplementary Figure 8 was performed with 2 nM ATTO 647N labelled imager strands with sequence X61 and 1 $\times$ PCA, 1 $\times$ PCD, 1 $\times$ Trolox in buffer C. TOM20

imaging in Supplementary Figure 8 was performed using 2 nM ATTO 647N labelled imager strands with sequence P1 and 1×PCA, 1×PCD, 1×Trolox in buffer C. The microscopy chamber in both cases was placed at the microscope and using low laser power the focal plane was adjusted. After equilibrating for 30 min without laser illumination, the focal plane was checked and if necessary re-adjusted before starting the acquisition. The liquid exchange in Figure 4 and Supplementary Figure 8 was performed using an electric syringe pump with tubing and a needle to remove the buffer out of the chamber. To minimize contact, hence shift of the sample chamber, new buffers were dripped through a small hole in the sample chamber lid using a pipette. The hole was made beforehand using a heated needle. Washing during Exchange-PAINT acquisition rounds was carried out until no single-molecule blinking was observed to minimize cross-talk of imager species.

### Microscopy Data Acquisition

The following computer system was used for all data acquisition: Dell XPS 15 9550 with Intel i7-6700HQ processor, Windows 10 Pro, 16 GB DDR4 RAM and 1 TB PCIe-SSD. Raw image data was acquired with the open-source software package Micro-Manager<sup>[27]</sup> version 1.4.22. Drivers for PCO cameras were downloaded from the PCO homepage. Thorlabs camera drivers were downloaded from the Thorlabs homepage. Cameras were installed as described in the manuals available at the vendor's and Micro-Manager's homepage. We note that a lower performance computer system is also able to acquire raw data and subsequently reconstruct the super-resolution images (using Picasso). We have also tested this using a laptop with the following configuration: Asus F541U with Intel i3-6006U processor, Windows 10, 8 GB DDR4 RAM and 1 TB HDD. We want to highlight, that some new sCMOS cameras (e.g. PCO.panda) operate only with USB 3.0 or higher.

### Super-Resolution Data Processing

Super-resolution DNA-PAINT reconstruction, drift correction, and alignment was carried out using the software package Picasso. The DNA origami data was first drift corrected with redundant cross-correlation (RCC). Second, the DNA origami structures were picked using Picasso's semiautomated particle picking tool and drift was corrected with the picked nanostructures as fiducial markers. Finally, individual docking sites of DNA origami were selected (same as above) and used for correction of residual drift. Cell data was first drift corrected with RCC and in a second step using immobilized gold particles on the glass surface. For the 3D super-resolution experiments, microsphere radius was determined using bright-field illumination and subsequent cross-sectional histogram analysis. The recorded latex microsphere data using DNA-PAINT in Figure 5a was first reconstructed using two-dimensional gaussian fitting and a dummy calibration curve. After lateral drift correction using redundant cross correlation, outliers with respect to the z position were filtered out. Finally, after z drift correction (Supplementary Figure 10d) the calibration data was fitted using sixth degree polynomial fit to generate the look-up table (see Supplementary Figure 10b). The 3D calibration analysis pipeline was integrated as a module into the software package Picasso, now available at GitHub. When using beads for calibration one will need to choose "Calibrate using Microspheres".

### Acknowledgements

We thank Jae Yen Shin and Joerg Schnitzbauer for helpful discussions about the platform name. We thank Gerhard Holst from PCO AG for providing the PCO.panda 4.2 camera and the CAD file of the interline-transfer CCD camera. We thank Nils Hommerstad and Guy Among from Toptica Photonics AG for providing the CAD file of the laser. We also thank Andreas Kucher and his team from the precision engineering workshop of the Max Planck Institute of Biochemistry. This work was supported in part by the DFG through the Emmy Noether Program (DFG JU 2957/1-1), the SFB 1032 (Nanoagents for spatiotemporal control of molecular and cellular reactions, Project A11), the ERC through an ERC Starting Grant (MolMap, Grant agreement number 680241) and an ERC Proof of Concept Grant (Resolve, Grant agreement number 790594), the Max Planck Society, the Max Planck Foundation and the Center for Nano-science (CeNS). A.A. and T.S. acknowledge support from the DFG through the Graduate School of Quantitative Biosciences Munich (QBM). M.T.S. acknowledges support from the International Max Planck Research School for Molecular and Cellular Life Sciences (IMPRS-LS).

### Conflict of Interest

The authors declare no conflict of interest.

**Keywords:** DNA · nanotechnology · photophysics · single-molecule microscopy · super-resolution imaging

- [1] S. W. Hell, S. J. Sahl, M. Bates, X. W. Zhuang, R. Heintzmann, M. J. Booth, J. Bewersdorff, G. Shtengel, H. Hess, P. Tinnefeld, A. Honigmann, S. Jakobs, I. Testa, L. Cagnet, B. Lounis, H. Ewers, S. J. Davis, C. Eggeling, D. Klenerman, K. I. Willig, G. Vicidomini, M. Castello, A. Diaspro, T. Cordes, *J. Phys. D* **2015**, *48*.
- [2] a) E. Betzig, G. H. Patterson, R. Sougrat, O. W. Lindwasser, S. Olenych, J. S. Bonifacino, M. W. Davidson, J. Lippincott-Schwartz, H. F. Hess, *Science* **2006**, *313*, 1642–1645; b) S. T. Hess, T. P. Girirajan, M. D. Mason, *Biophys. J.* **2006**, *91*, 4258–4272.
- [3] a) M. J. Rust, M. Bates, X. W. Zhuang, *Nat. Methods* **2006**, *3*, 793–795; b) M. Heilemann, S. van de Linde, M. Schüttel, R. Kasper, B. Seefeldt, A. Mukherjee, P. Tinnefeld, M. Sauer, *Angew. Chem. Int. Ed.* **2008**, *47*, 6172–6176; *Angew. Chem.* **2008**, *120*, 6266–6271.
- [4] S. W. Hell, J. Wichmann, *Opt. Lett.* **1994**, *19*, 780–782.
- [5] aP. Kanchanawong, G. Shtengel, A. M. Pasapera, E. B. Ramko, M. W. Davidson, H. F. Hess, C. M. Waterman, *Nature* **2010**, *468*, 580–584; b) K. Xu, G. Zhong, X. Zhuang, *Science* **2013**, *339*, 452–456.
- [6] a) R. Jungmann, C. Steinhauer, M. Scheible, A. Kuzky, P. Tinnefeld, F. C. Simmel, *Nano Lett.* **2010**, *10*, 4756–4761; b) J. Schnitzbauer, M. T. Strauss, T. Schlichthaerle, F. Schueder, R. Jungmann, *Nat. Protoc.* **2017**, *12*, 1198–1228.
- [7] R. Jungmann, M. S. Avendano, J. B. Woehrstein, M. J. Dai, W. M. Shih, P. Yin, *Nat. Methods* **2014**, *11*, 313–U292.
- [8] R. Jungmann, M. S. Avendano, M. Dai, J. B. Woehrstein, S. S. Agasti, Z. Feiger, A. Rodal, P. Yin, *Nat. Methods* **2016**, *13*, 439–442.
- [9] a) T. Holm, T. Klein, A. Loschberger, T. Klamp, G. Wiebusch, S. van de Linde, M. Sauer, *ChemPhysChem* **2014**, *15*, 651–654; b) H. Ma, R. Fu, J. Xu, Y. Liu, *Sci. Rep.* **2017**, *7*, 1542.
- [10] D. Axelrod, *J. Cell Biol.* **1981**, *89*, 141–145.
- [11] M. Tokunaga, N. Imamoto, K. Sakata-Sogawa, *Nat. Methods* **2008**, *5*, 159–161.
- [12] aH. P. Kao, A. S. Verkman, *Biophys. J.* **1994**, *67*, 1291–1300; b) F. Huang, G. Sirinakis, E. S. Allgeyer, L. K. Schroeder, W. C. Duim, E. B. Kromann, T. Phan, F. E. Rivera-Molina, J. R. Myers, I. Irnov, M. Lessard, Y. Zhang, M. A.

- Handel, C. Jacobs-Wagner, C. P. Lusk, J. E. Rothman, D. Toomre, M. J. Booth, J. Bewersdorf, *Cell* **2016**, *166*, 1028–1040.
- [13] C. Cabriel, N. Bourg, G. Dupuis, S. Leveque-Fort, *Opt. Lett.* **2018**, *43*, 174–177.
- [14] P. W. K. Rothmund, *Nature* **2006**, *440*, 297–302.
- [15] a) F. Schueder, J. Lara-Gutierrez, B. J. Beliveau, S. K. Saka, H. M. Sasaki, J. B. Woehrstein, M. T. Strauss, H. Grabmayr, P. Yin, R. Jungmann, *Nat. Commun.* **2017**, *8*, 2090; b) M. T. Strauss, F. Schueder, D. Haas, P. C. Nickels, R. Jungmann, *Nat. Commun.* **2018**, *9*, 1600.
- [16] U. Endesfelder, S. Malkusch, F. Fricke, M. Heilemann, *Histochem. Cell Biol.* **2014**, *141*, 629–638.
- [17] a) G. T. Dempsey, J. C. Vaughan, K. H. Chen, M. Bates, X. Zhuang, *Nat. Methods* **2011**, *8*, 1027–1036; b) M. Mikhaylova, B. M. Cloin, K. Finan, R. van den Berg, J. Teeuw, M. M. Kijanka, M. Sokolowski, E. A. Katrukha, M. Maidorn, F. Opazo, S. Moutel, M. Vantard, F. Perez, P. M. van Bergen en Henegouwen, C. C. Hoogenraad, H. Ewers, L. C. Kapitein, *Nat. Commun.* **2015**, *6*, 7933; c) Y. Li, M. Mund, P. Hoess, J. Deschamps, U. Matti, B. Nijmeijer, V. J. Sabinina, J. Ellenberg, I. Schoen, J. Ries, *Nat. Methods* **2018**, *15*, 367–369.
- [18] S. S. Agasti, Y. Wang, F. Schueder, A. Sukumar, R. Jungmann, P. Yin, *Chem. Sci.* **2017**, *8*, 3080–3091.
- [19] M. H. Heggeness, M. Simon, S. J. Singer, *Proc. Natl. Acad. Sci. USA* **1978**, *75*, 3863–3866.
- [20] B. Huang, W. Q. Wang, M. Bates, X. W. Zhuang, *Science* **2008**, *319*, 810–813.
- [21] R. Iinuma, Y. G. Ke, R. Jungmann, T. Schlichthaerle, J. B. Woehrstein, P. Yin, *Science* **2014**, *344*, 65–69.
- [22] A. Ashkin, J. M. Dziedzic, J. E. Bjorkholm, S. Chu, *Opt. Lett.* **1986**, *11*, 288.
- [23] T. R. Strick, J. F. Allemand, D. Bensimon, A. Bensimon, V. Croquette, *Science* **1996**, *271*, 1835–1837.
- [24] G. Binnig, C. F. Quate, C. Gerber, *Phys. Rev. Lett.* **1986**, *56*, 930–933.
- [25] A. Jain, R. Liu, Y. K. Xiang, T. Ha, *Nat. Protoc.* **2012**, *7*, 445–452.
- [26] J. Schnitzbauer, M. T. Strauss, T. Schlichthaerle, F. Schueder, R. Jungmann, *Nat. Protoc.* **2017**, *12*, 1198–1228.
- [27] A. D. Edelstein, M. A. Tsuchida, N. Amodaj, H. Pinkard, R. D. Vale, N. Stuurman, *J. Biol. Methods* **2014**.

---

Manuscript received: July 3, 2018

Accepted manuscript online: September 12, 2018

Version of record online: October 8, 2018



# 5

## nanoTRON: a Picasso module for MLP-based classification of super-resolution data

In the previous chapters 3 and 4, progress in the experimental aspect of super-resolution microscopy was discussed. Following the image acquisition, the final step in the workflow typically involves the analysis of the collected raw data. This chapter addresses the automation of previously tedious manual work in data evaluation.

### 5.1 SUPER-RESOLUTION MICROSCOPY PROCESSING OF NANOPATTERNS USING PICASSO

In 2016 Schnitzbauer et al. published a comprehensive study containing a wide range of experimental protocols for DNA-PAINT imaging [45]. Accompanying this publication, the Python-based [111] software package Picasso including various programs for the analysis of super-resolution microscopy, was released. For example, the software tool Picasso *Localize* can be used for processing of the raw data. Here, diffraction-limited SMLM movies (see **Figure 2.5**) can be processed, where single-molecule signals are identified and localized by fitting of 2D distribution functions, described in the chapter 2.3.2. The gathered localization (molecule) lists can be plotted as a 2D histogram and interactively visualized as a heatmap using the software program Picasso *Render*. Additionally to plotting, Picasso *Render* features a tool called *Pick tool* that allows the manual selection of nano-scaled regions in the heatmap for higher analysis. For example, nanopatterns of protein complexes could be selected and processed for structure analysis [6] or DNA origami could be utilized as calibration standards [112]. **Figure 5.1** illustrates nano-scaled patterns (nanopattern) originating from DNA origami imaged with DNA-PAINT. The yellow circles mark the selection using Picasso *Render*'s *Pick tool*.



**Figure 5.1: Nanopatterns.** DNA-PAINT super-resolution microscopy image of four distinct DNA origami targets. Every DNA origami class was modified with a different nanopattern (the design is illustrated on the left) for DNA-PAINT imaging. Yellow circle, described by center coordinates and a pick diameter, mark the selected region using Picasso's *Pick tool*. Scale bar 100 nm.

## 5.2 SELECTION OF NANOPATTERNS

DNA-PAINT blinking is based on transient DNA hybridization. Their "kinetic fingerprint" can identify target signals originating from DNA-PAINT docking sites. This kinetic behavior can easily be estimated via the measured parameters  $k_{on}$  and  $k_{off}$  of an imager sequence and the concentration of imager in solution [50, 7]. *Pick similar*, another tool in *Picasso Render* takes advantage of this predictable feature. Usually, in *Picasso Render*, one selects a handful of regions containing the nanopatterns manually via the *Pick tool*. Subsequently, the whole super-resolution image can be screened and marked for areas with comparable numbers of localization events using the tool *Pick similar*. Importantly, the shape of those nanopatterns in the picked regions is not considered. Typically, a single field of view in a super-resolved microscopy image can contain up to tens of thousands of nanopatterns, depending on the spatial density. This approach, therefore, allows a fast and semi-automatic selection of nanopatterns in a non-differentiating way.

## 5.3 DEEP LEARNING-ASSISTED CLASSIFICATION

The software package *Picasso* features a fast method of selecting nanopatterns using *Picasso Render's Pick tool* and *Pick similar*. However, during the picking, the shape of the nanopatterns are not taken into account. This deficit results in a miscellaneous selection of different nanopatterns. Besides tedious manually selecting, sequential imaging with Exchange-PAINT of the different targets can overcome this problem. With this approach, however, the imaging process is extended by the factor of the number of distinct nanopatterns. Every distinct nanopattern requires an imaging round using Exchange-PAINT. To keep the overall data acquisition time low, but still enabling the shape-based separation of selected nanopatterns, a novel *Picasso* software tool was written. The software program is called nanoTRON (nanoscale perceptron) and enables a deep learning-based classification and export of nanopatterns, selected with the help of *Picasso Render Pick tool*. nanoTRON is based on MLPs and provides a user-friendly graphical user interface (GUI) to set up and train ANNs and subsequently use the trained models for nanopattern classification.

## 5.4 A MLP INSTEAD OF A CNN IMPLEMENTATION

To justify the implementation of the multilayer perceptron, the LeNet-5 CNN (described in **Figure 2.19**) was compared with a nanoTRON 1-hidden-layer MLP with 550 nodes. Given the benchmarking results, the final implementation of the ANN design was mainly influenced by three practical aspects:

Performance: During the rendering process of the super-resolution data, the localization coordinates are plotted in a 2D histogram. Hence, nanopatterns are small arrays of gray values. Typically, these single-color renderings contain less information or features compared to colored images of dogs, cars or similar objects with background from daily life. A performance comparison between the 1-hidden layer MLP with 550 nodes and the 7-layer CNN LeNet-5 implemented with the deep learning package Keras [113], was performed. Ultimately, the train and test accuracies proved to be almost identical.

Availability: The MLP of scikit-learn covers straightforward support of a wide range of computers, as the training using a central processing unit (CPU) processor, proved to be more universally applicable. Typically, for more complex networks, a high-performance GPU is recommended. Mobile devices like laptops usually lack high-performance graphics cards, which support GPU processing for deep learning. The LeNet-5 CNN trained on a high-performance server with 24 CPU cores and required >1.5 days computing time for the proof-of-concept experiment with four different

classes, while training with the MLP was completed with similar accuracy after only 47 minutes.

Maintenance: The Python package scikit-learn is a software library that is already used by Picasso. Deep learning packages like Keras, Theano [114], or PyTorch [115] usually come with a larger list of dependencies for additional packages. This could, in the future, complicate the maintenance of Picasso, as version conflicts between packages can become more likely.



**nanoTRON: a Picasso module for MLP-based classification of super-resolution data**

BY

**Alexander Auer**, Maximilian T. Strauss, Sebastian Strauss, and Ralf Jungmann

PUBLISHED IN

*Bioinformatics*, (2020), *in press*.  
doi: 10.1093/bioinformatics/btaa154

The accepted version of the manuscript is reprinted from ref. [3].  
CC-BY-NC 4.0



---

*Bioimage informatics*

# nanoTRON: a Picasso module for MLP-based classification of super-resolution data

Alexander Auer<sup>1,2</sup>, Maximilian T. Strauss<sup>2</sup>, Sebastian Strauss<sup>1,2</sup>, and Ralf Jungmann<sup>1,2,\*</sup>

<sup>1</sup>Department of Physics and Center for Nanoscience, Ludwig Maximilian University, 80539 Munich, Germany, <sup>2</sup>Max Planck Institute of Biochemistry, 82152 Martinsried near Munich, Germany

\*To whom correspondence should be addressed.

Associate Editor: XXXXXXXX

Received on XXXXX; revised on XXXXX; accepted on XXXXX

## Abstract

**Motivation:** Classification of images is an essential task in higher-level analysis of biological data. By bypassing the diffraction-limit of light, super-resolution microscopy opened up a new way to look at molecular details using light microscopy, producing large amounts of data with exquisite spatial detail. Statistical exploration of data usually needs initial classification, which is up to now often performed manually.

**Results:** We introduce nanoTRON, an interactive open-source tool, which allows super-resolution data classification based on image recognition. It extends the software package Picasso with the first deep learning tool with a graphic user interface.

**Availability:** nanoTRON is written in Python and freely available under the MIT license as a part of the software collection Picasso on GitHub (<http://www.github.com/jungmannlab/picasso>).

**Contact:** jungmann@biochem.mpg.de

**Supplementary information:** Supplementary data are available at *Bioinformatics* online.

---

## 1 Introduction

Super-resolution fluorescence microscopy allows researchers to visualize structures and dynamics below the classical diffraction limit of light (Sahl, et al., 2017). Stochastic super-resolution techniques use switching of fluorescent molecules between so-called dark and bright states in combination with single-molecule localization. The switching creates an apparent blinking of target molecules, which is recorded in a movie and fitted with sub-diffraction precision in post-processing, and the resulting spatial coordinates of localized fluorophores are combined into two-dimensional histograms to render a super-resolution image (Sauer and Heilemann, 2017). DNA-PAINT (Jungmann, et al., 2010) uses the transient binding of dye-labeled DNA oligonucleotides (called ‘imager’ strands, freely diffusing in solution) to their target-bound complementary strands (called ‘docking’ strands) to create the necessary target “blinking” for super-resolution (**Figure 1**). DNA-PAINT is part of a large variety of techniques, which are enabled by the use of programmable interactions of DNA molecules: DNA Nanotechnology (Ramezani and Dietz, 2019). One of the most prominent approaches in structural DNA Nanotechnology is undoubtedly DNA origami (Rothenmund, 2006). Here, a long single-stranded DNA molecule is “folded” via self-assembly into almost arbitrary shapes and patterns using hundreds of short oligonucleotides. DNA origami enables the manufacturing of millions of nanoscopic structures with nanometer precision in a highly controlled and parallel fashion. These very properties of DNA origami structures and their nanoscale dimensions have led to a symbiotic relationship with super-resolution approaches:

DNA origami either serves as testbed for assaying new super-resolution approaches (Balzarotti, et al., 2017; Jungmann, et al., 2016; Schueder, et al., 2019; Steinhauer, et al., 2009), or super-resolution is used to characterize properties of DNA nanostructures (Johnson-Buck, et al., 2013; Strauss, et al., 2018). Super-resolution instrumentation, probe design, and sample preparation methods are progressing at a rapid pace, enabling cost-efficient, molecular-scale resolution on a routine basis (Auer, et al., 2018). Data analysis and post-processing software, however, are currently somewhat lacking behind, in most cases often still exclusively focusing on spot-detection and subsequent binning of localizations to visualize super-resolution data (Sage, et al., 2019). Especially more advanced yet increasingly essential post-processing tasks such as particle classification in super-resolution data is often still performed manually. Only recently, the super-resolution community turned their attention to more automated as well as machine-learning- and neuronal-network-based analysis approaches (Belthangady and Royer, 2019; Danial and Garcia-Saez, 2019; Ouyang, et al., 2018; von Chamier, et al., 2019). Advances in deep-learning are promising for the automation of algorithmic workflows such as detecting specific shapes or pattern, e.g. recognizing handwritten digits (Lecun, et al., 1998). This is particularly exciting in the context of super-resolution microscopy applied to the ever-increasing complexity of DNA-origami-based assays (Blanchard and Salaita, 2019). By combining super-resolution microscopy, DNA

nanotechnology, and deep-learning, we here present a new software module, termed nanoTRON.

## 2 Implementation

nanoTRON was implemented in Python (v3.7 and higher) as a component of the Picasso software suite (Schnitzbauer, et al., 2017). It deploys the multi-layer perceptron of the Python machine-learning framework sci-kit learn (Pedregosa, et al., 2011). The software combines two of the most important workflows for model-based neural-network-assisted data analysis: (i) user-friendly setup and training of artificial neural networks, (ii) classification and export of predicted data for subsequent analysis in a plug-and-play manner, see **Supplementary Text 1** and **Supplementary Text 4**. Super-resolution data sets can be loaded into nanoTRON for immediate classification and export, **Supplementary Figure 2**. The software allows the training of models for classifying of arbitrary patterns via the module ‘Train Model’, **Supplementary Figure 2**. Super-resolution data can be loaded, annotated and converted to 2-dimensional super-resolution images – gray-scale images – with a defined resolution (‘oversampling’), see **Supplementary Figure 3** and **Supplementary Figure 9**. By rotation of every image in multiple steps, the training set can be augmented, **Supplementary Figure 3**. nanoTRON supports multi-layer perceptron up to three hidden layers. For the evaluation of the trained network, nanoTRON uses a train-test data split of 30% of the training set. The learning curve of the training and the confusion matrix generated from the test set visualize the performance of the trained neural-network, **Supplementary Figure 2**. An exemplary application with DNA origami (**Supplementary Figure 1** and **Supplementary Figure 4-7**) is described in **Supplementary Text 2**. Additionally, we included a biological application with DNA origami and the nuclear pore complex (Schlichthaerle, et al., 2019; Thevathasan, et al., 2019) described in **Supplementary Text 3** and visualized with **Supplementary Figure 8** and **Supplementary Figure 12**.

## 3 Outlook

nanoTRON enables plug-and-play classification of super-resolution data using deep-learning of arbitrary nanoscopic pattern. We expect nanoTRON to serve as important tool in the Picasso software collection, which due to the user-friendly design brings deep-learning closer to biological researchers. We see nanoTRON as an instrument, which boosts the analysis of highly multiplexed biophysical assays, where e.g. automated detection and analysis of a plethora of barcoded structures (Lin, et al., 2012) for high-content and high-throughput studies would become feasible.

## Acknowledgements

We thank the Ries and Ellenberg labs at EMBL for providing the GFP-modified cell line. We thank Florian Schueder for fruitful discussions. A.A. and S.S. acknowledge support from the DFG through the Graduate School of Quantitative Biosciences Munich (QBM).

## Funding

This work was supported in part by the DFG through the Emmy Noether Program (DFG JU2957/1-1), the SFB 1032 (Nanoagents for spatiotemporal control of molecular and cellular reactions, Project A11), the ERC through an ERC Starting Grant (MolMap, Grant agreement number 680241) and an ERC Proof of Concept Grant (Resolve, Grant agreement number 790594), and the Max Planck Society. Conflict of Interest: none declared.

## References

Auer, A., et al. Nanometer-scale Multiplexed Super-Resolution Imaging with an Economic 3D-DNA-PAINT Microscope. *Chemphyschem* 2018;19(22):3024-3034.  
Balzarotti, F., et al. Nanometer resolution imaging and tracking of fluorescent molecules with minimal photon fluxes. *Science* 2017;355(6325):606-612.

Belthangady, C. and Royer, L.A. Applications, promises, and pitfalls of deep learning for fluorescence image reconstruction. *Nature Methods* 2019;16(12):1215-1225.  
Blanchard, A.T. and Salaita, K. Emerging uses of DNA mechanical devices. *Science* 2019;365(6458):1080-1081.  
Danial, J.S.H. and Garcia-Saez, A.J. Quantitative analysis of super-resolved structures using ASAP. *Nature Methods* 2019;16(8):711-714.  
Johnson-Buck, A., et al. Multifactorial modulation of binding and dissociation kinetics on two-dimensional DNA nanostructures. *Nano Lett* 2013;13(6):2754-2759.  
Jungmann, R., et al. Quantitative super-resolution imaging with qPAINT. *Nat Methods* 2016;13(5):439-442.  
Jungmann, R., et al. Single-molecule kinetics and super-resolution microscopy by fluorescence imaging of transient binding on DNA origami. *Nano Lett* 2010;10(11):4756-4761.  
Lecun, Y., et al. Gradient-based learning applied to document recognition. *P IEEE* 1998;86(11):2278-2324.  
Lin, C., et al. Submicrometre geometrically encoded fluorescent barcodes self-assembled from DNA. *Nat Chem* 2012;4(10):832-839.  
Ouyang, W., et al. Deep learning massively accelerates super-resolution localization microscopy. *Nat Biotechnol* 2018;36(5):460-468.  
Pedregosa, F., et al. Scikit-learn: Machine Learning in Python. *J Mach Learn Res* 2011;12:2825-2830.  
Ramezani, H. and Dietz, H. Building machines with DNA molecules. *Nat Rev Genet* 2019.  
Rothmund, P.W.K. Folding DNA to create nanoscale shapes and patterns. *Nature* 2006;440(7082):297-302.  
Sage, D., et al. Super-resolution fight club: assessment of 2D and 3D single-molecule localization microscopy software (vol 16, pg 387, 2019). *Nature Methods* 2019;16(6):561-561.  
Sahl, S.J., Hell, S.W. and Jakobs, S. Fluorescence nanoscopy in cell biology. *Nat Rev Mol Cell Biol* 2017;18(11):685-701.  
Sauer, M. and Heilemann, M. Single-Molecule Localization Microscopy in Eukaryotes. *Chem Rev* 2017;117(11):7478-7509.  
Schlichthaerle, T., et al. Direct Visualization of Single Nuclear Pore Complex Proteins Using Genetically-Encoded Probes for DNA-PAINT. *Angew Chem Int Edit* 2019;58(37):13004-13008.  
Schnitzbauer, J., et al. Super-resolution microscopy with DNA-PAINT. *Nat Protoc* 2017;12(6):1198-1228.  
Schueder, F., et al. An order of magnitude faster DNA-PAINT imaging by optimized sequence design and buffer conditions. *Nat Methods* 2019.  
Steinhauer, C., et al. DNA origami as a nanoscopic ruler for super-resolution microscopy. *Angew Chem Int Ed Engl* 2009;48(47):8870-8873.  
Strauss, M.T., et al. Quantifying absolute addressability in DNA origami with molecular resolution. *Nat Commun* 2018;9(1):1600.  
Thevathasan, J.V., et al. Nuclear pores as versatile reference standards for quantitative superresolution microscopy. *Nature Methods* 2019;16(10):1045-+.  
von Chamier, L., Laine, R.F. and Henriques, R. Artificial intelligence for microscopy: what you should know. *Biochem Soc T* 2019;47:1029-1040.

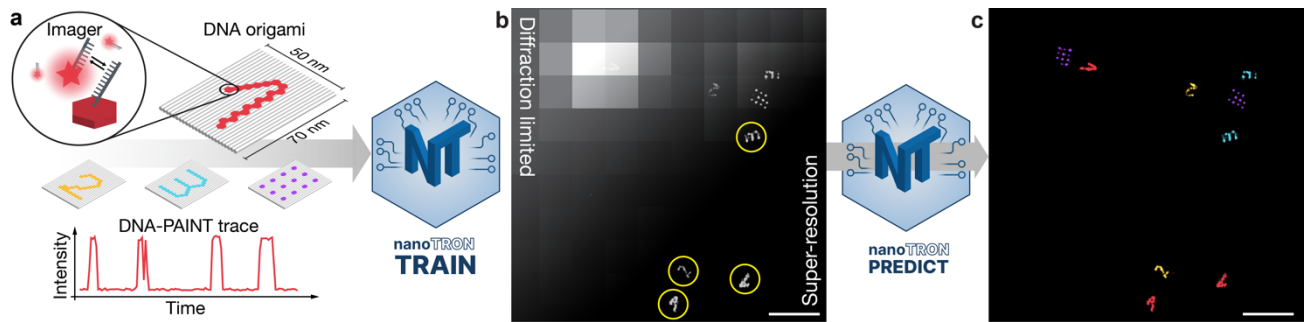


**Figure 1. nanoTRON workflow.** (a) DNA-PAINT imaging of DNA origami nanostructures uses transient binding of dye-labeled imager strands to their structure-bound complements, leading to target ‘blinking’ (see time trace) and enables subsequent super-resolution reconstruction of molecular patterns. (b) Diffraction-limited and super-resolved imaging of DNA origami structures immobilized on a glass surface. Four different patterns (digit 1, digit 2, digit 3 and 20-nm-grid, **Supplementary Figure 1**) were simultaneously imaged using DNA-PAINT. The individual patterns were grouped using Picasso’s pick function, highlighted with yellow circles. (c) Classified super-resolution image of the DNA-PAINT data in **b** shows the correct prediction of the four different nanoscopic patterns. Scale bars: 200 nm (**b**, **c**).



# 6

## Outlook

Recently, the imaging technology DNA-PAINT has established as a powerful next-generation super-resolution microscopy technology. It provides a relatively-easy-to-implement solution to sub-diffraction imaging with nanometer spatial resolution. Exchange-PAINT allows extensive multi-color imaging while eliminating the trade-off between spatial resolution performance and multiplexing capability. The technological advancements presented in this thesis promote the universal applicability of DNA-based super-resolution microscopy, by speeding up DNA-PAINT with FRET-PAINT imaging probes, introducing the drastically cost-reduced imaging platform LiteTIRF, and accelerating data analysis with the deep learning software tool nanoTRON. Faster, more affordable, and automation; Improvements that are necessary for a broader adaptation of super-resolution microscopy methods. Ultimately, requirements for technology transfer from scientific research to biomedical applications. A universal super-resolution imaging platform with precise and extensive fluidic exchange systems would have great potential and a wide range of applications.

A potential utilization for this universal imaging platform could be optical mapping for DNA sequence determination. Accessing DNA sequence information, ideally from single DNA molecules, will lead to an improved diagnosis of certain diseases, the early detection of genetic predispositions, and ultimately result in an improved drug development process and person-tailored medicine. This challenge mainly directed the development of next-generation sequencing (NGS) methods [116]. State-of-the-art NGS technologies, however, do not yet fulfill the ultimate sequencing promises of simultaneously providing long sequence read lengths, a low error rate, cost-efficient instrumentation and sample preparation, and ultimately single-molecule sensitivity. Optical mapping with extremely high spatial resolution using super-resolution could, in theory, meet these promises. **Figure 6.1** illustrates a proof-of-concept experiment, where DNA molecule are imaged in a stretched configuration using DNA-PAINT super-resolution microscopy.

Additionally, the universal super-resolution platform can be utilized on a much broader scale in the context of protein imaging in the cellular environment. Quantitative super-resolution on a single-molecule level could provide excellent opportunities for early diagnostics of certain diseases and facilitate drug development with optical read-out on a single-cell basis. However, there are still significant technological obstacles that need to be overcome to really integrate super-resolution microscopy into the single-cell diagnostic field. Probably, the most significant bottleneck is still the finding of robust labeling probes for protein targets. The requirements for this are challenging. Ideally, the labeling agents achieve high reliability, which means that the probes can be manufactured, stored, and applied without extreme diligence. Experimental results should not vary from batch to batch, and therefore, persistent quality of labeling probes needs to be ensured. Another important aspect is the availability. Labeling probes should be readily available, but cumbersome manufacturing processes like immunization of animal donors prolong production. With this re-

quirement, the element of universality comes hand in hand. Labeling probes should be available for a broad range of molecule targets to maximize the adoption in various biomedical applications. On a more technical level, labeling probes should provide stoichiometric labeling to enable quantitative analysis. In the case of DNA-PAINT, the agent should carry a single docking site. Lastly, the labeling efficiency of agents should be high to minimize cost and to be able to make qualitative and significant observations. The search for possible labeling problems is in full swing, but the perfect candidate has not yet been found [117].

Finally, at the end of every application will be the data analysis. Here, fast and robust processing of the gathered raw data will be a crucial issue that needs to be tackled. With the general adoption of super-resolution microscopy, the amount and type of raw data will require novel bioinformatics algorithms to extract biological features and ultimately gain insights in a truly quantitative fashion. The area of data science will also influence experimental research and become an integral part of scientific research projects, strengthening cooperation between experimentalists, theoreticians, and bioinformaticians.

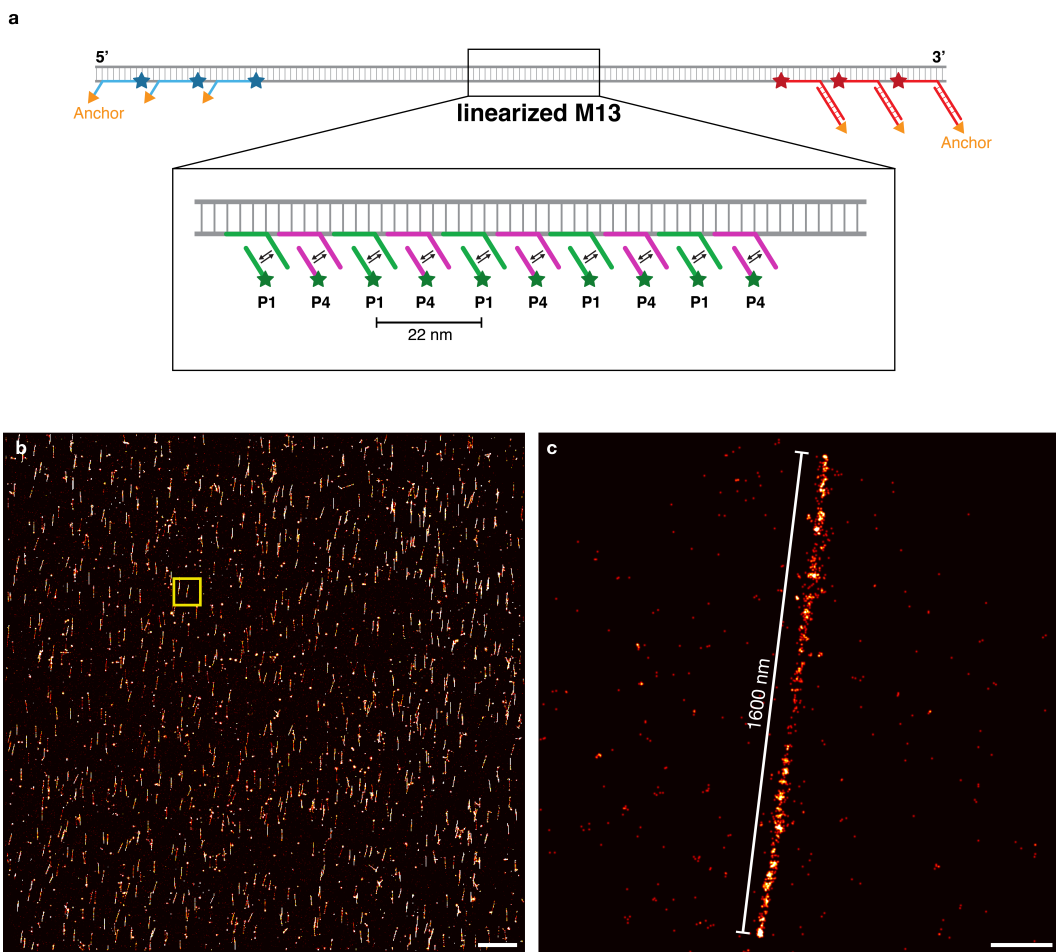


**Figure 6.1: Stretched DNA.** (a) Proof-of-concept design of a target DNA molecule for optical mapping using super-resolution microscopy. M13 genomic DNA was linearized and DNA-PAINT docking sites were hybridized along the DNA molecules. (b) DNA-PAINT super-resolution microscopy image of DNA molecules stretched and attached on the cover slip surface. (c) Zoom-in of the highlighted area in **b** displays a single DNA molecule that is stretched and anchored to the surface. DNA-PAINT imaging along the target molecule reveals a length of 1.6 μm, which indicates that the DNA strand is not fully stretched. Scale bars: 5 μm (b), 200 nm (c).

# A

## Appendix

A.1 SUPPORTING INFORMATION FOR ASSOCIATED PUBLICATION P1

### Supporting Information

Fast, Background-Free DNA-PAINT Imaging Using FRET-Based Probes

BY

Alexander Auer, Maximilian T. Strauss, Thomas Schlichthärle, and Ralf Jungmann

PUBLISHED IN

*Nano Letters*, (2017), 17, 6428–6434

Reprint with permission from ref. [1].  
Copyright 2017, American Chemical Society.



# Supporting Information

## Fast, background-free DNA-PAINT imaging using FRET-based probes

Alexander Auer<sup>#,§</sup>, Maximilian T. Strauss<sup>#,§</sup>, Thomas Schlichthaerle<sup>#,§</sup> and Ralf Jungmann<sup>#,§,\*</sup>

<sup>#</sup> Department of Physics and Center for Nanoscience, Ludwig Maximilian University, Munich, Germany.

<sup>§</sup> Max Planck Institute of Biochemistry, Martinsried, Germany.

\*Email: [jungmann@biochem.mpg.de](mailto:jungmann@biochem.mpg.de), Phone: +49 89 8578 3410

<b>Figure S1</b>	Fluorescence spectra of Atto 488 and Atto 647N dyes
<b>Figure S2</b>	NeNA localization precision distribution of Figure 2
<b>Figure S3</b>	NeNA localization precision distribution of Figure 3
<b>Figure S4</b>	NeNA localization precision distribution of Figure 4
<b>Figure S5</b>	Line profiles of single tubulin filaments from Figure 4
<b>Table S1</b>	Microscope parameters in Figure 1
<b>Table S2</b>	Microscope parameters in Figure 2
<b>Table S3</b>	Microscope parameters in Figure 3
<b>Table S4</b>	Microscope parameters in Figure 4
<b>Table S5</b>	M13mp18 sequence
<b>Table S6</b>	Rothemund rectangle origami staple strands
<b>Table S7</b>	Biotinylated staple strands
<b>Table S8</b>	DNA-PAINT extensions
<b>Table S9</b>	FRET-PAINT extensions
<b>Table S10</b>	DNA-PAINT imager sequences
<b>Table S11</b>	FRET-PAINT imager sequences
<b>Materials</b>	
<b>Optical setup</b>	
<b>DNA origami self-assembly</b>	
<b>Super-resolution FRET-PAINT and DNA-PAINT imaging with DNA origami</b>	
<b>Antibody conjugation</b>	
<b>Immunolabeling and fixation</b>	
<b>Super-resolution FRET-PAINT imaging in cells</b>	
<b>Super-resolution data processing</b>	

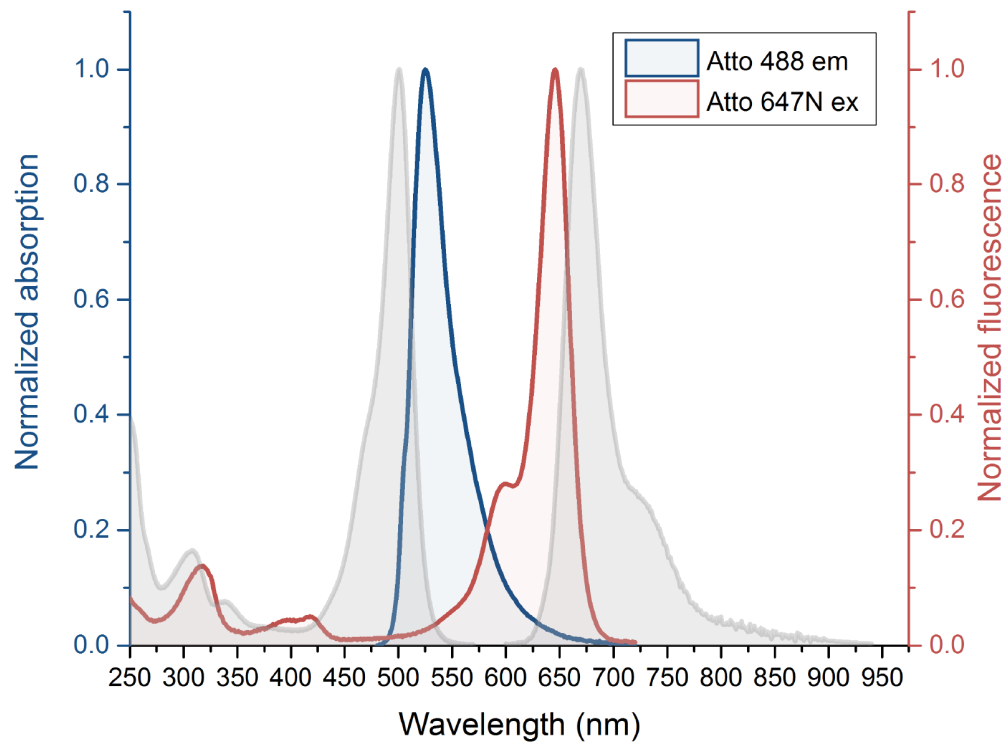


**Figure S1 | Fluorescence spectra of Atto 488 and Atto 647N dyes.** Absorption of the Atto 647N dye at the donor excitation wavelength 488 nm is around 0.013.

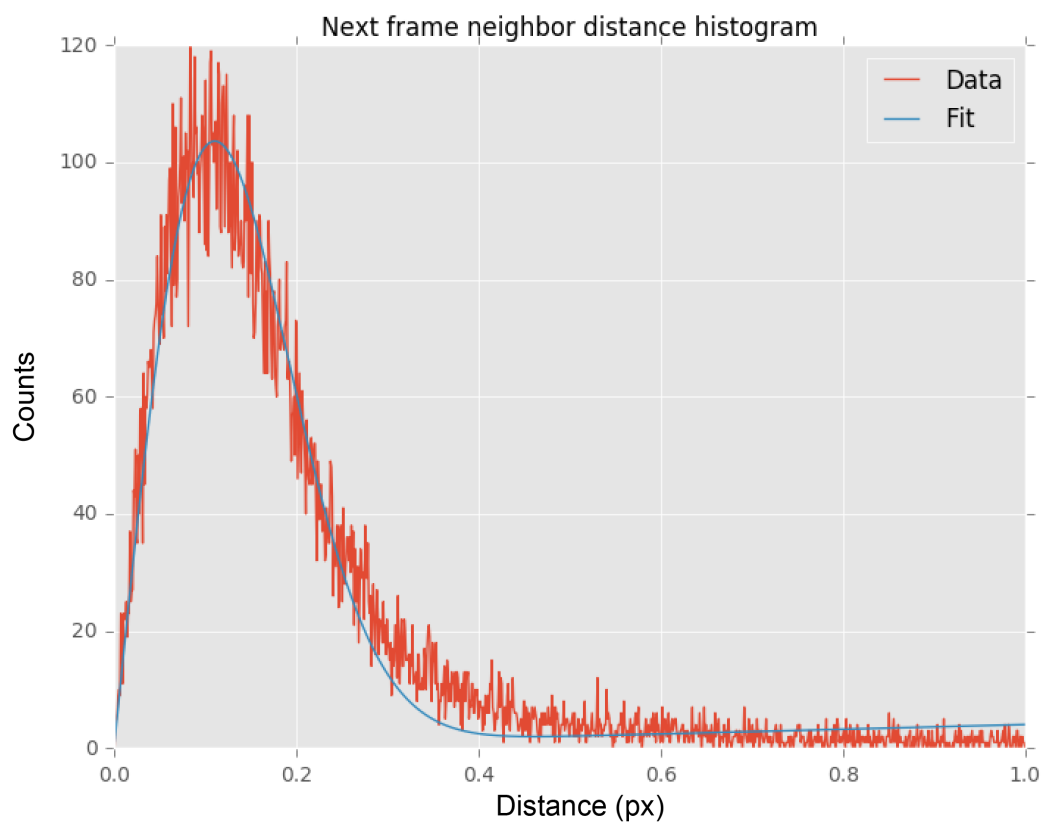


**Figure S2 | NeNA localization precision distribution of Figure 2.** Based on nearest neighbor analysis (NeNA)<sup>1</sup> we observe an average localization precision of 17.6 nm. Experimental data is plotted in red. A fitted curve is represented in blue.

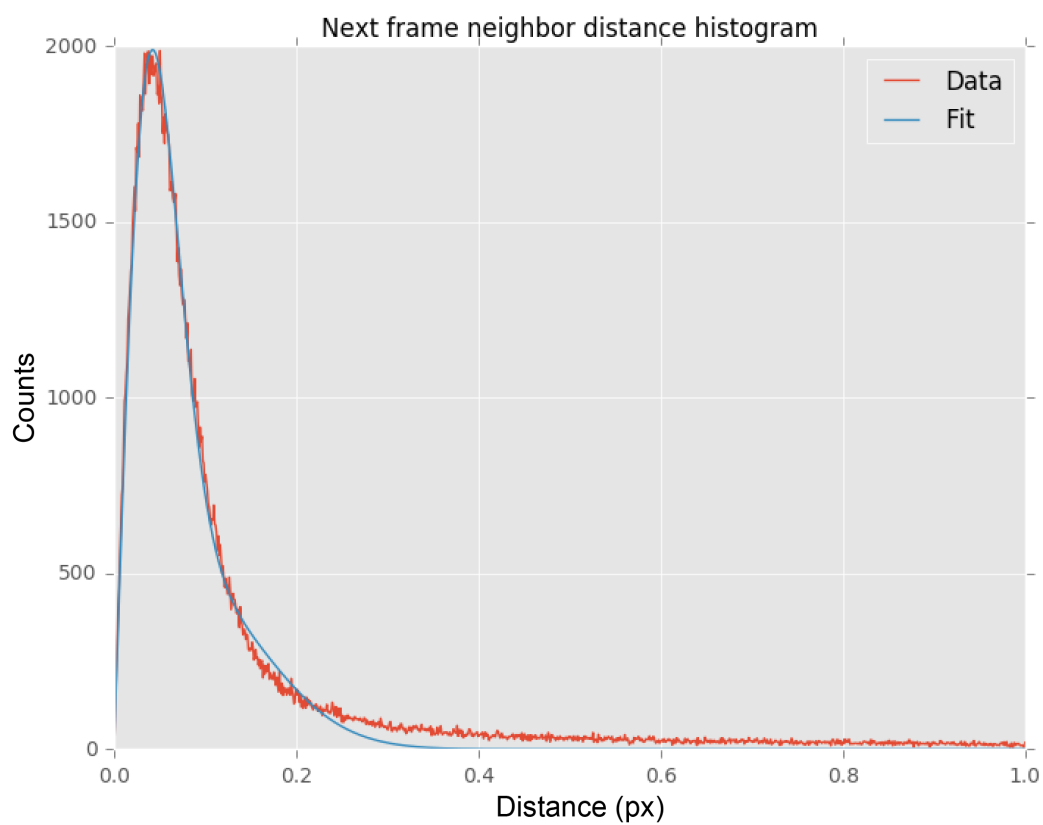


**Figure S3 | NeNA localization precision distribution of Figure 3.** Based on nearest neighbor analysis (NeNA) we observe an average localization precision of 6.4 nm. Experimental data is plotted in red. A fitted curve is represented in blue.

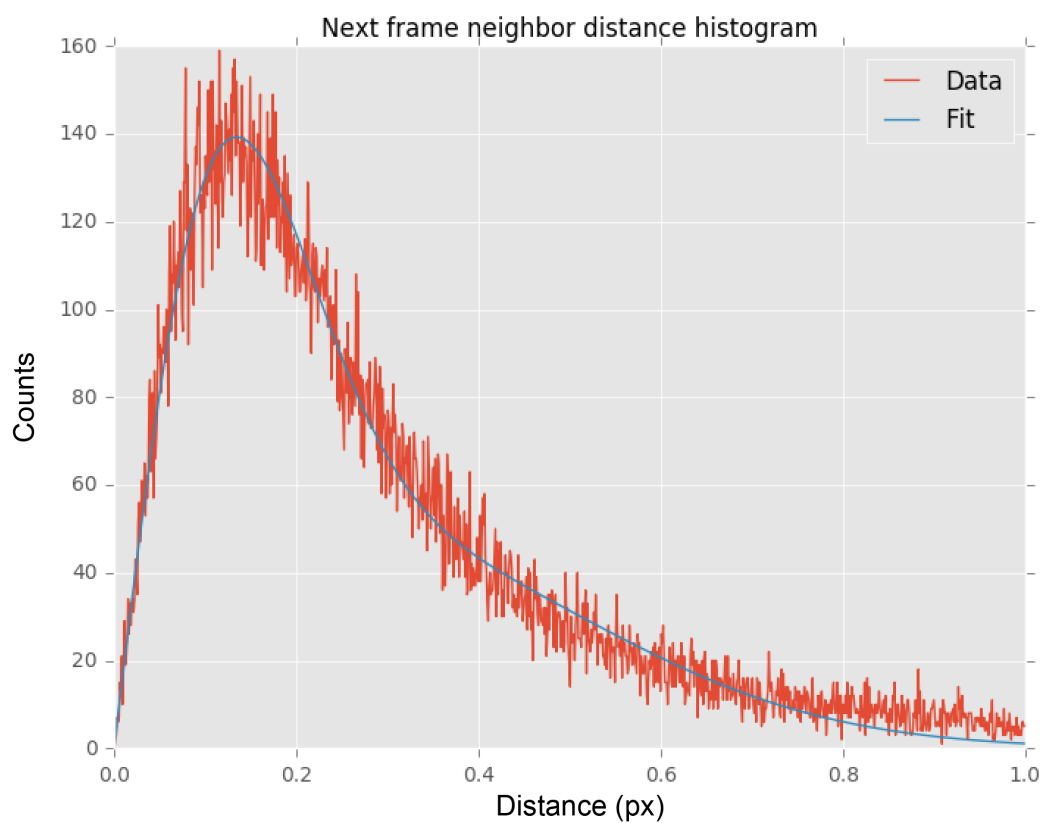


**Figure S4 | NeNA localization precision distribution of Figure 4.** Based on nearest neighbor analysis (NeNA) we observe an average localization precision of 19.5 nm. Experimental data is plotted in red. A fitted curve is represented in blue.

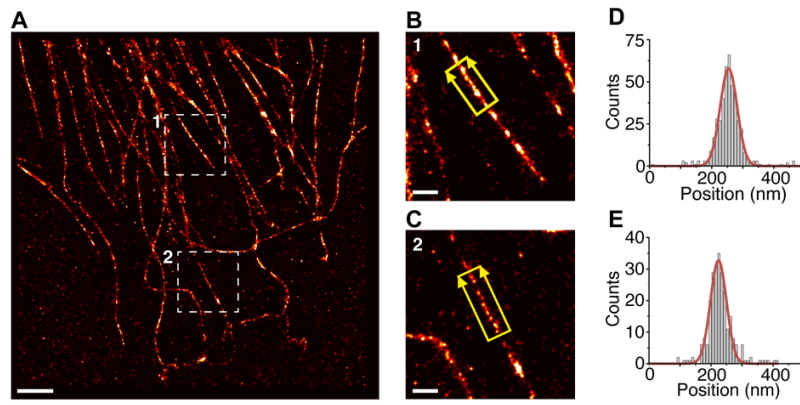


**Figure S5 | Line profiles of single tubulin filaments in Figure 4. (A)** Super-resolution image of microtubule network of Figure 4. **(B, C)** Zoom-ins of highlighted areas (1 and 2) in **A**. **(D, E)** Cross-sectional histograms from the highlighted areas in **B** and **D** fitted to a Gaussian reveals a tubulin diameter (FWHM) of  $\sim 62$  nm. Scale bars,  $2 \mu\text{m}$  (overview in **A**),  $500$  nm (zoom-in images in **B, C**).

**Table S1 | Microscope parameters in Figure 1C and 1D**

<b>Setting</b>	<b>Condition</b>
Microscope	Zeiss Elyra PS.1
Gain camera channel (C) 561 channel (D) 647	(C) EM gain: 1 (D) EM gain: 50
Gain camera channel 488	(D) EM gain: 50
Field of view	(C) 512 x 512 pixel (D) 256 x 256 pixel
Frames	(C) 7500 (D) 7500
Exposure time	(C) 200 ms (D) 100 ms
Binning	No binning
Tube lens	(C) 1,6 x (D) 1,0 x
Excitation laser	(C) 561 [max power 200 mW] (D) 488 [max power 200 mW]
Excitation lens	(C) no lens (D) HP lens
Laser Power	(C) 20 % (D) 20 %

**Table S2 | Microscope parameters in Figure 2**

<b>Setting</b>	<b>Condition</b>
Microscope	Zeiss Elyra PS.1
Gain camera 647	EM gain: 100
Gain camera 488	EM gain: 1
Field of view	256 x 256 pixel
Frames	1000
Exposure time	35 ms
Binning	No binning
Tube lens	1,0 x
Excitation laser	488 [max power 200 mW]
Excitation lens	HP lens
Laser Power	85 %

**Table S3 | Microscope parameters in Figure 3**

<b>Setting</b>	<b>Condition</b>
Microscope	Nikon Ti-Eclipse
Pre-amp	Gain: 3
Readout mode	3 MHz
Gain	Conventional Gain
Field of view	256 x 256 pixel
Frames	10 000
Exposure time	300 ms
Binning	No binning
Tube lens	1,0 x
Excitation laser	488 [max power 200 mW]
Laser Power	20 mW at laser port

**Table S4 | Microscope parameters in Figure 4**

<b>Setting</b>	<b>Condition</b>
Microscope	Zeiss Elyra PS.1
Gain camera 647	EM gain: 10
Gain camera 488	EM gain: 1
Field of view	128 x 128 pixel
Frames	4000
Exposure time	14 ms
Binning	No binning
Tube lens	1,0 x
Excitation laser	488 [max power 200 mW]
Excitation lens	HP lens
Laser Power	100 %

**Table S5 | M13mp18 sequence**

TTCCCTTCCTTCTCGCCACGTTTCGCCGGCTTTCCCGCTCAAGCTCTAAATCGGGGGCTCCCTTAGGGTTCCGATTTAGTGCTTTACGGCACCTCGACCCCAAAAACT  
TGATTTGGGTGATGGTTCACGTAGTGGGCCATCGCCCTGATAGACGGTTTTTCGCCCTTTGACGTTGGAGTCCACGTTCTTTAATAGTGGACTCTTGTCCAACTGGAA  
CAACTCAACCCTATCTCGGGCTATCTTTTGATTTATAAGGGATTTTGGCGATTTTCGGAACCACCATCAAAACAGGATTTTCGCCTGCTGGGGCAAACCAGCGTGGACC  
GCTTGCTGCAACTCTCTCAGGGCCAGGCGGTGAAGGGCAATCAGCTGTTGCCCGTCTCACTGGTGAAGAAAGAAAAACCACCTGGCGCCCAATACGCAAACCGCCTCTCCC  
CGCGCTTGGCCGATTCATTAATGCAGCTGGCAGCAGAGTTTCCCGACTGGAAGCGGGCAGTGAGCGCAACGCAATTAATGTGAGTTAGCTCACTCATTAGGCACCCC  
AGGCTTTACACTTTATGCTTCCGGCTCGTATGTTGTGGAATTTGAGCGGATAACAATTTACACAGGAAACAGCTATGACCATGATTACGAATTCGAGCTCGGTACC  
CGGGGATCCTCTAGAGTCGACCTGCAGGCATGCAAGCTTGGCACTGGCCGTCGTTTTACAACGTCGTGACTGGGAAAAACCTGGCGTTACCCAACCTAATCGCCTTGACG  
CACATCCCCCTTTGCCAGCTGGCGTAATAGCGAAGAGGCCCGCACCGATCGCCCTTCCCAACAGTTGCGCAGCCTGAATGGCGAATGGCGCTTTGCCTGGTTTTCCGGCA  
CCAGAAGCGGTGCCGAAAGCTGGCTGGAGTGCATCTTCTGAGCCGATACTGTCTGTCGCCCTCAAACCTGGCAGATGCACGGTTACGATGGCCCATCTACACCAA  
CGTGACCTATCCATTACGGTCAATCCGCCGTTTTGTTCCACAGGAGAATCCGACGGGTTGTTACTCGCTCACATTTAATGTTGATGAAAGCTGGCTACAGGAAGGCCAGA  
CGCAATTTATTTTGATGGCGTTTCTATTGGTTAAAAAATGAGCTGATTTAACAAAAATTTAATGCGAATTTAACAAAAATTTAACGTTTACAATTTAAATATTTGCTT  
ATACAATCTTCTGTTTTTGGGGCTTTTCTGATTATCAACCGGGTACATATGATTGACATGCTAGTTTTACGATTACCGTTCATCGATTCTCTGTTTTGCTCCAGACTC  
TCAGGCAATGACCTGATAGCCTTTGTAGATCTCTCAAAAATAGCTACCCTCTCCGGCATTAAATTTATCAGCTAGAACGGTTGAATATCATATTGATGGTGAATTTGACTGT  
CTCCGGCCTTTCTCACCCCTTTGAATCTTTACCTACACATTACTCAGGCATTCGATTTAAAAATATAGAGGGTCTAAAAATTTTTATCCTTGCCTGAAATAAAGGCTT  
CTCCCGCAAAAGTATTACAGGGTCATAATGTTTTTGGTACAACCGATTTAGCTTTATGCTCTGAGGCTTTATTTGCTTAATTTTGCTAAATTTTGCCTTGCCCTGTATGAT  
TTATTGGATGTTAATGCTACTACTATTAGTAGAATTTGATGCCACCTTTTTCAGCTCGCGCCCAAAATGAAAAATAGCTAAACAGGTTATTGACCATTTGCGAAATGTATC  
TAATGGTCAAACCTAAATCTACTCGTTCGAGAAATGGGAATCACTGTTATATGGAATGAACTCCAGACACCGTACTTTAGTTGCATATTTAAAACATGTTGAGCTAC  
AGCATTTATTTACAGCAATTAAGCTCTAAGCCATCCGCAAAAATGACCTCTTATCAAAAGGAGCAATTAAGGTACTCTCTAATCCTGACCTGTTGGAGTTTGTCTCCGGT  
CTGGTTCCGCTTTGAAGCTCGAATTAACGCGATATTTGAAGTCTTTCGGGCTTCTCTTAATCTTTTTGATGCAATCCGCTTTGCTTCTGACTATAATAGTCAGGGTAA  
AGACCTGATTTTTGATTTATGGTCAATCTCGTTTTCTGAAGCTTTTAAAGCATTGAGGGGGATTCATGAATATTTATGACGATTCGCGAGTATTGGACGCTATCCAGT  
CTAAACATTTACTATTACCCCTCTGGCAAAACTCTTTTGCAAAGCCTCTCGCTATTTTTGGTTTTTATCGCTCTGGTAAACGAGGGTTATGATAGTGTGCTCTT  
ACTATGCCTCGTAATTCCTTTTGGCGTTATGTATCTGCATTAGTTGAATGTGGTATTCCTAAATCTCAACTGATGAATCTTTCTACCTGTAATAATGTTGTTCCGTTAGT  
TCGTTTTATTAACGTAGATTTTTCTTCCCAACGCTCTGACTGGTATAATGAGCCAGTCTTAAAAATCGCATAAGGTAATTCACAATGATTAAGGTTGAATTAACCATC  
TCAAGCCCAATTTACTACTGTTCTGGTGTCTTCTGTCAGGGCAAGCCTTATTCACTGAATGACAGCTTTGTTACGTTGATTTGGGTAATGAATATCCGGTCTTGTCA  
AGATTACTCTTGATGAAGGTCAGCCAGCCTATGCGCCTGGTCTGTACACCGTTCATCTGCTCTTTCAAAGTTGGTCAGTTCCGGTTCCTTATGATTGACCGTCTGCGC  
CTCGTTCCGGTAAGTAACATGGAGCAGGTCGCGGATTTTCGACACAATTTATCAGGGATGATACAAATCTCCGTTGTACTTTGTTTTCCGCTTGGTATAATCGCTGGGG  
GTCAAAGATGAGTGTTTAGTGTATCTTTTGCCTCTTTCGTTTTAGGTTGGTGCCTTCGTAGTGGCATTACGTATTTTACCCGTTAATGAAACTTCTCATGAAAA  
GTCTTTAGTCTCAAAGCCTCTGTAGCCGTTGCTACCCTCGTTCGATGCTGTCTTTTCGCTGTGAGGGTACGATCCCGCAAAAGCGGCCTTTAACTCCCTGCAAGCCT  
CAGCGACCGAATATATCGGTTATGCGTGGCGATGGTGTGTCATTTGCGCGCAACTATCGGTATCAAGCTGTTAAGAAATTCACCTCGAAAGCAAGCTGATAAACC  
GATACAATTAAGGCTCCTTTTGGAGCCTTTTTTTGGAGATTTCAACGTGAAAAAATATATTATTCGCAATTCCTTTAGTTGTTCTTCTATTTCTACTCCGCTGAAA  
CTGTTGAAAGTTGTTTAGCAAAATCCCATACAGAAAATTCATTTACTAACGTCTGAAAGACGACAAAACCTTAGATCGTTACGTAACATGAGGGCTGTCTGTGGAAT  
GCTACAGGCGTTGATTTGTTACTGGTACGAACTCAGTGTACGGTACATGGGTTCCATTTGGGCTTGTATCCCTGAAAATGAGGGTGGTGGCTCTGAGGTGGCGG  
TTCTGAGGGTGGCGGTTCTGAGGGTGGCGGTACTAAACCTCCTGAGTACGGTATACACCTATTCGGGGTATACCTTATATCAACCCTCTCGACGGCACTTATCCGCTG  
GTACTGAGCAAAACCCGCTAATCCTAATCCTTCTTCTGAGGAGTCTCAGCCTTTAATACTTTTATGTTTTCAGAATAATAGGTTCCGAAATAGGCAGGGGGCATTAACT  
GTTTATACGGGCACTGTTACTCAAGGCACCTGACCCCGTTAAAACCTTATTACCAGTACACTCCTGTATCATCAAAGCCATGATGACGCTTACTGGAACGGTAAATTCAG  
AGACTGCGCTTTCATCTGGCTTTAATGAGGATTTATTTGTTGTGAATATCAAGGCCAATCGTCTGACCTGCCTCAACCTCCTGTCAATGCTGGCGGCGCTCTGGTG  
GTGGTTCTGGTGGCGGCTCTGAGGGTGGTGGCTCTGAGGGTGGCGGTTCTGAGGGTGGCGGCTCTGAGGGAGGCGGTTCCGGTGGTGGCTCTGGTTCCGGTGATTTGAT  
TATGAAAAGATGGCAACGCTAATAAGGGGCTATGACCGAAAATGCCGATGAAAACGCGCTACAGCTGACGCTAAAGGCAAACTTGATTCTGTGCTACTGATTACGG  
TGCTGCTATCGATGGTTTCATTGGTACGTTTCCGGCCTTGCTAATGGTAATGGTGTACTGGTGATTTTGTGGCTCTAATTCCAAATGGCTCAAGTCCGGTACGGTG  
ATAATCACCTTTAATGAATAATTTCCGTCATATTTACCTTCCCTCCCTCAATCGGTTGAATGTCGCCCTTTTGTCTTTGGCGCTGGTAAACCATATGAATTTCTATT  
GATTGTGACAAAATAAACTTATCCGTTGGTGTCTTTGCGTTCTTTTATATGTTGCCACCTTTATGATGATTTTTCTACGTTTGGTAAACATACTGCCTAATAAGGAGTC  
TTAATCATGCCAGTTCTTTTGGGTATCCGTTATTTATTGCGTTTCCCTCGGTTTCTTCTGTTAACTTTGTTCCGGCTATCTGCTTACTTTTCTTAAAAAGGGCTTCGGTAA  
GATAGCTATTGCTATTTTCTGCTCTTATTATTGGGCTTAACTCAATCTTGTGGGTTATCTCTCTGATATTAGCGCTCAATACCCTCTGACTTTGTTTCAGG  
GTGTTACAGTTAATCTCCGCTCAATGCGCTTCCCTGTTTTATGTTATCTCTCTGTAAAGGCTGCTATTTTCAATTTTGGAGCTTAAACAAAAATCGTTTCTTATTTG  
GATTGGGATAAATAATAGGCTGTTTATTTTGTAACTGGCAAATTAGGCTCTGAAAGACGCTCGTTAGCGTTGGTAAAGATTAGGATAAAATTTAGCTGGGTGCAAAA  
TAGCAACTAATCTGATTTAAGGCTTCAAACCTCCCGAAGTCGGGAGGTTGCTAAAACGCTCGCGTTCTAGAATACCGGATAAGCCTTCTATATCTGATTTGCTT  
GCTATTGGGCGCGGTAATGATTCTACGATGAAAATAAAAACGGCTTGCTTGTCTCGATGAGTGCGGTACTTGGTTAATACCCTTCTTGAATGATAAGGAAAGACA  
GCCGATTATTGATTGGTTTCTACATGCTCGTAAATTAGGATGGGATATTTTTTCTTGTTCAGGACTTATCTATTGTTGATAAACAGGCGGCTTCTGCATTAGCTGAAC

ATGTTGTTTATTGTCGTCGTCGGACAGAATTACTTTACCTTTTGTGCGTACTTTATATTCTCTTATTACTGGCTCGAAAAATGCCTCTGCCTAAATTACATGTTGGCGTT  
 GTTAAATATGGCGATCTCAATTAAGCCCTACTGTTGAGCGTTGGCTTTATACTGGTAAGAATTTGTATAACGCATATGATACTAAACAGGCTTTTCTAGTAATTATGA  
 TTCCGGTGTATTCTTATTTAACGCCTTATTTATCACACGGTCGGTATTTCAAACCATTAATTTAGGTCAGAAGATGAAATTAACATAAAATATATTTGAAAAAGTTTT  
 CTCGCGTTCTTTGCTTGGCATTGGATTGCATCAGCATTACATATAGTTATATAACCCCAACCTAAGCCGGAGGTTAAAAAGGTAGTCTCTCAGACCTATGATTTTGAT  
 AAATTCATATTGACTCTTCTCAGCGTCTTAATCTAAGCTATCGCTATGTTTTCAAGGATTCTAAGGGAAAAATTAATTAATAGCGACGATTTACAGAAGCAAGGTTATC  
 ACTCACATATATTGATTTATGTACTGTTTCCATTAATAAAGGTAATTCAAATGAAATGTTAAATGTAATTAATTTGTTTTCTTGATGTTGTTTCATCATCTTCTTTT  
 GCTCAGGTAATTGAAATGAATAATTCGCCTCTGCGCGATTTTGTAACTTGGTATTCAAAGCAATCAGGCGAATCCGTTATTGTTTTCTCCGATGTAAGGACTGTTAC  
 TGTATATTCATCTGACGTTAAACCTGAAAACTACGCAATTTCTTTATTTCTGTTTTACGTGCAAATAATTTGATATGGTAGGTTCTAACCCCTCCATTATTCAGAAGT  
 ATAATCCAAACAATCAGGATTATATTGATGAATTGCCATCATCTGATAATCAGGAATATGATGATAATCCGCTCCTTCTGGTGGTTTTCTTTGTTCCGCAAAATGATAAT  
 GTTACTCAAACCTTTTAAATTAATAACGTTGCGGCAAAGGATTTAATACGAGTTGTCGAATGTTTGTAAAGTCTAATACTTCTAAATCCTCAAATGTATTATCTATTGA  
 CGGCTCTAATCTATTAGTTGTTAGTCTCCTAAAGATATTTAGATAACCTTCCCTCAATTCCTTCAACTGTTGATTTGCCAAGTACCAGATATTGATTGAGGGTTTGA  
 TATTTGAGGTTACAGCAAGGTGATGCTTTAGATTTTTCAATTTGCTGCTGGCTCTCAGCGTGGCACTGTTGCAGGCGGTGTTAATACTGACCCCTCACCTCTGTTTTATCT  
 TCTGCTGGTGGTTTCGTTTCGTTATTTTTAATGGCGATGTTTTAGGGCTATCAGTTCCGCGATTAAGACTAATAGCCATTCAAAAAATATTGCTGTGCCAGTATTCTTAC  
 GCTTTCAGGTCAGAAGGTTCTATCTGTTGGCCAGAATGTCCTTTTTATTACTGGTCGTGTACTGGTGAATCTGCCAATGTAATAATCCATTTACAGACGATTGAGC  
 GTCAAAATGTAGGATTTCCATGAGCGTTTTTCTGTTGCAATGGCTGGCGGTAATATTGTTCTGGATATTACCAGCAAGGCCGATAGTTTG

**Table S6 | Rothmund rectangle origami staple strands**

Position	Name	Sequence
A1	21[32]23[31]BLK	TTTTCACTCAAAGGGCGAAAAACCATCACC
B1	23[32]22[48]BLK	CAAATCAAGTTTTTTGGGGTCGAAACGTGGA
C1	21[56]23[63]BLK	AGCTGATTGCCCTTCAGAGTCCACTATTAAAGGGTGCCGT
D1	23[64]22[80]BLK	AAAGCACTAAATCGGAACCTAATCCAGTT
E1	21[96]23[95]BLK	AGCAAGCGTAGGGTTGAGTGTGTAGGGAGCC
F1	23[96]22[112]BLK	CCCGATTTAGAGCTTGACGGGGAAAAAGAATA
G1	21[120]23[127]BLK	CCCAGCAGGGCAAAAAATCCCTTATAAATCAAGCCGGCG
H1	21[160]22[144]BLK	TCAATATCGAACCTCAAATATCAATTCGGAAA
I1	23[128]23[159]BLK	AACGTGGCGAGAAAGGAAGGAAACCAGTAA
J1	23[160]22[176]BLK	TAAAAGGGACATTCTGGCCAACAAAGCATC
K1	21[184]23[191]BLK	TCAACAGTTGAAAGGAGCAAATGAAAAATCTAGAGATAGA
L1	23[192]22[208]BLK	ACCCTTCTGACCTGAAAGCGTAAGACGCTGAG
M1	21[224]23[223]BLK	CTTTAGGGCCTGCAACAGTGCCAATACGTG
N1	23[224]22[240]BLK	GCACAGACAATATTTTTGAATGGGGTCAGTA
O1	21[248]23[255]BLK	AGATTAGAGCCGTCAAAAAACAGAGGTGAGGCCATTAGT
P1	23[256]22[272]BLK	CTTTAATGCGCGAACTGATAGCCCCACCAG
A2	19[32]21[31]BLK	GTCGACTTCGGCCAACGCGGGGTTTTTC
B2	22[47]20[48]BLK	CTCCAACGCAGTGAGACGGGCAACCAGCTGCA
D2	22[79]20[80]BLK	TGGAACAACCGCCTGGCCCTGAGGCCCGCT
E2	19[96]21[95]BLK	CTGTGTGATTGCGTTGCGCTCACTAGAGTTGC
F2	22[111]20[112]BLK	GCCCGAGAGTCCACGCTGGTTTGCAGCTAACT
H2	19[160]20[144]BLK	GCAATTCACATATTCCTGATTATCAAAGTGTA
I2	22[143]21[159]BLK	TCGGCAAAATCCTGTTTGTGGTGGACCCCTCAA
J2	22[175]20[176]BLK	ACCTTGCTTGGTCAGTTGGCAAGAGCGGA

L2	22[207]20[208]BLK	AGCCAGCAATTGAGGAAGGTTATCATCATTTT
M2	19[224]21[223]BLK	CTACCATAGTTTGAGTAACATTTAAAATAT
N2	22[239]20[240]BLK	TTAACACCAGCACTAACAATAATCGTTATTA
P2	22[271]20[272]BLK	CAGAAGATTAGATAATACATTTGTCGACAA
A3	17[32]19[31]BLK	TGCATCTTTCCAGTCACGACGGCCTGCAG
B3	20[47]18[48]BLK	TTAATGAACTAGAGGATCCCCGGGGGTAACG
D3	20[79]18[80]BLK	TTCCAGTCGTAATCATGGTCATAAAAGGGG
E3	17[96]19[95]BLK	GCTTTCGGATTACGCCAGCTGGCGGCTGTTTC
F3	20[111]18[112]BLK	CACATTTAAAATGTTATCCGCTCATGCGGGCC
H3	17[160]18[144]BLK	AGAAAACAAAGAAGATGATGAAACAGGCTGCG
I3	20[143]19[159]BLK	AAGCCTGGTACGAGCCGGAAGCATAGATGATG
J3	20[175]18[176]BLK	ATTATCATTTCAATATAATCCTGACAATTAC
L3	20[207]18[208]BLK	GCGGAACATCTGAATAATGGAAGGTACAAAAT
M3	17[224]19[223]BLK	CATAAATCTTTGAATACCAAGTGTAGAAC
N3	20[239]18[240]BLK	ATTTTAAAATCAAAATTTATTTGCACGGATTCG
P3	20[271]18[272]BLK	CTCGTATTAGAAAATGCGTAGATACAGTAC
A4	15[32]17[31]BLK	TAATCAGCGGATTGACCGTAATCGTAACCG
B4	18[47]16[48]BLK	CCAGGGTTGCCAGTTTGAGGGGACCCGTGGGA
C4	15[64]18[64]BLK	GTATAAGCCAACCCGTGCGATTCTGACGACAGTATCGGCCGCAAGGCG
D4	18[79]16[80]BLK	GATGTGCTTCAGGAAGATCGCACAAATGTGA
E4	15[96]17[95]BLK	ATATTTTGGCTTTCATCAACATTATCCAGCCA
F4	18[111]16[112]BLK	TCTTTCGCTGCACCGCTTCTGGTGC GGCTTCC
G4	15[128]18[128]BLK	TAAATCAAAAATAATTCGCGTCTCGGAAACCAGGCAAAGGGAAGG
H4	15[160]16[144]BLK	ATCGCAAGTATGTAATGCTGATGATAGGAAC
I4	18[143]17[159]BLK	CAACTGTTGCGCCATTTCGCCATTCAAACATCA
J4	18[175]16[176]BLK	CTGAGCAAAAATTAATTACATTTTGGGTTA
K4	15[192]18[192]BLK	TCAAATATAACCTCCGGCTTAGGTAACAATTTTCATTTGAAGGCGAATT
L4	18[207]16[208]BLK	CGCGCAGATTACCTTTTTTAAATGGGAGAGACT
M4	15[224]17[223]BLK	CCTAAATCAAAATCATAGGTCTAACAGTA
N4	18[239]16[240]BLK	CCTGATTGCAATATATGTGAGTGATCAATAGT
O4	15[256]18[256]BLK	GTGATAAAAAGACGCTGAGAAGAGATAACCTTGCTTCTGTTCCGGAGA
P4	18[271]16[272]BLK	CTTTTACAAAATCGTCGCTATTAGCGATAG
A5	13[32]15[31]BLK	AACGCAAAATCGATGAACGGTACCGGTTGA
B5	16[47]14[48]BLK	ACAAACGGAAAAGCCCCAAAAACACTGGAGCA
C5	13[64]15[63]BLK	TATATTTTGTCAATTGCCTGAGAGTGAAGATT
D5	16[79]14[80]BLK	GCGAGTAAAAATATTTAAATGTTACAAAG
E5	13[96]15[95]BLK	TAGGTAAACTATTTTTGAGAGATCAAACGTTA
F5	16[111]14[112]BLK	TGTAGCCATTAAAATTCGCATTAAATGCCGGA
G5	13[128]15[127]BLK	GAGACAGCTAGCTGATAAATAATTTTGT
H5	13[160]14[144]BLK	GTAATAAGTTAGGCAGAGGCATTTATGATATT
I5	16[143]15[159]BLK	GCCATCAAGCTCATTTTTTAACCACAAATCCA
J5	16[175]14[176]BLK	TATAACTAACAAAGAACGCGAGAACGCCAA

K5	13[192]15[191]BLK	GTAAAGTAATCGCCATATTTAACAAAACTTTT
L5	16[207]14[208]BLK	ACCTTTTTATTTTAGTAAATTCATAGGGCTT
M5	13[224]15[223]BLK	ACAACATGCCAACGCTCAACAGTCTTCTGA
N5	16[239]14[240]BLK	GAATTTATTTAATGGTTGAAATATTCCTTACC
O5	13[256]15[255]BLK	GTTTATCAATATGCGTTATACAAACCGACCGT
P5	16[271]14[272]BLK	CTTAGATTTAAGGCGTTAAATAAAGCCTGT
A6	11[32]13[31]BLK	AACAGTTTTGTACCAAAAACATTTTATTTTC
B6	14[47]12[48]BLK	AACAAGAGGGATAAAAAATTTTAGCATAAAGC
C6	11[64]13[63]BLK	GATTTAGTCAATAAAGCCTCAGAGAACCCTCA
D6	14[79]12[80]BLK	GCTATCAGAAATGCAATGCCTGAATTAGCA
E6	11[96]13[95]BLK	AATGGTCAACAGGCAAGGCAAAGAGTAATGTG
F6	14[111]12[112]BLK	GAGGGTAGGATTCAAAGGGTGAGACATCCAA
G6	11[128]13[127]BLK	TTTGGGGATAGTAGTACATTAAGGCCG
H6	11[160]12[144]BLK	CCAATAGCTCATCGTAGGAATCATGGCATCAA
I6	14[143]13[159]BLK	CAACCGTTTCAAATCACCATCAATTCGAGCCA
J6	14[175]12[176]BLK	CATGTAATAGAATATAAAGTACCAAGCCGT
K6	11[192]13[191]BLK	TATCCGGTCTCATCGAGAACAAGCGACAAAAG
L6	14[207]12[208]BLK	AATTGAGAATTCTGTCCAGACGACTAAACCAA
M6	11[224]13[223]BLK	GCGAACCTCCAAGAACGGGTATGACAATAA
N6	14[239]12[240]BLK	AGTATAAAGTTCAGCTAATGCAGATGTCTTTC
O6	11[256]13[255]BLK	GCCTTAAACCAATCAATAATCGGCACGCGCCT
P6	14[271]12[272]BLK	TTAGTATCACAAATAGATAAGTCCACGAGCA
A7	9[32]11[31]BLK	TTTACCCCAACATGTTTTAAATTTCCATAT
B7	12[47]10[48]BLK	TAAATCGGGATFCCAATTCGCGATATAATG
C7	9[64]11[63]BLK	CGGATTGCAGAGCTTAATTGCTGAAACGAGTA
D7	12[79]10[80]BLK	AAATTAAGTTGACCATTAGATACTTTTGCG
E7	9[96]11[95]BLK	CGAAAGACTTTGATAAGAGGTCATATTTTCGCA
F7	12[111]10[112]BLK	TAAATCATATAACCTGTTTAGCTAACCTTTAA
G7	9[128]11[127]BLK	GCTTCAATCAGGATTAGAGAGTTATTTTCA
H7	9[160]10[144]BLK	AGAGAGAAAAAATGAAAAATAGCAAGCAAAC
I7	12[143]11[159]BLK	TTCTACTACGCGAGCTGAAAAGGTTACCGCGC
J7	12[175]10[176]BLK	TTTTATTTAAGCAAATCAGATATTTTTTGT
K7	9[192]11[191]BLK	TTAGACGGCCAAATAAGAAACGATAGAAGGCT
L7	12[207]10[208]BLK	GTACCGCAATTCCTAAGAACGCGAGTATTATTT
M7	9[224]11[223]BLK	AAAGTCACAAAATAAACAGCCAGCGTTTTTA
N7	12[239]10[240]BLK	CTTATCATTCCTCGACTTGCGGGAGCTAATTT
O7	9[256]11[255]BLK	GAGAGATAGAGCGTCTTCCAGAGGTTTTGAA
P7	12[271]10[272]BLK	TGTAGAAATCAAGATTAGTTGCTCTTACCA
A8	7[32]9[31]BLK	TTTAGGACAAATGCTTAAACAATCAGGTC
B8	10[47]8[48]BLK	CTGTAGCTTGACTATATAGTCAGTTCATTGA
C8	7[56]9[63]BLK	ATGCAGATACATAACGGGAATCGTCATAAATAAAGCAAAG
D8	10[79]8[80]BLK	GATGGCTTATCAAAAAGATTAAGAGCGCTCC

E8	7[96]9[95]BLK	TAAGAGCAAATGTTTAGACTGGATAGGAAGCC
F8	10[111]8[112]BLK	TTGCTCCTTTCAAATATCGCGTTTGAGGGGGT
G8	7[120]9[127]BLK	CGTTTACCAGACGACAAAGAAGTTTGGCCATAATTCGA
H8	7[160]8[144]BLK	TTATTACGAAGAACGGCATGATTGCGAGAGG
I8	10[143]9[159]BLK	CCAACAGGAGCGAACCAGACCGGAGCCTTTAC
J8	10[175]8[176]BLK	TTAACGTCTAACATAAAAAACAGGTAAACGGA
K8	7[184]9[191]BLK	CGTAGAAAATACATACCGAGGAAACGCAATAAGAAGCGCA
L8	10[207]8[208]BLK	ATCCCAATGAGAATTAAGTGAACAGTTACCAG
M8	7[224]9[223]BLK	AACGCAAAGATAGCCGAACAAACCTGAAC
N8	10[239]8[240]BLK	GCCAGTTAGAGGGTAATTGAGCGCTTTAAGAA
O8	7[248]9[255]BLK	GTTTATTTTGTCAAACTTTACCGAAGCCCTTTAATATCA
P8	10[271]8[272]BLK	ACGCTAACACCCACAAGAATGAAAAATAGC
A9	5[32]7[31]BLK	CATCAAGTAAAACGAACCTAACGAGTTGAGA
B9	8[47]6[48]BLK	ATCCCCCTATACCACATTCAACTAGAAAAATC
D9	8[79]6[80]BLK	AATACTGCCCAAAGGAATTACGTGGCTCA
E9	5[96]7[95]BLK	TCATTTCAGATGCGATTTTAAGAACAGGCATAG
F9	8[111]6[112]BLK	AATAGTAAACACTATCATAACCCCTCATTTGTA
H9	5[160]6[144]BLK	GCAAGGCTCACCAGTAGCACCATGGGCTTGA
I9	8[143]7[159]BLK	CTTTTGCAGATAAAAACAAAATAAAGACTCC
J9	8[175]6[176]BLK	ATACCCAACAGTATGTTAGCAAATTAGAGC
L9	8[207]6[208]BLK	AAGGAAACATAAAGGTGGCAACATTTACCCG
M9	5[224]7[223]BLK	TCAAGTTTCATTAAGGTGAATATAAAAAGA
N9	8[239]6[240]BLK	AAGTAAGCAGACACCACGGAATAATATTGACG
P9	8[271]6[272]BLK	AATAGCTATCAATAGAAAATTCACATTC
A10	3[32]5[31]BLK	AATACGTTTGAAAGAGGACAGACTGACCTT
B10	6[47]4[48]BLK	TACGTTAAAGTAATCTTGACAAGAACC
D10	6[79]4[80]BLK	TTATACCACCAAATCAACGTAACGAACGAG
E10	3[96]5[95]BLK	ACACTCATCCATGTTACTTAGCCGAAAGCTGC
F10	6[111]4[112]BLK	ATTACCTTTGAATAAGGCTTGCCCAAATCCGC
H10	3[160]4[144]BLK	TTGACAGGCCACCACCAGAGCCGCGATTTGTA
I10	6[143]5[159]BLK	GATGGTTTGAACGAGTAGTAAATTTACCATTA
J10	6[175]4[176]BLK	CAGCAAAGGAAACGTCACCAATGAGCCGC
L10	6[207]4[208]BLK	TCACCGACGCACCGTAATCAGTAGCAGAACCG
M10	3[224]5[223]BLK	TTAAAGCCAGAGCCGCCACCTCGACAGAA
N10	6[239]4[240]BLK	GAAATTATTGCCTTTAGCGTCAGACCGGAACC
P10	6[271]4[272]BLK	ACCGATTGTCGGCATTTTCGGTCATAATCA
A11	1[32]3[31]BLK	AGGCTCCAGAGGCTTTGAGGACACGGGTAA
B11	4[47]2[48]BLK	GACCAACTAATGCCACTACGAAGGGGGTAGCA
C11	1[64]4[64]BLK	TTTATCAGGACAGCATCGGAACGACACCAACCTAAAACGAGGTCAATC
D11	4[79]2[80]BLK	GCGCAGACAAGAGGCAAAAGAATCCCTCAG
E11	1[96]3[95]BLK	AAACAGCTTTTTCGGGGATCGTCAACACTAAA
F11	4[111]2[112]BLK	GACCTGCTCTTTGACCCCGAGGAGGAGTTA

G11	1[128]4[128]BLK	TGACAACCTCGCTGAGGCTTGCATTATACCAAGCGCGATGATAAA
H11	1[160]2[144]BLK	TTAGGATTGGCTGAGACTCCTCAATAACCGAT
I11	4[143]3[159]BLK	TCATCGCCAACAAAGTACAACGGACGCCAGCA
J11	4[175]2[176]BLK	CACCAGAAAGGTTGAGGCAGGTCATGAAAG
K11	1[192]4[192]BLK	GCGGATAACCTATTATTTCTGAAACAGACGATTGGCCTTGAAGAGCCAC
L11	4[207]2[208]BLK	CCACCCCTCTATTCACAAACAAATACCTGCCTA
M11	1[224]3[223]BLK	GTATAGCAAACAGTTAATGCCCAATCCTCA
N11	4[239]2[240]BLK	GCCTCCCTCAGAAATGGAAAGCGCAGTAACAGT
O11	1[256]4[256]BLK	CAGGAGGTGGGGTTCAGTGCCTTGAGTCTCTGAATTTACCGGGAACCAG
P11	4[271]2[272]BLK	AAATCACCTTCCAGTAAGCGTCAGTAATAA
A12	0[47]1[31]BLK	AGAAAGGAACAACATAAGGAATTCAAAAAAA
B12	2[47]0[48]BLK	ACGGCTACAAAAGGAGCCTTTAATGTGAGAAT
C12	0[79]1[63]BLK	ACAACCTTCAACAGTTTCAGCGGATGTATCGG
D12	2[79]0[80]BLK	CAGCGAAACTTGCTTTTCGAGGTGTTGCTAA
E12	0[111]1[95]BLK	TAAATGAATTTTCTGTATGGGATTAATTTCTT
F12	2[111]0[112]BLK	AAGGCCGCTGATACCGATAGTTGCGACGTTAG
G12	0[143]1[127]BLK	TCTAAAGTTTTGTCTGCTTTCCAGCCGACAA
H12	0[175]0[144]BLK	TCCACAGACAGCCCTCATAGTTAGCGTAACGA
I12	2[143]1[159]BLK	ATATTCGGAACCATCGCCACGCAGAGAAGGA
J12	2[175]0[176]BLK	TATTAAGAAGCGGGGTTTTGCTCGTAGCAT
K12	0[207]1[191]BLK	TCACCAGTACAACTACAACGCCCTAGTACCAG
L12	2[207]0[208]BLK	TTTCGGAAAGTCCCGTCGAGAGGGTGAATTTCCG
M12	0[239]1[223]BLK	AGGAACCCATGTACCCTAACACTTGATATAA
N12	2[239]0[240]BLK	GCCCGTATCCGGAATAGGTGTATCAGCCCAAT
O12	0[271]1[255]BLK	CCACCCCTCATTTTCAGGGATAGCAACCGTACT
P12	2[271]0[272]BLK	GTTTTAACTTAGTACCGCCACCCAGAGCCA

**Table S7 | Biotinylated staple strands.**

Position	Name	Sequence	Modification
C02	18[63]20[56]BIOTIN	ATTAAGTTTACCGAGCTCGAATTCGGGAAACCTGTCGTGC	5' - Biotin
C09	4[63]6[56]BIOTIN	ATAAGGGAACCGGATATTCATTACGTCAGGACGTTGGGAA	5' - Biotin
G02	18[127]20[120]BIOTIN	GCGATCGGCAATTCCACACAACAGGTGCCTAATGAGTG	5' - Biotin
G09	4[127]6[120]BIOTIN	TTGTGTCGTGACGAGAAAACCAAATTTCAACTTTAAT	5' - Biotin
K02	18[191]20[184]BIOTIN	ATTCATTTTTGTTTGGATTATACTAAGAAACCACAGAAG	5' - Biotin
K09	4[191]6[184]BIOTIN	CACCCCTCAGAAACCATCGATAGCATTGAGCCATTTGGGAA	5' - Biotin
O02	18[255]20[248]BIOTIN	AACAATAACGTAAAACAGAAATAAAAATCCTTTGCCCGAA	5' - Biotin
O09	4[255]6[248]BIOTIN	AGCCACCCTGTAGCGCGTTTTCAAGGGAGGGAAGGTAAA	5' - Biotin

**Table S8 | DNA-PAINT extensions.**

Name	Sequence	Modification
X66 docking strand	TAAATTTCCC	

**Table S9 | FRET-PAINT extensions.**

Name	Sequence	Modification
Fixed FRET-PAINT staple extension	TTTTTATACATCTA	5' - Atto 647N
Fixed FRET-PAINT antibody DNA strand	TTTTTATACATCTA	5' - Atto 647N 3' - Thiol
Dynamic FRET-PAINT strand	TCATTACTTCTTTTTTATACATCTA	

**Table S10 | DNA-PAINT imager sequences.**

Name	Sequence	Modification
Imager X66	GGGAAATTTA	3' - Cy3B

**Table S11 | FRET-PAINT imager sequences.**

Name	Sequence	Modification
Donor imager P1 9 nt	CTAGATGTAT	3' - Atto 488
Donor imager P1 7 nt	CGATGTAT	3' - Atto 488
Acceptor imager P3*	AGAAGTAATG	5' - Atto 647N

**Materials.** Unmodified DNA oligonucleotides, fluorescently modified DNA oligonucleotides and biotinylated DNA oligonucleotides were purchased from MWG Eurofins. M13mp18 scaffold was obtained from New England BioLabs (cat: N4040S). Agarose (cat: 01280.100) was purchased from biomol. SYBR safe (cat: SS33102) was ordered from Invitrogen. DNA gel loading dye (cat: R0611) was purchased from ThermoFisher. Freeze 'N Squeeze columns (cat: 732-6165) were ordered from Bio-Rad. BSA-Biotin was obtained from Sigma-Aldrich (cat: A8549). Streptavidin was ordered from Invitrogen (cat: S-888). Tris 1M pH 8.0 (cat: AM9856), EDTA 0.5M pH 8.0 (cat: AM9261), Magnesium 1M (cat: AM9530G) and Sodium Chloride 5M (cat: AM9759) were ordered from Ambion. Ultrapure water (cat: 10977-035) was purchased from Gibco. Glass slides (cat: 48811-703) were obtained from VWR. Coverslips were purchased from Marienfeld (cat: 0107032). Silicon (cat.1300 1000) was ordered from picodent. Double sided tape (cat: 665D) was ordered from Scotch. HeLa cells (cat. no. ACC-57)

were purchased from the Leibniz Institute DSMZ: Catalogue of Human and Animal Cell Lines. Secondary antibodies Anti-Rat IgG (cat. no. 712-005-150) and Anti-Rabbit (cat. no. 711-005-152) were purchased from Jackson ImmunoResearch. 16 % Paraformaldehyde (cat. no. 15710) was obtained from Electron Microscopy Sciences. 25% Glutaraldehyde (cat. no. 23115.01) was ordered from SERVA. Sodium borohydride (cat. no. 4051.1) and Triton X-100 (6683.1) were purchased from Carl Roth. BSA (cat. no. A4503-10g) was obtained from Sigma-Aldrich. 1xPBS (cat. no. 20012-019) was purchased from Thermo Fisher Scientific. DMEM (cat. no. 10566-016), fetal bovine serum (cat. no. 10500-064), Penicillin-Streptomycin (cat. no. 15140-122) and Trypsin-EDTA (cat. no. 25300-054) were obtained from Thermo Fisher Scientific. Primary monoclonal rat  $\alpha$ -Tubulin (Y/L) antibody (cat. no. MA1-80017) was ordered from Thermo Fishes Scientific. Tom20 primary rabbit polyclonal antibody (cat. no. sc-11415) was purchased from Santa Cruz. Maleimide-PEG2-succinimidyl ester (cat. no. 746223) was purchased from Sigma-Aldrich. No-Weigh Format DTT (cat. no. 20291) was purchased from Thermo Fisher Scientific. Micro BCA Protein Assay Kit was obtained from Thermo Fisher Scientific (cat. no. 23235). Amicon spin filters, 100 kDa and 3 kDa (cat. no. UFC510096 and UFC500396) and 0.22  $\mu$ m sterile filters (cat. no. SLGS033SS) were purchased from Merck/EMD Millipore. Nap5 columns (cat. no. 17-0853-02) were ordered from GE Healthcare. Zeba desalting spin columns (cat. no. 89882) were obtained from Thermo Fisher Scientific.

Three buffers were used for sample preparation and imaging: Buffer A (10 mM Tris-HCl pH 7.5, 100 mM NaCl, 0.05% Tween 20, pH 7.5); Buffer B (5 mM Tris-HCl pH 8, 10 mM MgCl<sub>2</sub>, 1 mM EDTA, 0.05% Tween 20, pH 8); Buffer C (1  $\times$  PBS pH 7.2, 500 mM NaCl). 100x Trolox: 100 mg Trolox, 430  $\mu$ l 100 % Methanol, 345  $\mu$ l 1 M NaOH in 3.2 ml H<sub>2</sub>O. 40x PCA: 154 mg PCA, 10 ml water and NaOH were mixed and adjusted to pH 9.0. 100x PCD: 9.3 mg PCD, 13.3 ml of buffer (100 mM Tris-HCl pH 8, 50 mM KCl, 1 mM EDTA, 50% glycerol).

**Optical setup.** Imaging for **Figure 1, 2** and **4** was carried out on an inverted Zeiss Elyra PS.1 microscope (Zeiss Germany) equipped with a dual camera adapter set (60N-2x60N for Elyra System, Zeiss Germany) and two electron-multiplying charge-coupled device (EMCCD) cameras (iXon EMCCD 879DU, Andor Technologies). For all experiments listed above an oil-immersion objective (alpha Plan Apochromat 100x/1,46 Oil DIC, Zeiss Germany) was used. Laser excitation was performed with optically pumped semiconductor lasers (OPSL) (488 nm and 561 nm, each 200 mW nominal power, Zeiss Germany). As dichroic mirror, a multi-bandpass filter was used (MBS 405/488/642 + EF BP 420-480/BP 495-560/LP 650, Zeiss Germany). Emission light was split by a dichroic mirror (1851-252, Zeiss

Germany) and filtered with emission filter, for the 488 channel (FF03-525/50, Semrock Inc), the 561 channel (FF01 609/54, Semrock Inc) and the 647 channel (1851-256, Zeiss Germany). Results from **Figure 3** were carried out on an inverted Nikon Ti-Eclipse microscope (Nikon Instruments) with the Perfect Focus System. For the experiment, an oil-immersion objective (Plan Apo 100 $\times$ , numerical aperture (NA) 1.45, oil, Nikon Instruments) was used. As excitation laser, a 488 nm (200 mW nominal, Toptica Photonics) was used. Excitation light was filtered with a laser clean-up filter (zet488/10 $\times$ , Chroma Technology Corp). As dichroic a laser dichroic mirror was used (zt561rdc-UF2, Chroma Technology Corp). Fluorescence light was spectrally filtered with an emission filter (et655lp, et705/72m, Chroma Technology Corp) and imaged on an electron-multiplying charge-coupled device (EMCCD) camera (iXon Ultra 879, Andor Technologies).

**DNA origami self-assembly.** The Rothmund rectangular origami (RRO) from **Figure 2** and **3** were synthesized in a one-pot reaction with 50  $\mu$ l total volume containing 10 nM scaffold strand (M13mp18), 100 nM core staples, 1  $\mu$ M biotinylated staples and 1  $\mu$ M DNA-PAINT handles. The folding buffer was 1 $\times$  TE buffer with 12.5 mM MgCl<sub>2</sub>. Structures were annealed using a thermal ramp. First, incubating for 5 min at 80 $^{\circ}$ C, then going from 65 $^{\circ}$ C to 4 $^{\circ}$ C over the course of 3 hours. After self-assembly, the structures were mixed with 1 $\times$  loading dye and then purified by agarose gel electrophoresis (1.5% agarose, 0.5 $\times$  TA, 10 mM MgCl<sub>2</sub>, 1 $\times$  SYBR Safe) at 3 V/cm for 2 hours. Gel bands were cut, crushed and filled into a Freeze 'N Squeeze column and spun for 5 min at 1,000 $\times$ g at 4  $^{\circ}$ C.

**Super-resolution FRET-PAINT and DNA-PAINT imaging with DNA origami.** For chamber preparation, a piece of coverslip (no. 1.5, 18  $\times$  18 mm<sup>2</sup>, ~0.17 mm thick) and a glass slide (3  $\times$  1 inch<sup>2</sup> 1 mm thick) were sandwiched together by two strips of double-sided tape to form a flow chamber with inner volume of ~20  $\mu$ l. First, 20  $\mu$ l of biotin-labeled bovine albumin (1 mg/ml, dissolved in buffer A) was flown into the chamber and incubated for 2 min. Then the chamber was washed using 40  $\mu$ l of buffer A. Second, 20  $\mu$ l of streptavidin (0.5mg/ml, dissolved in buffer A) was then flown through the chamber and incubated for 2 min. Next, the chamber was washed with 20  $\mu$ l of buffer A and subsequently with 20  $\mu$ l of buffer B. Then ~500 pM of the DNA origami structures (RRO) were flown into the chamber and allowed to attach to the surface for 2 min. Finally, the imaging buffer with buffer B with dye-labeled imager strands was flowed into the chamber. For **Figure 1C** 5 nM Cy3B labeled imager (Sequence X66, 10 nt) and 1 $\times$  PCA, 1 $\times$ PCD, 1 $\times$  Trolox in buffer B was used. In **Figure 1D** 50 nM Atto 488 labeled imager strands (Sequence P1, 9 nt) and 1 $\times$  PCA, 1 $\times$  PCD, 1 $\times$  Trolox in buffer B was used. The experiment in **Figure 2** was carried out using 1200 nM Atto 488 (Sequence P1, 7 nt) labeled imager

strand and 5x PCA, 5x PCD, 1x Trolox in buffer B. For **Figure 3** 50 nM Atto 647N labeled imager strands (Sequence P3\*, 10 nt) as acceptor, Atto 488 labeled imager strands (Sequence P1, 9 nt) as donor and 1x PCA, 1x PCD, 1x Trolox in buffer B imaging buffer were used.

**Antibody conjugation.** Antibodies were labeled with DNA strands as previously described<sup>2</sup>. In short, secondary antibodies were concentrated via amicon 100 kDa spin filters to 1-3 mg/ml. 100  $\mu$ l of antibody was labeled using a Maleimide-Peg2-succinimidyl ester for 90 min at 10x molar excess at 4 deg C on a shaker. Crosslinker stocks of 10 mg/ml in DMF were diluted in 1x PBS to reach 10x molar excess in 5  $\mu$ l, which were subsequently added to the antibody. After the reaction had been done, unreacted crosslinker was removed via a zeba spin column. Thiolated DNA was reduced using DTT for 2 h at room temperature. DTT was purified from the reduced DNA via a Nap5 column and fractions containing DNA were concentrated via 3 kDa amicon spin filters. The reduced DNA was then added to the antibody bearing a functional maleimide group in 10x molar excess and incubated over night at 4 deg C on a shaker in the dark. Antibody-DNA constructs were finally purified via 100 kDa amicon spin filters.

**Cell culture.** Cells were cultured in Dulbecco's Modified Eagle Medium (DMEM) supplemented with 10% FBS and 1% Pencillin and Streptomycin, they were passaged every other day until 90% confluency was reached using standard cell culture methods. HeLa cells for imaging were used between passage number 6 and 20.

**Immunofixation.** 24h before fixation, HeLa cells were seeded to 70% confluency. For microtubule imaging cells were prefixed with prewarmed 0.4 % Glutaraldehyde and 0.25 % Triton X-100 in 1xPBS for 90 s and fixed with 3 % Glutaraldehyde in 1x PBS for 15 min. Quenching was performed via freshly prepared 1 mg/ml Sodium Borohydride in 1x PBS for 7 min. Cells were washed 1x for 1 min and 3x for 5 min in 1xPBS. Blocking and permeabilization were performed using 3 % BSA and 0.25 % Triton X-100 in 1xPBS for 90 min. Microtubule primary antibody was incubated for 1 h at RT with gentle shaking in 5% BSA in 1xPBS in the dark. Cells were washed 3x in 1xPBS for 5 min. Conjugated secondary antibody was incubated for 1 h at RT in the dark in 5% BSA in 1xPBS. The cells were finally washed 3x in 1x PBS for 5 min and were ready for imaging.

**Super-resolution FRET-PAINT imaging with Cells.** The experiment in **Figure 4** was performed using 500 nM Atto 488 labeled imager strands and 5x PCA, 5x PCD, 2x Trolox in buffer C.

**Super-resolution data processing.** Super-resolution DNA-PAINT reconstruction, drift correction, and

alignment was carried out using the software package Picasso. Zeiss Elyra data (.czi files) was converted for processing in Picasso with a custom ImageJ Plugin (available at <https://github.com/jungmannlab/imagej-raw-yaml-export.git>).

### Supplementary References

1. Endesfelder, U.; Malkusch, S.; Fricke, F.; Heilemann, M., A simple method to estimate the average localization precision of a single-molecule localization microscopy experiment. *Histochem Cell Biol* **2014**, *141* (6), 629-638.
2. Schnitzbauer, J.; Strauss, M. T.; Schlichthaerle, T.; Schueder, F.; Jungmann, R., Super-resolution microscopy with DNA-PAINT. *Nat Protoc* **2017**, *12* (6), 1198-1228.



**Supporting Information**

Nanometer-scale Multiplexed Super-Resolution Imaging with an  
Economic 3D-DNA-PAINT Microscope

BY

Alexander Auer, Thomas Schlichthärle, Johannes B. Wöhrstein, Florian Schüder, Maximilian T.  
Strauss, Heinrich Grabmayr, and Ralf Jungmann

PUBLISHED IN

*ChemPhysChem*, (2018), 19, 3024–3034

Reprint with permission from ref. [2].  
Copyright 2018, WILEY-VCH.



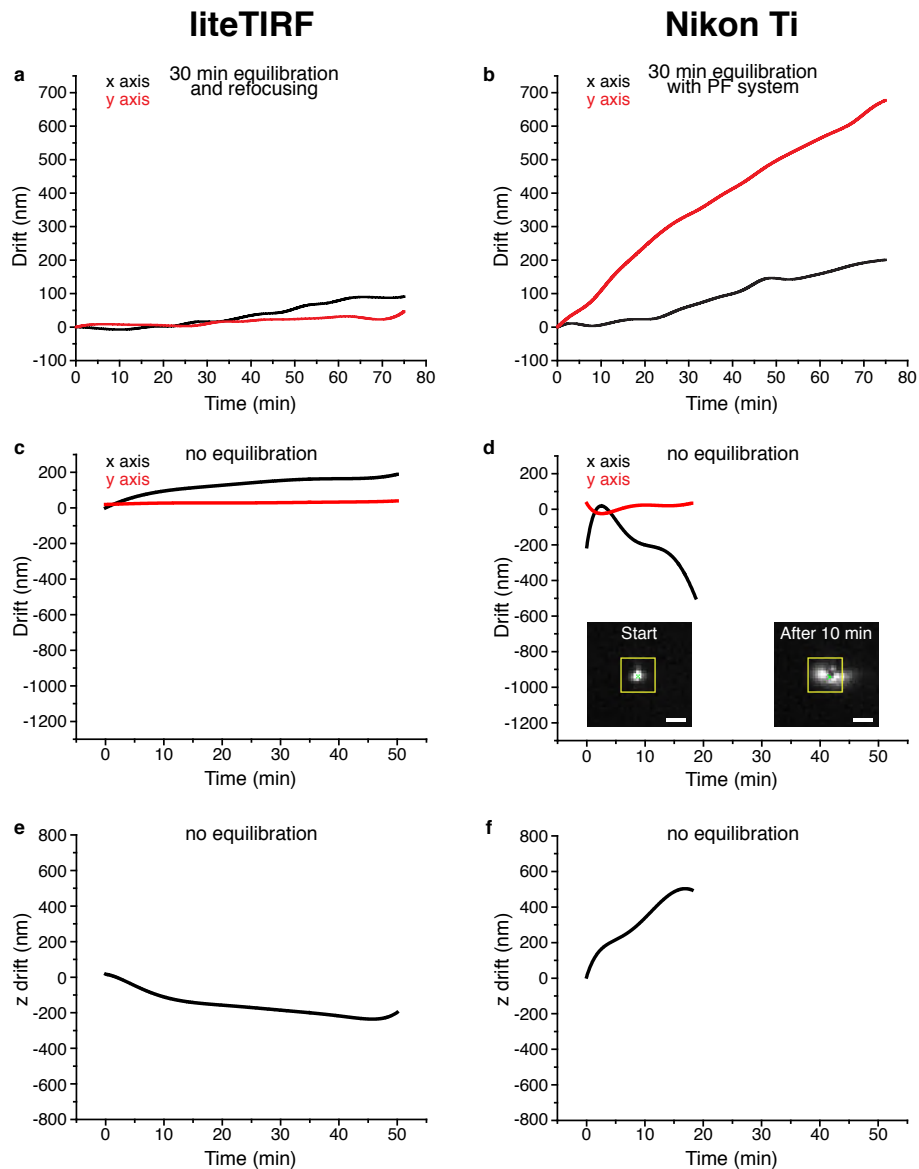
## Supporting Information

© Copyright Wiley-VCH Verlag GmbH & Co. KGaA, 69451 Weinheim, 2018

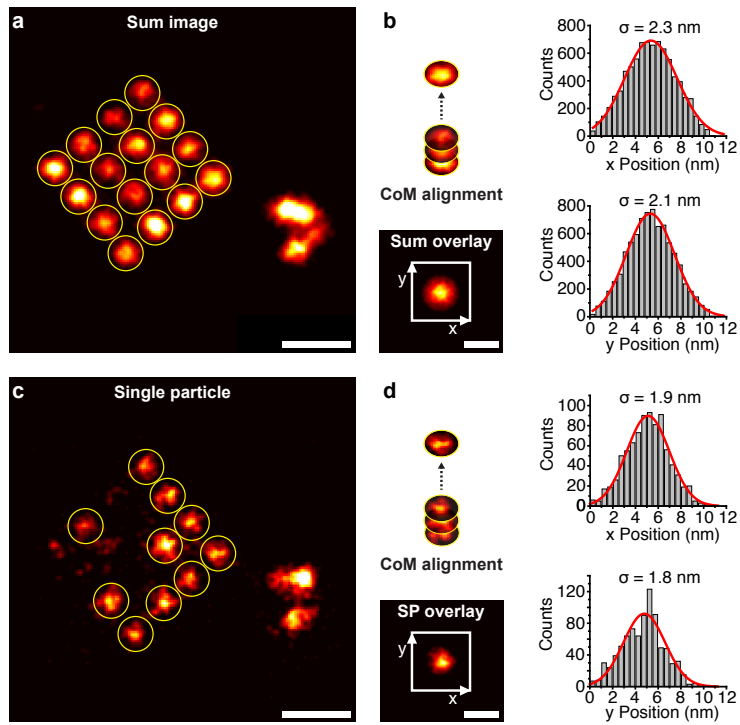
### **Nanometer-scale Multiplexed Super-Resolution Imaging with an Economic 3D-DNA-PAINT Microscope\*\***

Alexander Auer, Thomas Schlichthaerle, Johannes B. Woehrstein, Florian Schueder,  
Maximilian T. Strauss, Heinrich Grabmayr, and Ralf Jungmann\*

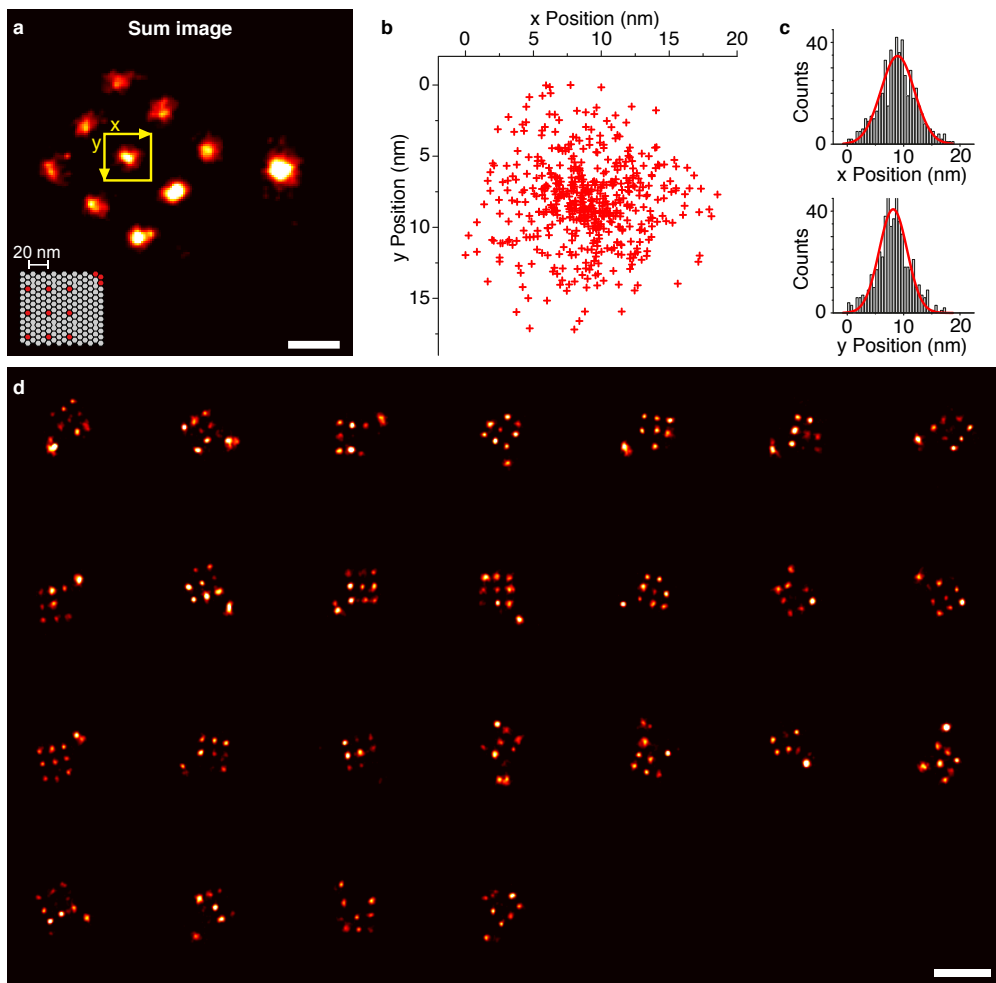
<b>Supplementary Figure 1</b>	liteTIRF drift performance
<b>Supplementary Figure 2</b>	Localization precision comparison of sum image and a single particle
<b>Supplementary Figure 3</b>	2D resolution capabilities of liteTIRF using an interline-transfer -CCD camera
<b>Supplementary Figure 4</b>	2D resolution capabilities of liteTIRF using a non-scientific CMOS camera
<b>Supplementary Figure 5</b>	Super-resolution imaging with dSTORM of DNA origami nanostructures
<b>Supplementary Figure 6</b>	Super-resolution imaging with DNA-PAINT of alpha-tubulin in a fixed COS7 cell
<b>Supplementary Figure 7</b>	NeNA analysis of data from Supplementary Figure 5
<b>Supplementary Figure 8</b>	Two-plex super-resolution imaging with Exchange-PAINT in a fixed HeLa cell
<b>Supplementary Figure 9</b>	Schematic view of the camera position in the emission path
<b>Supplementary Figure 10</b>	Calibration curve generated using DNA-PAINT with latex microspheres
<b>Supplementary Table 1</b>	Components of the liteTIRF platform
<b>Supplementary Table 2</b>	Experimental conditions in Figure 2 (10 nm grid DNA origami)
<b>Supplementary Table 3</b>	Experimental conditions in Figure 3 (tubulin)
<b>Supplementary Table 4</b>	Experimental conditions in Figure 4 (tubulin)
<b>Supplementary Table 5</b>	Experimental conditions in Figure 4 (TOM20)
<b>Supplementary Table 6</b>	Experimental conditions in Figure 5 (microspheres)
<b>Supplementary Table 7</b>	Experimental conditions in Figure 6 (tetrahedron DNA origami)
<b>Supplementary Table 8</b>	Experimental conditions in Supplementary Figure 3 (20 nm grid DNA origami)
<b>Supplementary Table 9</b>	Experimental conditions in Supplementary Figure 4 (20 nm grid DNA origami)
<b>Supplementary Table 10</b>	Experimental conditions in Supplementary Figure 5 (dSTORM)
<b>Supplementary Table 11</b>	Experimental conditions in Supplementary Figure 6 (tubulin)
<b>Supplementary Table 12</b>	Experimental conditions in Supplementary Figure 8 (tubulin)
<b>Supplementary Table 13</b>	Experimental conditions in Supplementary Figure 8 (TOM20)
<b>Supplementary Table 14</b>	M13mp18 p7249 sequence
<b>Supplementary Table 15</b>	Rectangular DNA origami staple strands
<b>Supplementary Table 16</b>	Biotinylated staple strands
<b>Supplementary Table 17</b>	DNA-PAINT docking site sequences
<b>Supplementary Table 18</b>	DNA-PAINT imager sequences



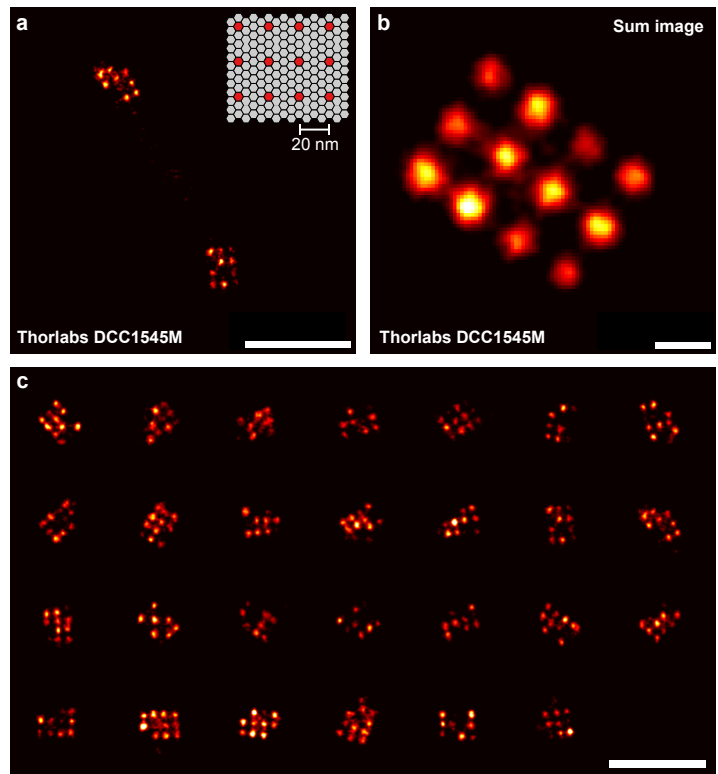
**Supplementary Figure 1 | liteTIRF drift performance.** Drift trajectories fitted with 7<sup>th</sup> order polynomial fit. **(a)** LiteTIRF shows less than 100 nm drift in x- and y-direction over the course of 80 min image acquisition after initial 30 min equilibration time and refocusing. **(b)** In comparison, a commercial setup drifts over more than 700 nm in x- and y-direction during the same time and the same settling time. **(c)** Exemplary drift curve of gold nanoparticles immobilized on the surface imaged with the liteTIRF platform and the cylindrical lens. Without the 30 min equilibration time the drift in x- and y-direction is less than 200 nm drift over the course of 50 min. We note that this can vary from sample to sample. **(d)** Same experiment performed on a commercial Nikon Ti without the use of the Perfect Focus System (PFS) shows drift up to 400 nm in x-y direction after 10 minutes. After 20 minutes the focus was lost and the single-molecule signals could not be localized reliably anymore. The left inset shows a single-molecule signal identified (yellow square) and localized (green cross) of one exemplary gold nanoparticle in the first frame. Inset right shows the same gold particle after 10 minutes. Due to the drift in z-direction, the localization algorithm could not localize the gold particle reliably. **(e)** Drift analysis of the experiment in **d** shows drift up to 200 nm in the z-direction. **(f)** The commercial setup shows up to 500 nm drift along the z-direction after 20 minutes without the active focusing system. Scale bars: 1  $\mu\text{m}$



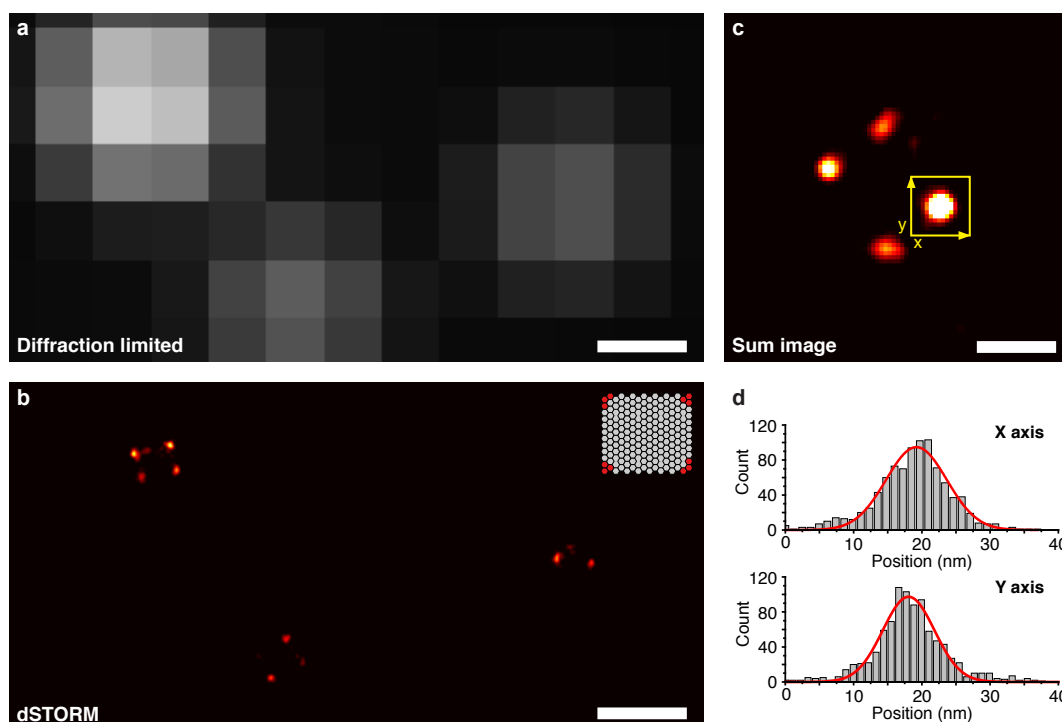
**Supplementary Figure 2 | Localization precision comparison of sum image and a single particle.** (a) Sum image of 10-nm-grid DNA origami depicted in **Figure 2**. Individual DNA-PAINT docking sites of the 10-nm-grid were selected (yellow circles). (b) Picked docking sites were aligned on to each other using center-of-mass calculations and visualized as a sum image. Histogram analysis along x and y direction yields a localization precision of 2.3 nm and 2.1 nm, respectively. (c) Super-resolution image of a single particle used in the sum image in **a** and **Figure 2**. Individual DNA-PAINT docking sites of the single particle were picked. (d) Selected docking sites of the single particle were aligned to each other using center-of-mass calculation and visualized as a sum image overlay. Subsequent histogram analysis in x and y direction yields a localization precision of 1.9 nm and 1.8 nm. This translates to a FWHM-limited resolution of 4.5 nm and 4.2 nm, respectively.



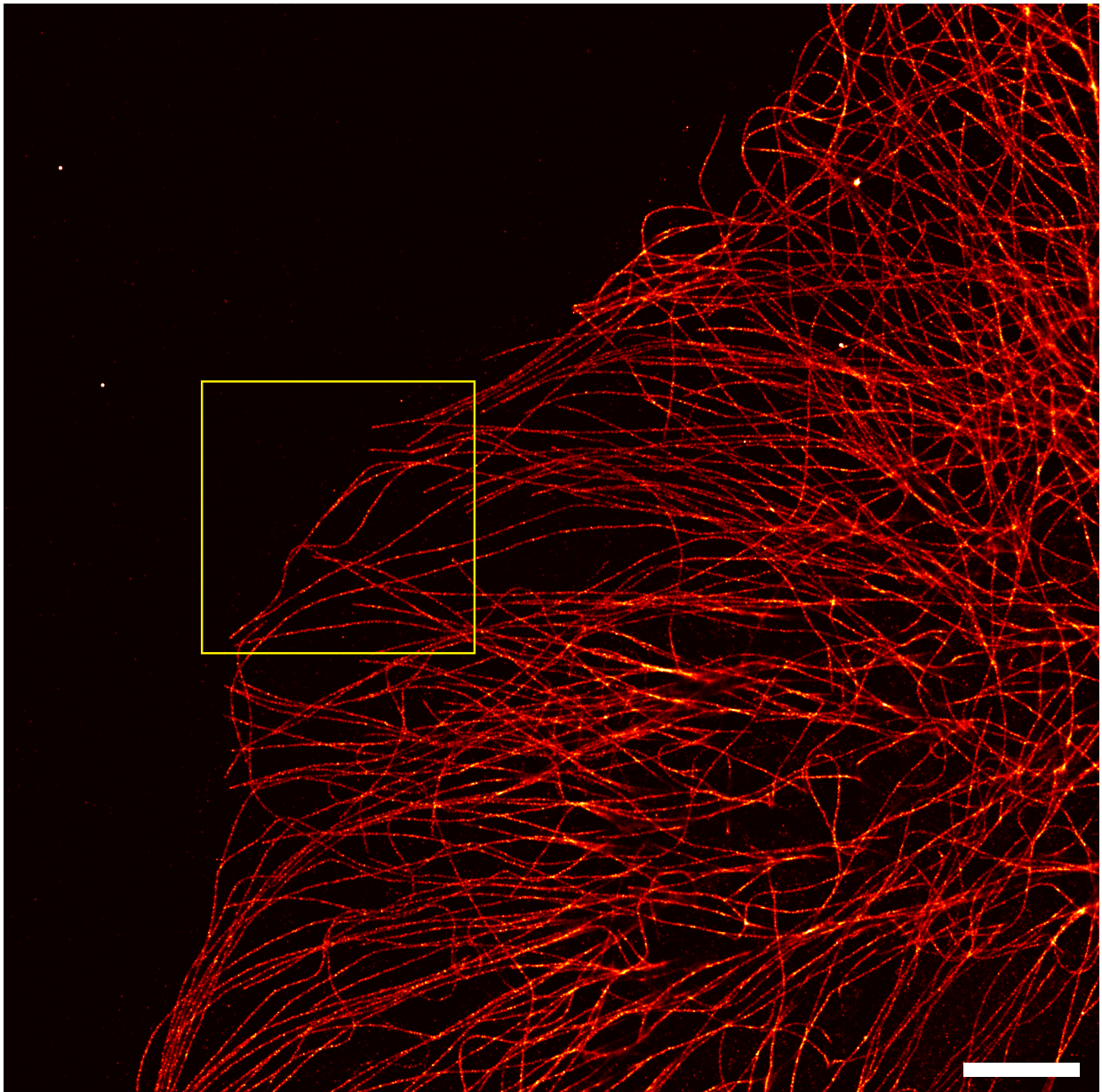
**Supplementary Figure 3 | 2D resolution capabilities of liteTIRF using an interline-transfer-CCD camera.** (a) Sum image of  $n = 25$  picked 20 nm gird DNA origami ( $3 \times 3$  pattern visualized in the inset) imaged using the liteTIRF microscope with DNA-PAINT employing an inline-CCD camera (PCO.pixelfly) and ATTO 647N-labeled imager strands. The  $3 \times 3$  pattern can be clearly resolved. (b) Scatter plot of the single docking site highlighted in a with 535 single-molecule localizations. (c) Histogram analysis along the x and y direction yields a localization precision of 2.7 nm, translating to a FWHM-limited resolution of 6.4 nm. (d) Super-resolution reconstruction montage of the 25 DNA origami structures used in the sum image in b. Scale bars: 20 nm (a), 100 nm (d).



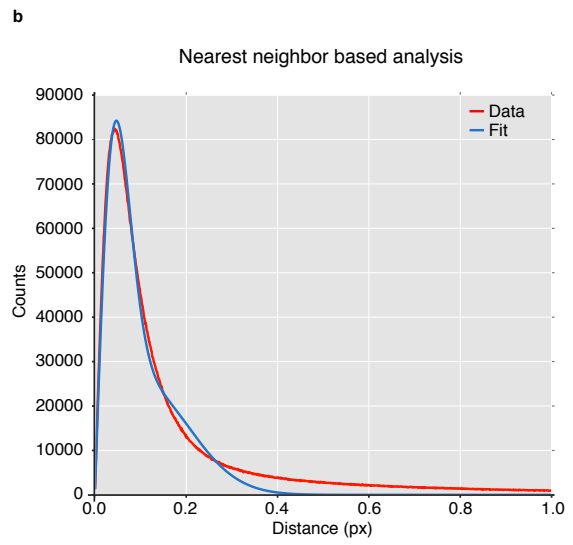
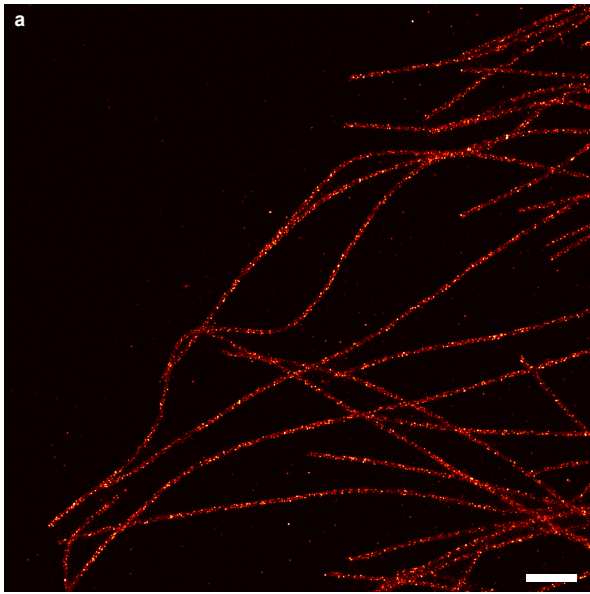
**Supplementary Figure 4 | 2D resolution capabilities of liteTIRF using a non-scientific CMOS camera. (a)** DNA-PAINT imaging using a non-scientific CMOS camera (Thorlabs DCC1545M, prized around 340 Euro) of DNA origami carrying a 3×4 grid pattern with a spacing of 20 nm. **(b)** Sum image created from  $n = 27$  individual DNA origami structures showing that the pattern can clearly be resolved. **(c)** Super-resolution reconstruction montage of the 27 DNA origami structures used in the sum image in **b**. Scale bars: 200 nm (**a**, **c**), 20 nm (**b**).



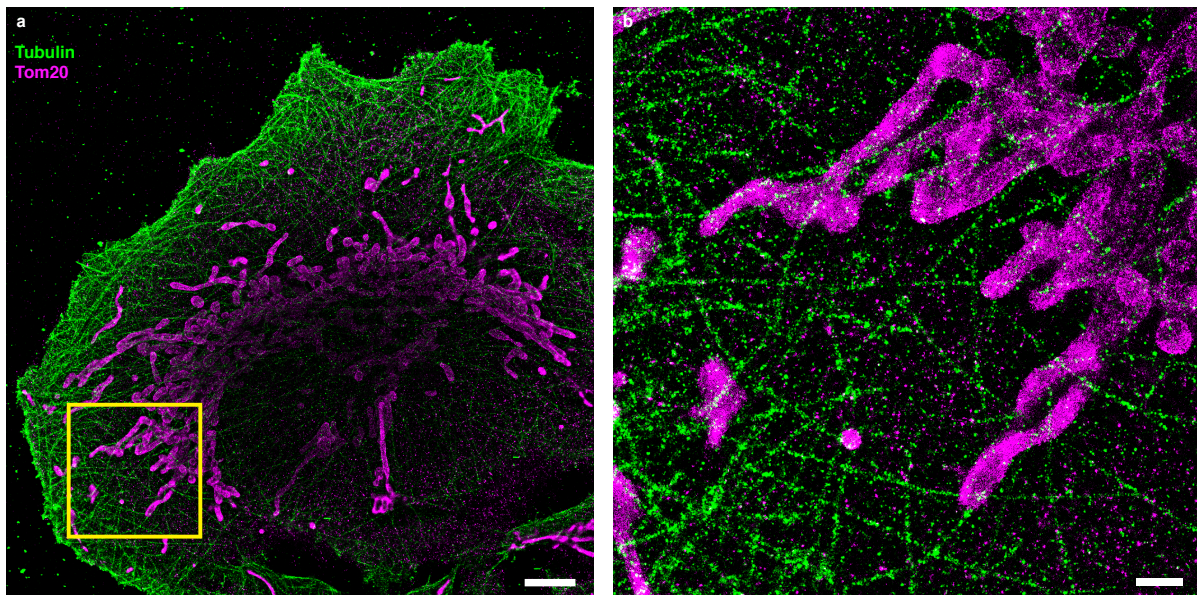
**Supplementary Figure 5 | Super-resolution imaging of DNA origami nanostructures with dSTORM.** (a) Diffraction-limited representation of DNA nanostructures carrying Alexa Fluor 647 labeled DNA strands stably bound to the DNA origami. (b) Super-resolution reconstruction with dSTORM of the same region in a displays individual DNA origami. The schematic inset shows the DNA origami with the Alexa Fluor 647 labeled staple strands, three fluorophores in every corner. dSTORM imaging was performed without controlling the blinking rate using a UV laser. (c) Sum image of  $n = 13$  picked DNA origami structures. (d) Histogram analysis along the x and y direction of the DNA origami corner highlighted in c yields a localization precision of  $\sim 4.1$  nm. Scale bars: 200 nm (a, b), 20 nm (c).



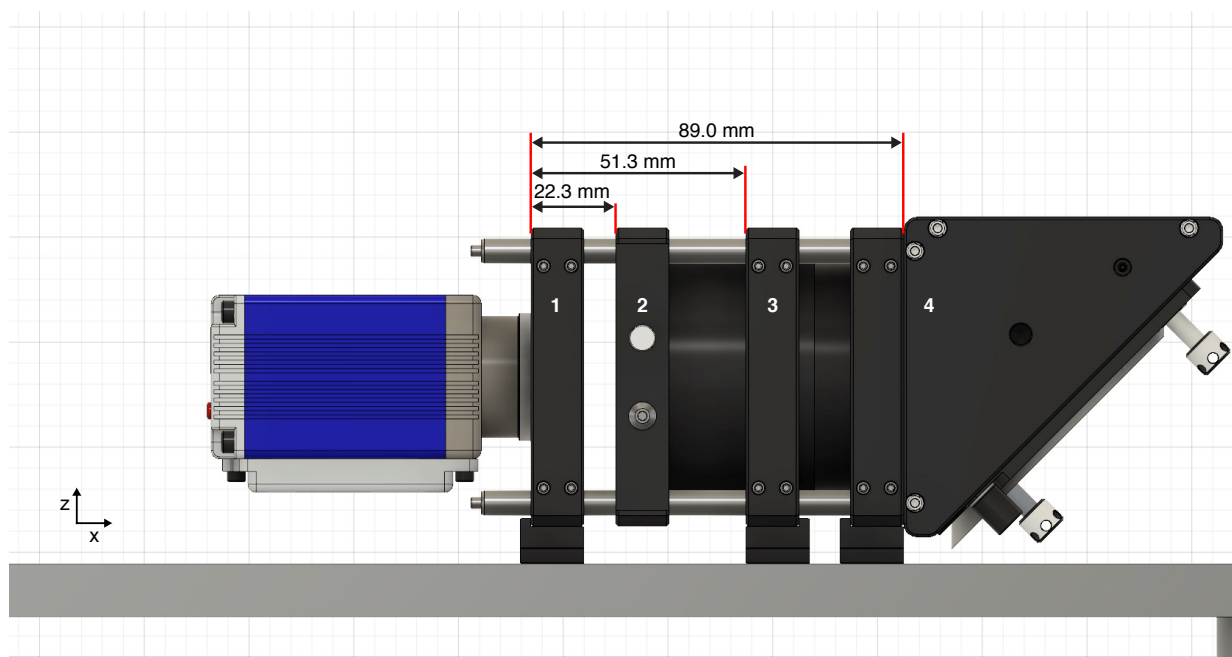
**Supplementary Figure 6 | Super-resolution imaging with DNA-PAINT of alpha-tubulin in a fixed COS7 cell.** DNA-PAINT imaging of alpha-tubulin labeled using primary-secondary antibodies in a fixed COS7 cell and ATTO 647N-labeled imager strands. Super-resolution imaging was carried out using the liteTIRF platform and a non-cooled scientific-CMOS camera (PCO.panda 4.2). Nearest neighbor analysis yields an experimental localization precision of 5.7 nm (**Supplementary Figure 6**). Scale bar: 5  $\mu$ m



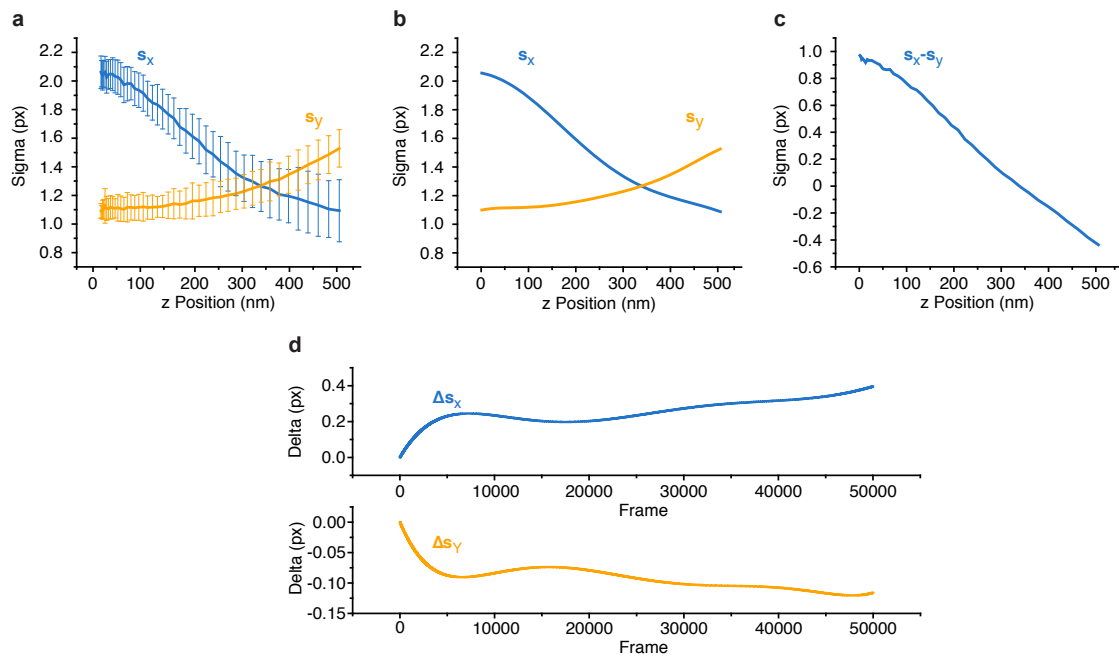
**Supplementary Figure 7 | Super-resolution imaging with DNA-PAINT of alpha-tubulin in a fixed COS7 cell. (a)** Zoom-in of the highlighted area in **Supplementary Figure 5**. Due to the high labeling density and high resolution individual microtubules appear as two parallel stripes, resulting from the 2D projection of the hollow three-dimensional structure. **(b)** Based on nearest neighbor analysis (NeNA), we observe an average localization precision of 5.7 nm. Experimental data is plotted in red. A fitted curve is represented in blue. Scale bar: 1  $\mu\text{m}$  **(a)**.



**Supplementary Figure 8 | Two-plex super-resolution imaging with Exchange-PAINT in a fixed HeLa cell.** (a) Two-color Exchange-PAINT imaging with liteTIRF in a fixed HeLa cell. Alpha tubulin, shown in green was labeled using primary-secondary antibodies and imaged with ATTO 647N-labeled imager strands. Subsequently, TOM20 (visualized in magenta) was imaged with primary-secondary antibodies and ATTO 647N-labeled imager strands. Both super-resolution reconstruction images were aligned using cross-correlation algorithms and fiducial markers. (b) Zoom-in of the highlighted region in a. The sparse labeling of alpha tubulin can be explained by the different fixation strategy, necessary to prevent degradation of lipid membranes. Scale bars: 5  $\mu\text{m}$  (a), 1  $\mu\text{m}$  (b).



**Supplementary Figure 9 | Schematic view of the camera position in the emission path.** The correct camera position relative to the tube lens is essential to achieve the best imaging performance. For guidance during replication of the liteTIRF platform, we measured the relative distances of the camera cage plate mount (1), the cylindrical lens cage mount (2) and the cage mount (3) relative to the 45 degree mirror mount (4).



**Supplementary Figure 10 | Calibration curve generated using DNA-PAINT with latex microspheres.** (a) Height-dependent width ( $s_x$  and  $s_y$ ) of the PSF averaged in every radial section along the x (blue) and y (orange) direction, Error bars represent the averaged standard deviation of widths in every section. (b) Sixth degree polynomial fit of the calibration data generated the look-up table for subsequent 3D calibrations. (c) Width difference of x and y direction with respect to the z position. (d) Width correction with respect to time, averaged over all radial sections, originating from z drift.

Supplementary Table 1 | Components of the liteTIRF platform

Item lot number	Item Name	Partused for	Manufacturer	Reseller	List Price (Euro, Aug 2018)	Quantity	Sum (Euro)
PCOgarda 4.2	SMOS Camera	Camera	PCO	PCO	5990	1	5990
ZET 8400E	Laser clean-up filter	Filter cube	Chroma	AHF	339	1	339
665L P ET	Excitation laser	Excitation laser	Thorlabs	AHF	339	1	339
IBEM5SMARF-640-S-150nm	Excitation laser 8 Power Supply	Objective	Thorlabs	Thorlabs	2170	1	2170
CP-P-Apo 100x Lambda OII N.A. 1.45	Nikon 100x TIRF NA, 1.45 Objective	Objective	Nikon	Nikon	4659	1	4659
M562-XYZ	ULTRAFIN Precision XYZ Linear Stage, 13 mm, Req. 3 Actuators, Metric	Sample stage (x and y direction)	Newport	Newport	2119	1	2119
SM-13	Venier micrometer	Sample stage (z direction)	Newport	Newport	477	2	954
M30345M	Differential micrometer	Sample stage (z direction)	Thorlabs	Thorlabs	2170	1	2170
RSFPI/M	Aluminum Beadboard 500 mm x 450 mm x 12.7 mm M6 Taps	Mounting plates base and first level	Thorlabs	Thorlabs	3222	2	6444
ER4-P4	025.0 mm Pedestal PilatPost M6 Taps, L = 100 mm	Connection of base with first level, first level with second level	Thorlabs	Thorlabs	18.36	3	55.08
KCBEC/M	Cage Plate Mounting Base for 60 mm Cage Plates Metric	Fixation of the emission cage to base plate	Thorlabs	Thorlabs	24.52	2	49.04
SM2L10	Cage Assembly Rod 4" Long O6 mm 4 Pack	Emission path cage	Thorlabs	Thorlabs	209.07	1	209.07
SM2L20	Right-Angle Kinematic Elliptical Mirror Mount	Emission path cage cover, cut down a 35 mm long piece	Thorlabs	Thorlabs	27.35	1	27.35
SM2L20	SM2 Slip-On Lens Tube Cover 24.1 Long	Emission path cage cover, cut down a 35 mm long piece	Thorlabs	Thorlabs	27.35	1	27.35
SM1A2	Adapter with External SM2 Threads and Internal M38 x 0.5 Threads	Tube lens	Thorlabs	Thorlabs	425.54	1	425.54
ER6-P4	Adapter with External SM1 Threads and Internal SM2 Threads	Emission path cage	Thorlabs	Thorlabs	43.18	1	43.18
LCPO2M	Cage Assembly Rod 6" Long O6 mm 4 Pack	Emission path cage	Thorlabs	Thorlabs	22.72	1	22.72
SCOL125	30 mm to 60 mm Cage Plate Adapter M4 Tap	Cage of optical path from base to third level and laser beam expander	Thorlabs	Thorlabs	29.88	2	59.76
SM1C20	SM1 Slip-On Lens Tube Cover 24 Long	Mounting of filter cube	Thorlabs	Thorlabs	36.16	1	36.16
SM1C20	SM1 Slip-On Lens Tube Cover 24 Long	Emission path below filter cube	Thorlabs	Thorlabs	11.44	1	11.44
CMH-DC/M	30 mm Cap-Cube with Democ. Filter Mount (Metric)	Emission path below filter cube, cut down a 35 mm long piece for emission path cover	Thorlabs	Thorlabs	14.99	2	29.98
ERH-P4	Cage Assembly Rod 1" Long O6 mm 4 Pack	Filter cube	Thorlabs	Thorlabs	150.2	1	150.2
SM1CP2	Externally SM1-Threaded End Cap	Connection of filter cube with filter cube mount	Thorlabs	Thorlabs	17.44	1	17.44
MTY/M	13 mm Translation Stage with Standard Micrometer M6 Taps	Filter cube	Thorlabs	Thorlabs	150.2	1	150.2
OC65	30 mm Cage System XY Translating Lens Mount for O1-Optics	Laser beam expander	Thorlabs	Thorlabs	270.74	1	270.74
OC65M	SM1 Threaded 30 mm Cage Plate 6 mm Thick	Laser beam expander	Thorlabs	Thorlabs	160.4	2	320.8
RS2P/M	025.0 mm Pedestal PilatPost M6 Taps, L = 50 mm	Laser beam expander mounting to plate	Thorlabs	Thorlabs	68.41	2	136.82
KM02/M	Cage-Compatible Cont. Variable Ret. ND Filter Wheel OD = 0 - 2.0 M4 Tap	Laser beam expander	Thorlabs	Thorlabs	24.8	2	49.6
BB05-E02	Kinematic Mirror Mount for O1 2.7 mm Optics M4 Taps	Laser alignment, mirror mount	Thorlabs	Thorlabs	436.7	2	873.4
RSHP/M	O1Z0 Broadband Dielectric Mirror 400 - 750 nm	Laser alignment, mirror mount	Thorlabs	Thorlabs	35.45	2	70.9
RSHP/M	O25.0 mm Pedestal PilatPost M6 Taps, L = 25 mm	Laser alignment, mirror mount	Thorlabs	Thorlabs	46.82	2	93.64
RSHP/M	025 mm Post Spacer Thickness = 2 mm	Laser alignment, mirror mount	Thorlabs	Thorlabs	20.86	2	41.72
RSHP/M	025 mm Post Spacer Thickness = 2 mm	Laser alignment, mirror mount	Thorlabs	Thorlabs	6.77	2	13.54
RSHP/M	025 mm Post Spacer Thickness = 2 mm	Laser alignment, mirror mount	Thorlabs	Thorlabs	6.21	2	12.42
RSHP/M	025.0 mm Pedestal PilatPost M4 Taps, L = 19 mm	Laser mount	Thorlabs	Thorlabs	6.21	2	12.42
RS07SP4M	Vertical Cage System Mounting Plate	Laser mount	Thorlabs	Thorlabs	19.47	2	38.94
SM2A6	Adapter with External SM2 Threads and Internal SM1 Threads	Optical path mounting to third level	Thorlabs	Thorlabs	39.87	1	39.87
SM1A3	Adapter with External SM1 Threads and Internal SM1 Threads	Camera mounting	Thorlabs	Thorlabs	22.72	1	22.72
RS1A3	025 mm Post Spacer Thickness = 10 mm	Third level mounting	Thorlabs	Thorlabs	18.17	1	18.17
LA11S1A-M/L	O1-1 N BK7 Plano-Convex Lens Internal M05 x 0.75 Threads	Third level mounting	Thorlabs	Thorlabs	8.33	4	33.32
LA1540-A-M/L	O1-1 N BK7 Plano-Convex Lens SM1-Threaded Mount l = 50.0 mm APC: 350-700 nm	Laser beam expander	Thorlabs	Thorlabs	14.72	1	14.72
SM1A6	O1-1 N BK7 Plano-Convex Lens SM05-Threaded Mount l = 15.0 mm APC: 350-700 nm	Laser beam expander	Thorlabs	Thorlabs	41.72	1	41.72
BBE5-E02	2" Broadband Dielectric Elliptical Mirror 400 - 750 nm	Laser beam expander	Thorlabs	Thorlabs	17.8	1	17.8
LCFH	60 mm Cage System Removable Filter Holder for O1-Optics Plate and Holder included 8-32 T/Omniflex lens cage mount	Emission path, 45 deg mirror	Thorlabs	Thorlabs	175.24	1	175.24
LT114M4-B	l = 300 mm O1-1 N BK7 Mounted Plano-Convex Round OY Lens APC: 650 - 1050 nm	Omniflex lens cage mount	Thorlabs	Thorlabs	89.94	1	89.94
Custom make	Sample holder	Sample holder, see CAD	Custom	Custom	110.33	1	110.33

206/2.5

**Supplementary Table 2 | Experimental conditions in Figure 2 (10 nm grid DNA origami)**

<b>Microscope setting</b>	<b>Condition</b>
Microscope	liteTIRF
Objective	CFI Plan Apo Lambda 100X Oil
Camera	PCO.panda 4.2
Field of view	512×512 pixel after binning
Frames	25 000
Exposure time	300 ms
Binning	2×2
Tube lens	1×
Excitation laser	642 nm [max power 150 mW]
Laser Power	150 mW

<b>Sample settings</b>	<b>Condition</b>
Sample target	10 nm grid DNA origami
Imager sequence	X61
Imager concentration	3 nM
Imaging buffer	B with PCA/PCD/TX
Dye	ATTO 647N
NeNA localization precision	2.2 nm

**Supplementary Table 3 | Experimental conditions in Figure 3 (tubulin)**

<b>Setting</b>	<b>Condition</b>
Microscope	liteTIRF
Objective	CFI Plan Apo Lambda 100X Oil
Camera	PCO.pixelfly
Field of view	696×520 pixel after binning
Frames	100 000
Exposure time	100 ms
Binning	2×2
Tube lens	1×
Excitation laser	642 nm [max power 150 mW]
Laser Power	130 mW

<b>Sample settings</b>	<b>Condition</b>
Sample target	Alpha tubulin prim/sec anti body
Cell type	HeLa
Imager sequence	X61
Imager concentration	3 nM
Imaging buffer	C with PCA/PCD/TX
Dye	ATTO 647N
NeNA localization precision	8.9 nm

**Supplementary Table 4 | Experimental conditions in Figure 4 (tubulin)**

<b>Setting</b>	<b>Condition</b>
Microscope	liteTIRF
Objective	CFI Plan Apo Lambda 100X Oil
Camera	PCO.panda 4.2
Field of view	512×512 pixel after binning
Frames	30 000
Exposure time	150 ms
Binning	2×2
Tube lens	1
Excitation laser	642 nm [max power 150 mW]
Laser Power	100 mW

<b>Sample settings</b>	<b>Condition</b>
Sample target	Alpha tubulin prim/sec anti body
Cell type	COS7
Imager sequence	P1
Imager concentration	500 pM
Imaging buffer	C with PCA/PCD/TX
Dye	ATTO 647N
NeNA localization precision	5.0 nm

**Supplementary Table 5 | Experimental conditions in Figure 4 (TOM20)**

<b>Setting</b>	<b>Condition</b>
Microscope	liteTIRF
Objective	CFI Plan Apo Lambda 100X Oil
Camera	PCO.panda 4.2
Field of view	512×512 pixel after binning
Frames	20 000
Exposure time	150 ms
Binning	2×2
Tube lens	1×
Excitation laser	642 nm [max power 150 mW]
Laser Power	100 mW

<b>Sample settings</b>	<b>Condition</b>
Sample target	TOM20 prim/sec anti body
Cell type	COS7
Imager sequence	P3
Imager concentration	1 nM
Imaging buffer	C with PCA/PCD/TX
Dye	ATTO 647N
NeNA localization precision	8.6 nm

**Supplementary Table 6 | Experimental conditions in Figure 5 (microspheres)**

<b>Setting</b>	<b>Condition</b>
Microscope	liteTIRF
Objective	CFI Plan Apo Lambda 100X Oil
Camera	PCO.pixelfly
Field of view	696×520 pixel after binning
Frames	50 000
Exposure time	200 ms
Binning	2×2
Tube lens	1×
Excitation laser	642 nm [max power 150 mW]
Laser Power	80 mW

<b>Sample settings</b>	<b>Condition</b>
Sample target	Latex-microsphere
Imager sequence	P1
Imager concentration	150 pM
Imaging buffer	B with PCA/PCD/TX
Dye	ATTO 647N
NeNA localization precision	4.2 nm

**Supplementary Table 7 | Experimental conditions in Figure 6 (tetrahedron DNA origami)**

<b>Setting</b>	<b>Condition</b>
Microscope	liteTIRF
Objective	CFI Plan Apo Lambda 100X Oil
Camera	PCO.pixelfly
Field of view	696×520 pixel after binning
Frames	15 000
Exposure time	300 ms
Binning	2×2
Tube lens	1×
Excitation laser	642 nm [max power 150 mW]
Laser Power	100 mW

<b>Sample settings</b>	<b>Condition</b>
Sample target	Tetrahedron DNA origami
Imager sequence	P1
Imager concentration	500 pM
Imaging buffer	B with PCA/PCD/TX
Dye	ATTO 647N
NeNA localization precision	3.6 nm

**Supplementary Table 8 | Experimental conditions in Supplementary Figure 2a (20 nm Grid DNA origami)**

<b>Setting</b>	<b>Condition</b>
Microscope	liteTIRF
Objective	CFI Plan Apo Lambda 100X Oil
Camera	PCO.pixelfly
Field of view	696×520 pixel after binning
Frames	30 000
Exposure time	150 ms
Binning	2×2
Tube lens	1×
Excitation laser	642 nm [max power 150 mW]
Laser Power	150 mW

<b>Sample settings</b>	<b>Condition</b>
Sample target	20 nm grid DNA origami
Imager sequence	X61
Imager concentration	4 nM
Imaging buffer	B with PCA/PCD/TX
Dye	ATTO 647N
NeNA localization precision	3.2 nm

**Supplementary Table 9 | Experimental conditions in Supplementary Figure 3 (20 nm Grid DNA origami)**

<b>Setting</b>	<b>Condition</b>
Microscope	liteTIRF
Objective	CFI Plan Apo Lambda 100X Oil
Camera	Thorlabs DCC1545M
Field of view	640×512 pixel after binning
Frames	5900
Exposure time	200 ms
Binning	2×2
Tube lens	1×
Excitation laser	642 nm [max power 150 mW]
Laser Power	100 mW

<b>Sample settings</b>	<b>Condition</b>
Sample target	20 nm grid DNA origami
Imager sequence	P1
Imager concentration	7 nM
Imaging buffer	B with PCA/PCD/TX
Dye	ATTO 647N
NeNA localization precision	4.2 nm

**Supplementary Table 10 | Experimental conditions in Supplementary Figure 4 (dSTORM)**

<b>Setting</b>	<b>Condition</b>
Microscope	liteTIRF
Objective	CFI Plan Apo Lambda 100X Oil
Camera	PCO.pixelfly
Field of view	696×520 pixel after binning
Frames	10 000
Exposure time	200 ms
Binning	2×2
Tube lens	1×
Excitation laser	642 nm [max power 150 mW]
Laser Power	150 mW

<b>Sample settings</b>	<b>Condition</b>
Sample target	4 Corner DNA origami
Imaging buffer	1×BME and 1×GLOX
Dye	Alexa Fluor 647
NeNA localization precision	4.6 nm

**Supplementary Table 11 | Experimental conditions in Supplementary Figure 5 (tubulin)**

<b>Setting</b>	<b>Condition</b>
Microscope	liteTIRF
Objective	CFI Plan Apo Lambda 100X Oil
Camera	PCO.panda 4.2
Field of view	512×512 pixel after binning
Frames	50 000
Exposure time	200 ms
Binning	2×2
Tube lens	1×
Excitation laser	642 nm [max power 150 mW]
Laser Power	140 mW

<b>Sample settings</b>	<b>Condition</b>
Sample target	Alpha tubulin prim/sec anti body
Cell type	COS7
Imager sequence	P1
Imager concentration	1 nM
Imaging buffer	C with PCA/PCD/TX
Dye	ATTO 647N
NeNA localization precision	5.7 nm

**Supplementary Table 12 | Experimental conditions in Supplementary Figure 7 (tubulin)**

<b>Setting</b>	<b>Condition</b>
Microscope	liteTIRF
Objective	CFI Plan Apo Lambda 100X Oil
Camera	PCO.pixelfly
Field of view	696×520 pixel after binning
Frames	20 000
Exposure time	200 ms
Binning	2×2
Tube lens	1×
Excitation laser	642 nm [max power 150 mW]
Laser Power	80 mW

<b>Sample settings</b>	<b>Condition</b>
Sample target	Alpha tubulin prim/sec anti body
Cell type	HeLa
Imager sequence	X61
Imager concentration	2 nM
Imaging buffer	C with PCA/PCD/TX
Dye	ATTO 647N
NeNA localization precision	9.1 nm

**Supplementary Table 13 | Experimental conditions in Supplementary Figure 7 (TOM20)**

<b>Setting</b>	<b>Condition</b>
Microscope	liteTIRF
Objective	CFI Plan Apo Lambda 100X Oil
Camera	PCO.pixelfly
Field of view	696×520 pixel after binning
Frames	20 000
Exposure time	200 ms
Binning	2×2
Tube lens	1×
Excitation laser	642 nm [max power 150 mW]
Laser Power	80 mW

<b>Sample settings</b>	<b>Condition</b>
Sample target	TOM20 prim/sec anti body
Cell type	HeLa
Imager sequence	P1
Imager concentration	2 nM
Imaging buffer	C with PCA/PCD/TX
Dye	ATTO 647N
NeNA localization precision	6.3 nm

Supplementary Table 14 | M13mp18 p7249 sequence

TTCCCTTCCTTTCTCGCCACGTTGCGCGGCTTTCCCGTCAAGCTCTAAATCGGGGGCTCCCTTAGGGTTCCGATTTAGTGCTTTACGGCACCTGACCCCAAAAACT  
TGATTTGGGTGATGGTTCACGTAGTGGCCATCGCCCTGATAGACGGTTTTTCGCCCTTTGACGTTGGAGTCCACGTTCTTTAATAGTGGACTCTGTTCACAACTGGAA  
CAACACTCAACCCTATCTCGGGCTATCTTTTGTATTTATAAGGGATTTTGCCGATTTTCGGAACCACCATCAAAACAGGATTTTCGCCTGCTGGGGCAAACAGCGTGGACC  
GCTTGCTGCAACTCTCTCAGGGCCAGGCGGTGAAGGGCAATCAGCTGTTGCCGCTCTACTGGTGAAGAAAGAAAAACCACCCTGGCGCCCAATACGCAAACCGCCTCTCCC  
CGCGCGTTGGCCGATTCATTAATGCAGCTGGCACGACAGGTTTTCCGACTGGAAAGCGGGCAGTGAAGCGCAACGCAATTAATGTGAGTTAGCTCACTCATTAGGCACCCC  
AGGCTTTACACTTTATGCTTCCGGCTCGTATGTTGTGTGGAATTTGTGAGCGGATAACAATTTACACAGGAAACAGCTATGACCATGATTACGAATTCGAGCTCGGTACC  
CGGGGATCCTCTAGAGTCGACCTGCAGGCATGCAAGCTTGGCACTGGCCGTCGTTTTACAACGTCGTACTGGGAAAACCTGGCGTTACCCAACCTAATTCGCCCTTGACG  
CACATCCCCCTTTCCGACGCTGGCGTAATAGCGAAGAGGCCCGCACCGATCGCCCTTCCCAACAGTTGCGCAGCCTGAATGGCGAATGGCGCTTTGCCTGGTTTCCGGCA  
CCAGAAGCGGTGCCGAAAGCTGGCTGGAGTGCATCTTCTGAGGCCGATACTGTGTCGTCGCCCTCAAACCTGGCAGATGCACGGTTACGATGGCCCATCTACACC  
CGTGACCTATCCATTACGGTCAATCCGCGCTTTGTTCCACGGAATCCGACGGGTTGTTACTCGCTCACATTTAATGTTGATGAAAGCTGGCTACAGGAAGGCCAGA  
CGCGAATATTTTTGATGGCGTTCCTATTGGTTAAAAATGAGCTGATTTAACAAAAATTAATGCGAATTTAACAAAAATTAACGTTTACAATTTAAATATTTGCTT  
ATACAATCTTCTGTTTTTGGGGCTTTTCTGATTATCAACCGGGGTACATATGATTGACATGCTAGTTTTACGATTACCCTTCATCGATTCTCTGTTTGTCTCCAGACTC  
TCAGGCAATGACCTGATAGCCTTTGTAGATCTCTCAAAAAATAGTACCCTCTCCGGCATTAATTTATCAGCTAGAACGGTTGAATATCATATTTGATGGTGGATTTGACTGT  
CTCCGGCCTTTCTCACCCCTTTGAATCTTACCTACACATTACTCAGGCATTCGATTTAAAAATATATGAGGGTTCTAAAAATTTTTATCCTTGCCTGGAATAAAGGCTT  
CTCCCGCAAAAGTATTACAGGGTCATAATGTTTTTGGTACAACCGATTTAGCTTTATGCTCTGAGGCTTTATGCTTAATTTTGTCTAATTTTGCCTTGCCCTGTATGAT  
TTATTGGATGTTAATGCTACTACTATTAGTAGAATTTGATGCCACCTTTTCAGCTCGCGCCCAATGAAAAATATAGCTAAACAGGTTATTGACCATTTGCGAAATGTATC  
TAATGGTCAAATAAATCTACTCGTTCGCGAATTTGGGAATCAACTGTTATATGGAATGAAACTCCAGACACCGTACTTTAGTTGCATATTTAAACATGTTGAGCTAC  
AGCATTATATTCAGCAATTAAGCTCTAAGCCATCCGCAAAAAATGACCTCTTATCAAAAGGAGCAATTAAGGTACTCTCTAATCTGACCTGTTGGAGTTGCTTCCGGT  
CTGGTTCGCTTTGAAGCTCGAATTAACACCGCATATTTGAAGTCTTTCGGGCTTCCTTAAATCTTTTTGATGCAATCCGCTTTGCTTCTGACTATAATAGTCAGGGTAA  
AGACCTGATTTTTGATTTATGGTCATCTCGTTTTCTGAACTGTTTAAAGCATTTGAGGGGGATCAATGAATATTTATGACGATTCCGCAGTATTGGACGCTATCCAGT  
CTAAACATTTTACTATTACCCCTCTGGCAAAACTCTTTTTGCAAAAGCCTCTCGTATTTTTGTTTTATCGTCTGTTGTAACGAGGGTTATGATAGTGTGCTCTT  
ACTATGCCTCGTAATTCCTTTTGGCGTTATGTATCTGCATTAGTTGAATGTGGTATTCTTAAATCTCAACTGATGAATCTTCTACCTGTAATAATGTTGTTCCGTTAGT  
TCGTTTTTAACTAGATTTTTTCTTCCCAACGTCCTGACTGGTATAATGAGCCAGTTCTTAAATCGCATAAGGAATTCACAAATGATTAAGGTTGAAATTAACCATC  
TCAAGCCCAATTTACTACTCGTTCTGGTGTCTTCTGTCAGGGCAAGCCTTATTCACTGAATGAGCAGCTTTGTTACGTTGATTTGGGTAATGAATATCCGGTTCTTGTCA  
AGATTACTCTTGATGAAGTTCAGCCAGCCTATGCGCCTGGTCTGTACACCGTTCATCTGTCTCTTTCAAAGTTGGTCAGTTCGGTTCCCTTATGATTGACCGTCTGCGC  
CTCGTTCGGCTAAGTAACATGGAGCAGGTCGCGGATTTTCGACACAATTTATCAGGCGATGATACAAATCTCCGTTGTACTTTGTTTCGCGCTTGGTATAATCGCTGGG  
GTCAAAGATGAGTGTGTTTAGTGTATCTTTTGCCTCTTTCGTTTTAGGTTGGTGCCTTCGTAGTGGCATTACGATTTTTACCCTTTAATGAAACTTCCTCATGAAAA  
GTCTTTAGTCTCAAAGCCTCTGTAGCCGTTGCTACCCTCGTTCCGATGCTGTCTTTCGCTGCTGAGGGTGACGATCCCGCAAAAGCGGCCTTTAACTCCCTGCAAGCCT  
CAGCGACCGAATATATCGGTTATGCGTGGGCGATGGTTGTTGTCATTGTCGGCGCAACTATCGGTATCAAGCTGTTTAAAGAAATTCACCTCGAAAGCAAGCTGATAAACC  
GATACAATTAAGGCTCCTTTTGGAGCCTTTTTTTGGAGATTTTCAACGTGAAAAAATATATTTTCGCAATTCCTTTAGTTGTTCTTTCTATTCTCACTCCGCTGAAA  
CTGTTGAAAGTGTGTTAGCAAAATCCCATACAGAAAAATCATTACTAACGCTGGAAGACGACAAAACTTAGATCGTTACGCTAACATGAGGGCTGTCTGTGGAAAT  
GCTACAGGCGTTGTAGTTTGTACTGGTGACGAAACTCAGTGTACGGTACATGGGTTCCATTTGGGCTTGCTATCCCTGAAAATGAGGGTGGTGGCTCTGAGGGTGGCGG  
TTCTGAGGGTGGCGTCTGAGGGTGGCGTACTAAACCTCTGAGTACGGTATACACTATTTCCGGCTATACTTATATCAACCTCTCGACGGCACTTATCCGCTG  
GTACTGAGCAAAACCCGCTAATCCTAATCTTCTTTGAGGAGTCTCAGCCTCTAATACTTTTATGTTTTCAGATAATAGGTTCCGAAATAGGCAGGGGCACTTAACT  
GTTTATACGGGCACTGTACTCAAGGCACTGACCCGTTAAAACTTATTACCAGTACACTCCTGTATCATCAAAAGCCATGTATGACGCTTACTGGAACGGTAAATTCAG  
AGACTGCGCTTTCCATTCTGGCTTTAATGAGGATTTATTTGTTTGTGAATATCAAGGCCAATCGTCTGACCTGCCTCAACCTCCTGTCAATGCTGGCGGCGCTCTGGTG  
GTGGTCTGTTGGCGGCTCTGAGGGTGGTGGCTCTGAGGGTGGCGGCTCTGAGGGAGGCGGTTCCGGTGGTGGCTCTGTTTCCGGTGAATTTTGTAT  
TATGAAAAGATGGCAACGCTAATAAGGGGGCTATGACCGAAAAATGCCGATGAAAACGCGCTACAGTCTGACGCTAAAGGCAAACTTGATTCTGTGCTACTGATTACGG  
TGCTGCTATCGATGGTTTCAATGGTGACGTTTCCGGCCTTGCTAATGGTAATGGTGTACTGGTGAATTTGCTGGCTCTAATTCCAAATGGCTCAAGTCGGTGACGGTG  
ATAATTCACCTTTAATGAATAATTTCCGTCATAATTTACCTTCCCTCCCTCAATCGGTTGAATGTCGCCCTTTTGTCTTTGGCGCTGGTAAACCATATGAATTTTCTATT  
GATTGTGACAAAATAAACTTATCCGTGGTGTCTTTGCGTTTTTTTATATGTTGCCACCTTTATGTATGATTTTCTACGTTTGTACATACTGCGTAATAAGGAGTC  
TTAATCATGCCAGTCTTTTGGGTATTCGGTATTTATGCGTTTCCCTCGGTTCCCTCTGGTAACTTTGTTCCGGCTATCTGCTTACTTTCTTAAAAAGGGCTTCGGTAA  
GATAGCTATTGCTATTTTCATGTTTCTGCTCTTATTATGGGCTTAACTCAATCTTGTGGGTATCTCTCTGATATTAGCGCTCAATACCCTCTGACTTTGTTTCAGG  
GTGTTGAGTTAATTCCTCCGCTCAATGCGCTTCCCTGTTTTATGTTATTTCTCTCTGTAAAGGCTGCTATTTTCATTTTTGACGTTAAACAAAAATCGTTTCTATTTG  
GATTGGGATAAATAATAGGCTGTTATTTTTGTAACGGCAATTAGGCTCTGAAAGACGCTCGTTAGCGTTGGTAAAGATTCAGGATAAAATTTAGCTGGGTGCAAAA  
TAGCAACTAATCTGATTTAAGGCTTCAAAACCTCCCGCAAGTCGGGAGGTTGCTTAAACGCCTCCGCTTCTAGAAATACCGGATAAGCCTTCTATATCTGATTTGCTT  
GCTATTTGGGCGCGGTAATGATTCCTACGATGAAAATAAAACGGCTGCTGTTGTTCTCGATGAGTGGTACTTTGGTTTAAATACCGCTTCTTGAATGATAAGGAAAGACA  
GCCGATTATTGATTGGTTTCTACATGCTCGTAAATTAGGATGGGATATATTTTTCTGTTTCAGGACTTATCTATTGTTGATAACAGGCGGCTTCTGCATTAGCTGAAC

```

ATGTTGTTTATTGTCGTCGTCCTGGACAGAATTACTTTACCTTTTGTGCGTACTTTATATTCTCTTATTACTGGCTCGAAAATGCCTCTGCCTAAATTACATGTTGGCGTT
GTTAAATATGGCGATTCTCAATTAAGCCCTACTGTTGAGCGTTGGCTTTATACTGGTAAGAATTTGTATAACGCATATGATACTAAACAGGCTTTTCTAGTAATTATGA
TTCCGGTGTATTATTCTATTAAACGCCTTATTTATCACACGGTGGTATTTCAAACCATTAATTTAGGTCAGAAGATGAAATTAACATAAATATATTTGAAAAAGTTT
CTCGCGTTCTTTGTCTTGGCATTGGATTGCATCAGCATTACATATAGTTATATAACCCAACTAAGCCGGAGGTAAAAAGGTAGTCTCTCAGACCTATGATTTTGTAT
AAATTCATATTGACTCTTCTCAGCGTCTTAATCTAAGCTATCGCTATGTTTTCAAGGATTCTAAGGGAAAAATTAATTAATAGCGACGATTTACAGAAGCAAGGTTATTC
ACTCACATATATTGATTTATGTACTGTTCCATTAAAAAAGGTAATCAAATGAAATGTTAAATGTAATTAATTTGTTTTCTTGATGTTTGTTCATCATCTCTTTT
GCTCAGGTAATGAAATGAATAATTCGCCTCTGCGCATTTTGTAACTTGGTATTCAAAGCAATCAGGCGAATCCGTTATTGTTTCTCCCGATGTAAGGTTACTGTTAC
TGTATATTCATCTGACGTTAAACCTGAAAATCTACGCAATTTCTTTATTTCTGTTTTACGTGCAATAATTTTGATATGGTAGGTTCTAACCTTCCATTATTCAGAAGT
ATAATCCAAACAATCAGGATTATATTGATGAATTGCCATCATCTGATAATCAGGAATATGATGATAATTCGGCTCCTTCTGGTGGTTTCTTTGTTCCGCAAAATGATAAT
GTTACTCAAACCTTTTAAATTAACAGTTCGGGCAAAGGATTAATACGAGTTGTCGAATGTTTGTAAAGTCTAATACTTCAAATCCTCAAATGTATTATCTATTGA
CGGCTCTAATCTATTAGTTGTTAGTGCTCTAAAGATATTTAGATAACCTTCTCAAATCCTTCAACTGTTGATTGCGCAACTGACCAGATATTGATTGAGGGTTTGA
TATTTGAGGTTACAGCAAGGTGATGCTTTAGATTTTTCATTTGCTGCTGGCTCTCAGCGTGGCAGTGTTCAGGCGGTGTTAATACTGACCCTCACCTCTGTTTTATCT
TCTGCTGGTGGTTCGTTCCGATTTTTAATGGCGATGTTTTAGGGCTATCAGTTCGCGCATTAAGACTAATAGCCATTCAAAAATATTGCTGTGCCAGTATTCTTAC
GCTTTCAGGTCAGAAGGTTCTATCTGTGGCCAGAAATGCCCTTTTATTACTGGTCTGTGACTGGTGAATCTGCCAATGTAATAATCCATTTCAGACGATTGAGC
GTCAAAATGTAGGTAATTTCCATGAGCGTTTTTCTGTTGCAATGGCTGGCGGTAATATTGTTCTGGATATTACCAGCAAGGCCGATAGTTT

```

**Supplementary Table 15 | Rectangular DNA origami staple strands**

Position	Name	Sequence
A1	21[32]23[31]BLK	TTTTCACTCAAAGGGCGAAAACCATCACC
B1	23[32]22[48]BLK	CAAATCAAGTTTTTTGGGGTCGAAACGTGGA
C1	21[56]23[63]BLK	AGCTGATTGCCCTTCAGAGTCCACTATTAAGGGTGCCGT
D1	23[64]22[80]BLK	AAAGCACTAAATCGGAACCTTAATCCAGTT
E1	21[96]23[95]BLK	AGCAAGCGTAGGGTTGAGTGTGTAGGGAGCC
F1	23[96]22[112]BLK	CCCGATTTAGAGCTTGACGGGGAAAAAGAATA
G1	21[120]23[127]BLK	CCCAGCAGCGGAAAAATCCCTTATAAATCAAGCCGGCG
H1	21[160]22[144]BLK	TCAATATCGAACCTCAAATATCAATTCGAAA
I1	23[128]23[159]BLK	AACGTGGCGAGAAAGGAAGGAAACCAGTAA
J1	23[160]22[176]BLK	TAAAAGGGACATTTCTGGCCAACAAAGCATC
K1	21[184]23[191]BLK	TCAACAGTTGAAAGGAGCAATGAAAAATCTAGAGATAGA
L1	23[192]22[208]BLK	ACCCTTCTGACCTGAAAGCGTAAGACGCTGAG
M1	21[224]23[223]BLK	CTTTAGGGCTGCAACAGTGCCAATACGTG
N1	23[224]22[240]BLK	GCACAGACAATATTTTGAATGGGGTCAGTA
O1	21[248]23[255]BLK	AGATTAGAGCCGTCAAAAAACAGAGGTGAGGCCATTAGT
P1	23[256]22[272]BLK	CTTTAATGCGCGAACTGATAGCCCCACCAG
A2	19[32]21[31]BLK	GTCGACTTCGGCCAACGCGCGGGGTTTTTC
B2	22[47]20[48]BLK	CTCCAACGCAGTGAGACGGGCAACCAGCTGCA
D2	22[79]20[80]BLK	TGGAACAACCGCTGGCCCTGAGGCCCGCT
E2	19[96]21[95]BLK	CTGTGTGATTGCGTTGCGCTCACTAGAGTTGC
F2	22[111]20[112]BLK	GCCCGAGAGTCCAGCTGGTTTGACAGCTAACT
H2	19[160]20[144]BLK	GCAATTCACATATTCCTGATTATCAAAGTGTA
I2	22[143]21[159]BLK	TCGGCAAATCCTGTTTGTGATGGTGACCCTCAA
J2	22[175]20[176]BLK	ACCTTGCTTGGTCAGTTGGCAAAGAGCGGA

L2	22[207]20[208]BLK	AGCCAGCAATTGAGGAAGGTTATCATCATTTT
M2	19[224]21[223]BLK	CTACCATAGTTTGTAGTAACATTTAAAAATAT
N2	22[239]20[240]BLK	TTAACACCAGCACTAACAACATAATCGTTATTA
P2	22[271]20[272]BLK	CAGAAGATTAGATAATACATTTGTCGACAA
A3	17[32]19[31]BLK	TGCATCTTTCCAGTCACGACGGCCTGCAG
B3	20[47]18[48]BLK	TTAATGAACTAGAGGATCCCCGGGGGTAACG
D3	20[79]18[80]BLK	TTCCAGTCGTAATCATGGTCATAAAAAGGG
E3	17[96]19[95]BLK	GCTTTCGGATTACGCCAGCTGGCGGCTGTTTC
F3	20[111]18[112]BLK	CACATTAATAATGTTATCCGCTCATGCGGGCC
H3	17[160]18[144]BLK	AGAAAACAAAGAAGATGATGAAACAGGCTGCG
I3	20[143]19[159]BLK	AAGCCTGGTACGAGCCGGAAGCATAGATGATG
J3	20[175]18[176]BLK	ATTATCATTCATATAATCCTGACAATTAC
L3	20[207]18[208]BLK	GCGGAACATCTGAATAATGGAAGGTACAAAAT
M3	17[224]19[223]BLK	CATAAATCTTTGAATACCAAGTGTAGAAC
N3	20[239]18[240]BLK	ATTTTAAATCAAATATTTGCACGGATTGCG
P3	20[271]18[272]BLK	CTCGTATTAGAAAATTGCGTAGATACAGTAC
A4	15[32]17[31]BLK	TAATCAGCGGATTGACCGTAATCGTAACCG
B4	18[47]16[48]BLK	CCAGGGTTGCCAGTTTGTAGGGGACCCGTGGGA
C4	15[64]18[64]BLK	GTATAAGCCAACCCGTCGGATTCTGACGACAGTATCGGCCCAAGGCG
D4	18[79]16[80]BLK	GATGTGCTTCAGGAAGATCGCACAAATGTGA
E4	15[96]17[95]BLK	ATATTTTGGCTTTCATCAACATTTATCCAGCCA
F4	18[111]16[112]BLK	TCTTCGCTGCACCGCTTCTGGTGCAGCCTTCC
G4	15[128]18[128]BLK	TAAATCAAATAATTCGCGTCTCGGAAACCAGGCAAAGGGAAGG
H4	15[160]16[144]BLK	ATCGCAAGTATGTAATGCTGATGATAGGAAC
I4	18[143]17[159]BLK	CAACTGTTGCGCCATTCGCCATTCAAACATCA
J4	18[175]16[176]BLK	CTGAGCAAAAATTAATTACATTTTGGGTTA
K4	15[192]18[192]BLK	TCAAATATAACCTCCGGCTTAGGTAACAATTTTCATTTGAAGCGAATT
L4	18[207]16[208]BLK	CGCGCAGATTACCTTTTTTAATGGGAGAGACT
M4	15[224]17[223]BLK	CCTAAATCAAATCATAGGTCTAAACAGTA
N4	18[239]16[240]BLK	CCTGATTGCAATATATGTGAGTATCAATAGT
O4	15[256]18[256]BLK	GTGATAAAAAGACGCTGAGAAGAGATAACCTTGCTTCTGTTCCGGGAGA
P4	18[271]16[272]BLK	CTTTTACAAAATCGTCGCTATTAGCGATAG
A5	13[32]15[31]BLK	AACGCAAAATCGATGAACGGTACCGGTTGA
B5	16[47]14[48]BLK	ACAAACGGAAAAGCCCCAAAAACACTGGAGCA
C5	13[64]15[63]BLK	TATATTTTGTCAATTGCCTGAGAGTGAAGATT
D5	16[79]14[80]BLK	GCGAGTAAAAATATTTAAATTGTTACAAAAG
E5	13[96]15[95]BLK	TAGGTAAACTATTTTTGAGAGATCAAACGTTA
F5	16[111]14[112]BLK	TGTAGCCATTAATAATTCGCATTAATGCCGGA
G5	13[128]15[127]BLK	GAGACAGCTAGCTGATAAATAATTTTTTGT
H5	13[160]14[144]BLK	GTAATAAGTTAGGCAGAGGCATTTATGATATT
I5	16[143]15[159]BLK	GCCATCAAGCTCATTTTTTAACCACAAATCCA
J5	16[175]14[176]BLK	TATAACTAACAAGAACGCGAGAACGCCAA

K5	13[192]15[191]BLK	GTAAGTAATCGCCATATTTAACAAAACCTTTT
L5	16[207]14[208]BLK	ACCTTTTTATTTTAGTTAATTTTCATAGGGCTT
M5	13[224]15[223]BLK	ACAACATGCCAACGCTCAACAGTCTTCTGA
N5	16[239]14[240]BLK	GAATTTATTTAATGGTTTGAATATTTCTTACC
O5	13[256]15[255]BLK	GTTTATCAATATGCGTTATACAACCGACCGT
P5	16[271]14[272]BLK	CTTAGATTTAAGGCGTTAAATAAAGCCTGT
A6	11[32]13[31]BLK	AACAGTTTTGTACCAAAAACATTTTATTTT
B6	14[47]12[48]BLK	AACAAGAGGGATAAAAATTTTAGCATAAAGC
C6	11[64]13[63]BLK	GATTTAGTCAATAAAGCCTCAGAGAACCCTCA
D6	14[79]12[80]BLK	GCTATCAGAAATGCAATGCCTGAATTAGCA
E6	11[96]13[95]BLK	AATGGTCAACAGGCAAGGCAAGAGTAATGTG
F6	14[111]12[112]BLK	GAGGGTAGGATTCAAAAGGGTGAGACATCCAA
G6	11[128]13[127]BLK	TTTGGGGATAGTAGTAGCATTAAAAGGCCG
H6	11[160]12[144]BLK	CCAATAGCTCATCGTAGGAATCATGGCATCAA
I6	14[143]13[159]BLK	CAACCGTTTCAAATCACCATCAATTCGAGCCA
J6	14[175]12[176]BLK	CATGTAATAGAATATAAAGTACCAAGCCGT
K6	11[192]13[191]BLK	TATCCGGTCTCATCGAGAACAAGCGACAAAAG
L6	14[207]12[208]BLK	AATTGAGAATTCTGTCCAGACGACTAAACCAA
M6	11[224]13[223]BLK	GCGAACCTCCAAGAACGGGTATGACAATAA
N6	14[239]12[240]BLK	AGTATAAAGTTCAGCTAATGCAGATGTCTTTC
O6	11[256]13[255]BLK	GCCTTAAACCAATCAATAATCGGCACGCGCCT
P6	14[271]12[272]BLK	TTAGTATCACAATAGATAAGTCCACGAGCA
A7	9[32]11[31]BLK	TTTACCCCAACATGTTTTAAATTTCCATAT
B7	12[47]10[48]BLK	TAAATCGGGATTCCTAATCTGCGATATAATG
C7	9[64]11[63]BLK	CGGATTGCAGAGCTTAATGTGTAACGAGTA
D7	12[79]10[80]BLK	AAATTAAGTTGACCATTAGATACTTTTGCG
E7	9[96]11[95]BLK	CGAAAGACTTTGATAAGAGGTCATATTTTCGCA
F7	12[111]10[112]BLK	TAAATCATATAACCTGTTTAGCTAACCTTTAA
G7	9[128]11[127]BLK	GCTTCAATCAGGATTAGAGAGTTATTTTCA
H7	9[160]10[144]BLK	AGAGAGAAAAAATGAAAATAGCAAGCAAAC
I7	12[143]11[159]BLK	TTCTACTACGCGAGCTGAAAAGGTTACCGCGC
J7	12[175]10[176]BLK	TTTTATTTAAGCAAAATCAGATATTTTTTGT
K7	9[192]11[191]BLK	TTAGACGGCCAATAAGAAACGATAGAAGGCT
L7	12[207]10[208]BLK	GTACCGCAATTCTAAGAACGCGAGTATTATTT
M7	9[224]11[223]BLK	AAAGTCACAAAATAAACAGCCAGCGTTTTA
N7	12[239]10[240]BLK	CTTATCATTCCTGACTTGCGGGAGCCTAATTT
O7	9[256]11[255]BLK	GAGAGATAGAGCGTCTTCCAGAGGTTTGAA
P7	12[271]10[272]BLK	TGTAGAAATCAAGATTAGTTGCTCTTACCA
A8	7[32]9[31]BLK	TTTAGGACAAATGCTTTAAACAATCAGGTC
B8	10[47]8[48]BLK	CTGTAGCTTGACTATTATAGTCAGTTCATTGA
C8	7[56]9[63]BLK	ATGCAGATACATAACGGGAATCGTCATAAATAAGCAAAG
D8	10[79]8[80]BLK	GATGGCTTATCAAAAAGATTAAGAGCGTCC

E8	7[96]9[95]BLK	TAAGAGCAAATGTTTAGACTGGATAGGAAGCC
F8	10[111]8[112]BLK	TTGCTCCTTCAAATATCGCGTTTGAGGGGGT
G8	7[120]9[127]BLK	CGTTTACCAGACGACAAAGAAGTTTGCCATAATTCGA
H8	7[160]8[144]BLK	TTATTACGAAGAACTGGCATGATTGCGAGAGG
I8	10[143]9[159]BLK	CCAACAGGAGCGAACCAGACCGGAGCCTTTAC
J8	10[175]8[176]BLK	TTAACGTCTAACATAAAAAACAGGTAACGGA
K8	7[184]9[191]BLK	CGTAGAAAATACATACCGAGGAAACGCAATAAGAAGCGCA
L8	10[207]8[208]BLK	ATCCCAATGAGAATTAACGAACAGTTACCAG
M8	7[224]9[223]BLK	AACGCAAAGATAGCCGAACAAACCTGAAC
N8	10[239]8[240]BLK	GCCAGTTAGAGGGTAATTGAGCGCTTTAAGAA
O8	7[248]9[255]BLK	GTTTTATTTGTGTCACAATCTTACCGAAGCCCTTTAATATCA
P8	10[271]8[272]BLK	ACGCTAACACCACAAGAATTGAAAAATAGC
A9	5[32]7[31]BLK	CATCAAGTAAAACGAACTAACAGAGTTGAGA
B9	8[47]6[48]BLK	ATCCCCCTATACCACATTCAACTAGAAAAATC
D9	8[79]6[80]BLK	AATACTGCCCAAAGGAATTACGTGGCTCA
E9	5[96]7[95]BLK	TCATTCAGATGCGATTTTAAGAACAGGCATAG
F9	8[111]6[112]BLK	AATAGTAAACACTATCATAACCCCTCATGTGA
H9	5[160]6[144]BLK	GCAAGGCCTCACCAGTAGCACCATGGGCTTGA
I9	8[143]7[159]BLK	CTTTTGCAGATAAAAAACAAAATAAAGACTCC
J9	8[175]6[176]BLK	ATACCCAACAGTATGTTAGCAAATTAGAGC
L9	8[207]6[208]BLK	AAGGAAACATAAAGGTGGCAACATTATCACCG
M9	5[224]7[223]BLK	TCAAGTTTCATTAAGGTGAATATAAAAAGA
N9	8[239]6[240]BLK	AAGTAAGCAGACACCACGGAATAATATTGACG
P9	8[271]6[272]BLK	AATAGCTATCAATAGAAAATTCACATTCA
A10	3[32]5[31]BLK	AATACGTTTGAAGAGGACAGACTGACCTT
B10	6[47]4[48]BLK	TACGTTAAAGTAATCTTGACAAGAACCGAAC
D10	6[79]4[80]BLK	TTATACCACCAAATCAACGTAACGAACGAG
E10	3[96]5[95]BLK	ACACTCATCCATGTTACTTAGCCGAAAGCTGC
F10	6[111]4[112]BLK	ATTACCTTTGAATAAGGCTTGCCCAAATCCGC
H10	3[160]4[144]BLK	TTGACAGGCCACCACCAGAGCCGCGATTTGTA
I10	6[143]5[159]BLK	GATGGTTTGAACGAGTAGTAAATTTACCATTA
J10	6[175]4[176]BLK	CAGCAAAAGGAAACGTCACCAATGAGCCGC
L10	6[207]4[208]BLK	TCACCGACGCACCGTAATCAGTAGCAGAACCG
M10	3[224]5[223]BLK	TTAAAGCCAGAGCCGCCACCTCGACAGAA
N10	6[239]4[240]BLK	GAAATTATTGCCTTTAGCGTCAGACCGGAACC
P10	6[271]4[272]BLK	ACCGATTGTCGGCATTTCGGTCATAATCA
A11	1[32]3[31]BLK	AGGCTCCAGAGGCTTTGAGGACACGGGTAA
B11	4[47]2[48]BLK	GACCAACTAATGCCACTACGAAGGGGGTAGCA
C11	1[64]4[64]BLK	TTTATCAGGACAGCATCGGAACGACACCAACCTAAAACGAGGTCAATC
D11	4[79]2[80]BLK	GCGCAGACAAGAGGCAAAAAGAAATCCCTCAG
E11	1[96]3[95]BLK	AAACAGCTTTTTGCGGGATCGTCAACACTAAA
F11	4[111]2[112]BLK	GACCTGCTCTTTGACCCCAAGCGAGGGAGTTA

G11	1[128]4[128]BLK	TGACAACCTCGCTGAGGCTTGCATTATAACCAAGCGCGATGATAAA
H11	1[160]2[144]BLK	TTAGGATTGGCTGAGACTCCTCAATAACCGAT
I11	4[143]3[159]BLK	TCATCGCCAACAAAGTACAACGGACGCCAGCA
J11	4[175]2[176]BLK	CACCAGAAAGGTTGAGGCAGGTCATGAAAAG
K11	1[192]4[192]BLK	GCGGATAACCTATTATTCTGAAACAGACGATTGGCCTTGAAGAGCCAC
L11	4[207]2[208]BLK	CCACCCTCTATTACAAAACAAATACCTGCCTA
M11	1[224]3[223]BLK	GTATAGCAAACAGTTAATGCCCAATCCTCA
N11	4[239]2[240]BLK	GCCCTCCCTCAGAATGGAAAGCGCAGTAACAGT
O11	1[256]4[256]BLK	CAGGAGTGGGGTTCAGTGCCTTGAGTCTCTGAATTTACCGGAACCAG
P11	4[271]2[272]BLK	AAATCACCTTCCAGTAAGCGTCAGTAATAA
A12	0[47]1[31]BLK	AGAAAGGAACAACATAAAGGAATTCAAAAAA
B12	2[47]0[48]BLK	ACGGCTACAAAAGGAGCCTTTAATGTGAGAAT
C12	0[79]1[63]BLK	ACAACCTTCAACAGTTTCAGCGGATGTATCGG
D12	2[79]0[80]BLK	CAGCGAAACTTGCTTTCGAGGTGTGCTAA
E12	0[111]1[95]BLK	TAAATGAATTTTCTGTATGGGATTAATTTCTT
F12	2[111]0[112]BLK	AAGGCCGCTGATACCGATAGTTGCGACGTTAG
G12	0[143]1[127]BLK	TCTAAAGTTTTGTCGTCTTTCAGCCGACAA
H12	0[175]0[144]BLK	TCCACAGACAGCCCTCATAGTTAGCGTAACGA
I12	2[143]1[159]BLK	ATATTCGGAACCATCGCCACGCAGAGAAGGA
J12	2[175]0[176]BLK	TATTAAGAAGCGGGTTTTGCTCGTAGCAT
K12	0[207]1[191]BLK	TCACCAGTACAACTACAACGCCTAGTACCAG
L12	2[207]0[208]BLK	TTTCGGAAGTGCCGTCGAGAGGGTGAGTTTCG
M12	0[239]1[223]BLK	AGGAACCCATGTACCGTAACACTTGATATAA
N12	2[239]0[240]BLK	GCCCGTATCCGGAATAGGTGTATCAGCCCAAT
O12	0[271]1[255]BLK	CCACCCTCATTTCAGGGATAGCAACCGTACT
P12	2[271]0[272]BLK	GTTTTAACTTAGTACCGCCACCCAGAGCCA

**Supplementary Table 16 | Biotinylated staple strands**

Position	Name	Sequence	Modification
C02	18[63]20[56]BIOTIN	ATTAAGTTTACCGAGCTCGAATTCGGGAACTGTCTGTC	5' - Biotin
C09	4[63]6[56]BIOTIN	ATAAGGGAACCGGATATTCATTACGTGAGGACGTTGGGAA	5' - Biotin
G02	18[127]20[120]BIOTIN	GCGATCGGCAATTCACACAACAGGTGCCTAATGAGTG	5' - Biotin
G09	4[127]6[120]BIOTIN	TTGTGTCGTGACGAGAAACACCAATTTCAACTTTAAT	5' - Biotin
K02	18[191]20[184]BIOTIN	ATTCATTTTGTGTTGGATTATACTAAGAAACCACCAGAAG	5' - Biotin
K09	4[191]6[184]BIOTIN	CACCCTCAGAAACCATCGATAGCATTGAGCCATTTGGGAA	5' - Biotin
O02	18[255]20[248]BIOTIN	AACAATAACGTAAAACAGAAATAAAAATCCTTTGCCCGAA	5' - Biotin
O09	4[255]6[248]BIOTIN	AGCCACCCTGTAGCGGTTTTCAAGGAGGGAAGGTAAA	5' - Biotin

**Supplementary Table 17 | DNA-PAINT docking site sequences**

Name	Sequence	Modification
X61 docking strand	TTTCCTCAATTA	-
P1 docking strand	TTATACATCTA	-
P3 docking strand	TTTCTTCATTA	-

**Supplementary Table 18 | DNA-PAINT imager sequences**

Name	Sequence	Modification
Imager X61	TAATTGAGGA	3' – ATTO 647N
Imager P1	CTAGATGTAT	3' – ATTO 647N
Imager P3	GTAATGAAGA	3' – ATTO 647N

**Supporting Information**

nanoTRON: a Picasso module for MLP-based classification of  
super-resolution data

BY

Alexander Auer, Maximilian T. Strauss, Sebastian Strauss, and Ralf Jungmann

PUBLISHED IN

*Bioinformatics*, (2020), *in press*.  
doi: 10.1093/bioinformatics/btaa154

The accepted version of the manuscript is reprinted from ref. [3].  
CC-BY-NC 4.0



# nanoTRON: a Picasso module for MLP-based classification of super-resolution data

Alexander Auer<sup>1,2</sup>, Maximilian T. Strauss<sup>2</sup>, Sebastian Strauss<sup>1,2</sup>, and Ralf Jungmann<sup>1,2,\*</sup>

<sup>1</sup>Department of Physics and Center for Nanoscience, Ludwig Maximilian University, Munich, Germany. <sup>2</sup>Max Planck Institute of Biochemistry, Martinsried, Germany.

\*Email: [jungmann@biochem.mpg.de](mailto:jungmann@biochem.mpg.de), Phone: +49 89 8578 3410

## Content

<b>Supplementary Text 1</b>	Exemplary Workflow with nanoTRON
<b>Supplementary Text 2</b>	Example application with DNA origami
<b>Supplementary Text 3</b>	Example application with DNA origami and nuclear pore complexes
<b>Supplementary Text 4</b>	Recommendations and limitations of nanoTRON
<b>Supplementary Figure 1</b>	Overview DNA origami design
<b>Supplementary Figure 2</b>	Graphical user interface
<b>Supplementary Figure 3</b>	Training data generation and augmentation
<b>Supplementary Figure 4</b>	Overview of training set <i>Digit 1</i>
<b>Supplementary Figure 5</b>	Overview of training set <i>Digit 2</i>
<b>Supplementary Figure 6</b>	Overview of training set <i>Digit 3</i>
<b>Supplementary Figure 7</b>	Overview of training set <i>20-nm-grid</i>
<b>Supplementary Figure 8</b>	Overview of training set Nup96
<b>Supplementary Figure 9</b>	Exemplary rendering of one pick of the <i>20-nm-grid</i> training set
<b>Supplementary Figure 10</b>	Model parameter tuning of the numbers of nodes in the 1-layer network
<b>Supplementary Figure 11</b>	Training and test score with different training set sizes using the 1-layer network
<b>Supplementary Figure 12</b>	Proof-of-concept experiment with biological target
<b>Supplementary Table 1</b>	Experimental conditions training set <i>Digit 1</i>
<b>Supplementary Table 2</b>	Experimental conditions in training set <i>Digit 2</i>
<b>Supplementary Table 3</b>	Experimental conditions training set <i>Digit 3</i>
<b>Supplementary Table 4</b>	Experimental conditions in training set <i>20-nm-grid</i>
<b>Supplementary Table 5</b>	Experimental conditions in validation set
<b>Supplementary Table 6</b>	M13mp18 p7249 sequence
<b>Supplementary Table 7</b>	Rectangular DNA origami staple strands
<b>Supplementary Table 8</b>	Biotinylated staple strands
<b>Supplementary Table 9</b>	DNA-PAINT docking site sequences

<b>Supplementary Table 10</b>	DNA-PAINT imager sequences
<b>Supplementary Table 11</b>	Training runtime comparison with various computers
<b>Supplementary Table 12</b>	Prediction runtime comparison with various computers
<b>Supplementary Table 13</b>	nanoTRON MLP compared with LeNet-5 CNN
<b>Supplementary Table 14</b>	LeNet-5 CNN Design
<b>Materials and buffers</b>	
<b>Optical setups</b>	
<b>DNA origami self-assembly</b>	
<b>Nanobody conjugation</b>	
<b>Super-resolution DNA-PAINT imaging with DNA origami</b>	
<b>Super-resolution DNA-PAINT imaging with nuclear pore complex</b>	
<b>Super-resolution reconstruction</b>	
<b>References</b>	

## Supplementary Text 1 | Exemplary Workflow with nanoTRON

### nanoTRON Train

- (1) **Collecting training data:** Training data can be either generated with dedicated experiments for every class, or already existing data for the nanopatterns can be utilized. In any case, training data for every class should be gathered.

Tip: Picasso command-line tool `Picasso csv2hdf` allows the conversion from ThunderSTORM .csv localization tables to the Picasso format.

- (2) **Selecting nanopattern:** After spot identification and localization using Picasso *Localize* was performed, one can visualize and, if necessary, drift correct the localization files in Picasso *Render*. Using the *Pick Tool* the nanopattern can be selected manually. Another function called *Pick Similar* provides an automated solution for picking patterns in the whole field of view. Therefore, one selects a few nanopatterns manually by hand and applies *Pick Similar*. It utilizes the predictable blinking kinetics of DNA-PAINT and selects regions with similar number of localizations in areas of the size of the pick diameter. Every pick gets assigned with a group id, see **Supplementary Figure 3a**. The picked localizations can be saved using *File* → *Save picked localizations*.
- (3) **Setting up nanoTRON Train:** If training data for every picked nanopattern is available, the training files can be loaded into the module nanoTRON *Train*, see **Supplementary Figure 2a**. First, the number of unique patterns needs to be set. In the box *Training Files*, all the files can be loaded and assigned with a class name. If necessary, the oversampling parameter can be modified, see **Supplementary Figure 3b**. *Expand Training Set* can be enabled to leverage the training data by augmentation, see **Supplementary Figure 3c**. After the image parameters are set up, *Prepare Data* converts the localization tables into grayscale images, see **Supplementary Figure 3b** and **Supplementary Figure 9**. In the box *Perceptron*, the neural network can be tuned. See the exemplary application described in **Supplementary Text 2** for more details on this step.

Attention: nanoTRON Train does not allow for duplicated class names. Every class needs to be assigned with a unique class name for the model.

Tip: With *Export Image Subset* ten images of every class can be exported. They are saved in the training file path.

- (4) **Training:** After the perceptron is set up accordingly, the training can be started with the button *Train*. The runtime of training can take up to hours, see **Supplementary Table 11** for a comparison between different hardware configurations. When the training has finished, the learning curve and confusion matrix can be inspected with *Show Learning Curve*. Using *Save Model*, the trained neural network can be saved for later use.

### nanoTRON Predict

- (1) **Collecting target data:** After the target data is processed with Picasso *Localize*, the nanopatterns are selected in Picasso *Render* using the *Pick Tool*, as described in the section *Selecting nanopattern for training*.
- (2) **Prediction:** The grouped localization file can be loaded into nanoTRON *predict* via drag and drop or *File* → *Open*. The corresponding model can be imported via *Tools* → *Load model*. All available classes for prediction are listed in the box *Export Structures*. The prediction is started with the button *Predict*.
- (3) **Export:** After the prediction finished, the classified nanopatterns can be exported in separate files. All nanopatterns, which should be exported, can be selected in the box *Export Structures*. Finally, nanoTRON exports all selected nanopatterns using the button *Export*.

Tip: With *Filter Probabilities*, the classified nanopattern can be filtered according to the prediction score.

Tip: With *Export Pick Regions*, a table of pick regions can be exported additionally to the localization tables.

Attention: The option *Regroup Export Files* reassigns the picks with new group ids for every exported file. The group ids before prediction do not correspond to the reassigned group ids.

### **Supplementary Text 2 | Example application with DNA origami.**

As a proof-of-concept demonstration, we acquired five DNA-PAINT (Jungmann, et al., 2010) super-resolution example data sets, each containing DNA origami (Rothemund, 2006). Four data sets display a unique DNA origami pattern of digits 1 to 3 or a 3×4-grid-structure with 20-nm-spacing, **Figure 1a** and **Supplementary Figure 4-7**. A subsequent acquisition with all four DNA origami designs in a single sample serves as a validation data set, **Figure 1b**. Imaging conditions are described in **Supplementary Table 1-5**, DNA origami design sequences are listed in **Supplementary Table 6-10**.

Using a 1-hidden-layer perceptron with 550 nodes and *ReLU* (Hahnloser, et al., 2000; He, et al., 2015) activation function and *adam* solver (Kingma, 2014), we could achieve a training accuracy of ~ 99%, test accuracy of ~ 98% and a validation accuracy ~ 94%, **Figure 1c** and **Supplementary Figure 10**. In the validation set, unidentifiable structures caused e.g. by structure misfolding, clustering, or loose attachment to the surface, were manually selected and excluded from the validation.

### **Supplementary Text 3 | Example application with DNA origami and nuclear pore complexes.**

As a proof-of-concept demonstration for the applicability with biological samples, we generated an artificially merged DNA-PAINT super-resolution data set, displayed in **Supplementary Figure 12**. It contains the validation data set with the DNA origami structures (digits 1-3 and the 3×4-grid-structure with 20-nm-spacing) of **Figure 1c** and biological DNA-PAINT super-resolution data of the GFP-tagged nuclear pore complex (NPC) protein Nup96. The artificial data set was generated in the following way, that a mask of the NUP96 related area of a 512 × 512 px super-resolution image the NUP96 experiment was created using *Picasso: Mask*, available in *Picasso Render*. The mask was then applied to the 512 × 512 px DNA origami validation image so that the Nup96 related areas were cleared of DNA origami localizations. Using the command-line function *picasso join file1 file2* the Nup96 localization file and the masked DNA origami localization file were combined. The artificial localization file was then loaded into *Picasso Render* and a few nuclear pore complexes and DNA origami were selected manually with the *Pick Tool*. Afterward, the whole image was screened for nuclear pore complexes and DNA origami with the automation picking tool *Pick Similar*, resulting in 12681 picks. For the classification of the DNA origami and NPCs, we used the four training sets of the DNA origami, **Supplementary Figures 4-7**, and one additional DNA-PAINT recording of the NUP96 labeled nuclear pore complex shown in **Supplementary Figure 8**. The trained model for the five classes achieved 99% training and 98% test accuracy. The neural network design was used as described in **Supplementary Text 2**. Oversampling was set to 40 and pick diameter to 1.5 px, resulting in grayscale images of 60 × 60 px size.

### **Supplementary Text 4 | Recommendations and limitations of nanoTRON.**

To make nanoTRON useful as a standard tool in data analysis, we here provide a few recommendations for best practices. Successful classification strongly depends on the quality of the training and the training data (Belthangady and Royer, 2019). Like every deep learning framework, nanoTRON has limitations in performance and usage. To best prepare the user, we want to comment on a few limitations and mitigation approaches.

## Recommendations

**Training data size:** The training set should contain a sufficient number of picks in every class. We recommend at least 200 picks per class, see **Supplementary Figure 11**. If possible, higher number of picks per class is favourable.

**Balanced data sets:** The whole training set should be balanced, meaning that the number of picks in every class should be similar. Unbalanced training sets can cause training and prediction artefacts.

**Data set augmentation:** For training, we always recommend the data augmentation option *Expand training set*. Increasing the number of training data by rotations yields higher training and test accuracy, see **Supplementary Figure 11**.

**Neural network design:** For the classification of nanopatterns similar to the examples in **Supplementary Text 1** and **Supplementary Text 2**, we propose to use a comparable layer design: 1 layer with 550 nodes and ReLU as activation function, see **Supplementary Figure 10** for more details.

**Hyper parameter testing:** We recommend testing different configurations for hyperparameters, like the number of layer and nodes, activation function etc. for training to achieve the best performing model.

**Image configuration:** The parameter oversampling depends on the resolution of the super-resolution data. In combination with the pick diameter, an image input size of 40–60 px should be ideal. We suggest using lower oversampling as the resolution of the super-resolution data would provide.

**Validation experiments:** We want to stress that new models should not be trusted “blindly”. Validation experiments should be made to understand the applicability and limitations of the trained model.

## Limitations

**Computation time:** In principle, there is no limitation in the size of the nanopatterns. However, increasing the size (pick diameter) with constant oversampling will also increase the image size and therefore computation time. Runtimes of training can last up to hours and days for very large nanopatterns.

**Computation resources:** We recommend  $\geq 16$ GB RAM for training with nanoTRON.

**Discovery:** nanoTRON will not discover new nanopatterns in the prediction data set. Structures, which were not included in training will be incorrectly classified. Therefore, for every unique nanopattern one needs to prepare training data and include that into the model.

**Model size:** nanoTRON Train GUI is limited to 10 different classes.

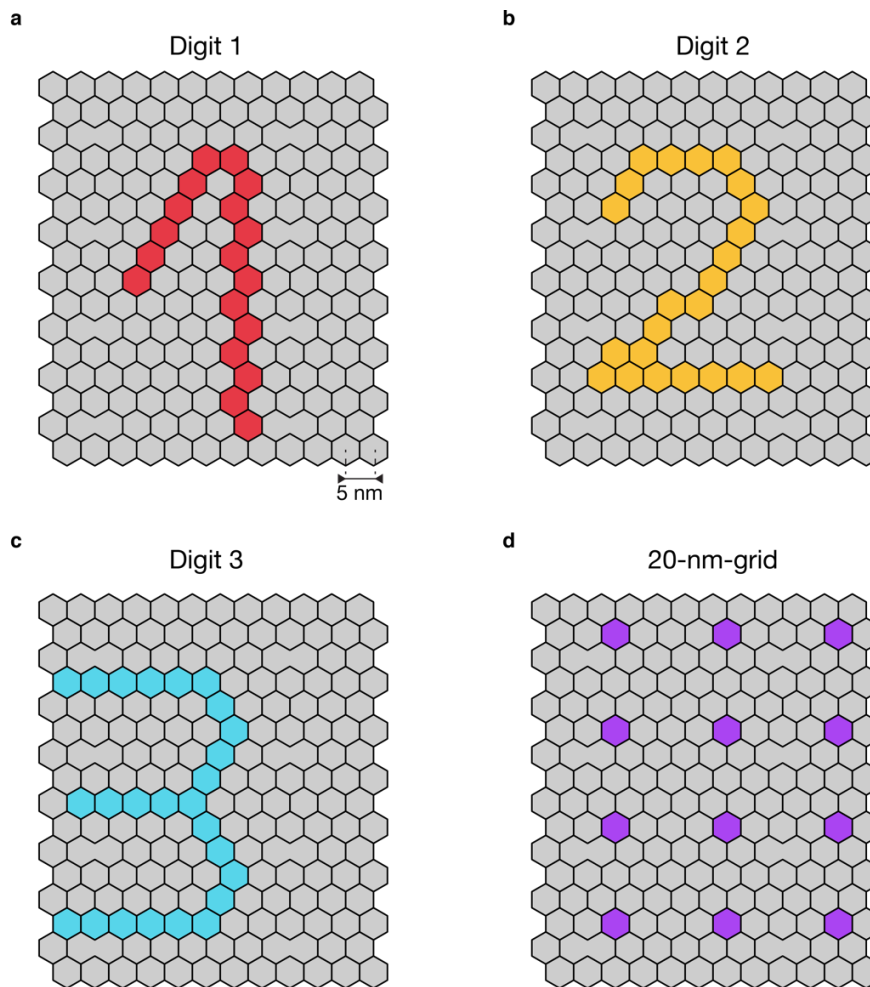
**Data quality:** The data quality of the training data set but also prediction data set strongly influences the performance of nanoTRON. Low quality data will likewise result in poor performance.

**Reproducibility:** nanoTRON model system is designed to export the model file in .sav format along with an YAML documentation file, which contains all necessary parameters of the trained model. Values for hyperparameters, as well as the path to the training files. While train and test accuracies are included in the documentation file, we propose saving also the learning curve and confusion matrix after training.

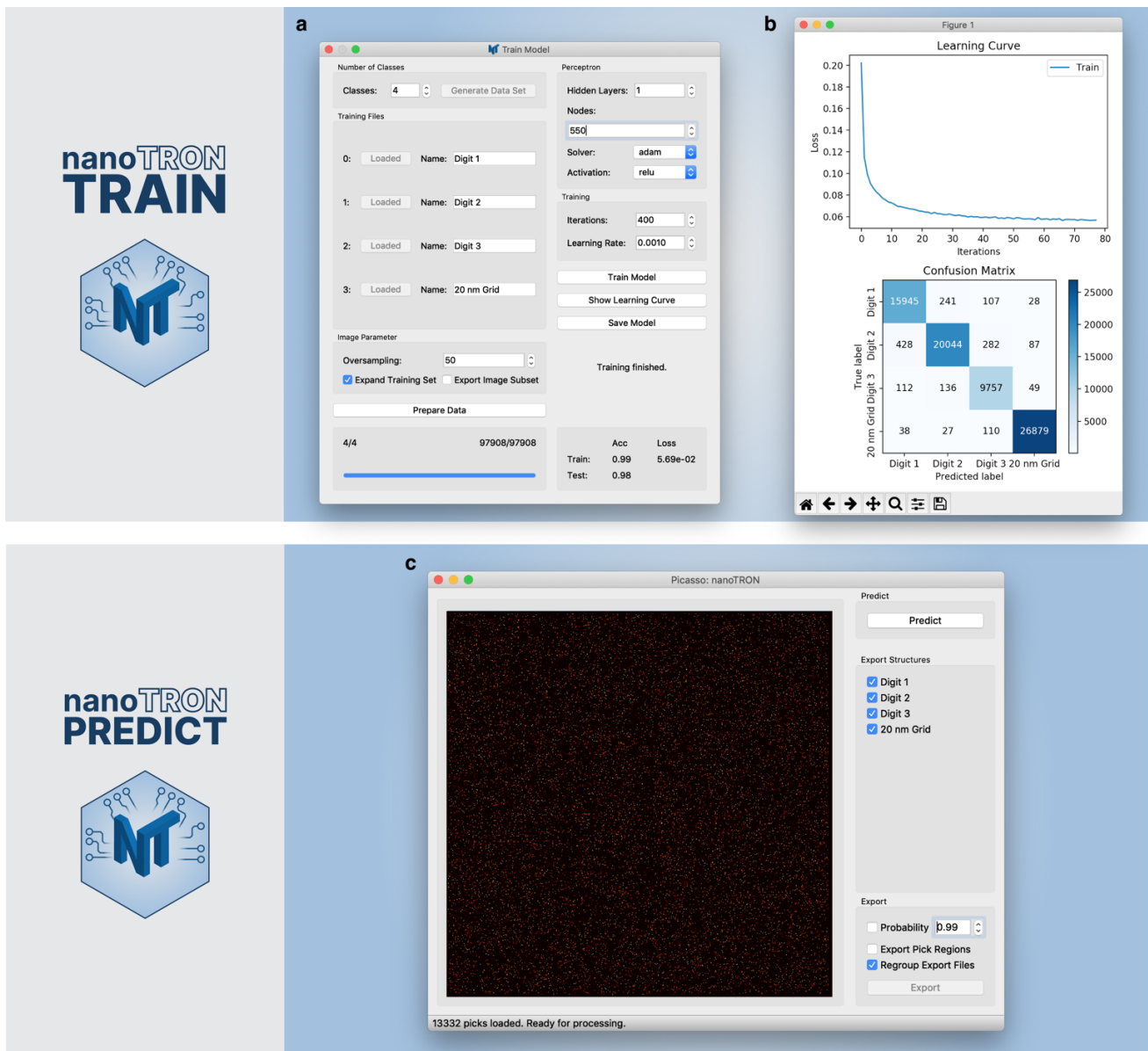
**Generalization:** Neural network training can suffer from “overfitting”, i.e. that a model performs well on the training data but fails to generalize on new data. In the context of super-resolution microscopy data, this could happen when the resolution of training and new data is different. Therefore, we recommend combining

multiple super-resolution images of the same class with varying spatial resolution for the training set, as suggested by Belthangady and Royer. The command-line function *picasso join file1 file2* offers a tool for combining localization files, see **Supplementary Text 3**. Combining multiple files will train the model for a more general usage. Attention: Picking the nanopatterns needs to be done after combining, otherwise the group ids will be doubled.

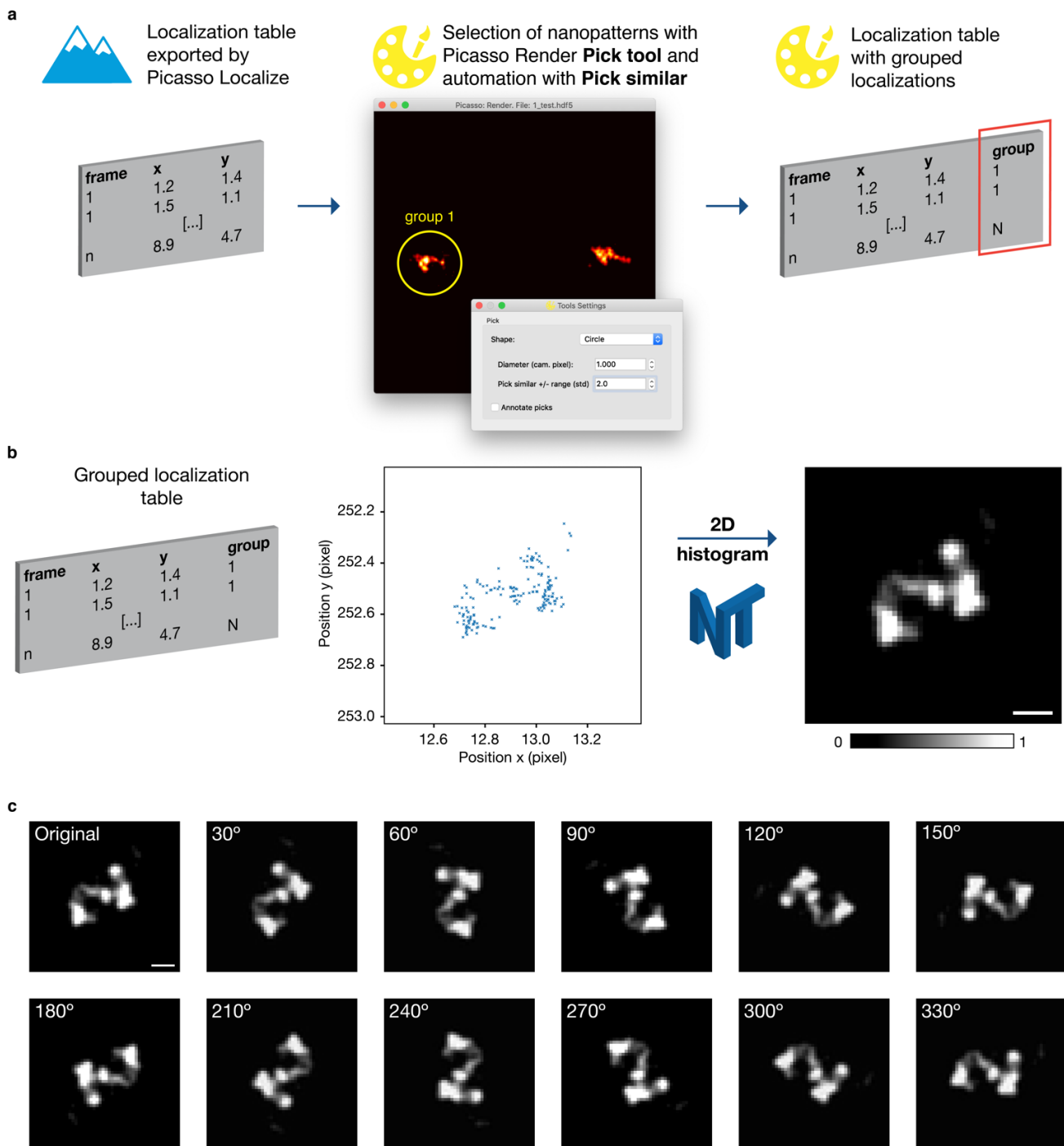
**Artefacts:** Real-world experiments contain artefacts and background signal. In the case of DNA origami, this could e.g. be misfolded structures. With biological targets, labelling issues can generate unwanted background signals. While selecting the nanopatterns with *Picasso Render* - especially if *Pick Similar* is used – we recommend screening the picks for artefacts and interactively excluding them in the training and prediction data set.



**Supplementary Figure 1 | Overview DNA origami design.** (a) Design of the 'Digit 1' structure. Red labeled hexagons mark the DNA staples, which are extended with the P1 docking sequence (**Supplementary Table 10**) for DNA-PAINT super-resolution imaging. Hexagon-to-hexagon distance is  $\sim 5$  nm. (b) Design of the 'Digit 2' DNA origami. Yellow hexagons indicate the P3 DNA-PAINT docking sites. (c) Design of the 'Digit 3' DNA origami. Cyan hexagons mark the P5 DNA-PAINT docking sites. (d) Design of the '20-nm-grid' DNA origami, a  $3 \times 4$ -grid-structure with 20 nm spacing. Hexagons colored magenta identify the P1 DNA-PAINT docking sites.

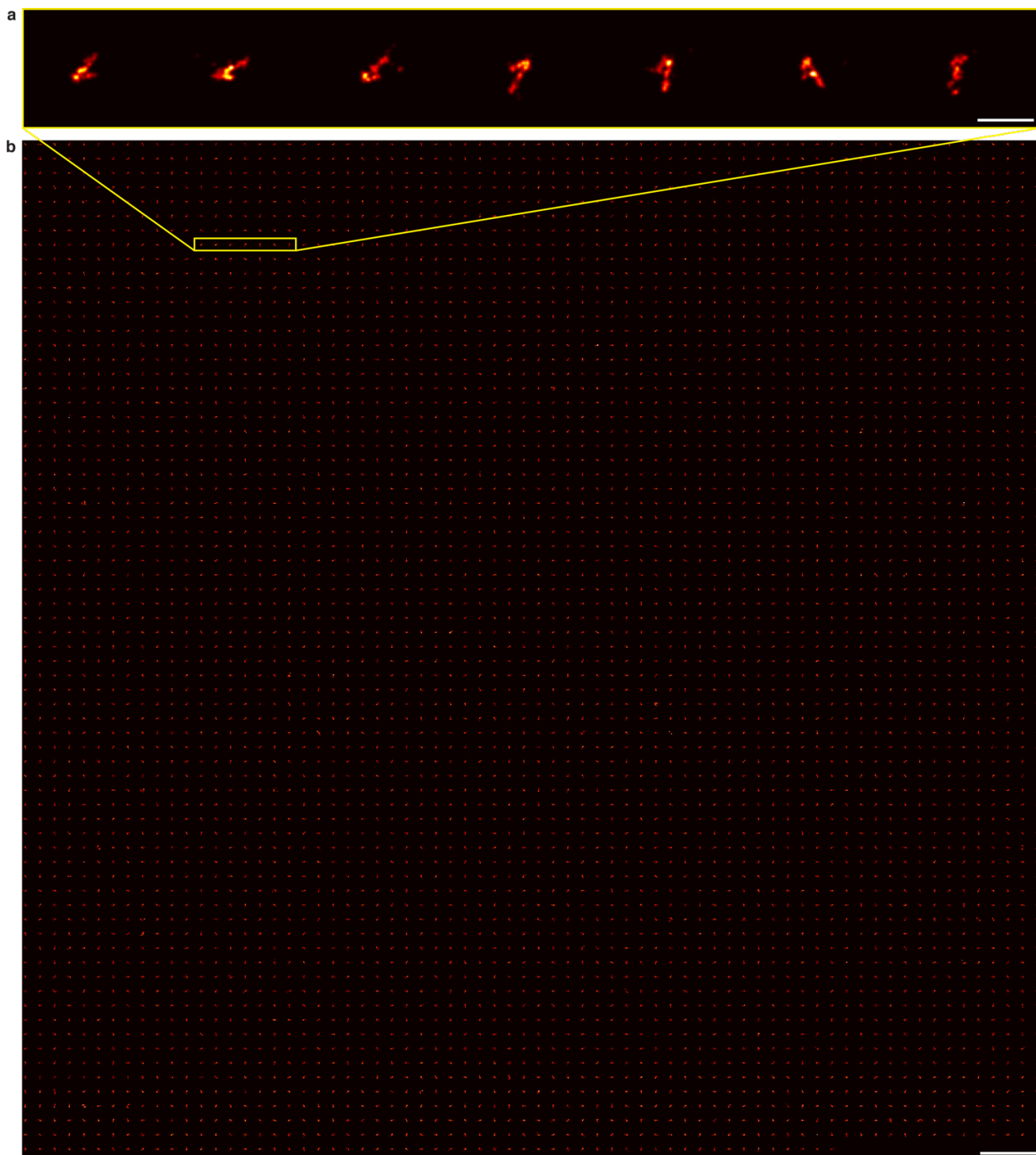


**Supplementary Figure 2 | Graphical user interface.** (a) GUI of nanoTRON: Train. Super-resolution training data sets are loaded into nanoTRON and converted to pixel images (Supplementary Figure 3 and Supplementary Figure 9). The artificial neural network is set up, trained, and saved. (b) Performance of the network can be visualized with a plot of the learning curve and the confusion matrix. (c) GUI of nanoTRON main window. Super-resolution data can be loaded into nanoTRON via drag and drop. Either a default or a saved model (Tools → Load model) of the artificial neural network can be used to classify the nanopatterns in the super-resolution data. The default model gets loaded when the software is started. After prediction, the labeled data can be filtered using the predicted probability and exported as individual data sets with the corresponding meta data file (YAML file). In addition to the super-resolution data, the Picasso's *pick regions* can be exported and subsequently used for further analysis.

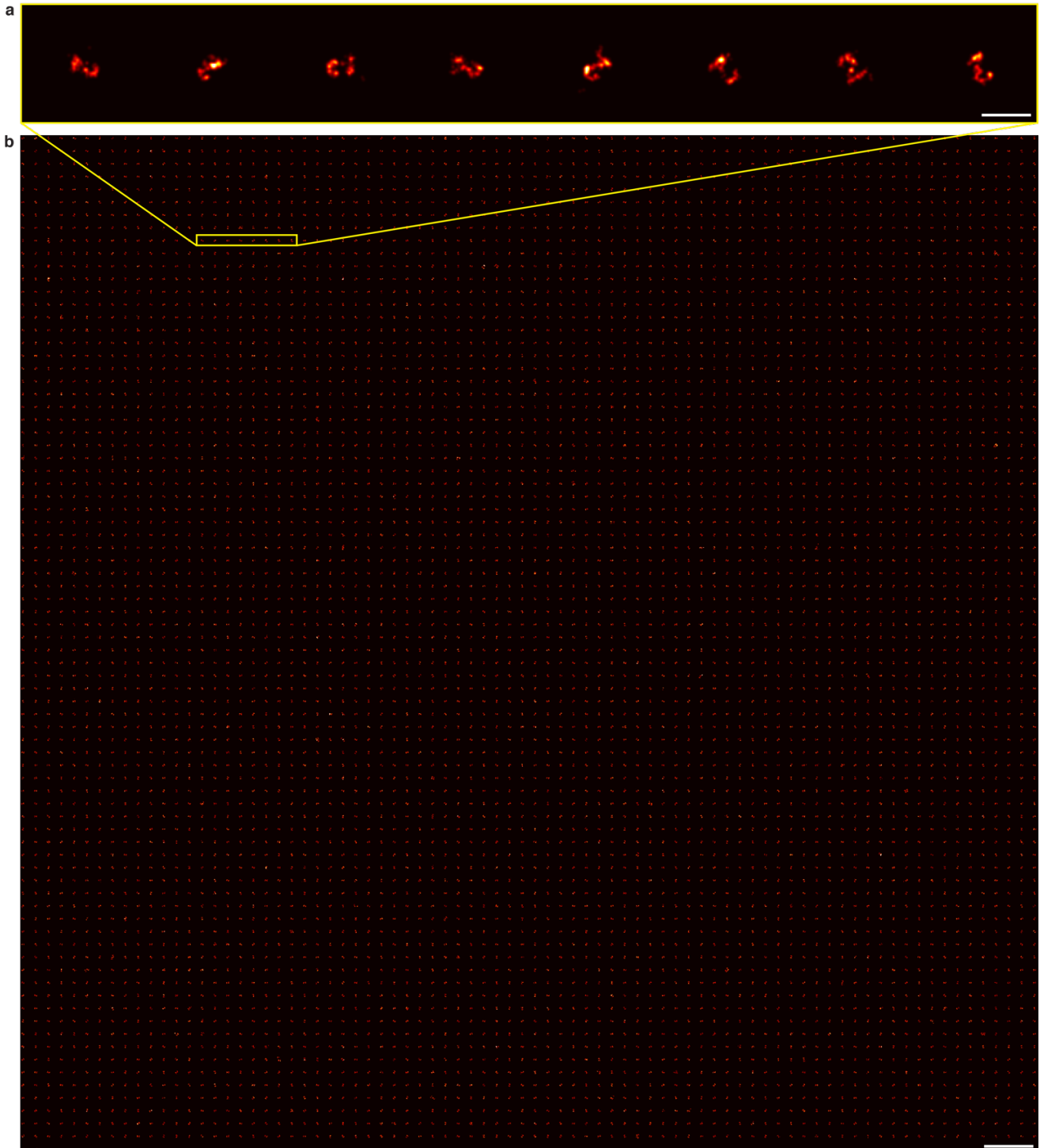


**Supplementary Figure 3 | Training data generation and augmentation.** (a) In localization-based super-resolution microscopy, diffraction-limited images get “converted” into tables of localizations by estimating the centers of single molecule emissions. In Picasso, the module *Localize* provides the graphical user interface for processing raw microscopy data and turning them into localization tables. In Picasso *Render*, the localization tables can then be rendered as an image. To utilize nanoTRON, first nanopatterns need to be selected. Using Picassos *Pick Tool*, nanopatterns can be manually selected by a center point and a pick diameter. One super-resolution image of e.g. DNA origami with 512 x 512 px can contain up to tens of thousands of nanopatterns. The tool *Pick similar* provides an automated solution for screening the whole image and picking comparable areas. Every pick is then assigned with a unique group id. (b) During training data preparation in nanoTRON, the localizations are converted into grayscale images and normalized between 0 and 1. Every pick corresponds to one nanopattern and consequently one grayscale image. One exemplary heatmap of a 20-nm-grid pick is visualized in **Supplementary Figure 9**. The resolution of the image can be set via the parameter ‘oversampling’, **Supplementary Figure 2a**. (c) The training set data can be augmented with rotated variants of every image. Ultimately,

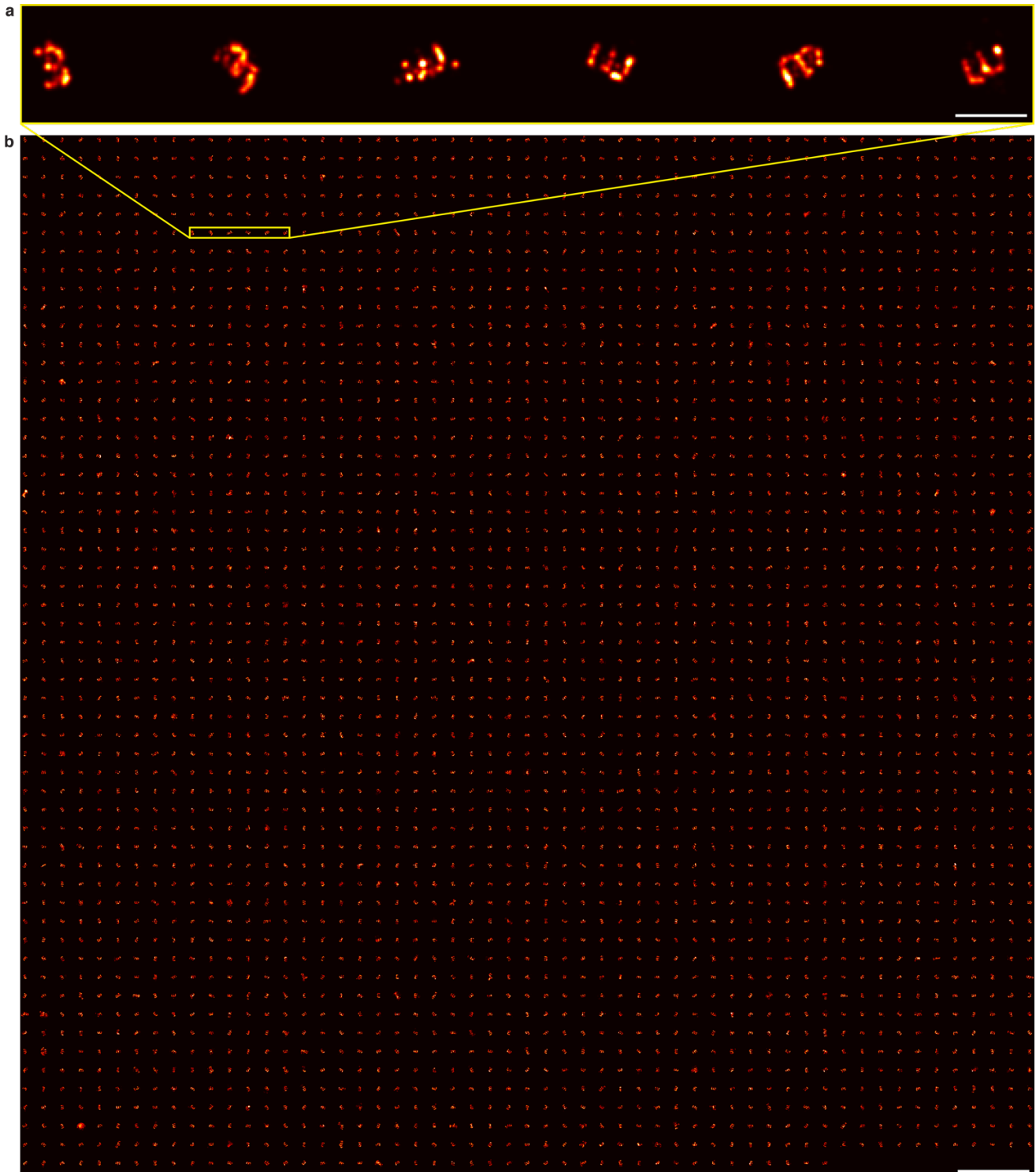
the original rendering of the super-resolution data is rotated 11 times around the center-of-mass with a step size of  $30^\circ$  effectively increasing the training data 11-fold. Scale bars, 20 nm (**a**, **b**)



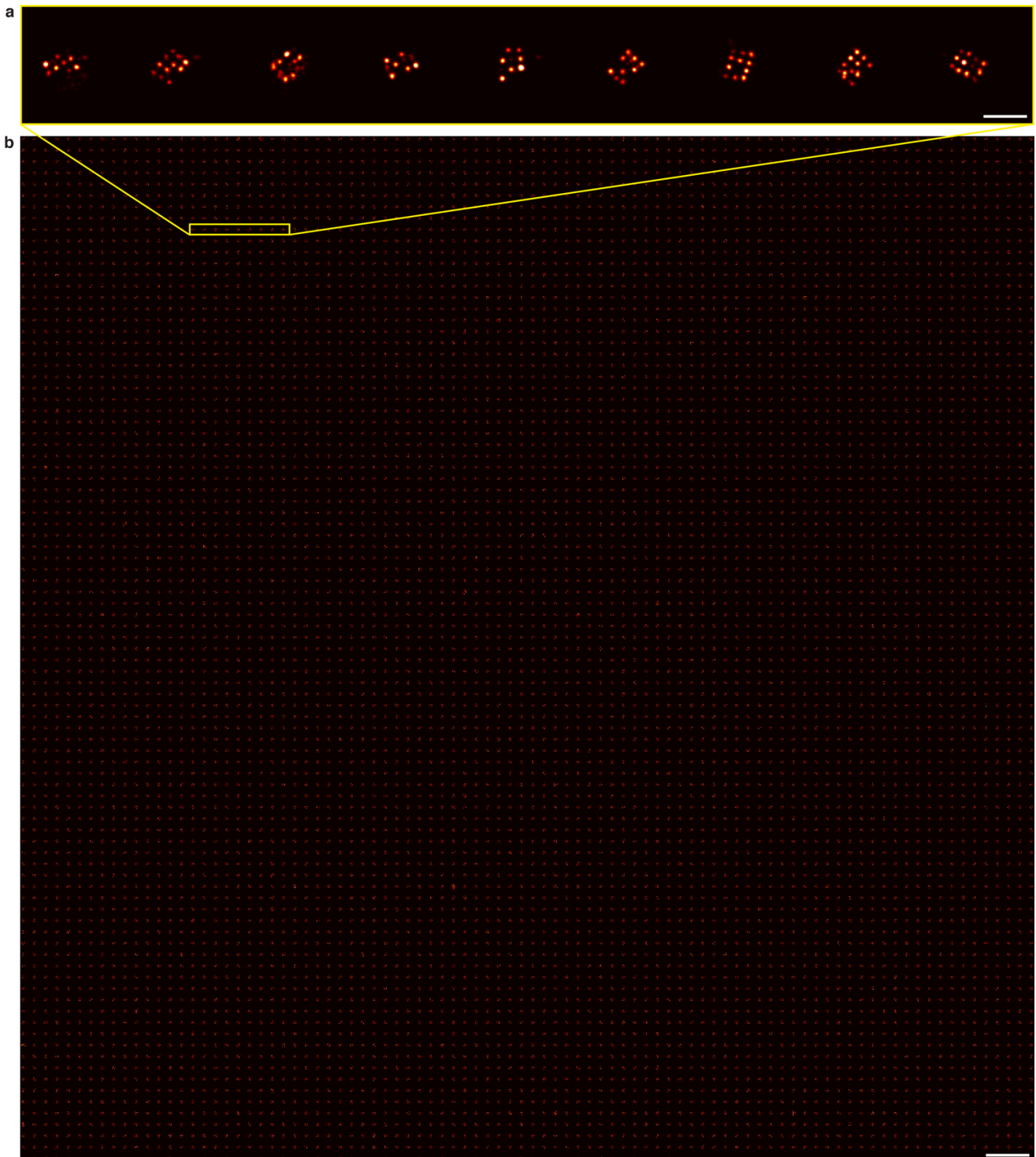
**Supplementary Figure 4 | Overview of training set *Digit 1*.** (a) Zoom-in of individual DNA origami imaged with DNA-PAINT (b) DNA-PAINT super-resolution mosaic image of 4955 DNA origami patterned with digit 1 (shown in **Supplementary Figure 1a**) DNA-PAINT docking sites with Sequence P1. Scale bars, 100 nm (a), 1  $\mu$ m (b).



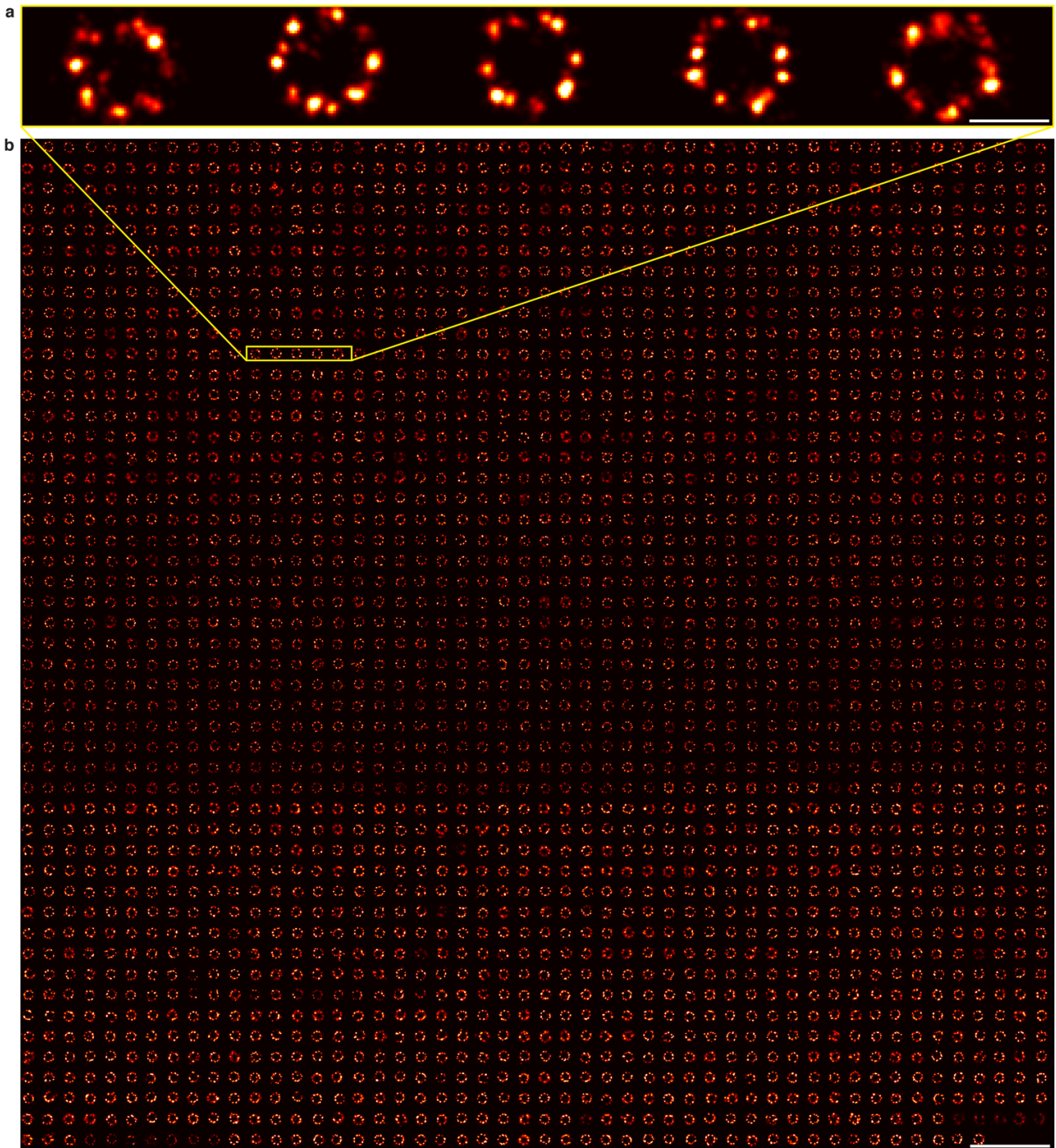
**Supplementary Figure 5 | Overview of training set *Digit 2*.** (a) Zoom-in of individual DNA origami imaged with DNA-PAINT (b) DNA-PAINT super-resolution mosaic image of 6321 DNA origami patterned with digit 2 (shown in **Supplementary Figure 1b**) DNA-PAINT docking sites with Sequence P1. Scale bars, 100 nm (a), 1  $\mu$ m (b).



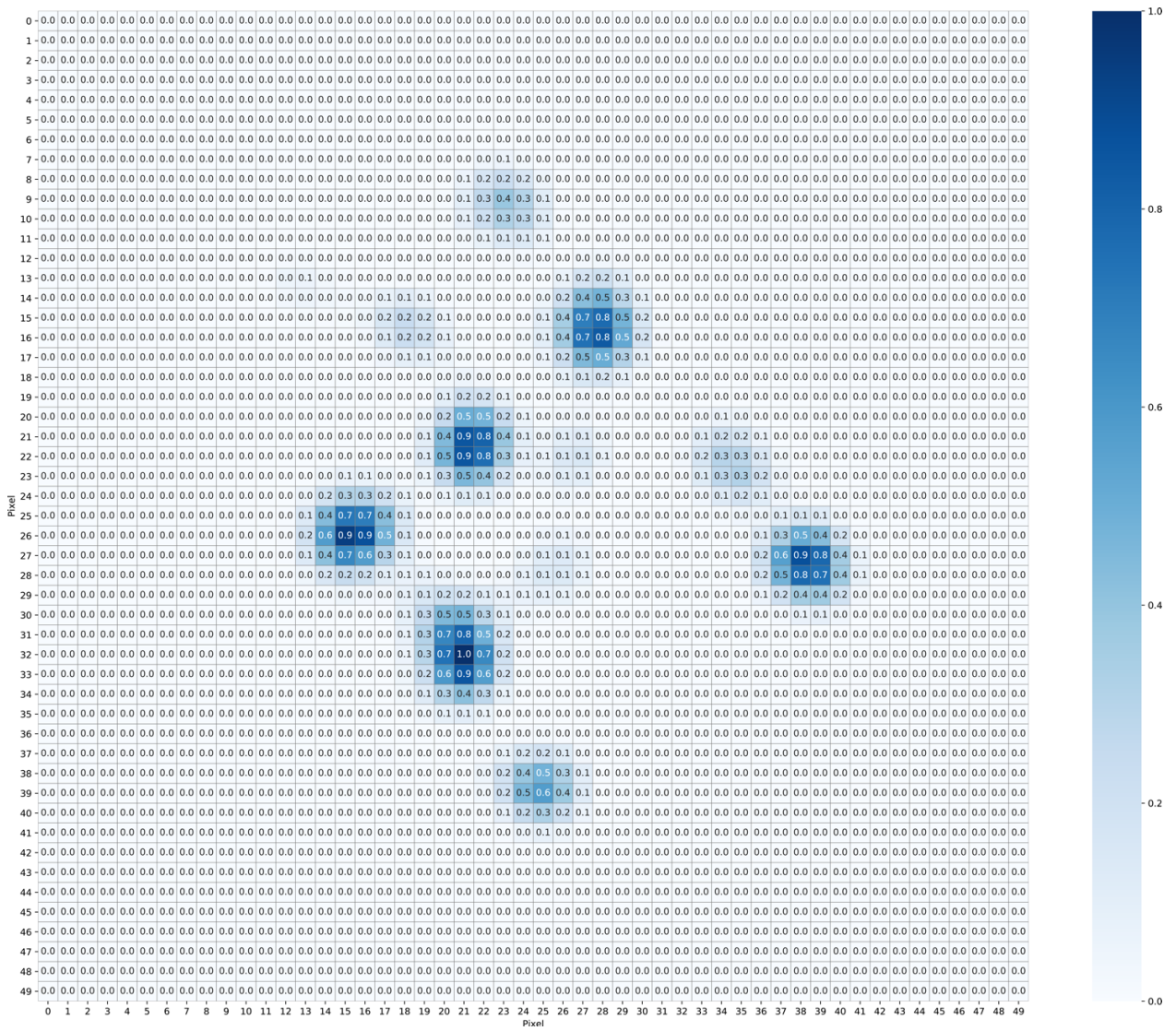
**Supplementary Figure 6 | Overview of training set *Digit 3*.** (a) Zoom-in of individual DNA origami imaged with DNA-PAINT (b) DNA-PAINT super-resolution mosaic image of 3068 DNA origami patterned with digit 3 (shown in **Supplementary Figure 1c**) DNA-PAINT docking sites with Sequence P1. Scale bars, 100 nm (a), 1  $\mu$ m (b).



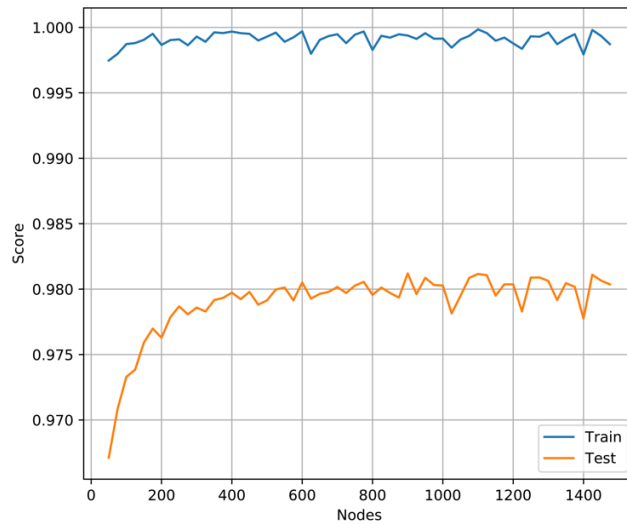
**Supplementary Figure 7 | Overview of training set *20-nm-grid*.** (a) Zoom-in of individual DNA origami imaged with DNA-PAINT (b) DNA-PAINT super-resolution mosaic image of 6321 DNA origami patterned with a  $3 \times 4$  grid with 20 nm spacing (shown in **Supplementary Figure 1d**) DNA-PAINT docking sites with Sequence P1. Scale bars, 100 nm (a), 1  $\mu\text{m}$  (b).



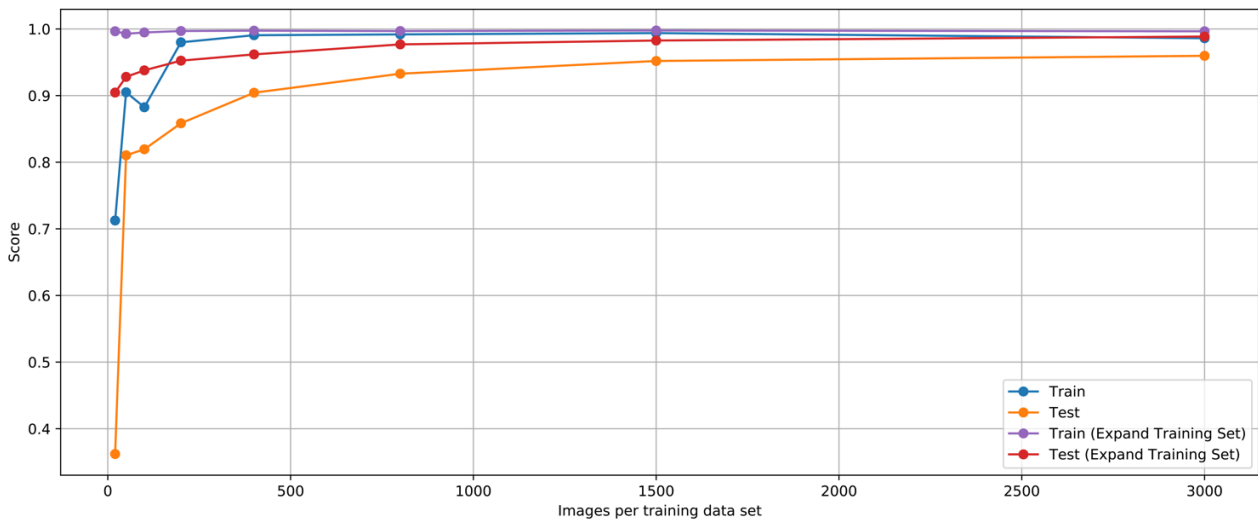
**Supplementary Figure 8 | Overview of training set Nup96.** (a) Zoom-in of individual Nup96 proteins of the nuclear pore complex in a fixed U2OS cell. (b) DNA-PAINT super-resolution mosaic image of 2447 nuclear pore complexes labeled with DNA-modified GFP nanobody. Scale bars, 100 nm (a), 1  $\mu$ m (b).



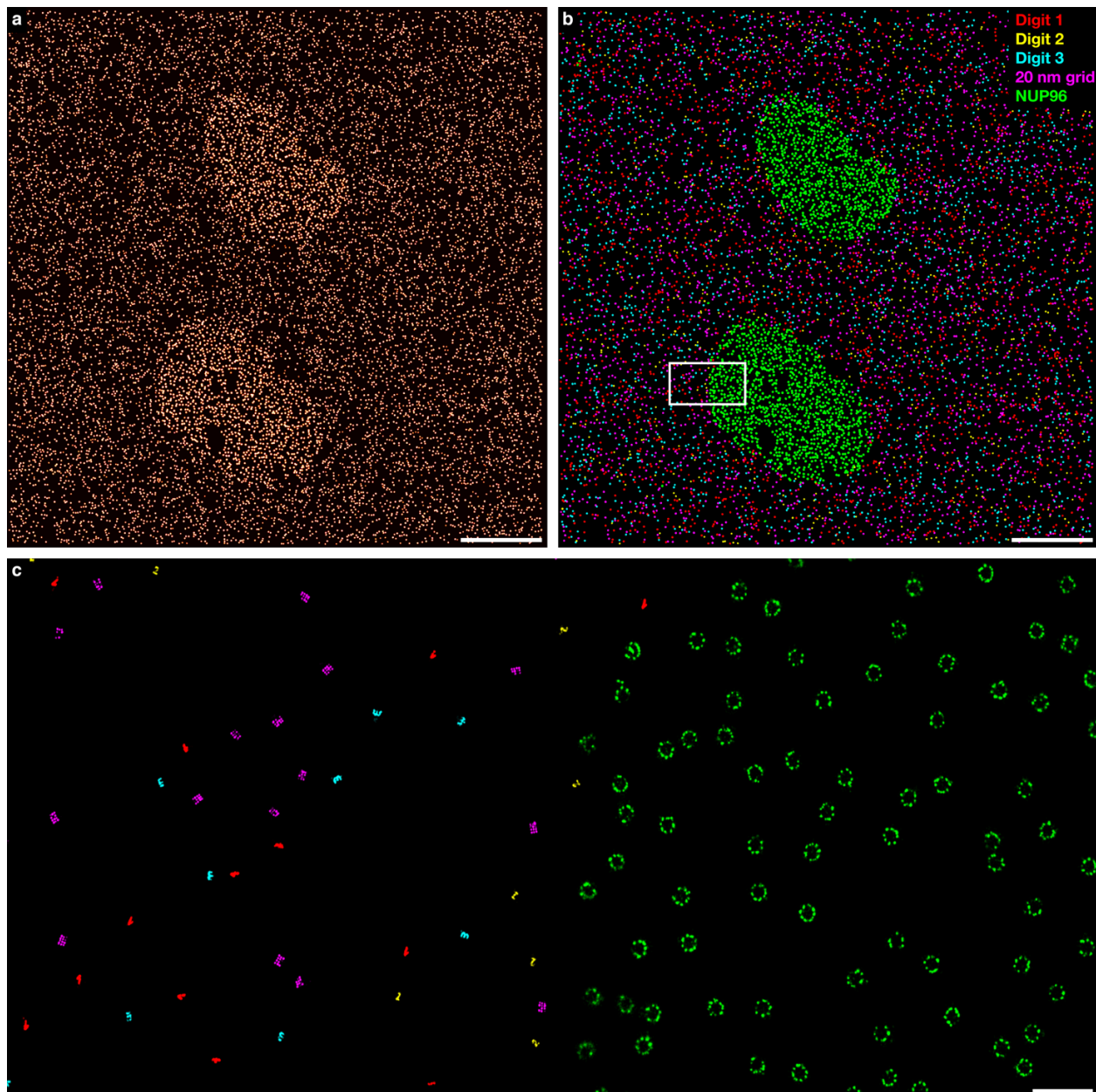
**Supplementary Figure 9 | Exemplary heatmap of one pick of the 20-nm-grid training set.** While preparing the data for training, nanoTRON converts the localizations of picks into grayscale images, as illustrated in **Supplementary Figure 3b**. The size of the image corresponds to the pick diameter and the chosen oversampling according to image size = pick diameter × oversampling. Every image gets scaled to gray values from 0 to 1. After converting all training sets to image stacks, the MLP is trained with the grayscale images. The exemplary heatmap displays one 20-nm-grid pick after conversion from localizations to an image with rounded gray values for clear visualization. nanoTRON does not round the gray values.



**Supplementary Figure 10 | Model parameter tuning of the numbers of nodes in the 1-layer network.** Training and test score achieved with the four classes training set with varying number of nodes from 50 to 1500. The final value was set to 550 nodes, indicating sufficient model complexity. Further increasing the number of nodes did not increase the test accuracy.



**Supplementary Figure 11 | Training and test score with different training set sizes using the 1-layer network.** Training and test scores achieved using the 4 classes. The number of picks in every unique training set were varied, starting from 20 up to 3000 picks per set. The scores were calculated with and without the nanoTRON option “Expand Training Set”, **Supplementary Figure 3c**. Using 200 images per unique training set and the data augmentation option, a test accuracy of ~0.95 could be realized. Without augmentation the test accuracy dropped to ~0.86. Larger training sets with 3000 picks per unique set increase test accuracy up to almost ~0.99.



**Supplementary Figure 12 | Proof-of-concept experiment with a biological target.** (a) Overview image of the artificial DNA-PAINT data set constructed as described in **Supplementary Text 3**. (b) Super-resolution image with classified nanopatterns using nanoTRON and a 5-class model, which was trained as described in **Supplementary Text 3**. The different colors (red, yellow, cyan and purple) visualize the respective DNA origami structures. The Nup96 protein of the nuclear pore complex is depicted in green. The overview image clearly shows the two cellular nuclei. (c) Zoom-in of the marked region in **b**. Scale bars, 10  $\mu\text{m}$  (**a**, **b**), 500 nm (**c**).

**Supplementary Table 1 | Experimental conditions training set *Digit 1***

<b>Microscope setting</b>	<b>Condition</b>
Microscope	Setup 1
Objective	Apo SR HP TIRF 100x
Camera	Zyla 4.2 Plus
Field of view	512×512 pixel after binning
Frames	15 000
Exposure time	200 ms
Binning	2×2
Tube lens	1×
Excitation laser	561 nm [max power 200 mW]
Laser Power	80 mW

<b>Sample settings</b>	<b>Condition</b>
Sample target	Digit 1 DNA origami
Imager sequence	P1
Imager concentration	1 nM
Imaging buffer	B with PCA/PCD/TX
Dye	Cy3B

**Supplementary Table 2 | Experimental conditions in training set *Digit 2***

<b>Setting</b>	<b>Condition</b>
Microscope	Setup 1
Objective	Apo SR HP TIRF 100x
Camera	Zyla 4.2 Plus
Field of view	512×512 pixel after binning
Frames	15 000
Exposure time	200 ms
Binning	2×2
Tube lens	1×
Excitation laser	561 nm [max power 200 mW]
Laser Power	80 mW

<b>Sample settings</b>	<b>Condition</b>
Sample target	Digit 2 DNA origami
Imager sequence	P3
Imager concentration	1 nM
Imaging buffer	B with PCA/PCD/TX
Dye	Cy3B

**Supplementary Table 3 | Experimental conditions training set *Digit 3***

<b>Setting</b>	<b>Condition</b>
Microscope	Setup 3
Objective	Apo SR HP TIRF 100x
Camera	Zyla 4.2 Plus
Field of view	512×512 pixel after binning
Frames	15 000
Exposure time	200 ms
Binning	2×2
Tube lens	1×
Excitation laser	560 nm [max power 500 mW]
Laser Power	100 mW

<b>Sample settings</b>	<b>Condition</b>
Sample target	Digit 3 DNA origami
Imager sequence	P5
Imager concentration	1 nM
Imaging buffer	B with PCA/PCD/TX
Dye	Cy3B

**Supplementary Table 4 | Experimental conditions in training set *20-nm-grid***

<b>Setting</b>	<b>Condition</b>
Microscope	Setup 3
Objective	Apo SR HP TIRF 100x
Camera	Zyla 4.2 Plus
Field of view	512×512 pixel after binning
Frames	15 000
Exposure time	200 ms
Binning	2×2
Tube lens	1×
Excitation laser	560 nm [max power 500 mW]
Laser Power	100 mW

<b>Sample settings</b>	<b>Condition</b>
Sample target	20-nm-grid DNA origami
Imager sequence	P1
Imager concentration	3 nM
Imaging buffer	B with PCA/PCD/TX
Dye	Cy3B

**Supplementary Table 5 | Experimental conditions in validation set**

<b>Setting</b>	<b>Condition</b>
Microscope	Setup 3
Objective	Apo SR HP TIRF 100x
Camera	Zyla 4.2 Plus
Field of view	512×512 pixel after binning
Frames	25 000
Exposure time	200 ms
Binning	2×2
Tube lens	1×
Excitation laser	560 nm [max power 500 mW]
Laser Power	100 mW

<b>Sample settings</b>	<b>Condition</b>
Sample target	Digit 1, Digit 2, Digit 3 and 20-nm-grid
Imager sequence	P1, P3, P5
Imager concentration	0,5 nM each
Imaging buffer	B with PCA/PCD/TX
Dye	Cy3B

Supplementary Table 6 | M13mp18 p7249 sequence

TTCCCTTCCTTTCTCGCCACGTTTCGCCGGCTTTCCCGCTCAAGCTCTAAATCGGGGGCTCCCTTAGGGTTCCGATTTAGTGCTTTACGGCACCTCGACCCCAAAAAA  
TGATTTGGGTGATGGTTCACGTAGTGGGCCATCGCCCTGATAGACGGTTTTTCGCCCTTTGACGTTGGAGTCCACGTTCTTTAATAGTGGACTCTGTTCAAACTGGAA  
CAACTCAACCCTATCTCGGGCTATCTTTTGATTTATAAGGGATTTTGCCGATTTCCGAACCACCATCAAACAGGATTTTCGCCTGCTGGGGCAAACCAGCGTGGACC  
GCTTGCTGCAACTCTCTCAGGGCCAGGCGGTGAAGGGCAATCAGCTGTTGCCCGTCTCACTGGTGAAGAAAAACCACCTGGCGCCCAATACGCAAACCGCCTCTCCC  
CGCGCTTGCCGATTCATTAATGCAGCTGGCAGCAGAGTTTCCCGACTGGAAGCGGGCAGTGAGCGCACGCAATTAATGTGAGTTAGCTCACTCATTAGGCACCCC  
AGGCTTTACACTTTATGCTTCCGGCTCGTATGTTGTGTGAATTTGAGCGGATAACAATTTACACAGGAAACAGCTATGACCATGATTACGAATTCGAGCTCGGTACC  
CGGGGATCCTCTAGAGTCGACCTGCAGGCATGCAAGCTTGGCACTGGCCGTCGTTTTACAACGTCGTACTGGGAAAAACCTGGCGTTACCCAACCTAATCGCCTTGCA  
CACATCCCCCTTTCCGACGCTGGCGTAATAGCGAAGAGGCCCGCACCGATCGCCCTTCCCAACAGTTGGCGAGCCTGAATGGCGAATGGCGCTTTGCCTGGTTCCGGCA  
CCAGAAGCGGTGCCGAAAGCTGGTGGAGTGCATCTTCTGAGCCGATACTGTGTCGTCCTCCCTCAAACCTGGCAGATGCACGGTTACGATGCGCCCATCTACACCAA  
CGTGACCTATCCATTACGGTCAATCCGCCGTTTGTTCACGAGGAAATCCGACGGGTTGTTACTCGCTCACATTTAATGTTGATGAAAGCTGGCTACAGGAAGGCCAGA  
CGCAATATTTTTGATGGCGTTCTATTTGGTTAAAAAATGAGCTGATTTAACAAAAATTTAATGCGAATTTAACAAAAATTTAACGTTTACAATTTAAATATTTGCTT  
ATACAATCTTCTGTTTTTGGGGCTTTTCTGATTATCAACCGGGTACATATGATTGACATGCTAGTTTTACGATTACCGTTCATCGATTCTCTGTTTTGCTCCAGACTC  
TCAGGCAATGACCTGATAGCCTTTGTAGATCTCTCAAAAATAGCTACCCTCTCCGGCATTAAATTTATCAGCTAGAACGGTTGAATATCATATTGATGGTGAATTTGACTGT  
CTCCGGCCTTTCTCACCTTTTGAATCTTTACCTACACATTACTCAGGCATTCGATTTAAAAATATATGAGGGTCTAAAAATTTTTATCCTTGCCTGAAATAAAGGCTT  
CTCCCGCAAAAGTATTACAGGGTCATAATGTTTTTGGTACAACCGATTTAGCTTTATGCTCTGAGGCTTTATTTGCTTAATTTTGCATAATCTTTGCCTTGCTGTATGAT  
TTATTGGATGTTAATGCTACTACTATTAGTAGAATGATGCCACCTTTTCACTCGCGCCCAAAATGAAAAATAGCTAAACAGGTTATTGACCATTTGCGAAATGATC  
TAATGGTCAAACCTAACTACTCGTTCGAGAAATGGGAATCACTGTTATATGGAATGAACTCCAGACACCGTACTTTAGTTGCATATTTAAAACATGTTGAGCTAC  
AGCATATATTCAGCAATTAAGCTCTAAGCCATCCGCAAAAATGACCTCTTATCAAAGGAGCAATTAAGGTACTCTCTAATCCTGACCTGTTGGAGTTTGTTCGGGT  
CTGGTTCCGCTTTGAAGCTCGAATTAACCGCATATTTGAAGTCTTTCGGGCTTCTCTTAATCTTTTTGATGCAATCCGCTTTGCTTCTGACTATAATAGTCAGGGTAA  
AGACCTGATTTTTGATTTATGGTCACTCTCGTTTTCTGAAGCTGTTAAAGCATTGAGGGGGATTCATGAATATTTATGACGATTCGGCAGTATTGGACGCTATCCAGT  
CTAACATTTTACTATTACCCCTCTGGCAAACTCTTTTGCAAAAGCCTCTCGCTATTTTGGTTTTTATCGCTGCTGGTAAACGAGGGTTATGATAGTGTGCTCTT  
ACTATGCCTCGTAATCCTTTTGGCGTTATGTATCTGCATTAGTTGAATGTGGTATTCCTAAATCTCAACTGATGAATCTTTCTACCTGTAATAATGTTGTTCCGTTAGT  
TCGTTTTATTAACGTAGATTTTTCTTCCCAACGTCCTGACTGGTATAATGAGCCAGTCTTAAAAATCGCATAAGGTAATTCACAATGATTAAGGTTGAATTAACCATC  
TCAAGCCCAATTTACTACTCGTTCGGTGTTCCTCGTCAGGGCAAGCCTTATTCACTGAATGAGCAGCTTTGTTACGTTGATTTGGGTAATGAATATCCGGTCTTGTCA  
AGATTACTCTTGATGAAGGTCAGCCAGCCTATGCGCCTGGTCTGTACACCGTTCATCTGCCTCTTCAAAGTTGGTCAGTTCCGGTTCCTTATGATTGACCGTCTGCGC  
CTCGTTCCGGTAAGTAACATGGAGCAGGTCGCGGATTTTCGACACAATTTATCAGGCATGATACAAAATCTCCGTTGTACTTTGTTTTCCGCTTGGTATAATCGCTGGGG  
GTCAAAGATGAGTGTTTAGTGTATCTTTGCTCTTTCGTTTTAGGTTGGTGCCTTCGTAGTGGCATTACGTATTTTACCCGTTAATGAAACTTCTCATGAAAA  
GTCTTTAGTCTCAAAGCCTCTGTAGCCGTTGCTACCCTCGTTCGATGCTGTCTTTTCGCTGCTGAGGGTACGATCCCGCAAAAGCGGCCTTTAACTCCCTGCAAGCCT  
CAGCGACCGAATATATCGGTTATGCGTGGCGATGGTGTGTCATTGTCGGCGCACTATCGGTATCAAGCTGTTAAGAAATTCACCTCGAAAGCAAGCTGATAAACC  
GATACAATTAAGGCTCCTTTTGGAGCCTTTTTTTTGGAGATTTTCAACGTGAAAAAATATTATTTCGCAATTCCTTTAGTTGTTCCCTTCTATTCTACTCCGCTGAAA  
CTGTTGAAAGTTGTTTAGCAAAAATCCCATACAGAAAATTCATTTACTAACGTCTGAAAGACGACAAAACCTTAGATCGTTACGCTAACATAGAGGGCTGTCTGTGAAT  
GCTACAGGCGTTGTAGTTTGTACTGGTACGAACTCAGTGTACGGTACATGGGTTCCCTATTGGGCTTGTATCCCTGAAAATGAGGGTGGTGGCTCTGAGGTGGCGG  
TTCTGAGGGTGGCGGTTCTGAGGGTGGCGGTACTAAACCTCCTGAGTACGGTATACACCTATTCGGGCTATACTTATATCAACCCTCTCGACGGCACTATCCGCTG  
GTACTGAGCAAAACCCGCTAATCCTAATCCTTCTCTGAGGAGTCTCAGCCTCTTAATACCTTTATGTTTCAAGATAATAGGTTCCGAAATAGGCAGGGGGCATTAACT  
GTTTATACGGGCACTGTTACTCAAGGCACCTGACCCCGTTAAAACCTTATTACCAGTACACTCCTGTATCATCAAAGCCATGATGACGCTTACTGGAACGGTAAATTCAG  
AGACTGCGCTTTCATCTGGCTTTAATGAGGATTTATTTGTTGTGAATATCAAGGCCAATCGTCTGACCTGCCTCAACCTCCTGTCAATGCTGGCGGGCCTCTGGTG  
GTGGTTCTGGTGGCGGCTCTGAGGGTGGTGGCTCTGAGGGTGGCGGTTCTGAGGGTGGCGGCTCTGAGGGAGGCGGTTCCGGTGGTGGCTCTGGTTCCGGTGATTTGAT  
TATGAAAAGATGGCAAACGCTAATAAGGGGGCTATGACCGAAAATGCCGATGAAAACGCGCTACAGCTGACGCTAAAGGCAAACCTGATTCTGTGCTACTGATTACGG  
TGCTGCTATCGATGGTTTCATTGGTACGTTTCCGGCCTTGCTAATGGTAATGGTGTACTGGTGATTTTGTGGCTCTAATTCCAAATGGCTCAAGTCCGGTACGGTG  
ATAATCACCTTTAATGAATAATTTCCGTCATATTTACCTCCCTCCCTCAATCGGTTGAATGTCGCCCTTTTGTCTTTGGCGCTGGTAAACCATATGAATTTCTATT  
GATTGTGACAAAATAAACTTATCCGTTGGTGTCTTTGCGTTCTTTTATATGTTGCCACCTTTATGATGATTTTTCTACGTTTGGTAAACATACTGCCTAATAAGGAGTC  
TTAATCATGCCAGTTCTTTTGGGATTTCCGTTATTTATGCGTTTCCCTCGGTTTCTCTGTTAACTTTGTTCCGGCTATCTGCTTACTTTTCTTAAAAAGGGCTTCGGTAA  
GATAGCTATTGCTATTTTCAATGTTTCTGTCTTATTATTTGGGCTTAACTCAATCTTGTGGGTTATCTCTCTGATATTAGCGCTCAATACCCTCTGACTTTGTTTCAGG  
GTGTTCAAGTTAATCTCCGCTCAATGCGCTTCCCTGTTTTATGTTATCTCTCTGTAAAGGCTGCTATTTTCAATTTTGGAGCTTAAACAAAAATCGTTTCTTATTTG  
GATTGGGATAAATAATAGGCTGTTTATTTGTAAGTGGCAAATAGGCTCTGAAAGACGCTCGTTAGCGTTGGTAAAGATTAGGATAAAATTTAGCTGGGTGCAAAA  
TAGCAACTAATCTGATTTAAGGCTTCAAACCTCCCGAAGTCCGGAGGTTTCGTAATAACGCTCGCGTTCTTAGAATACCGGATAAGCCTTCTATATCTGATTTGCTT  
GCTATTGGGCGCGGTAATGATTCTACGATGAAAATAAAAACGGCTTGCTTGTCTCGATGAGTGCAGTACTTGGTTAATACCCGTTCTTGAATGATAAGGAAAGACA  
GCCGATTTAGATTGGTTTCTACATGCTCGTAAATTAGGATGGGATATTTTTTCTGTTTCCAGGACTTATCTATTGTTGATAAACAGGCGGCTTCTGCATTAGCTGAAC

ATGTTGTTTATTGTCGTCGCTGGACAGAATTACTTTACCTTTTGTGCGTACTTTATATTCTCTTATTACTGGCTCGAAAAATGCCTCTGCCTAAATTACATGTTGGCGTT  
 GTTAAATATGGCGATTCTCAATTAAGCCCTACTGTTGAGCGTTGGCTTTATACTGGTAAGAATTTGTATAACGCATATGATACTAAACAGGCTTTTCTAGTAATTATGA  
 TTCCGGTGTATTCTTATTTAACGCCTTATTTATCACACGGTCGGTATTTCAAACCATTAATTTAGGTCAGAAGATGAAATTAACATAAAATATATTTGAAAAAGTTTT  
 CTCGCGTTCTTTGCTTTCGCGATTGGATTGCATCAGCATTTACATATAGTTATATAACCCCAACCTAAGCCGGAGGTTAAAAAGGTAGTCTCTCAGACCTATGATTTTGAT  
 AAATTCACTATTGACTCTTCTCAGCGTCTTAATCTAAGCTATCGCTATGTTTTCAAGGATTCTAAGGGAAAAATTAATTAATAGCGACGATTTACAGAAGCAAGGTTATTC  
 ACTCACATATATTGATTTATGTACTGTTTTCCATTAATAAAGGTAATTCAAATGAAATGTTAAATGTAATTAATTTGTTTTCTTGATGTTTGTTCATCATCTCTTTTT  
 GCTCAGGTAATTGAAATGAATAATTCGCCCTCTGCGGATTTTGTAACTGGTATTCAAAGCAATCAGGCGAATCCGTTATTGTTTTCTCCGATGTAAGGACTGTTTAC  
 TGTATATTCATCTGACGTTAAACCTGAAAACTACGCAATTTCTTTATTTCTGTTTTACGTGCAAATAATTTGATATGGTAGGTTCTAACCTTCCATTATTCAGAAGT  
 ATAATCCAAACAATCAGGATTATATTGATGAATTGCCATCATCTGATAATCAGGAATATGATGATAATCCGCTCCTTCTGGTGGTTTTCTTTGTTCCGCAAAATGATAAT  
 GTTACTCAAACCTTTTAAATTAATAACGTTTCGGGCAAAGGATTTAATACGAGTTGTCGAATGTTTGTAAAGTCTAATACTTCTAAATCCTCAAATGTATTATCTATTGA  
 CGGCTCAATCTATTAGTTGTTAGTCTCCTAAAGATATTTAGATAACCTTCCCTCAATTCCTTCAACTGTTGATTTGCCAAGTACCAGATATTGATTGAGGGTTTGA  
 TATTTGAGGTTACAGCAAGGTGATGCTTTAGATTTTTCAATTTGCTGCTGGCTCTCAGCGTGGCACTGTTGCAGGCGGTGTTAATACTGACCGCCTCACCTCTGTTTTATCT  
 TCTGCTGGTGGTTTCGTTTCGATTTTTAATGGCGATGTTTTAGGGCTATCAGTTCCGCGATTAAGACTAATAGCCATTCAAAAAATATTGCTGTGCCAGTATTCTTAC  
 GCTTTCAGGTCAGAAGGTTCTATCTGTTGGCCAGAATGTCCTTTTTATTACTGGTCGTGTACTGGTGAATCTGCCAATGTAATAATCCATTTCAGACGATTGAGC  
 GTCAAAATGTAGGTTATTTCCATGAGCGTTTTTCTGTTGCAATGGCTGGCGGTAATATTGTTCTGGATATTACCAGCAAGGCCGATAGTTTG

**Supplementary Table 7 | Rectangular DNA origami staple strands**

Plate	Pos	Name	Sequence	Digit 1	Digit 2	Digit 3	20-nm-grid
1	A1	21[32]23[31]BLK	TTTTCACTCAAAGGGCGAAAAACCATCACC				
1	A2	19[32]21[31]BLK	GTCGACTTCGGCCAACGCGGGGTTTTTC				
1	A3	17[32]19[31]BLK	TGCATCTTTCCAGTCACGACGGCTGCAG				
1	A4	15[32]17[31]BLK	TAATCAGCGGATTGACCGTAATCGTAACCG				
1	A5	13[32]15[31]BLK	AACGCAAAATCGATGAACGGTACCGGTTGA				
1	A6	11[32]13[31]BLK	AACAGTTTTGTACCAAAAACATTTTATTTTC				
1	A7	9[32]11[31]BLK	TTTACCCCAACATGTTTTAAATTTCCATAT				
1	A8	7[32]9[31]BLK	TTTAGGACAAATGCTTTAACAATCAGGTC				
1	A9	5[32]7[31]BLK	CATCAAGTAAAACGAACTAACGAGTTGAGA				
1	A10	3[32]5[31]BLK	AATACGTTTGAAAGAGGACAGACTGACCTT				
1	A11	1[32]3[31]BLK	AGGCTCCAGAGGCTTTGAGGACACGGGTAA				
1	A12	0[47]1[31]BLK	AGAAAAGAAACAATAAAGGAATCAAAAAAA				
1	B1	23[32]22[48]BLK	CAAATCAAGTTTTTTGGGGTCGAAACGTGGA				
1	B2	22[47]20[48]BLK	CTCCAACGCAGTGAGACGGGCAACCAGCTGCA				
1	B3	20[47]18[48]BLK	TTAATGAACTAGAGGATCCCGGGGGTAACG				P1
1	B4	18[47]16[48]BLK	CCAGGTTGCCAGTTTGGGGACCCGTGGGA				
1	B5	16[47]14[48]BLK	ACAAACGGAAAAGCCCCAAAAACACTGGAGCA				
1	B6	14[47]12[48]BLK	AACAAGAGGGATAAAAATTTTAGCATAAAGC				
1	B7	12[47]10[48]BLK	TAAATCGGATTCCTCAATTCGCGATATAATG				P1
1	B8	10[47]8[48]BLK	CTGTAGCTTGACTATTATAGTCAGTTCATTGA				
1	B9	8[47]6[48]BLK	ATCCCCCTATACCACATTCAACTAGAAAAATC				
1	B10	6[47]4[48]BLK	TACGTTAAAGTAATCTTGACAAGAACCGAACT				
1	B11	4[47]2[48]BLK	GACCAACTAATGCCACTACGAAGGGGGTAGCA				P1
1	B12	2[47]0[48]BLK	ACGGCTACAAAAGGAGCCTTTAATGTGAGAAAT				
1	C1	21[56]23[63]BLK	AGCTGATTGCCCTCAGAGTCCACTATTAAGGGTGCCGT				
1	C4	15[64]18[64]BLK	GTATAAGCCAACCCGTCGGATTCTGACGACAGTATCGGCCGCAAGGCG				
1	C5	13[64]15[63]BLK	TATATTTTGTCAATTCCTGAGAGTGAAGATT				
1	C6	11[64]13[63]BLK	GATTTAGTCAATAAAGCCTCAGAGAACCCTCA				

1	C7	9[64]11[63]BLK	CGGATTGCAGAGCTTAATTGCTGAAACGAGTA				
1	C8	7[56]9[63]BLK	ATGCAGATACATAACGGGAATCGTCATAAATAAGCAAAG				
1	C11	1[64]4[64]BLK	TTTATCAGGACAGCATCGGAACGACACCAACCTAAAACGAGGTCAATC				
1	C12	0[79]1[63]BLK	ACAACTTTCAACAGTTTCAGCGGATGTATCGG				
1	D1	23[64]22[80]BLK	AAAGCACTAAATCGGAACCCCTAATCCAGTT				P5
1	D2	22[79]20[80]BLK	TGGAACAACCGCCTGGCCCTGAGGCCCGCT				P5
1	D3	20[79]18[80]BLK	TTCCAGTCGTAATCATGGTCATAAAAGGGG				P5
1	D4	18[79]16[80]BLK	GATGTGCTTCAGGAAGATCGCACAAATGTGA			P3	P5
1	D5	16[79]14[80]BLK	GCGAGTAAAAATATTTAAATTTGTTACAAAAG			P3	P5
1	D6	14[79]12[80]BLK	GCTATCAGAAATGCAATGCCTGAATTAGCA	P1		P3	
1	D7	12[79]10[80]BLK	AAATTAAGTTGACATTAGATACTTTTTCGG	P1		P3	
1	D8	10[79]8[80]BLK	GATGGCTTATCAAAAAGATTAAGAGCGTCC				
1	D9	8[79]6[80]BLK	AATACTGCCCAAAAGGAATTACGTGGCTCA				
1	D10	6[79]4[80]BLK	TTATACCACCAATCAACGTAACGAACGAG				
1	D11	4[79]2[80]BLK	GCGCAGACAAGAGGCAAAAAGAAATCCCTCAG				
1	D12	2[79]0[80]BLK	CAGCGAACTTGCTTTTCGAGGTGTGCTAA				
1	E1	21[96]23[95]BLK	AGCAAGCGTAGGTTGAGTGTGTAGGGAGCC				
1	E2	19[96]21[95]BLK	CTGTGTGATTGCGTTGCGCTCACTAGAGTTGC				
1	E3	17[96]19[95]BLK	GCTTTCCGATTACGCCAGCTGGCGCTGTTTC				
1	E4	15[96]17[95]BLK	ATATTTTGGCTTTCATCAACATTATCCAGCCA			P3	
1	E5	13[96]15[95]BLK	TAGGTAAACTATTTTTGAGAGATCAAACGTTA				
1	E6	11[96]13[95]BLK	AATGGTCAACAGGCAAGGCAAGAGTAATGTG	P1			
1	E7	9[96]11[95]BLK	CGAAAGACTTTGATAAGAGGTCATATTTTCGCA				P5
1	E8	7[96]9[95]BLK	TAAGAGCAAATGTTTAGACTGGATAGGAAGCC	P1		P3	
1	E9	5[96]7[95]BLK	TCATTCAGATGCGATTTTAAGAACAGGCATAG				
1	E10	3[96]5[95]BLK	ACACTCATCCATGTTACTTAGCCGAAAGCTGC				
1	E11	1[96]3[95]BLK	AAACAGCTTTTTGCGGGATCGTCAACACTAAA				
1	E12	0[111]1[95]BLK	TAAATGAATTTTCTGTATGGGATTAATTTCTT				
1	F1	23[96]22[112]BLK	CCCGATTTAGAGCTTGACGGGAAAAAGAATA				
1	F2	22[111]20[112]BLK	GCCCGAGAGTCCACGCTGGTTTGCAGCTAACT				
1	F3	20[111]18[112]BLK	CACATFAAAATGTTATCCGCTCATGCGGGCC			P3	P1
1	F4	18[111]16[112]BLK	TCTTCGCTGCACCCTTCTGGTGCAGCCCTTC				
1	F5	16[111]14[112]BLK	TGTAGCCATTAATAATCGCATTAATGCCGGA	P1			
1	F6	14[111]12[112]BLK	GAGGGTAGGATTCAAAAGGGTGAGACATCCAA				
1	F7	12[111]10[112]BLK	TAAATCATATAACCTGTTTAGCTAACCTTTAA	P1		P5	P1
1	F8	10[111]8[112]BLK	TTGCTCCTTTCAAATATCGCGTTTGGGGGT			P3	
1	F9	8[111]6[112]BLK	AATAGTAAACACTATCATAACCCCTCATTTGTA				
1	F10	6[111]4[112]BLK	ATTACCTTTGAATAAGGCTTGCCCAAATCCGC				
1	F11	4[111]2[112]BLK	GACCTGCTCTTTGACCCCAAGGAGGAGTTA				P1
1	F12	2[111]0[112]BLK	AAGGCCGCTGATACCGATAGTTGCGACGTTAG				
1	G1	21[120]23[127]BLK	CCCAGCAGGCGAAAAATCCCTTATAAATCAAGCCGGCG				
1	G4	15[128]18[128]BLK	TAAATCAAAAATAATTCGCGTCTCGGAAACCAGGCAAAAGGAAGG				
1	G5	13[128]15[127]BLK	GAGACAGCTAGCTGATAAAATTAATTTTGT	P1			
1	G6	11[128]13[127]BLK	TTTGGGGATAGTAGTAGCATTAAGGCCG				
1	G7	9[128]11[127]BLK	GCTTCAATCAGGATTAGAGAGTTATTTTCA				P5
1	G8	7[120]9[127]BLK	CGTTTACCAGACGACAAAGAAGTTTTGCCATAATTCGA	P1		P3	
1	G11	1[128]4[128]BLK	TGACAACCTCGTGAGGCTTGCAATATACCAAGCGCGATGATAAA				
1	G12	0[143]1[127]BLK	TCTAAAGTTTTGTCGTCTTTCAGCCGACAA				

1	H1	21[160]22[144]BLK	TCAATATCGAACCTCAAATATCAATTCCGAAA				
1	H2	19[160]20[144]BLK	GCAATTCACATATTCCTGATTATCAAAGTGTA				
1	H3	17[160]18[144]BLK	AGAAAACAAGAAGATGATGAAACAGGCTGCG				
1	H4	15[160]16[144]BLK	ATCGCAAGTATGTAAATGCTGATGATAGGAAC	P1			
1	H5	13[160]14[144]BLK	GTAATAAGTTAGGCAGAGGCATTTATGATATT				
1	H6	11[160]12[144]BLK	CCAATAGCTCATCGTAGGAATCATGGCATCAA			P5	
1	H7	9[160]10[144]BLK	AGAGAGAAAAAATGAAAAATAGCAAGCAAAC	P1	P3		
1	H8	7[160]8[144]BLK	TTATTACGAAGAACTGGCATGATTGCGAGAGG				
1	H9	5[160]6[144]BLK	GCAAGGCCCTACCAGTAGCACCATGGGCTTGA				
1	H10	3[160]4[144]BLK	TTGACAGGCCACCACCAGAGCCGCGATTGTGA				
1	H11	1[160]2[144]BLK	TTAGGATTGGCTGAGACTCCTCAATAACCGAT				
1	H12	0[175]0[144]BLK	TCCACAGACAGCCCTCATAGTTAGCGTAAACGA				
2	A1	23[128]23[159]BLK	AACGTGGCGAGAAAGGAAGGAAACCAGTAA			P5	
2	A2	22[143]21[159]BLK	TCGGCAAATCCTGTTTGTATGGTGGACCTCAA			P5	
2	A3	20[143]19[159]BLK	AAGCCTGGTACGAGCCGGAAGCATAGATGATG			P5	
2	A4	18[143]17[159]BLK	CAACTGTTGCGCCATTGCGCCATTCAAACATCA	P1		P5	
2	A5	16[143]15[159]BLK	GCCATCAAGCTCATTTTTTAACCACAAATCCA			P5	
2	A6	14[143]13[159]BLK	CAACCGTTTCAAATCACCATCAATTCGAGCCA			P5	
2	A7	12[143]11[159]BLK	TTCTACTACGCGAGCTGAAAAGGTTACCGCGC		P3		
2	A8	10[143]9[159]BLK	CCAACAGGAGCGAACCAGACCCGAGCCTTAC	P1			
2	A9	8[143]7[159]BLK	CTTTTGCAGATAAAAAACAAAATAAAGACTCC				
2	A10	6[143]5[159]BLK	GATGGTTTGAACGAGTAGTAAATTTACCATTA				
2	A11	4[143]3[159]BLK	TCATCGCCAAACAAAGTACAACGGACGCCAGCA				
2	A12	2[143]1[159]BLK	ATATTCGGAACCATCGCCACGCAGAGAAGGA				
2	B1	23[160]22[176]BLK	TAAAAGGGACATTCTGGCCAACAAAGCATC				
2	B2	22[175]20[176]BLK	ACCTTGCTTGGTCAGTTGGCAAAGAGCGGA				
2	B3	20[175]18[176]BLK	ATTATCATTCAATATAATCCTGACAATTAC				P1
2	B4	18[175]16[176]BLK	CTGAGCAAAAATTAATTACATTTTGGGTTA				
2	B5	16[175]14[176]BLK	TATAACTAACAAAGAACGCGAGAACGCCAA		P3		
2	B6	14[175]12[176]BLK	CATGTAATAGAATATAAAGTACCAAGCCGT		P3	P5	
2	B7	12[175]10[176]BLK	TTTTATTTAAGCAAATCAGATATTTTTTGT	P1			P1
2	B8	10[175]8[176]BLK	TTAACGTCTAACATAAAAAACAGGTAACGGA				
2	B9	8[175]6[176]BLK	ATACCCAACAGTATGTTAGCAAATTAGAGC				
2	B10	6[175]4[176]BLK	CAGCAAAAAGGAAACGTCACCAATGAGCCGC				
2	B11	4[175]2[176]BLK	CACCAGAAAGGTTGAGGCAGGTCATGAAAG				P1
2	B12	2[175]0[176]BLK	TATTAAGAAGCGGGTTTTGCTCGTAGCAT				
2	C1	21[184]23[191]BLK	TCAACAGTTGAAAGGAGCAAAATGAAAAATCTAGAGATAGA				
2	C4	15[192]18[192]BLK	TCAAATATAACCTCCGGCTTAGGTAACAATTTTCATTTGAAGGCGAATT				
2	C5	13[192]15[191]BLK	GTAAAGTAATCGCCATATTTAACAAAACTTTT		P3		
2	C6	11[192]13[191]BLK	TATCCGGTCTCATCGAGAACAAGCGACAAAAG				
2	C7	9[192]11[191]BLK	TTAGACGGCCAAATAAGAAACGATAGAAGGCT			P5	
2	C8	7[184]9[191]BLK	CGTAGAAAAATACATACCAGGAAACGCAATAAGAAGCGCA	P1			
2	C11	1[192]4[192]BLK	GCGGATAACCTATTATCTGAAAACAGACGATTGGCCTTGAAGGCCAC				
2	C12	0[207]1[191]BLK	TCACCAGTACAACTACAACGCCCTAGTACCAG				
2	D1	23[192]22[208]BLK	ACCCTTCTGACCTGAAAGCGTAAGACGCTGAG				
2	D2	22[207]20[208]BLK	AGCCAGCAATTGAGGAAGGTTATCATCATTTTT				
2	D3	20[207]18[208]BLK	GCGGAACATCTGAATAATGGAAGGTACAAAAT		P3		
2	D4	18[207]16[208]BLK	CGCGCAGATTACCTTTTTTAAATGGGAGAGACT		P3		

2	D5	16[207]14[208]BLK	ACCTTTTTATTTTAGTTAATTTTCATAGGGCTT				
2	D6	14[207]12[208]BLK	AATTGAGAATTTGTCCAGACGACTAAACCAA				
2	D7	12[207]10[208]BLK	GTACCGCAATTTCAAGAACGCGAGTATTATTT	P1		P5	
2	D8	10[207]8[208]BLK	ATCCCAATGAGAATTAACAGAACAGTTACCAG				
2	D9	8[207]6[208]BLK	AAGGAAACATAAAGGTGGCAACATTATCACCG				
2	D10	6[207]4[208]BLK	TCACCGACGCACCGTAATCAGTAGCAGAACCG				
2	D11	4[207]2[208]BLK	CCACCTCTATTACAAAACAAATACCTGCCTA				
2	D12	2[207]0[208]BLK	TTTCGGAAGTGCCGTCGAGAGGGTGAGTTTCG				
2	E1	21[224]23[223]BLK	CTTTAGGGCCTGCAACAGTGCCAATACGTG				
2	E2	19[224]21[223]BLK	CTACCATAGTTTGAGTAAACATTTAAAAATAT				
2	E3	17[224]19[223]BLK	CATAAATCTTTGAATACCAAGTGTAGAAC		P3		
2	E4	15[224]17[223]BLK	CCTAAATCAAAATCATAGGTCTAAACAGTA		P3		
2	E5	13[224]15[223]BLK	ACAACATGCCAACGCTCAACAGTCTTCTGA		P3		
2	E6	11[224]13[223]BLK	GCGAACCTCCAAGAACGGGTATGACAATAA		P3		
2	E7	9[224]11[223]BLK	AAAGTCACAAAATAAACAGCCAGCGTTTTA		P3	P5	
2	E8	7[224]9[223]BLK	AACGCAAAGATAGCCGAACAAACCTGAAC	P1	P3		
2	E9	5[224]7[223]BLK	TCAAGTTTCATTTAAAGGTGAATATAAAAGA		P3		
2	E10	3[224]5[223]BLK	TTAAAGCCAGAGCCGCCACCTCGACAGAA				
2	E11	1[224]3[223]BLK	GTATAGCAAACAGTTAATGCCCAATCCTCA				
2	E12	0[239]1[223]BLK	AGGAACCCATGTACCGTAACACTTGATATAA				
2	F1	23[224]22[240]BLK	GCACAGACAATATTTTGAATGGGGTCAGTA			P5	
2	F2	22[239]20[240]BLK	TTAACACCAGCACTAACAACTAATCGTTATTA			P5	
2	F3	20[239]18[240]BLK	ATTTTAAAAATCAAAATTTATTTGCACGGATTCCG			P5	P1
2	F4	18[239]16[240]BLK	CCTGATTGCAATATATGTGAGTGATCAATAGT			P5	
2	F5	16[239]14[240]BLK	GAATTTATTTAATGGTTTGAATATCTTACC			P5	
2	F6	14[239]12[240]BLK	AGTATAAAGTTCAGCTAATGCAGATGTCTTTC			P5	
2	F7	12[239]10[240]BLK	CTTATCATCCCGACTTGCGGGAGCCTAATTT	P1			P1
2	F8	10[239]8[240]BLK	GCCAGTTAGAGGGTAATTGAGCGCTTTAAGAA				
2	F9	8[239]6[240]BLK	AAGTAAGCAGACACCACGGAATAATTTGACG				
2	F10	6[239]4[240]BLK	GAAATTTATGCTTTAGCGTCAGACCGGAACC				
2	F11	4[239]2[240]BLK	GCCTCCCTCAGAATGGAAAGCGCAGTAACAGT				P1
2	F12	2[239]0[240]BLK	GCCCGTATCCGGAATAGGTGTATCAGCCCAAT				
2	G1	21[248]23[255]BLK	AGATTAGAGCCGTCAAAAACAGAGGTGAGGCTATTAGT				
2	G4	15[256]18[256]BLK	GTGATAAAAAAGCGCTGAGAAGAGATAACCTTCTGTTCGGGAGA				
2	G5	13[256]15[255]BLK	GTTTATCAATATGCGTTATACAAACCGACCGT				
2	G6	11[256]13[255]BLK	GCCTTAAACCAATCAATAATCGGCACGCGCCT				
2	G7	9[256]11[255]BLK	GAGAGATAGAGCGTCTTCCAGAGGTTTTGAA				
2	G8	7[248]9[255]BLK	GTTTATTTGTCCACAATCTTACCGAAGCCCTTAATATCA	P1			
2	G11	1[256]4[256]BLK	CAGGAGGTGGGGTCAGTGCCTTGAGTCTCTGAATTTACCGGGAACCAG				
2	G12	0[271]1[255]BLK	CCACCTCATTTTTCAGGGATAGCAACCGTACT				
2	H1	23[256]22[272]BLK	CTTTAATGCGGGAAGTATAGCCCCACCAG				
2	H2	22[271]20[272]BLK	CAGAAGATTAGATAATACATTTGTCGACAA				
2	H3	20[271]18[272]BLK	CTCGTATTAGAAATGCGTAGATACAGTAC				
2	H4	18[271]16[272]BLK	CTTTTACAAAATCGTCGTATTAGCGATAG				
2	H5	16[271]14[272]BLK	CTTAGATTTAAGGCGTTAAATAAAGCCTGT				
2	H6	14[271]12[272]BLK	TTAGTATCACAATAGATAAGTCCACGAGCA				
2	H7	12[271]10[272]BLK	TGTAGAAATCAAGATTAGTTGCTCTTACCA				
2	H8	10[271]8[272]BLK	ACGCTAACACCCACAAGAATTGAAAATAGC				

2	H9	8[271]6[272]BLK	AATAGCTATCAATAGAAAATTCAACATTCA				
2	H10	6[271]4[272]BLK	ACCGATTGTCGGCATTTCGGTCATAATCA				
2	H11	4[271]2[272]BLK	AAATCACCTTCCAGTAAGCGTCAGTAATAA				
2	H12	2[271]0[272]BLK	GTTTTAACTTAGTACCGCCACCCAGAGCCA				

### Supplementary Table 8 | Biotinylated staple strands

Position	Name	Sequence	Modification
C02	18[63]20[56]BIOTIN	ATTAAGTTTACCAGACTCGAATTCGGGAAACCTGTCGTGC	5' - Biotin
C09	4[63]6[56]BIOTIN	ATAAGGGAACCGGATATTCATTACGTCAGGACGTTGGGAA	5' - Biotin
G02	18[127]20[120]BIOTIN	GCGATCGGCAATTCCACACAACAGGTGCCTAATGAGTG	5' - Biotin
G09	4[127]6[120]BIOTIN	TTGTGTCGTGACGAGAAACACCAAATTTCAACTTTAAT	5' - Biotin
K02	18[191]20[184]BIOTIN	ATTCATTTTTGTTGGATTATACTAAGAAACCACCAGAAG	5' - Biotin
K09	4[191]6[184]BIOTIN	CACCCTCAGAAACCATCGATAGCATTGAGCCATTTGGGAA	5' - Biotin
O02	18[255]20[248]BIOTIN	AACAATAACGTAAAACAGAAATAAAAATCCTTTGCCCGAA	5' - Biotin
O09	4[255]6[248]BIOTIN	AGCCACCACTGTAGCGCGTTTTCAAGGGAGGGAAGGTAAA	5' - Biotin

### Supplementary Table 9 | DNA-PAINT docking site sequences

Name	Sequence	Modification
P1 docking strand	TTATACATCTA	-
P3 docking strand	TTTCTTCATTA	-
P5 docking strand	TTCAATGTATG	-

### Supplementary Table 10 | DNA-PAINT imager sequences

Name	Sequence	Modification
Imager P1	CTAGATGTAT	3' – Cy3B
Imager P3	GTAATGAAGA	3' – Cy3B
Imager P5	CATACATTGA	3' – Cy3B

**nanoTRON Train:** *Digit 1, Digit 2, Digit 3 and 20 nm grid DNA origami*

Computer	CPU	Cores	Total runtime	Runtime per epoch
MacBook Pro 13 (early-2015)	Intel® Core™ i5-5257U @ 2.70GHz	2	~ 30 min	~ 1.1 min
MacBook Pro 15 (mid-2014)	Intel® Core™ i7-4980HQ @ 2.80GHz	4	~ 15 min	~ 0.5 min
Dell XPS 15 (9550)	Intel® Core™ i7-6700HQ @ 2.60GHz	4	~ 37 min	~ 1.3 min
Dell Precision T7910	2x Intel® Xeon® E5-2680 v3 @ 2.50GHz	24	~ 47 min	~ 1.7 min
Dell Precision T7910	2x Intel® Xeon® E5-2660 v3 @ 2.60GHz	20	~ 25 min	~ 0.9 min

**Supplementary Table 11 | Training runtime comparison with various computers.** The runtime for training of the 1-layer MLP with 550 nodes and the training data from **Supplementary Figure 4-7** was recorded on different computer systems. Three mobile devices and two high-performance workstations. Computation time ranges from 15 – 47 minutes. The training was performed using 247522 grayscale images.

**nanoTRON Predict:** 13332 nanopatterns with *Digit 1, Digit 2, Digit 3 and 20 nm grid DNA origami*

Computer	CPU	Cores	Runtime
MacBook Pro 13 (early-2015)	Intel® Core™ i5-5257U @ 2.70GHz	2	~ 9.3 min
MacBook Pro 15 (mid-2014)	Intel® Core™ i7-4980HQ @ 2.80GHz	4	~ 5.6 min
Dell XPS 15	Intel® Core™ i7-6700HQ @ 2.60GHz	4	~ 4.9 min
Dell Precision T7910	2x Intel® Xeon® E5-2680 v3 @ 2.50GHz	24	~ 4.2 min
Dell Precision T7910	2x Intel® Xeon® E5-2660 v3 @ 2.60GHz	20	~ 3.4 min

**Supplementary Table 12 | Prediction runtime comparison with various computers.** The runtime for prediction of the validation data set with four unique DNA origami nanopatterns (**Figure 1c**) was recorded on different computer systems. The nanoTRON model described in **Supplementary Text 2** was used. 13332 nanopatterns were classified between 3.4 – 9.3 minutes.

Training with *Digit 1*, *Digit 2*, *Digit 3* and 20 nm grid DNA origami

Neural network	Layout	Processed with	Total runtime	Runtime per epoch	Train accuracy	Test accuracy
nanoTRON MLP	1-layer FC 550 nodes	CPU	~ 47 min	~ 1.7 min	~ 0.99	~ 0.98
Keras LeNet-5	7-layer CNN	CPU	~ 36 h	~ 53 min	~ 0.99	~ 0.98
		GPU	~ 12 min	~ 0.3 min	~ 0.99	~ 0.98

CPU: 2x Intel® Xeon® E5-2680 v3 @ 2.50GHz (24 cores)

GPU: NVIDIA GeForce GTX 1080 Ti

**Supplementary Table 13 | nanoTRON MLP compared with LeNet-5 CNN.** Runtime and performance evaluation of the nanoTRON 1-layer perceptron described in **Supplementary Text 2** and the LeNet-5 convolutional neural network (CNN) (Lecun, et al., 1998) implemented in Keras (Chollet, 2015). The 7-layer CNN network design is listed in **Supplementary Table 14**. For the comparison, the augmented training data from **Supplementary Text 2** was used. The networks were trained in total with 247522 grayscale images. Input shape was 50 x 50 pixels with gray values from 0 to 1. Early stop callback was monitoring validation accuracy (10% split of training data) with a minimum change of 1E-4 over at least 10 epochs. Solver was set in all cases to “adam”. Both neural networks classified the test set of 74257 images with a test accuracy of around ~ 0.98. nanoTRON MLP reached the early stop after ~ 47 minutes with CPU processing, while the training of the LeNet-5 CNN lasted almost 1.5 days using the CPU. The same network trained with the high-performance GPU finished after ~ 12 min. This implies that CNN training is practically only feasible using GPU processing.

Layer type	Layer configuration	Output shape	Parameter #
Conv2D	Filter 6, Kernel 5, Stride 1, tanh	(None, 50, 50, 6)	156
Average Pooling 2D	Pool 2, Stride 1	(None, 25, 25, 6)	0
Conv2D	Filter 16, Kernel 5, Stride 1, tanh	(None, 21, 21, 16)	2416
Average Pooling 2D	Pool 2, Stride 1	(None, 10, 10, 16)	0
Conv2D	Filter 120, Kernel 5, Stride 1, tanh	(None, 6, 6, 120)	48120
Flatten		(None, 4320)	0
Dense	Units 84, tanh	(None, 84)	362964
Dense	Units 4, softmax	(None, 4)	340

Total parameters: 413,996

Trainable parameters: 413,996

Non-trainable parameters: 0

**Supplementary Table 14 | LeNet-5 CNN Design.** Convolutional neural network model design of the LeNet-5 implemented in Keras and used for comparison with the nanoTRON 1-layer MLP, described in **Supplementary Text 2**.

**Materials and buffers.** Unmodified DNA oligonucleotides, fluorescently modified DNA oligonucleotides and biotinylated DNA oligonucleotides were purchased from MWG Eurofins. M13mp18 scaffold was obtained from Tilibit. BSA-Biotin was obtained from Sigma-Aldrich (cat: A8549). Streptavidin was ordered from Invitrogen (cat: S-888). Tris 1M pH 8.0 (cat: AM9856), EDTA 0.5M pH 8.0 (cat: AM9261), Magnesium 1M (cat: AM9530G) and Sodium Chloride 5M (cat: AM9759) were ordered from Ambion. Ultrapure water (cat: 10977-035) was purchased from Gibco. Polyethylene glycol (PEG)-8000 (catalog no. 6510-1KG) was purchased from Merck. Glass slides (cat: 48811-703) were obtained from VWR. Coverslips were purchased from Marienfeld (cat: 0107032). Silicon (cat: 1300 1000) was ordered from picodent. Double sided tape (cat: 665D) was ordered from Scotch.

Two buffers were used for sample preparation and imaging:

- Buffer A (10 mM Tris-HCl pH 7.5, 100 mM NaCl, 0.05% Tween 20, pH 7.5)
- Buffer B (5 mM Tris-HCl pH 8, 10 mM MgCl<sub>2</sub>, 1 mM EDTA, 0.05% Tween 20, pH 8).
- Imaging Buffer B was supplemented with: 1× Trolox, 1× PCA and 1× PCD (see paragraph below for details). This photo-stabilization system allowed us to maximize the number of photons per event and thus achieve optimal spatial resolution.

Trolox, PCA and PCD stocks:

- 100× Trolox: 100mg Trolox, 430µl 100% methanol, 345 µl 1M NaOH in 3.2ml H<sub>2</sub>O.
- 40× PCA: 154mg PCA, 10ml water and NaOH were mixed and the pH was adjusted to 9.0.
- 100× PCD: 9.3mg PCD, 13.3ml of buffer was used (100 mM Tris-HCl pH 8, 50 mM KCl, 1mM EDTA, 50% glycerol).

### Optical setups.

Super-resolution setup 1: Fluorescence imaging was partly carried out (see Imaging conditions) on an inverted microscope (Nikon Instruments, Eclipse Ti) with the Perfect Focus System, applying an objective-type TIRF configuration with an oil-immersion objective (Nikon Instruments, Apo SR HP TIRF ×100, numerical aperture 1.49, Oil). A 561nm (Coherent Sapphire, 200 mW, DPSS-system) laser was used for excitation. The laser beam was passed through cleanup filters (Chroma Technology, ZET561/10) and coupled into the microscope objective using a beam splitter (Chroma Technology, ZT561rdc). Fluorescence light was spectrally filtered with an emission filter (Chroma Technology, ET600/50m and ET575lp) and imaged on a sCMOS camera (Andor, Zyla 4.2 Plus) without further magnification, resulting in an effective pixel size of 130nm (after 2×2 binning).

Super-resolution setup 3: Fluorescence imaging was partly carried out (see Imaging conditions) on an inverted microscope (Nikon Instruments, Eclipse Ti2) with the Perfect Focus System, applying an objective-type TIRF configuration with an oil-immersion objective (Nikon Instruments, Apo SR HP TIRF ×100, numerical aperture 1.49, Oil). A 560 nm (MPB Communications Inc., 500 mW, DPSS-system) laser was used for excitation. The laser beam was passed through cleanup filters (Chroma Technology, ZET561/10) and coupled into the microscope objective using a beam splitter (Chroma Technology, ZT561rdc). Fluorescence light was spectrally filtered with an emission filter (Chroma Technology, ET600/50m and ET575lp) and imaged on a sCMOS camera (Andor, Zyla 4.2 Plus) without further magnification, resulting in an effective pixel size of 130nm (after 2×2 binning).

**DNA origami self-assembly.** The Rothmund rectangular origami (RRO) from **Figure 1** were synthesized in a one-pot reaction with 50 µl total volume containing 10 nM scaffold strand (M13mp18), 100 nM core staples, 1 µM biotinylated staples and 1 µM DNA-PAINT handles. Sequences are listed in **Supplementary Table 6-9**. The folding buffer was 1x TE buffer with 12.5 mM MgCl<sub>2</sub>. Structures were annealed using a thermal ramp. First, incubating for 5 min at 80°C, then going from 65°C to 4°C over the course of 3 hours. DNA origami

structures were purified via two rounds of PEG precipitation by adding the same volume of PEG-buffer, centrifuging at 14,000g at 4°C for 30min, removing the supernatant and resuspending in folding buffer.

**Nanobody conjugation.** Unconjugated GFP Nanobody (Fluotag-Q anti-GFP) was purchased from Nanotag. The nanobody DNA conjugation was performed according to the protocol described before (Schlichthaerle, et al., 2018).

**Super-resolution DNA-PAINT imaging with DNA origami.** For chamber preparation, a piece of coverslip (no. 1.5, 18 × 18 mm, ~0.17 mm thick) and a glass slide (76 × 26 mm, 1 mm thick) were sandwiched together by two strips of double-sided tape to form a flow chamber with inner volume of ~20 µl. First, 20 µl of biotin-labeled bovine albumin (1 mg/ml, dissolved in buffer A) was flown into the chamber and incubated for 2 min. Then the chamber was washed using 40 µl of buffer A. Second, 20 µl of streptavidin (0.5mg/ml, dissolved in buffer A) was then flown through the chamber and incubated for 2 min. Next, the chamber was washed with 20 µl of buffer A and subsequently with 20 µl of buffer B. Then ~500 pM of the DNA origami structures (RRO) were flown into the chamber and allowed to attach to the surface for 2 min. Finally, the imaging buffer with buffer B with dye-labeled imager strands was flowed into the chamber and sealed with silicon. Imaging conditions are listed in **Supplementary Table 1-5**. Imager sequences are stated in **Supplementary Table 10**.

**Super-resolution DNA-PAINT imaging with nuclear pore complex.** Nuclear Pore Complex (NPC) imaging was performed using a U2OS cell line genetically modified with an EGFP fused to Nup96 proteins. The cells were fixed in 2.4% paraformaldehyde in PBS for 30 min. After fixation, cells were washed three times with PBS followed by permeabilization with 0.25% Triton-X-100 in PBS for 5 min. Then, cells were blocked in blocking buffer (3% BSA + 0.02% Tween-20) for 60 min. Anti-GFP nanobody conjugated to a DNA-PAINT docking site was diluted in blocking buffer to approximately 25 nM and incubated overnight at 4°C. On the next day, cells were washed 2x with PBS followed by an incubation with gold nanoparticles for 5 min. Cells were washed two times with PBS, then the imaging solution (PBS + 500 mM NaCl) was added containing 250 pM Cy3B labeled imager strands (Schueder, et al., 2019).

**Super-resolution reconstruction.** Raw fluorescence data was subjected to spot-finding and subsequent super-resolution reconstruction using the Picasso software package. The drift correction was performed with a redundant cross-correlation (segmentation: 1000) and subsequently *Undrift from picked* with all picked DNA origami structures. The DNA origami were picked using Picasso *Pick Tool* and *Pick similar*.

## References

- Belthangady, C. and Royer, L.A. Applications, promises, and pitfalls of deep learning for fluorescence image reconstruction. *Nature Methods* 2019;16(12):1215-1225.
- Chollet, F.a.o. 2015. Keras
- Hahnloser, R.H., et al. Digital selection and analogue amplification coexist in a cortex-inspired silicon circuit. *Nature* 2000;405(6789):947-951.
- He, K.M., et al. Delving Deep into Rectifiers: Surpassing Human-Level Performance on ImageNet Classification. *Ieee I Conf Comp Vis* 2015:1026-1034.
- Jungmann, R., et al. Single-molecule kinetics and super-resolution microscopy by fluorescence imaging of transient binding on DNA origami. *Nano Lett* 2010;10(11):4756-4761.
- Kingma, D.P., Ba, Jimmy. Adam: A Method for Stochastic Optimization. In.: arXiv e-prints; 2014. p. arXiv:1412.6980.
- Lecun, Y., et al. Gradient-based learning applied to document recognition. *P Ieee* 1998;86(11):2278-2324.
- Rothmund, P.W.K. Folding DNA to create nanoscale shapes and patterns. *Nature* 2006;440(7082):297-302.
- Schlichthaerle, T., et al. Site-Specific Labeling of Affimers for DNA-PAINT Microscopy. *Angew Chem Int Ed Engl* 2018;57(34):11060-11063.
- Schueder, F., et al. An order of magnitude faster DNA-PAINT imaging by optimized sequence design and buffer conditions. *Nat Methods* 2019.



## References

- [1] Alexander Auer et al.  
“Fast, Background-Free DNA-PAINT Imaging Using FRET-Based Probes.”  
In: *Nano Letters* 17.10 (Sept. 2017), pp. 6428–6434.
- [2] Alexander Auer et al. “Nanometer-scale Multiplexed Super-Resolution Imaging with an Economic 3D-DNA-PAINT Microscope.”  
In: *ChemPhysChem* 19.22 (2018), pp. 3024–3034.
- [3] Alexander Auer et al.  
“nanoTRON: a Picasso module for MLP-based classification of super-resolution data.”  
In: *Bioinformatics* (2020).
- [4] Nina S. Deußner-Helfmann et al.  
“Correlative Single-Molecule FRET and DNA-PAINT Imaging.”  
In: *Nano Letters* 18.7 (June 2018), pp. 4626–4630.
- [5] Thomas Schlichthaerle et al.  
“Bacterially Derived Antibody Binders as Small Adapters for DNA-PAINT Microscopy.”  
In: *ChemBioChem* 20.8 (2019), pp. 1032–1038.
- [6] Thomas Schlichthaerle et al. “Direct Visualization of Single Nuclear Pore Complex Proteins Using Genetically-Encoded Probes for DNA-PAINT.”  
In: *Angewandte Chemie International Edition* 58.37 (2019), pp. 13004–13008.
- [7] Florian Schueder et al. “An order of magnitude faster DNA-PAINT imaging by optimized sequence design and buffer conditions.”  
In: *Nature Methods* 16.11 (Oct. 2019), pp. 1101–1104.
- [8] Ernst Abbe.  
“Beiträge zur Theorie des Mikroskops und der mikroskopischen Wahrnehmung.”  
In: *Archiv für mikroskopische Anatomie* 9.1 (1873), pp. 413–418.
- [9] Eric Betzig et al. “Imaging Intracellular Fluorescent Proteins at Nanometer Resolution.”  
In: *Science* 313.5793 (2006), pp. 1642–1645.
- [10] Stefan W. Hell and Jan Wichmann. “Breaking the diffraction resolution limit by stimulated emission: stimulated-emission-depletion fluorescence microscopy.”  
In: *Optics Letters* 19.11 (June 1994), pp. 780–782.
- [11] NobelPrize.org. *The Nobel Prize in Chemistry 2014*. Nobel Media AB 2020.
- [12] Ralf Dahm.  
“Discovering DNA: Friedrich Miescher and the early years of nucleic acid research.”  
In: *Human Genetics* 122.6 (2008), pp. 565–581.
- [13] Phoebus A. Levene. “The structure of yeast nucleic acid: IV. Ammonia Hydrolysis.”  
In: *Journal of Biological Chemistry* 40.2 (Dec. 1919), pp. 415–424.
- [14] Rosalind E. Franklin and Raymond G. Gosling.  
“Molecular Configuration in Sodium Thymonucleate.”  
In: *Nature* 171.4356 (Apr. 1953), pp. 740–741.
- [15] James D. Watson and Francis H. C. Crick.  
“Molecular Structure of Nucleic Acids: A Structure for Deoxyribose Nucleic Acid.”  
In: *Nature* 171.4356 (Apr. 1953), pp. 737–738.

- [16] Nadrian C. Seeman. “Nucleic acid junctions and lattices.”  
In: *Journal of Theoretical Biology* 99.2 (1982), pp. 237–247.
- [17] Paul W. K. Rothemund. “Folding DNA to create nanoscale shapes and patterns.”  
In: *Nature* 440.7082 (Mar. 2006), pp. 297–302.
- [18] Shawn M. Douglas et al.  
“Self-assembly of DNA into nanoscale three-dimensional shapes.”  
In: *Nature* 459.7245 (May 2009), pp. 414–418.
- [19] Hendrik Dietz, Shawn M. Douglas, and William M. Shih.  
“Folding DNA into twisted and curved nanoscale shapes.”  
In: *Science* 325.5941 (Aug. 2009), pp. 725–30.
- [20] Tim Liedl et al.  
“Self-assembly of three-dimensional prestressed tensegrity structures from DNA.”  
In: *Nature Nanotechnology Nanotechnol* 5.7 (July 2010), pp. 520–4.
- [21] Nadrian C. Seeman. “DNA in a material world.”  
In: *Nature* 421.6921 (Jan. 2003), pp. 427–431.
- [22] David L. Poole and Alan K. Mackworth.  
*Artificial intelligence: foundations of computational agents*.  
New York: Cambridge University Press, 2010.
- [23] Ian Goodfellow, Yoshua Bengio, and Aaron Courville. *Deep Learning*. MIT Press, 2016.
- [24] Aleksander Jablonski. “Efficiency of anti-stokes fluorescence in dyes.”  
In: *Nature* 131 (Jan. 1933), pp. 839–840.
- [25] George Gabriel Stokes. “On the change of refrangibility of light.”  
In: *Philosophical Transactions of the Royal Society of London* 142 (1852), pp. 463–562.
- [26] Graham T. Dempsey et al. “Evaluation of fluorophores for optimal performance in localization-based super-resolution imaging.”  
In: *Nature Methods* 8.12 (Dec. 2011), pp. 1027–1036.
- [27] Joseph R. Lakowicz. *Principles of Fluorescence Spectroscopy*. 3rd ed.  
New York: Springer, 2006.
- [28] ATTO-TEC. *Spectral Properties ATTO 565 Fluorescence Dye*.  
ATTO-TEC GmbH. Am Eichenhang 50, 57076 Siegen, Jan. 2020.
- [29] Edmund J. Ambrose. “A Surface Contact Microscope for the study of Cell Movements.”  
In: *Nature* 178.4543 (1956), pp. 1194–1194.
- [30] Nancy L. Thompson, Thomas P. Burghardt, and Daniel Axelrod.  
“Measuring surface dynamics of biomolecules by total internal reflection fluorescence with photobleaching recovery or correlation spectroscopy.”  
In: *Biophysical Journal* 33.3 (Mar. 1981), pp. 435–54.
- [31] Mel N. Kronick and William A. Little. “A new immunoassay based on fluorescence excitation by internal reflection spectroscopy.”  
In: *Journal of Immunological Methods* 8.3 (1975), pp. 235–240.
- [32] H. Michelle Grandin et al. “Waveguide excitation fluorescence microscopy: A new tool for sensing and imaging the biointerface.”  
In: *Biosensors and Bioelectronics* 21.8 (Feb. 2006), pp. 1476–1482.
- [33] Anna Archetti et al. “Waveguide-PAINT offers an open platform for large field-of-view super-resolution imaging.” In: *Nature Communications* 10.1 (Mar. 2019), p. 1267.

- [34] Andrea L. Stout and Daniel Axelrod.  
“Evanescence field excitation of fluorescence by epi-illumination microscopy.”  
In: *Applied Optics* 28.24 (Dec. 1989), pp. 5237–5242.
- [35] Makio Tokunaga, Naoko Imamoto, and Kumiko Sakata-Sogawa.  
“Highly inclined thin illumination enables clear single-molecule imaging in cells.”  
In: *Nature Methods* 5.2 (Feb. 2008), pp. 159–161.
- [36] Thomas A. Klar and Stefan W. Hell.  
“Subdiffraction resolution in far-field fluorescence microscopy.”  
In: *Optics Letters* 24.14 (July 1999), pp. 954–956.
- [37] Thomas A. Klar et al. “Fluorescence microscopy with diffraction resolution barrier broken by stimulated emission.”  
In: *Proceedings of the National Academy of Sciences* 97.15 (July 2000), pp. 8206–10.
- [38] Lord Rayleigh Sec. Robert Strutt.  
“XV. On the theory of optical images, with special reference to the microscope.”  
In: *The London, Edinburgh, and Dublin Philosophical Magazine and Journal of Science* 42.255 (1896), pp. 167–195.
- [39] Hermann von Helmholtz. “Ueber die Grenzen der Leistungsfähigkeit der Mikroskope.”  
In: *Monatsbericht der Königlich-Preussischen Akademie der Wissenschaften zu Berlin* (Oct. 1873), pp. 625–626.
- [40] Hermann von Helmholtz.  
“Die theoretische Grenze für die Leistungsfähigkeit der Mikroskope.”  
In: *Annalen der Physik und Chemie*. Jubelband (1874), pp. 557–584.
- [41] Ulrich Kubitscheck. “Principles of Light Microscopy.” In: *Fluorescence Microscopy*. 2nd. Wiley-VCH Verlag GmbH & Co. KGaA, 2017, pp. 33–95.
- [42] Emmanuel J. Candès and Carlos Fernandez-Granda.  
“Towards a Mathematical Theory of Super-resolution.”  
In: *Communications on Pure and Applied Mathematics* 67.6 (2014), pp. 906–956.
- [43] George H. Patterson and Jennifer Lippincott-Schwartz.  
“A photoactivatable GFP for selective photolabeling of proteins and cells.”  
In: *Science* 297.5588 (Sept. 2002), pp. 1873–1877.
- [44] Johannes Hohlbein et al.  
“Surfing on a new wave of single-molecule fluorescence methods.”  
In: *Physical Biology* 7.3 (Aug. 2010), p. 031001.
- [45] Joerg Schnitzbauer et al. “Super-resolution microscopy with DNA-PAINT.”  
In: *Nature Protocols* 12.6 (June 2017), pp. 1198–1228.
- [46] Daniel Sage et al. “Super-resolution fight club: assessment of 2D and 3D single-molecule localization microscopy software.” In: *Nature Methods* 16.5 (Mai 2019), pp. 387–+.
- [47] Russell E. Thompson, Daniel R. Larson, and Watt W. Webb.  
“Precise nanometer localization analysis for individual fluorescent probes.”  
In: *Biophysical Journal* 82.5 (May 2002), pp. 2775–2783.
- [48] Michael J. Rust, Mark Bates, and Xiaowei Zhuang. “Sub-diffraction-limit imaging by stochastic optical reconstruction microscopy (STORM).”  
In: *Nature Methods* 3.10 (Oct. 2006), pp. 793–796.
- [49] Bo Huang, Mark Bates, and Xiaowei Zhuang.  
“Super-Resolution Fluorescence Microscopy.”  
In: *Annual Review of Biochemistry* 78.1 (2009). PMID: 19489737, pp. 993–1016.

- [50] Ralf Jungmann et al. “Single-molecule kinetics and super-resolution microscopy by fluorescence imaging of transient binding on DNA origami.”  
In: *Nano Letters* 10.11 (Nov. 2010), pp. 4756–61.
- [51] Alexey Sharonov and Robin M. Hochstrasser.  
“Wide-field subdiffraction imaging by accumulated binding of diffusing probes.”  
In: *Proceedings of the National Academy of Sciences* 103.50 (Dezember 2006),  
pp. 18911–18916.
- [52] Ralf Jungmann et al. “Multiplexed 3D cellular super-resolution imaging with DNA-PAINT and Exchange-PAINT.”  
In: *Nature Methods* 11.3 (Mar. 2014), pp. 313–8.
- [53] Albert Einstein. “Zur Quantentheorie der Strahlung.”  
In: *Mitteilungen der Physikalischen Gesellschaft Zürich. Nr. 18* (1916).
- [54] Francisco Balzarotti et al. “Nanometer resolution imaging and tracking of fluorescent molecules with minimal photon fluxes.” In: *Science* 355.6325 (Feb. 2017), pp. 606–612.
- [55] Klaus C. Gwosch et al.  
“MINFLUX nanoscopy delivers 3D multicolor nanometer resolution in cells.”  
In: *Nature Methods* (Jan. 2020).
- [56] Theodor Förster. “Zwischenmolekulare Energiewanderung und Fluoreszenz.”  
In: *Annalen der Physik* 437.1-2 (1948), pp. 55–75.
- [57] B. Wieb van der Meer. “Förster Theory.” In: *FRET – Förster Resonance Energy Transfer*. John Wiley & Sons, Ltd, 2013. Chap. 3, pp. 23–62.
- [58] David L. Dexter. “A Theory of Sensitized Luminescence in Solids.”  
In: *The Journal of Chemical Physics* 21.5 (1953), pp. 836–850.
- [59] B. Wieb van der Meer, Daniel M. van der Meer, and Steven S. Vogel. “Optimizing the Orientation Factor Kappa-Squared for More Accurate FRET Measurements.” In: *FRET – Förster Resonance Energy Transfer*. John Wiley & Sons, Ltd, 2013. Chap. 4, pp. 63–104.
- [60] Thermo Fisher Scientific. *Spectral Properties Cy3 and Cy5 Fluorescence Dye*. Thermo Fisher Scientific Corporation. Waltham, Massachusetts, USA, Jan. 2020.
- [61] Niko Hildebrandt. “How to Apply FRET: From Experimental Design to Data Analysis.”  
In: *FRET – Förster Resonance Energy Transfer*. John Wiley & Sons, Ltd, 2013. Chap. 5, pp. 105–163.
- [62] Victor A. Bloomfield, Donald M. Crothers, and Ignacio Tinoco.  
*Nucleic acids: structures, properties, and functions*.  
Sausalito, Calif.: University Science Books, 2000.
- [63] Horace R. Drew et al. “Structure of a B-DNA dodecamer: conformation and dynamics.”  
In: *Proceedings of the National Academy of Sciences* 78.4 (Apr. 1981), pp. 2179–83.
- [64] Schrödinger, LLC.  
“The PyMOL Molecular Graphics System, Version 2.3.4 Schrödinger, LLC.” Nov. 2015.
- [65] Ralf Jungmann et al.  
“DNA origami-based nanoribbons: assembly, length distribution, and twist.”  
In: *Nanotechnology* 22.27 (July 2011), p. 275301.
- [66] Thomas Schlichthaerle et al. “DNA nanotechnology and fluorescence applications.”  
In: *Current Opinion in Biotechnology* 39 (June 2016), pp. 41–47.

- [67] Mingjie Dai, Ralf Jungmann, and Peng Yin. “Optical imaging of individual biomolecules in densely packed clusters.” In: *Nature Nanotechnology* 11.9 (Sept. 2016), pp. 798–807.
- [68] Nina S. Deußner-Helfmann et al. “Correlative Single-Molecule FRET and DNA-PAINT Imaging.” In: *Nano Letters* 18.7 (July 2018), pp. 4626–4630.
- [69] Johannes Stein et al. “Toward Absolute Molecular Numbers in DNA-PAINT.” In: *Nano Letters* 19.11 (2019), pp. 8182–8190.
- [70] Hamidreza Heydarian et al. “Template-free 2D particle fusion in localization microscopy.” In: *Nature Methods* 15.10 (Oct. 2018), pp. 781–784.
- [71] Jonas Mücksch et al. “Quantifying Reversible Surface Binding via Surface-Integrated Fluorescence Correlation Spectroscopy.” In: *Nano Letters* 18.5 (May 2018), pp. 3185–3192.
- [72] Christian Steinhauer et al. “DNA origami as a nanoscopic ruler for super-resolution microscopy.” In: *Angewandte Chemie* 48.47 (2009), pp. 8870–3.
- [73] Florian Schueder et al. “Multiplexed 3D super-resolution imaging of whole cells using spinning disk confocal microscopy and DNA-PAINT.” In: *Nature Communications* 8.1 (Dec. 2017), p. 2090.
- [74] Mario Raab et al. “Using DNA origami nanorulers as traceable distance measurement standards and nanoscopic benchmark structures.” In: *Scientific Reports* 8.1 (Jan. 2018), p. 1780.
- [75] Lusheng Gu et al. “Molecular resolution imaging by repetitive optical selective exposure.” In: *Nature Methods* 16.11 (Nov. 2019), pp. 1114–1118.
- [76] Lex Fridman et al. “MIT Advanced Vehicle Technology Study: Large-Scale Naturalistic Driving Study of Driver Behavior and Interaction With Automation.” In: *IEEE Access* 7 (2019), pp. 102021–102038.
- [77] Andre Esteva et al. “A guide to deep learning in healthcare.” In: *Nature Methods* 25.1 (Jan. 2019), pp. 24–29.
- [78] Yann LeCun, Yoshua Bengio, and Geoffrey Hinton. “Deep learning.” In: *Nature* 521.7553 (May 2015), pp. 436–44.
- [79] Gao Huang et al. “Densely Connected Convolutional Networks.” In: *CVPR*. IEEE Computer Society, 2017, pp. 2261–2269.
- [80] Kaiming He et al. “Deep Residual Learning for Image Recognition.” In: *CVPR*. IEEE Computer Society, 2016, pp. 770–778.
- [81] Warren S. McCulloch and Walter Pitts. “A logical calculus of the ideas immanent in nervous activity.” In: *The Bulletin of Mathematical Biophysics* 5.4 (1943), pp. 115–133.
- [82] Donald O. Hebb. *The organization of behavior; a neuropsychological theory*. Oxford, England: Wiley, 1949, pp. xix, 335–xix, 335.
- [83] Frank Rosenblatt. “The perceptron: a probabilistic model for information storage and organization in the brain.” In: *Psychological Review* 65.6 (Nov. 1958), pp. 386–408.
- [84] John D. Kelleher. *Deep Learning*. MIT Press Essential Knowledge series. MIT Press, 2019.

- [85] Simon S. Haykin. *Neural networks and learning machines*. 3rd ed. New York: Prentice Hall, 2009.
- [86] Yann Lecun et al. “Gradient-based learning applied to document recognition.” In: *Proceedings of the IEEE* 86.11 (Nov. 1998), pp. 2278–2324.
- [87] Alex Krizhevsky, Ilya Sutskever, and Geoffrey E. Hinton. “ImageNet Classification with Deep Convolutional Neural Networks.” In: *NIPS*. 2012, pp. 1106–1114.
- [88] Alex Krizhevsky, Ilya Sutskever, and Geoffrey E. Hinton. “ImageNet classification with deep convolutional neural networks.” In: *Communications of the ACM* 60.6 (2017), pp. 84–90.
- [89] Christian Szegedy et al. “Going deeper with convolutions.” In: *CVPR*. IEEE Computer Society, 2015, pp. 1–9.
- [90] Kevin Jarrett et al. “What is the best multi-stage architecture for object recognition?” In: *ICCV*. IEEE Computer Society, 2009, pp. 2146–2153.
- [91] Christopher Bishop. *Pattern Recognition and Machine Learning*. Ed. by 5th Edition. Information science and statistics. Springer-Verlag New York, 2006.
- [92] Bernard Widrow and Marcian E. Hoff. “Adaptive Switching Circuits.” In: *1960 IRE WESCON Convention Record, Part 4*. New York: IRE, 1960, pp. 96–104.
- [93] M. Minsky, S.A. Papert, and L. Bottou. *Perceptrons: An Introduction to Computational Geometry*. MIT Press, 2017.
- [94] Frank Rosenblatt. *Principles of neurodynamics: perceptrons and the theory of brain mechanisms*. Washington: Spartan Books, 1962.
- [95] Jürgen Schmidhuber. “Deep learning in neural networks: an overview.” In: *Neural Networks* 61 (Jan. 2015), pp. 85–117.
- [96] Drew McDermott et al. “The Dark Ages of AI: A Panel Discussion at AAAI-84.” In: *AI Magazine* 6.3 (1985), pp. 122–134.
- [97] Tim Menzies. “Guest Editor’s Introduction: 21st Century AI: Proud, Not Smug.” In: *IEEE Intelligent Systems* 18.3 (2003), pp. 18–24.
- [98] David E. Rumelhart, James L. McClelland, and CORPORATE PDP Research Group, eds. *Parallel Distributed Processing: Explorations in the Microstructure of Cognition, Vol. 1: Foundations*. Cambridge, MA, USA: MIT Press, 1986.
- [99] David E. Rumelhart, James L. McClelland, and CORPORATE PDP Research Group, eds. *Parallel Distributed Processing: Explorations in the Microstructure of Cognition, Vol. 2: Psychological and Biological Models*. Cambridge, MA, USA: MIT Press, 1986.
- [100] Kevin P. Murphy. *Machine learning: a probabilistic perspective*. Adaptive computation and machine learning series. Cambridge, MA: MIT Press, 2012.
- [101] Jürgen Kiefer and Jacob Wolfowitz. “Stochastic Estimation of the Maximum of a Regression Function.” In: *The Annals of Mathematical Statistics* 23.3 (Sept. 1952), pp. 462–466.
- [102] Herbert Robbins and Sutton Monro. “A Stochastic Approximation Method.” In: *The Annals of Mathematical Statistics* 22.3 (Sept. 1951), pp. 400–407.
- [103] Yann Lecun. “Generalization and network design strategies.” English (US). In: *Connectionism in perspective*. Ed. by R. Pfeifer et al. Elsevier, 1989.

- [104] Kunihiko Fukushima. “Neocognitron: a self organizing neural network model for a mechanism of pattern recognition unaffected by shift in position.”  
In: *Biological Cybernetics* 36.4 (1980), pp. 193–202.
- [105] Kyoung-Su Oh and Keechul Jung. “GPU implementation of neural networks.”  
In: *Pattern Recognition* 37.6 (2004), pp. 1311–1314.
- [106] Fang Huang et al. “Video-rate nanoscopy using sCMOS camera-specific single-molecule localization algorithms.” In: *Nature Methods* 10.7 (July 2013), pp. 653–8.
- [107] Bi-Chang Chen et al. “Lattice light-sheet microscopy: Imaging molecules to embryos at high spatiotemporal resolution.” In: *Science* 346.6208 (Oktober 2014), pp. 439–+.
- [108] Rory M. Power and Jan Huiskens.  
“Putting advanced microscopy in the hands of biologists.”  
In: *Nature Methods* 16.11 (Nov. 2019), pp. 1069–1073.
- [109] Bo Huang et al. “Three-dimensional super-resolution imaging by stochastic optical reconstruction microscopy.” In: *Science* 319.5864 (Feb. 2008), pp. 810–813.
- [110] Clément Cabriel et al.  
“Aberration-accounting calibration for 3D single-molecule localization microscopy.”  
In: *Optics Letters* 43.2 (Jan. 2018), pp. 174–177.
- [111] Guido Van Rossum and Fred L. Drake. *Python 3 Reference Manual*.  
Scotts Valley, CA: CreateSpace, 2009.
- [112] Ralf Jungmann et al. “Quantitative super-resolution imaging with qPAINT.”  
In: *Nature Methods* 13.5 (2016), pp. 439–442.
- [113] François Chollet et al. *Keras*. <https://keras.io>. 2015.
- [114] Theano Development Team.  
“Theano: A Python framework for fast computation of mathematical expressions.”  
In: *arXiv abs/1605.02688* (May 2016).
- [115] Adam Paszke et al.  
“PyTorch: An Imperative Style, High-Performance Deep Learning Library.”  
In: *Advances in Neural Information Processing Systems* 32. Ed. by H. Wallach et al. Curran Associates, Inc., 2019, pp. 8024–8035.
- [116] Sara Goodwin, John D. McPherson, and W. Richard McCombie.  
“Coming of age: ten years of next-generation sequencing technologies.”  
In: *Nature reviews. Genetics* 17.6 (May 2016), pp. 333–51.
- [117] Daniel J. Nieves, Katharina Gaus, and Matthew A. B. Baker.  
“DNA-Based Super-Resolution Microscopy: DNA-PAINT.”  
In: *Genes (Basel)* 9.12 (Dec. 2018).

